MSc Thesis

Experimental Investigation of Compressibility Effects on the Flow Field and Aerodynamic Loads of the FFA-W3-211 Wind Turbine Airfoil in Transonic Conditions

AE5122: Thesis Aerodynamics & Wind Energy

J.A. Villalta Alas

Delft University of Technology

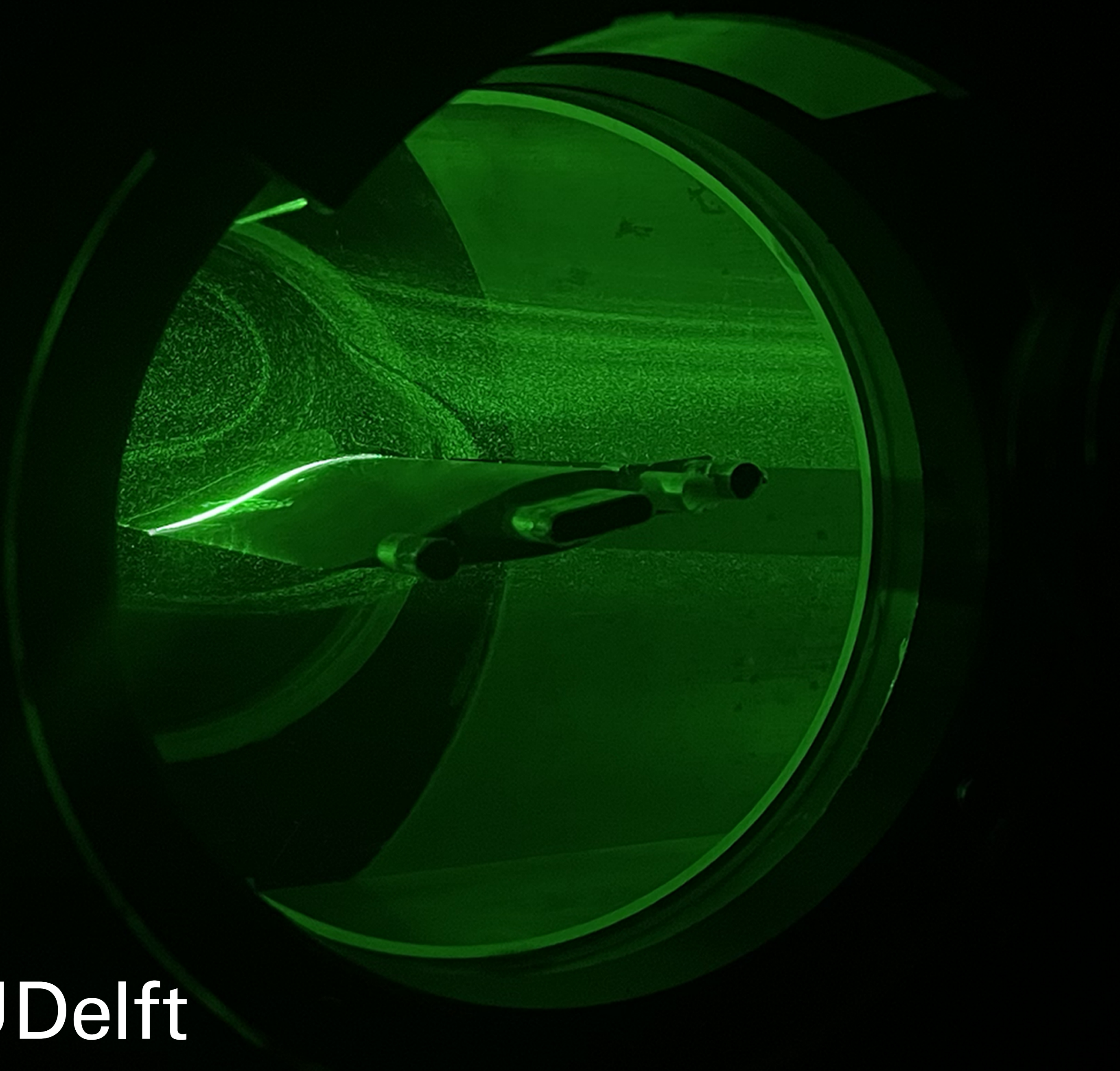

TU Delft

MSc Thesis

Experimental Investigation of Compressibility Effects on the Flow Field and Aerodynamic Loads of the FFA-W3-211 Wind Turbine Airfoil in Transonic Conditions

by

J.A. Villalta Alas

Student Name	Student Number
Jose Villalta	5095077

TU Delft supervisor:	Delphine De Tavernier
Project Duration:	July, 2024 - June, 2025
Faculty:	Faculty of Aerospace Engineering, Delft

TU Delft

Preface

This report documents the work conducted by Jose Andres Villalta Alas during his thesis project from July 2024 to June 2025, within the faculty of Aerospace Engineering at the Technical University of Delft.

In recent years, I have been captivated by sustainability, and, in particular, the transition into renewable sources of energy. As an engineer, I feel the drive and responsibility to be involved in projects that contribute positively to sustainability. Given my background in Aerospace engineering, a specialisation in Aerodynamics, and having completed my minor in Offshore wind energy, I soon found interest in the world of wind energy. My thesis project focuses on the experimental assessment of the aerodynamic loads on a wind turbine airfoil under transonic conditions. Although the conditions tested may be considered relatively far from current expectations, this study will provide information on the effects of compressibility at the airfoil level of wind turbines.

I would like to acknowledge the contributions of people that have made it possible for me to complete my thesis project. I would like to thank my friends in El Salvador and in The Netherlands for their support and amazing memories. I would like to extend my gratitude to the Aerodynamics technical staff. Thank you Peter and Frits, for helping me with the experimental setup, for your time sitting next to me and Abhyuday in the control room, and keeping up with the countless number of experimental runs (82 to be exact!). I am grateful for my amazing supervisors Delphine De Tavernier and Abhyuday Adidtya, who welcomed me into their team with open arms. My experience would have been incomplete without your passion, kind support and guidance. Thank you, Ferry and Bas, for your time, insightful feedback and guidance throughout the entire project.

To my family back in El Salvador, les dedico este trabajo a ustedes. Jose Freddy, Katia Alas, Camila Renee, Mamá Yoly, Mamá Maru, Papá René, Papá Freddy, fue su gran esfuerzo y apoyo constante lo que me brindó la oportunidad de estudiar en el extranjero, de completar mi licenciatura y ahora mi maestría en una universidad tan prestigiosa. La distancia nos ha separado por más de seis años, pero siempre los he llevado cerca en mi corazón. Siempre estaré agradecido con ustedes, Jose Freddy y Katia Alas, por creer en mí, por todos sus sacrificios y por su amor incondicional, que me ha guiado en los momentos buenos y malos. Nunca me hubiera imaginado llegar tan lejos sin su ayuda y la de Dios. A el le agradezco por darme una familia tan especial.

J.A. Villalta Alas
Delft, June 2025

Summary

As wind turbine rotors grow larger, compressibility effects near the blade tip become an emerging concern. This research experimentally investigated compressibility effects on the flow field and aerodynamic performance of the FFA-W3-211 wind turbine airfoil at Mach numbers within 0.5-0.65 and angles of attack from -4° to -11°. An experimental campaign was conducted at the TST-27 wind tunnel at TU Delft using Particle Image Velocimetry (PIV) and Schlieren techniques. Non-intrusive pressure field reconstruction and load determination methods are used to infer the aerodynamic loads from the flow field data.

Results show that compressibility strongly influences the mean flow field and aerodynamic loads of the FFA-W3-211 airfoil. Trends toward transonic flow and unsteady shock waves were identified with increasing absolute AoA and freestream Mach number. The results at $\alpha = -6°$ display a 30% reduction in the negative lift coefficient from $c_l = -0.43$ to -0.31 and a 190% increase in drag coefficient from $c_d = 0.026$ to 0.075, with increasing Mach number from $M_\infty = 0.5$ to 0.65. For the same Mach number range, the lift coefficient results at $\alpha = -10°$ display a plateau around $c_l \approx -0.65$ to -0.67, and a 100% increase in drag coefficient, from $c_d = 0.085$ to 0.174. At moderate AoA, the increased mean drag was influenced by the growth of trailing edge separation. Beyond $M_\infty - 0.6$, the emergence of shock waves plays a greater role in inducing an earlier separation and less efficient pressure recovery. The growth of the separation region decreases the mean negative lift for $\alpha \leq$-6°. For $\alpha \geq$-8°, conversely, the emergence of supersonic flow and lower pressures over the trailing edge counteract the effects of increased separation. For the phase-averaged analysis of the transonic buffet cycle at $\alpha = -10°$ and $M_\infty = 0.65$, the phase-averaged lift coefficient varies periodically in a range of approximately ~22% of the time-averaged lift coefficient, while the phase-averaged drag coefficient varies up to ~80% of the time-averaged drag coefficient.

This work is part of the foundation for understanding the effects of compressibility in wind turbine airfoils and wind turbines. It identifies the complex interplay of shock waves, separation, and SWBLI in the transonic regime. The results highlight and challenge current assumptions of incompressible flow for the design and operation of modern and future large-scale wind turbines that rely on incompressible aerodynamic polars.

Contents

Preface i

Summary ii

Nomenclature xi

1 Introduction 1
1.1 Research objectives, questions and hypotheses . . . 2

2 Literature Review 4
2.1 Wind turbine aerodynamics . . . 5
2.1.1 Basic principles . . . 5
2.1.2 Wind turbine aerodynamic performance . . . 7
2.1.3 The emergence of compressible and transonic flow in wind turbines . . . 10
2.2 Compressible and transonic aerodynamics of airfoils . . . 13
2.2.1 Basic principles . . . 13
2.2.2 Shock Wave - Boundary Layer Interaction . . . 16
2.2.3 Transonic buffet . . . 19
2.2.4 State-of-the-art research for wind turbine airfoils in transonic flow . . . 21
2.3 Experimental measurement techniques . . . 25
2.3.1 Wind tunnel facilities . . . 26
2.3.2 Flow-field measurements . . . 26
2.3.3 Pressure and aerodynamic load measurements . . . 28

3 Experimental setup 30
3.1 Wind tunnel facility . . . 30
3.1.1 TST-27 Components . . . 31
3.1.2 Transonic Mach number control . . . 31
3.2 Blockage correction . . . 32
3.3 Airfoil geometry and experimental models . . . 33
3.3.1 The FFA-W3-211 airfoil . . . 33
3.3.2 The NACA 0012 airfoil . . . 34
3.4 Schlieren technique . . . 35
3.4.1 Working principles of Schlieren . . . 35
3.4.2 Schlieren setup . . . 37
3.5 Particle Image Velocimetry technique . . . 37
3.5.1 From instantaneous snapshots to velocity fields . . . 38
3.5.2 PIV setup . . . 39
3.6 Testing conditions . . . 45
3.6.1 Schlieren campaign . . . 46
3.6.2 Oil flow campaign . . . 48
3.6.3 PIV campaign . . . 48

4 Data processing and analysis 51
4.1 Spectral Analysis using Schlieren data . . . 51
4.2 Pre-processing of PIV velocity data . . . 52
4.3 Mean flow field analysis . . . 54
4.3.1 Separated flow and supersonic flow criteria . . . 54
4.3.2 Pressure field reconstruction . . . 55
4.3.3 Aerodynamic load calculation . . . 57
4.4 Phased-averaged flow field analysis . . . 60

4.4.1 Shock wave identification . . . 60
4.4.2 Phase-definition . . . 61
4.5 Aerodynamic load uncertainty estimation . . . 62
4.5.1 Measurement chain uncertainty assessment . . . 63
4.5.2 External uncertainty assessment . . . 64

5 Results and discussion 66
5.1 Verification of the methodology implemented . . . 66
5.1.1 Reconstructed pressure field . . . 66
5.1.2 Aerodynamic loading . . . 68
5.2 Instantaneous flow feature characterization . . . 71
5.2.1 Shock Waves, boundary Layer interactions, and separation . . . 71
5.2.2 A case study on transonic buffet . . . 74
5.2.3 Compressibility in tripped vs. free-transition conditions . . . 77
5.3 Mean Flow field analysis . . . 80
5.3.1 Velocity field and separation characteristics . . . 80
5.3.2 Mach number field and supersonic region characteristics . . . 85
5.3.3 Reconstructed mean pressure field . . . 90
5.4 Phase-averaged analysis . . . 93
5.4.1 Phase distinction . . . 93
5.4.2 Supersonic and separation characteristics . . . 94
5.4.3 Reconstructed pressure and total pressure . . . 97
5.4.4 Reynolds stresses contribution . . . 100
5.5 Aerodynamic loading . . . 101
5.5.1 Mean flow results . . . 101
5.5.2 Phase-averaged results . . . 104
5.6 Compressibility and its implication for wind turbines . . . 107

6 Conclusion 109
6.1 Recommendations for the present study . . . 110
6.1.1 Experimental setup . . . 110
6.1.2 Theoretical approach . . . 110
6.1.3 Data processing approach . . . 111

References 112

A Aerodynamic load sensitivity to contour definition 116

B Phase-averaged lift contributions across the contour segments 118

C Mean flow field for the NACA 0012 experiments 119

List of Figures

2.1 HAWT configuration 5
2.2 Airfoil shape parameters (Liang et al., 2014) 5
2.3 Velocity and force diagram for a blade element (Timmer & Bak, 2023) 6
2.4 Operational conditions of IEA15 MW turbine at r/R = 0.97 in normal turbulent wind of class A at 25m/s. The supersonic boundary is derived for the tip-airfoil FFA-W3-211 at $Re = 10 \times 10^6$ (De Tavernier & Von Terzi, 2022) 11
2.5 Locally achieved Mach number for different mean inflow conditions at various spanwise locations. 25-75 percentile, 10-90 percentile and the min/max visualized. De Tavernier and Von Terzi, 2022 12
2.6 The development of supersonic flow region over an airfoil, terminated by a near-normal shock (Babinsky & Harvey, 2011) 15
2.7 The effect of the Mach number on airfoil drag (Anderson, 2011) 16
2.8 Transonic flow separation characterization (Pearcey, 1955). *Left:* Type 'A', Separation originates at the shock.*Right:* Type 'B', Separation originates at the trailing edge. 17
2.9 Topology of a weak SWBLI (Moulden, 1984) 18
2.10 Topology of a strong SWBLI (Vos & Farokhi, 2015) 18
2.11 Flow patterns for laminar and turbulent separated boundary layer interaction (Haines et al., 1957) 19
2.12 Classifications for the Type II transonic buffet into types A, B and C, as distinguished by Tijdeman, 1977 20
2.13 Subsonic-supersonic boundary for the FFA-W3-211 wind turbine tip airfoil (using Xfoil): configurations selected for URANS threshold (grey crosses), configurations in which a supersonic regime is established (red circles), and configurations in which shock waves appear (green square). Results shown for $Re = 1.8 \times 10^6$ (M. Vitulano et al., 2024) . . . 22

3.1 TST-27 Transonic/Supersonic wind tunnel at TU Delft 30
3.2 TST-27 Transonic/Supersonic wind tunnel components technical drawing (Blume, 2007) 31
3.3 TST-27 with solid wall and slotted wall configuration (Blume, 2007), with sections of interest marked by A_{t1}, A_{test} and A_{t2} (van Rijswijk, 2012) 32
3.4 Transonic choke mechanism, featuring biconvex rods and a wing located in the second throat of the TST-27 (van Rijswijk, 2012) 32
3.5 FFA-W3-211 airfoil geometry presented in its nominal configuration 34
3.6 FFA-W3-211 airfoil models, left: 67mm chord, right: 50mm chord, with a transition strip on the suction surface at a chord-wise location x/c = 5% 34
3.7 NACA 0012 airfoil geometry 34
3.8 NACA 0012 airfoil model with a chord of 100mm, mounted inside the wind tunnel 35
3.9 Toepler Schlieren configuration. Sketch by D'Aguanno, 2023 36
3.10 Z-configuration Schlieren setup featuring a light source, lenses, a pinhole, mirrors, a knife edge and a camera. Sketch done by D'Aguanno, 2023 37
3.11 The three key components of PIV, seeding particles in the flow, their illumination and their imaging. Image provided by Raffel et al., 2018 38
3.12 Instantaneous PIV snapshot displaying the illuminated particles in the laser sheet plane 38
3.13 Illustration of the seeding introduced in the settling chamber, the laser setup downstream of the airfoil, and camera 1 capturing the LE of the airfoil, while camera 2 captures the TE region. 39
3.14 PIV laser setup 40
3.15 PIV laser probe 41
3.16 PIV camera setup 42

3.17 Effective FOV around the FFA-W3-211 airfoil, estimated for the two cameras and both airfoil configurations at an angle of attack of $\alpha = 10°$. Red corresponds to the inverted configuration, while blue corresponds to the nominal configuration FOVs. The estimated shadow region is visualised as the shaded red and blue region ahead of the airfoil. . . . 43
3.18 Programmable Timing Unit in charge of synchronising the camera and laser input trigger signals . . . 44
3.19 Calibration objects used for all airfoil models tested . . . 44
3.20 Calibration of the inverted FOVs using the calibration object, using two points with a known distance. The origin for FOV$_1$ is set to the LE. The origin of FOV$_2$ is set to the TE. A visible point to both FOVs is marked. . . . 44
3.21 Subsonic-supersonic boundary for the FFA-W3-211 wind turbine tip airfoil (using Xfoil) at Re_c= 1.8 million: configurations selected for URANS threshold (grey crosses), configurations in which a supersonic regime is established (red circles), and configurations in which shock waves appear (green square) (M. C. Vitulano et al., 2024). . . . 45

4.1 Illustration of a window used to obtain a time series for the average light intensity. Variations in window average intensity are due to the presence of an oscillating shock wave and the static window location. . . . 51
4.2 FOV grid translation into the grid of inverted FOV 1, using a reference point, P, common to both inverted FOVs. Inverted FOVs are coloured in red, Nominal FOVs coloured in blue. . . . 53
4.3 Linear weighting functions for FOV$_1$ (left) and FOV$_2$ (right) used to merge the velocity data defined in the inverted FOVs. Blue represents a weight of 1, white represents a weight of 0, and intermediate weights are shown in the overlapping region. . . . 53
4.4 Nominal (right) and inverted (left) field regions for which the flow is assumed to be isentropic. The unshaded domain describes the region in which the pressure-integration scheme is used. Green markers define the start of the integration front . . . 57
4.5 Propagation of pressure field across the integration domain, starting with a minimum number of required neighbors $N_{min} = 4$. Red grid points represent the boundary conditions, while blue grid points represent the integration domain. Grid point numbering represent the order in which these are determined . . . 57
4.6 Control volume considered for the integral momentum conservation (Anderson, 2011) . 58
4.7 Contour shape and boundary . . . 59
4.8 Shock wave detection algorithm within the search region (Dotted box). All markers represent the boundary between supersonic and subsonic flow. Only cyan markers satisfy all requirements to be considered part of the front. The cyan line represents the derived shock location. . . . 60
4.9 Sensitivity of the percentage of frames with a detected shock wave to the choice of M_{sub} and n_{sho}, for the cases $\alpha = -6°$,$M_\infty = 0.65$ (right) and $\alpha = -10°$,$M_\infty = 0.65$ (left) . . . 61
4.10 Contour variations for the lift coefficient visualised (red). Wake integral variations visualised (blue) . . . 64

5.1 Difference between the CFD pressure field and reconstructed pressure field visualised through the difference in the pressure coefficient Δc_p field. Red and blue dashed lines distinguish between the regions where pressure is integrated, as described in chapter 4, for the nominal and inverted FOV distinguished by the black dashed line. . . . 67
5.2 Schlieren images for cases at $\alpha = -10°$ (left) and $\alpha = -6°$ (right). Mach number increases from 0.5 (bottom row) to 0.65 (top row). . . . 71
5.3 Probability density function of the non-dimensional shock wave location, x_{sho}, for cases where a shock develops. The distribution is scaled by the corresponding probability of detecting a shock, P_{sho}. . . . 74
5.4 Instantaneous Schlieren visualizations of the transonic buffet cycle, illustrating the periodic variation in shock strength as it oscillates, along with the cyclic expansion and contraction of the wake. . . . 75
5.5 Power Spectral Density at the different windows considered, for the case at $\alpha = -10°$ at M = 0.65. . . . 76

5.6 Windows considered for the spectral analysis. 76
5.7 Detected shock waves during the transonic buffet cycle. The dotted box represents the shock detection window, and the dashed cyan line represents the x/c location. 77
5.8 Oil flow visualization results for the development along the airfoil's suction side between a fixed transition at $x/c = 5\%$ (left span) and free-transition (right span) along the airfoil's suction side 77
5.9 Schlieren images for cases at $\alpha = -10°$ (left) and $\alpha = -6°$ (right) with free-transition. Mach number increases from 0.55 (bottom row) to 0.65 (top row). 78
5.10 Identification of shock waves from Schlieren visualization in the (α, M) domain. Green markers indicate shock waves, while grey markers represent cases with no observed shock. Results are shown for fixed transition (left) and free transition (right). 79
5.11 Schlieren images for cases at $\alpha = -4°$ at Mach 0.6 for tripped and free transition experiments 80
5.12 Mean non-dimensional freestream-aligned velocity field, u/U_∞, for cases at $\alpha = -10°$ (left) and $\alpha = -6°$ (right). Mach number increases from 0.5 (bottom row) to 0.65 (top row). The dashed line encloses the region where $u \leq 0$, indicating flow reversal. 81
5.13 Mean non-dimensional vertical velocity field, v/U_∞, for cases at $\alpha = -10°$ (left) and $\alpha = -6°$ (right). Mach number increases from 0.5 (bottom row) to 0.65 (top row). The dashed contour corresponds to $v = 0$. 82
5.14 Spatial probability distribution of separated flow for cases at $\alpha = -10°$ (left) and $\alpha = -6°$ (right). Mach number increases from 0.5 (bottom row) to 0.65 (top row). The dashed contour represents a 5% probability. The unmasked region lies above the red line. 84
5.15 Mean Mach number field for cases at $\alpha = -10°$ (left) and $\alpha = -6°$ (right). Mach number increases from 0.5 (bottom row) to 0.65 (top row). The sonic line (M = 1) is indicated by the dashed contour. 86
5.16 Spatial probability distribution of supersonic flow for cases at $\alpha = -10°$ (left) and $\alpha = -6°$ (right). The dashed contour represents a 5% probability. The unmasked region lies above the red line. 88
5.17 Standard deviation of the mean Mach number field for cases at $\alpha = -10°$ (left) and $\alpha = -6°$ (right). Mach number increases from 0.5 (bottom row) to 0.65 (top row). 89
5.18 Mean pressure coefficient field for cases at $\alpha = -10°$ (left) and $\alpha = -6°$ (right). Mach number increases from 0.5 (bottom row) to 0.65 (top row). The arrows represent local velocity magnitude and flow direction. 90
5.19 Mean pressure coefficient distribution for cases at $\alpha = -10°$ (left) and $\alpha = -6°$ (right). Marker colour differentiates freestream Mach numbers: 0.5 (red), 0.6 (blue), 0.65 (black). Filled circles represent the suction surface, while unfilled triangles denote the pressure surface. 91
5.20 Joint Probability Density Function between shock wave location and separated area. for $\alpha = -10°$ at $M_\infty = 0.65$. Red dashed lines represent the distinction between the four different shock phases, identified through the red numering. 93
5.21 Phase-averaged Mach number field for the transonic buffet cycle at $\alpha = -10°$, M_∞ = 0.65. The sonic line (M = 1) is indicated by the black dashed contour. The cyan dashed line encloses the region where $\bar{u} \leq 0$, indicating flow reversal. 95
5.22 Phase-averaged supersonic and separation spatial distribution field for the transonic buffet cycle at $\alpha = -10°$, M_∞ = 0.65. The respective dashed contours represent a 5% probability. The unmasked region lies above the red dashed line. 96
5.23 Phase-averaged pressure coefficient field for the transonic buffet cycle at $\alpha = -10°$, M_∞ = 0.65. The arrows represent local velocity magnitude and flow direction. 98
5.24 Phase-averaged pressure coefficient distribution for the transonic buffet phses at $\alpha = -10°$, M_∞ = 0.65. Marker colour differentiates all phases. Filled circles represent the suction surface, while unfilled triangles denote the pressure surface. The unfilled circles represent the mean flow distribution over the suction surface. 99
5.25 Phase-averaged total pressure deficit in the wake at a distance $x/c = 1.2$ for the transonic buffet cycle at $\alpha = -10°$, M_∞ = 0.65. The line colour differentiates all phases. The dashed line, 'MF', represents the time-averaged flow. 100

5.26 Phase-averaged Turbulent Kinetic Energy field for the transonic buffet cycle at $\alpha = -10°$, M_∞ = 0.65. The unmasked region lies above the dashed red line. 101
5.27 Contour-based lift and wake deficit drag coefficient data for all cases. Error bars correspond to 1σ due to variations in the contour definition. 103
5.28 Phase-averaged aerodynamic loads across the different stages of the transonic buffet cycle at $\alpha = -10°$, $M_\infty = 0.65$. The mean aerodynamic loads are shown for comparison, under the label 'Mean flow'. 105
5.29 Contribution of the various segments to the phase-averaged lift coefficient 106

A.1 Sensitivity of the lift coefficient for different contour variations, for all AoAs and freestream Mach numbers. The dashed line coincides with Contour 4, from which all results have been derived and from which the sensitivity was performed. 116
A.2 Sensitivity of the lift coefficient for different contour variations, for all AoAs and freestream Mach numbers. The dashed line coincides with Contour 4, from which all results have been derived and from which the sensitivity was performed. 117

B.1 Contribution to the lift across the four contour segments. Line colour distinguishes phase. The 118

C.1 Mean non-dimensional freestream-aligned velocity field, u/U_∞ (left), and vertical velocity field, v/U_∞ (right), for the NACA 0012 experiments at $\alpha = -6°, -8°$ and $-10°$ at $M_\infty = 0.6$. The dashed line encloses the region where $u \leq 0$ or $v \leq 0$. 120
C.2 Mean Mach number field, M (left), and mean pressure coefficient field, c_p (right), for the NACA 0012 experiments at $\alpha = -6°, -8°$ and $-10°$ at $M_\infty = 0.6$. 121
C.3 Total pressure wake deficit for the NACA 0012 experiments at a distance $x/c = 1.2$, for $M_\infty = 0.6$ 122

List of Tables

2.1 Comparison of velocity measurement techniques: LDA, HWA, PIV 27

3.1 Optics setup details for FOV$_1$, for the different airfoil model experiments. 42
3.2 Optics setup details for FOV$_2$, for the different airfoil model experiments. 42
3.3 Freestream conditions and Reynolds number (million) for all conditions and models tested. 46
3.4 Reynolds number (million) for all conditions and models tested. An estimate for the corrected quantities for blockage effects is shown in parentheses for the FFA-W3-211 experiments. 46
3.5 Schlieren test matrix for the FFA-W3-211 airfoil model with 67mm chord and free transition 47
3.6 Schlieren test matrix for the FFA-W3-211 airfoil model with 67mm chord and fixed transition at x/c = 5% 47
3.7 Oil flow test matrix for the FFA-W3-211 airfoil model with 67mm chord. Half model span with fixed transition at x/c = 5%, and remaining span with free transition. 48
3.8 PIV test matrix for the FFA-W3-211 airfoil model with 67mm chord 49
3.9 PIV test matrix for the FFA-W3-211 airfoil model with 50mm chord 50
3.10 PIV test matrix for the NACA 0012 airfoil model 50

4.1 Top and bottom boundary locations for the different contours used for the FFA-W3-211 airfoil lift sensitivity study 65
4.2 Wake-deficit x-location used for the FFA-W3-211 airfoil drag sensitivity study 65
4.3 Top and bottom boundary locations for the different contours used for the NACA 0012 airfoil lift sensitivity study 65
4.4 Wake-deficit x-location used for the NACA 0012 drag sensitivity study 65

5.1 Comparison of uncorrected lift and drag coefficients for the NACA 0012 airfoil at Mach 0.6. $^{(1)}$ Momentum integral (PIV-based). $^{(2)}$ Load Balance measurement. $^{(3)}$ Simulation (Panel code based). $^{(4)}$ Pressure orifices. $^{(a)}$ Momentum integral (PIV-based). $^{(b)}$ Wake deficit (PIV-based). $^{(c)}$ Wake deficit (Wake rake-based). $^{(d)}$ Simulation (Panel code based). 68
5.2 Comparison of lift and drag coefficients for the NACA 0012 airfoil at Mach 0.6. $^{(1)}$ Momentum integral (PIV-based). $^{(2)}$ Load Balance measurement. $^{(3)}$ Simulation (Panel code based). $^{(4)}$ Pressure orifices. $^{(a)}$ Momentum integral (PIV-based). $^{(b)}$ Wake deficit (PIV-based). $^{(c)}$ Wake deficit (Wake rake-based). $^{(d)}$ Simulation (Panel code based). . . 69
5.3 Sensitivity of the estimated uncorrected lift and drag coefficients to changes in contour/ wake integral definitions according to Table 4.3 and Table 4.4 69
5.4 Percentage of frames with a detected shock, P_{sho}, mean non-dimensional shock location, $\overline{x/c}_{sho}$, and its corresponding standard deviation,$\sigma_{\overline{x/c}_{sho}}$, for all cases. 73
5.5 Non-dimensional separated area of the mean flow, $A_{sep,mf}$, mean non-dimensional separated area, $\bar{A}_{sep}$, and corresponding standard deviation, $\sigma_{\bar{A}_{sep}}$, for all test conditions. Areas non-dimensionalized by c^2. 83
5.6 Probability of supersonic flow, P_{sup}, non-dimensional supersonic area of the mean flow, $A_{sup,mf}$, mean non-dimensional supersonic area, $\bar{A}_{sup}$, and corresponding standard deviation, $\sigma_{\bar{A}_{sup}}$, for all test conditions. All areas are non-dimensional by c^2. 87
5.7 Definition for the different phases of the transonic buffet cycle at $\alpha = -10°$, $M_\infty = 0.65$. 93
5.8 Measures for separation and supersonic area across the different phases of the transonic buffet cycle at $\alpha = -6°$, $M_\infty = 0.65$. 94
5.9 Mean lift and drag coefficients obtained using the contour-based method, represented by the subscript 'ct'. Drag based on the wake deficit method is represented by the subscript 'wd'. Simulation values from XFOIL are included for comparison. 102

5.10 Mean flow and phase-averaged aerodynamic loads determined with the inclusion of Reynolds stresses (subscript RS), and otherwise without the contribution of Reynolds stresses. 104
5.11 Contribution to the lift coefficient from the (1) top and bottom contour segments, (2) left and right contour segments. 106

Nomenclature

Abbreviations

Abbreviation	Definition
ISA	International Standard Atmosphere
BEM	Blade Element Momentum
PIV	Particle Image Velocimetry
HWA	Hot Wire Anemometry
LDA	Laser Doppler Anemometry
IT	Infrared Thermography
SBLI	Shock wave Boundary Layer Interaction
NACA	National Advisory Committee for Aeronautics
NREL	National Renewable Energy Laboratory

Symbols

Symbol	Definition	Unit
a	Speed of sound	[m s^{-1}]
c	Airfoil chord length	[-]
c_l	Lift coefficient	[-]
c_d	Drag coefficient	[-]
C_T	Thrust coefficient	[-]
C_P	Power coefficient	[-]
c_p	pressure coefficient	[-]
f	Frequency	[Hz]
f	Focal length	[m]
$f_\#$	F-stop number	[-]
f	Shock buffet frequency	[Hz]
M	Mach number	[-]
M_{cr}	Critical Mach number	[-]
p	Pressure	[Pa]
R	Balde radius	[m]
Re	Reynolds number	[m]
S	Surface area	[m^2]
T	Temperature	[K]
t/c	Airfoil thickness ratio	[-]
V	Velocity	[m s^{-1}]
V_∞	Freestream velocity	[m s^{-1}]
ρ	Density	[kg m^{-3}]
ω	Rotational speed	[rad/s]

Symbol	Definition	Unit
Γ	Circulation	[m^{2}s^{-1}]
γ	Ratio of specific heats	[m^{2}s^{-1}]

1 Introduction

Ever since the start of the Industrial Revolution in the 18th century, the use of fossil fuels such as coal, and more recently natural gas and petroleum products became key in the development of humankind. By the mid-twentieth century, "electricity networks, automated manufacturing, the internal combustion engine and petrochemicals" had become fossil fuel-dependent systems and driven inventions (Pirani, 2018). The increasing use of fossil fuels and related technologies over the last century has led to significant resource exploitation (Hubbert, 1949) (Pirani, 2018). This raises concerns about sustainability, environmental, social and economic impacts. Amongst the ecological impacts are effects on ecosystems, humans, and animals caused by greenhouse gases and pollutants released from their usage (Barbir et al., 1990). As a result, fossil fuels are considered among the greatest contributors to climate change (Nations, n.d.-b), creating a growing demand for clean and renewable energy technologies.

Significant efforts to mitigate, reduce and revert climate change have to be made to ensure societies can develop sustainably. The Paris Agreement established commitments to take action to limit the global average temperature to below 2° above pre-industrial levels and 1.5° above pre-industrial levels (UNFCCC, 2015). Amongst the 17 Sustainable Development Goals (SDGs) proposed by the United Nations are calls for urgent action towards affordable and clean energy, as well as responsible consumption and production (Nations, n.d.-a). These initiatives call for cleaner, renewable, sustainable and green sources of energy. Wind energy satisfies these requirements, and has shown its potential to become a dominant force driving the energy transition (Gielen et al., 2019). 116.6 GW of new wind power capacity was added worldwide in 2023, 50% more than in 2022 bringing total installed wind capacity to 1,021 GW, a growth of 13% compared with last year (Council, 2024). In the Netherlands, new wind power installations grew by 1302 MW in 2022 and by 2.457 GW in 2023, for a total capacity of 11.513 GW in 2023 (Council, 2024), highlighting a rapidly growing market.

Accelerated demands for wind energy have led to rapid advancements in its power generation capabilities, with trends favouring increased rotor sizes (Enevoldsen & Xydis, 2019). New aerodynamic challenges arise at the tip section of the blade, where speeds can result in greater Mach numbers. According to Sørensen et al., 2018, the blade tip speed for wind turbines with a rotor radius around 100m may reach relative velocities of up to 30% of the speed of sound. Although steady design conditions may remain below supersonic conditions, the presence of turbulence, wind gusts, or blade/turbine deflections may cause a significant increase in the velocity (De Tavernier & Von Terzi, 2022). This raises new concerns about the validity of the incompressible flow assumption made when designing and operating wind turbines, and the implications compressible flow effects may have on wind turbine performance and structural integrity. To the authors' knowledge, no experimental studies have been conducted at a wind turbine level. Limited numerical studies, however, may already highlight the importance of exploring these effects (De Tavernier & Von Terzi, 2022; Mezzacapo et al., 2023; Wood, 1997; Yan & Archer, 2018). Airfoils are the fundamental building block of a wind turbine, and thus, it is crucial to understand their performance in compressible flow conditions. For wind turbine airfoils, this area of research features a limited amount of numerical studies, and only one experimental study was found (Aditya et al., 2024). A knowledge gap exists regarding the experimental investigations on the performance of wind turbine airfoils in compressible and transonic conditions, which is a vital step towards understanding these effects at a large-scale turbine.

To address the challenge that compressible and transonic flow may pose for wind turbines, this research aims to experimentally investigate the effects of compressibility on the aerodynamic performance of the FFA-W3-211 airfoil. This airfoil is relevant for the study, as it is used in the IEA 15MW (Gaertner et al., 2020), and the most recent IEA 22 MW (Zahle et al., 2024) reference wind turbines. The research objectives are (1) to experimentally **investigate** the effects of **compressibility** on the time-averaged aerodynamic **loading** and **flow field** features of the FFA-W3-211 wind turbine airfoil under **compressible** flow and (2) To experimentally **quantify** dynamic variations in aerodynamic **loads** and the **flow field** features of the FFA-W3-211 wind turbine airfoil in **transonic buffet** conditions. Experimental tests using the Particle Image Velocimetry (PIV) and Schlieren technique are performed on the 2-D stationary blade element at the TST-27 transonic-supersonic blowdown-type wind tunnel at the TU Delft. These measurement techniques qualitatively and quantitatively capture the flow field and its features. The research builds upon the limited experimental work available (Aditya et al., 2024) by experimentally evaluating the aerodynamic load and flow field of the FFA-W3-211 wind turbine airfoil in transonic conditions, motivating further research into the effect of compressibility for wind turbine applications.

The structure of this thesis is divided into several chapters. chapter 2 offers the reader basic principles of wind turbine aerodynamics, followed by the current state-of-the-art research regarding the emergence of transonic flow over wind turbines, with an experimental focus on wind turbine airfoil performance under transonic flow conditions. Here, several experimental measurement techniques are considered. chapter 3 presents a detailed description of the experimental setup carried out at the TST-27 Transonic/Supersonic wind tunnel at TU Delft, including an overview of the wind tunnel facility, descriptions of the various flow visualisation and measurement techniques and the specific testing conditions for each measurement campaign. chapter 4 presents the different ways in which data from Schlieren and PIV have been processed, analysed and a motivation for the estimation of the aerodynamic load uncertainty. chapter 5 presents an analysis of the effects of compressibility on the flow field and aerodynamic performance of the FFA-W3-211 airfoil through the results of the Schlieren and PIV experiments. chapter 6 documents the concluding remarks of the thesis project, summarising the results, and motivating future work and recommendations.

1.1. Research objectives, questions and hypotheses

The research objective, questions, and hypotheses presented below were developed based on insights derived from the literature review.

Research objectives

1. To experimentally **investigate** the effects of **compressibility** on the time-averaged aerodynamic **loading** and **flow field** features of the FFA-W3-211 wind turbine airfoil under **compressible** flow.
2. To experimentally **quantify** dynamic variations in aerodynamic **loads** and the **flow field** features of the FFA-W3-211 wind turbine airfoil in **transonic buffet** conditions.

Research questions

1. How does increasing the freestream Mach number affect the time-averaged lift, drag, and flow field characteristics of the FFA-W3-211 airfoil at negative angles of attack?

   Sub-questions

   - How do instantaneous flow features support the observed trends in the mean flow field
   - How does the time-averaged supersonic and separated area and intensity vary with Mach number and angle of attack?
   - How can the flow field features reflect the trends observed for the time-averaged lift and drag coefficients, and how do these scale with Mach number?

   Hypotheses

- The time-averaged lift coefficient at a fixed negative angle of attack is hypothesised to increase with freestream Mach number following the Prandtl–Glauert rule. Beyond a critical value and the emergence of shocks or strong separation, the lift may plateau or even decrease.
- The drag coefficient is hypothesised to increase with M_∞, displaying a significant rise beyond a critical point referred to as the drag-divergence Mach number. This is expected due to shock wave formation and increased separation incident on the FFA-W3-211 airfoil, which is not optimized to operate in transonic flow.
- The time-averaged supersonic area and separation area on the suction-side of the airfoil are hypothesised to both grow with freestream Mach number and angle of attack, influenced heavily by the development of shock waves. The separation characteristics are expected to correlate positively with the increase in drag coefficient.
- It is hypothesized that the time-averaged aerodynamic loads may be understood through an analysis of quantitative metrics such as the supersonic and separated flow area and their extent, in addition to the pressure field and a qualitative interpretation of SWBLI.

2. How is the dynamic influence of shock waves reflected in the lift, drag and flow field characteristics of the FFA-W3-211 wind turbine airfoil?
   Sub-questions
   - Which combinations of freestream Mach number and angles of attack result in the emergence of supersonic flow, shock waves and transonic buffet?
   - How do lift and drag coefficients evolve through the transonic buffet cycle?
   - How does the evolution of aerodynamic loads reflect the observed development in the flow field?

   Hypotheses
   - Based on literature available on the FFA-W3-211 airfoil, a critical freestream Mach number is hypothesised to exist for every angle of attack, above which the suction-side supersonic region then terminates in a shock wave. Shock waves (and transonic buffet) emerge at a lower Mach number as the magnitude of the angle of attack increases.
   - The phase-averaged lift coefficient is hypothesised to be periodic and centred around its time-averaged value. Based on the literature available on transonic buffet for supercritical airfoils, the phase-averaged lift may be highest when the shock is most aft due to the increased supersonic region, and lowest when the shock is at its most upstream position.
   - The phase-averaged drag coefficient is hypothesised to be periodic and centred around its time-averaged value. Based on the literature available on transonic buffet for supercritical airfoils, the phase-averaged drag may be highest when the shock is most upstream due to the increased separated region, and lowest when the shock is at its most downstream position.

2

Literature Review

Given the significant role of renewable energy in combating the issues of climate change (Gielen et al., 2019), in particular wind energy developments, there is increasing concern about the aerodynamic challenges brought by larger wind turbine sizes. Specifically, the increased relative velocities at the blade-tip regions of modern turbines may become vulnerable to compressibility and transonic effects that were previously considered negligible. This chapter is a comprehensive review of the literature on wind turbine aerodynamic performance under compressible conditions, with a particular focus on the implications for wind turbine airfoils. The purpose of this literature review is to synthesize existing research, identify gaps in the current knowledge, and help develop a research plan that addresses these gaps effectively.

The literature review begins with section 2.1, discussing the fundamental principles of wind turbine aerodynamics, which are required to understand the subsequent sections. The section ends by exploring the emergence of transonic flow over wind turbines, providing a rationale to focus on wind turbine airfoil performance. In section 2.2 a review of compressibility and transonic flow, including their effects on airfoil performance is presented, followed by the state-of-the-art research specific to wind turbine airfoils. The section concludes with a rationale for an experimental focus, progressing towards the available experimental measurement techniques in section 2.3. Here, the experimental techniques relevant to the objectives of this study are evaluated to identify the most suitable methods for capturing the necessary data.

2.1. Wind turbine aerodynamics

Wind turbines vary widely in design, the most common type being the horizontal-axis wind turbines (HAWT) (Balat, 2009). A typical HAWT configuration is depicted by Figure 2.1.

Figure 2.1: HAWT configuration

This section focuses on the basic aerodynamic principles governing performance and the potential impact of compressibility phenomena on HAWTs. This provides a ground for understanding the aerodynamic issues raised by modern wind turbine designs.

2.1.1. Basic principles

Wind turbines convert the kinetic energy in wind into mechanical energy through the rotor mechanism, which is then converted into electrical power for distribution to various consumers. A turbine rotor consists of rotor blades designed to generate sufficient torque, which is needed for power generation. Airfoils are a fundamental element in blade design, as the shape and size of each blade section directly influence the aerodynamic loads that contribute to the generated torque.

An airfoil can be defined by its geometrical characteristics along its chord line direction x, which is defined between the leading edge and trailing edge points. These include the chord length, c [m], upper camber, $Z_u(x)$ [m] and lower camber, $Z_u(x)$ [m]. The mean camber line is the locus of points midway between the upper and lower surfaces. The airfoil's maximum thickness measured perpendicular to the camber is generally expressed relative to its chord length, denoted as t/c. These parameters are illustrated by Figure 2.2.

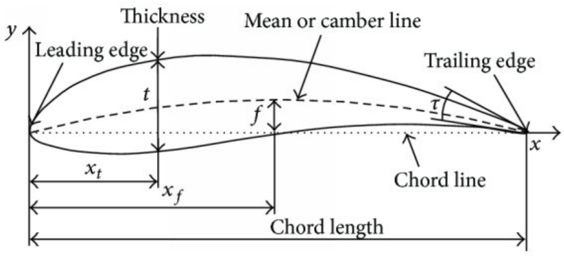

Figure 2.2: Airfoil shape parameters (Liang et al., 2014)

The first turbines featured airfoils designed for aviation, such as those compiled by the National Advisory Committee for Aeronautics (NACA) 4- and 6- digit airfoils in the 1970s (of Energy, 2023) (Timmer & Bak, 2023). The shortcomings of early wind turbine performance were largely attributed to the poor airfoil performance at the given operating conditions, sparking newer airfoil families specifically intended for wind turbine applications (of Energy, 2023). Nowadays, wind turbine airfoils are significantly different from traditional aviation airfoils, opting for a higher design lift, ample off-design capabilities, and smoother stall characteristics, making them suitable for their application.

From the root to the tip section of modern wind turbine blades, the airfoil shape, thickness and pitch vary substantially to achieve optimal performance in the different operating conditions encountered along the spanwise location of the blade. For example, the rotor design for the new IEA Wind 22-Megawatt Offshore Reference Wind Turbine is based on over 7 different airfoils from the FFA-W3 airfoil family, with a blend into a circular profile towards the root section (Zahle et al., 2024). For this specific rotor, the tip airfoil features a relative thickness t/c = 21.1%, reaching values of t/c = 48% near the root section due to structural reasons. Understanding why airfoil geometry plays a key role in blade design and the generation of torque to produce power can be demonstrated by analyzing the velocity and force diagram at an arbitrary blade element dr along the span.

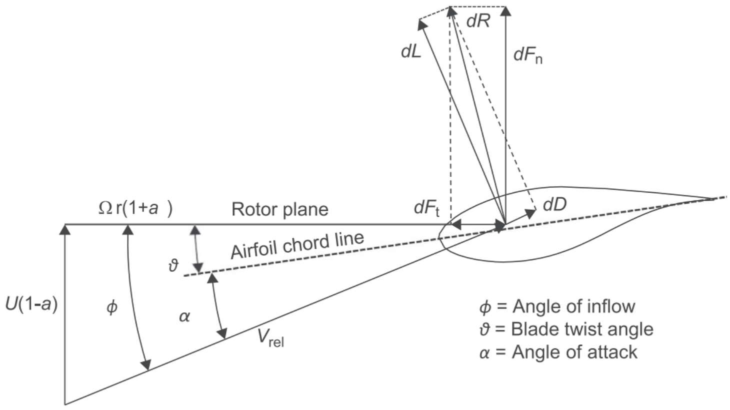

Figure 2.3: Velocity and force diagram for a blade element (Timmer & Bak, 2023)

For the discussion, the azimuthal and axial induction factors are ignored. For the given blade element with given airfoil, infinitesimal length, dr, and blade twist relative to the rotor plane ϑ subject to the contributions from the blade rotational velocity V_{rot} and the wind speed V_∞, the operating conditions are effectively a relative incoming flow speed V_{rel}, expressed by Equation 2.1, at an inflow angle $\phi = \tan^{-1}(V_\infty/V_{\mathrm{rot}})$, at a positive angle of attack (AoA).

$$V_{\mathrm{rel}} = \sqrt{V_\infty^2 + (r\omega)^2} \tag{2.1}$$

Here, ω is the rotor angular speed. Consequently, a flow region of high pressure and decelerated flow is present over the airfoil's section bottom side, and a region of low pressure and accelerated flow over its top side. The resultant circulation over the airfoil element results in an aerodynamic force referred to as the lift dL. A resulting drag force dD is also generated through the parasitic and induced drag from the generation of lift. The lift force acts perpendicular to the chord line, and the drag force acts parallel to it, with expressions as shown by Equation 2.2 and Equation 2.3 respectively. Where ρ is the free stream density, c_l is the non-dimensional lift coefficient and c_d is the non-dimensional drag coefficient, which reflects the dependency of the aerodynamic forces on the geometrical and operational parameters of the airfoil. These coefficients will demonstrate to be crucial for wind turbine design.

$$dL = \frac{1}{2}\rho V_{\mathrm{rel}}^2 c_l dr \tag{2.2}$$

$$dD = \frac{1}{2}\rho V_{\mathrm{rel}}^2 c_d dr \tag{2.3}$$

The total force experienced by the blade element is then dR = $\sqrt{dL^2 + dD^2}$. Two important non-dimensional factors that affect the lift and drag characteristics of an airfoil are the operating chord-based Reynolds number, Re, and the freestream Mach number, M_∞. The Reynolds number is a non-dimensional measure for the ratio between inertial and viscous forces in a fluid, defined by Equation 2.4. Here μ is the fluid viscosity [kg/(ms)], L [m] the characteristic length (equal to the chord length for airfoil analysis), and V the reference velocity [m/s].

$$Re = \frac{\rho V L}{\mu} \tag{2.4}$$

The Mach number is a measure of the compressibility characteristics in the flow, defined by Equation 2.5, where c is the speed of sound, a function of the fluid ratio of the specific heat capacity γ, the specific gas constant R, and the absolute temperature T.

$$M_\infty = \frac{V_\infty}{a}, \qquad a = \sqrt{\gamma R T} \tag{2.5}$$

Compressibility effects are generally assumed to be negligible below $M < 0.3$. Often, for wind turbine design, flow is treated as incompressible. The concept of compressibility and its effects will be discussed in further detail throughout the study.

Decomposing the aerodynamic forces into a components perpendicular and along the rotor plane results in expressions for the normal force, dF_n, and torque force,dF_t, as expressed by Equation 2.6 and Equation 2.6 respectively.

$$dF_n = dL\cos\phi + dD\sin\phi = \frac{1}{2}\rho V_{\text{rel}}^2 c_l c \left(\cos\phi + \frac{\sin\phi}{c_l/c_d}\right) dr \tag{2.6}$$

$$dF_t = dL\sin\phi - dD\cos\phi = \frac{1}{2}\rho V_{\text{rel}}^2 c_l c \left(\sin\phi - \frac{\cos\phi}{c_l/c_d}\right) dr \tag{2.7}$$

Thus, for a given relative velocity and pitch setting, the lift-drag ratio c_l/c_d and the product $c_l \cdot c$ are demonstrated to be important parameters in the generation of the torque and normal force, with a greater c_l/c_d ratio being beneficial in increasing torque and reducing the normal force. Following the discussion in (Timmer & Bak, 2023), lower values for the chord length are beneficial to limit blade parking loads, meaning the design lift coefficient of wind turbine airfoils must be high to maintain a good $c_l \cdot c$ value. A lower chord length lowers the structural stiffness of the blade, resulting in thicker airfoils being beneficial to reduce blade weight. Thicker blades, however, may result in more drag, thus also playing a role in the design c_l/c_d ratio, stressing the challenge of finding a balance between aerodynamic efficiency and structural integrity in the blade.

The aerodynamic principles discussed highlight the role of airfoil design and environmental conditions in generating torque forces along the blade span. Thus, aerodynamic and structural design considerations are strongly influenced by the lift and drag characteristics of the airfoil sections used along the blade span.

In the next section, the performance aspects of wind turbines will be examined, exploring how these aerodynamic principles translate into key performance metrics such as torque, power and thrust coefficients.

2.1.2. Wind turbine aerodynamic performance

A simple estimation of the total torque, Q, generated by the rotor with blade radius R is obtained from the integration of the product between the integral torque forces at each blade element dF_t and their corresponding radial distance from the rotor hub r, multiplied by the total number of blades, B, yielding the expression as shown by Equation 2.8.

$$Q = B \int_0^R \frac{1}{2}\rho V_{\text{rel}}^2 c_l c \left(\sin\phi - \frac{\cos\phi}{C_l/C_d}\right) r dr \tag{2.8}$$

Torque coefficient

The torque generated is directly linked to one of a wind turbine's key performance indicators, namely the well-known torque coefficient, C_Q, which is a measure of how effectively a turbine converts wind energy into torque relative to its size and wind speed and is defined by Equation 2.9, where $A = \pi R^2$ is the swept area of the rotor.

$$C_Q = \frac{Q}{\frac{1}{2}\rho A V_\infty^2 R} \tag{2.9}$$

Power coefficient

As discussed in the previous section, torque is essential for power generation P [W] of a wind turbine. The simple relationship is given by Equation 2.10.

$$P = Q\omega \tag{2.10}$$

The power generated is directly linked to one of a wind turbine's key performance indicators, namely the well-known power coefficient, C_P, which is a measure for the ratio of the power harnessed by the wind turbine compared to the energy present in the wind stream, and is defined by Equation 2.11.

$$C_P = \frac{P}{\frac{1}{2}\rho A V_\infty^3} \tag{2.11}$$

Thrust coefficient

In a similar fashion to the calculation of the total torque, the thrust force generated by the rotor with blade radius R is simply obtained from the integration of the product between the integral normal forces at each blade element dF_n, multiplied by the total number of blades, B, yielding the expression as shown by Equation 2.12.

$$T = B\int_0^R \frac{1}{2}\rho V_{\text{rel}}^2 c_l c \left(\cos\phi + \frac{\sin\phi}{c_l/c_d}\right) dr \tag{2.12}$$

The thrust force generated is directly linked to one of a wind turbine's key performance indicators, namely the well-known thrust coefficient, C_T, which is a measure for the force the turbine applies in the direction of the airflow, defined by Equation 2.13.

$$C_T = \frac{T}{\frac{1}{2}\rho A V_\infty^2} \tag{2.13}$$

The driving design and operational parameters present in all key performance indicators include V_{rel}, c_l, c_l/c_d, R, B ω and c. Most modern HAWT feature 3 blades, a choice due to structural and aerodynamic considerations. Since slender blades with low chord length are desirable, high lift coefficients c_l, and values for V_{rel} are beneficial for power generation capabilities.

An important result can be derived by introducing the Tip-Speed Ratio (TSR), λ,

$$\lambda = \frac{R\omega}{V_\infty} \tag{2.14}$$

which allows the expression of the power and torque coefficients via the TSR.

$$C_P = C_Q\lambda$$

Rewriting the expression for the relative velocity yields Equation 2.15.

$$V_{\text{rel}} = V_{\infty}\sqrt{1 + \left(\frac{r}{R}\right)^2 \lambda^2} \tag{2.15}$$

The TSR plays a role in determining the relative velocity experienced by blade sections. Given that relative velocity is an important parameter in all performance indicators, it follows that wind turbine performance is sensitive to changes in the TSR, with the power and torque coefficients being directly linked through its value. Thus, the operating TSR has also been demonstrated to be an important design and operating consideration. Modern turbines operate at a design TSR in the order of 10, however, this may shift according to wind speed variations, control system strategy/limitations, start up and shut down. Above rated wind speeds, for example, the control system strategy prioritises wind turbine structural integrity by pitching out blades, reducing the aerodynamic loads and the TSR.

Methodologies for assessing WT performance

In practice, wind turbine performance may be determined with the help of theoretical models, numerical simulations, and experimental simulations. Each method offers its own set of strengths and weaknesses.

Blade Element Momentum (BEM) theory remains one of the biggest tools for rotor performance during conceptual design stages. This is largely due to their conceptual and computational simplicity. BEM theory uses a similar approach to the one presented earlier to determine wind turbine performance. Other examples of theoretical models for determining rotor performance that may be implemented numerically include lifting line theory models, actuator disk theory models, and vortex panel theory models. The practical application of some of these models, including BEM, converts them into numerical tools once implemented computationally. Amongst the tools based on these theories is `Openfast`, a physics-based engineering tool for simulating the coupled dynamic response of wind turbines. One of the most popular panel code implementations for the analysis at a wind turbine airfoil-level is `XFOIL`. Amongst many others, one of the biggest limitations of these and many other theoretical models lies in the incompressible flow assumption, and the use of corrections to account for it Wood, 1997. The incompressible flow assumption have been valid for early and most modern wind turbines, however, it may be of special interest for large and future turbines, as will be discussed in a later section.

Numerical simulations based on resolving the non-linear, time-varying Navier Stokes equations can predict wind turbine aerodynamic performance at a higher fidelity level compared to theoretical models, at an increased computational and complexity expense. Computational Fluid Dynamics (CFD) is one of the biggest numerical tools to model wind turbine performance. These may model the effect of turbulence through increasing levels of accuracy, with the Reynolds Averaged Numerical Simulation (RANS) resolving the mean flow, Large Eddy Simulation (LES) solving the large turbulent scales, and Direct Numerical Simulation (DNS) resolving all flow features. With an adequate mesh to discretise the flow domain, the flow field solution and surface loads can be resolved for a wind turbine and airfoils with high accuracy. These methods are highly complex, computationally expensive and require an adequate setup, especially when trying to model flow around large objects. For a DNS, which allows for the most accurate flow reconstruction, the computational expense, otherwise known as the number of operations during a simulation, scales roughly with Re^3. Modern wind turbines can reach Reynolds numbers in the order of 3-15 $\times$ 10^6, meaning a wind turbine simulation is expensive. Nevertheless, literature is available for studies using RANS at the level of wind turbines (Shourangiz-Haghighi et al., 2020). CFD has also been used extensively to evaluate the performance of wind turbine airfoils (Bertagnolio et al., 2001). CFD simulations are used during the detailed design phase of a wind turbine, however, they depend on experimental work to validate their results, something which can be achieved through wind tunnel testing and may not always be possible.

Experimental simulations are an important step to validate CFD results and may provide additional insights into flow phenomena. At the level of a turbine, experiments have been conducted for small turbines (Chen & Liou, 2011), medium turbines (Krogstad & Eriksen, 2013) and a full-size NREL phase 4 wind turbine (Hand et al., 2001). One of the limitations of experimental testing for wind turbines is the size of the testing area. No wind tunnel ever constructed could fit a modern wind turbine with a size such as the reference IEA Wind 22-Megawatt Offshore turbine with a 284-meter rotor and a hub height of 170 meters (Zahle et al., 2024). For this reason, the performance can be assessed on a scaled-down model, which requires proper scaling and similarity of conditions. Extensive literature is available on experimental work to assess the performance of wind turbine airfoils, such as the work conducted by Bertagnolio et al., 2001. One of the drawbacks of experimental simulations is the need for measurement techniques to infer flow conditions, surface loads or aerodynamic force measurements. Suitable experimental measurement techniques for wind turbine airfoils is a topic discussed extensively section 2.3.

Challenges for future performance assessments

The European AVATAR (AdVanced Aerodynamic Tools of lArge Rotors) project focused on the aerodynamic modelling of large wind turbines. Their results show that, amongst others, BEM theory-based models, panel codes and CFD simulations could not yet be validated and calibrated for wind turbines whose blade tips operate at high Mach or Reynolds numbers, creating additional uncertainty in the simulations (Schepers et al., 2018). For a wind turbine operating at a tip-speed ratio in the order of 10, and at freestream speeds in the order of 10 m/s the tip speed can reach values of $V_{\mathrm{rel}} \approx 100.5$ m/s. When assuming a speed of sound at sea level of 340 m/s, the incoming freestream Mach number at the blade tip reaches values of $M \approx 100.5/340 \approx 0.295$. As stated by Yan and Archer, 2018, most wind turbines operate around an optimum TSR value of around 8, rarely greater than 12. The incoming freestream is also rarely above 15 m/s, meaning that these operating conditions don't occur frequently. Although in these conditions the relative velocity remains arguably on the verge of invalidating the incompressible flow assumption, the presence of turbulence, wind gusts, or blade/turbine deflections, may cause a significant instantaneous increase in the velocity perceived by the blades (De Tavernier & Von Terzi, 2022).

There are several reasons why accurately assessing the aerodynamic performance near the tip region of a rotor is crucial for rotor design. This region features high-speed flow due to the high rotational velocity. A significant amount of aerodynamic force is generated near the blade tip region, contributing highly to the power generated and rotor loading. In addition, losses in energy due to tip vortices are the most significant near the tip. All these considerations have to be taken into account when trying to optimize blade design and operation.

The previous discussions highlighted how airfoils' aerodynamic properties are involved in key performance indicators for wind turbines, including the torque, power, and thrust coefficients. The aerodynamic performance assessment methods for wind turbine applications include theory-based models, numerical simulations, and experimental simulations. However, the limitations of theory-based models and CFD for large wind turbine rotors raise a challenge for performance assessments, predominantly due to the uncertainty in accurately capturing the aerodynamics of high tip-speed phenomena. The next section discusses the emergence of transonic flow on wind turbines and its implications for performance

2.1.3. The emergence of compressible and transonic flow in wind turbines

To appreciate the challenges and implications of compressible and transonic flow in modern turbines, it is essential to briefly review the concepts of compressibility and the flow speed regime. Earlier in subsection 2.1.2, the Mach number was introduced as a measure of compressibility. Different speed regimes are characterized as follows: subsonic when $M < 1$, transonic when $M \approx 1$, supersonic when $M > 1$, and hypersonic when $M > 5$. In subsection 2.1.2, the inflow Mach number at the blade tip was estimated to reach around 0.3 or even higher in the presence of turbulence, wind gusts, or blade/turbine deflections. Additionally, the curvature and associated pressure field over the blade accelerate the flow further, and may potentially reach transonic flow conditions. Compressibility refers to the change in fluid density in response to pressure variations. At low speeds, pressure variations primarily lead to changes in velocity. In high flow speeds, some of the energy of the flow is also used to compress the air and change the local density of air. At the extreme case of compressibility over airfoils, localized supersonic regions may develop and eventually result in the emergence of shock waves. Shock waves are flow field disturbances that manifest as a discontinuity between supersonic and lower-speed flow. The extent to which flow is slowed down after a shock depends on the strength and nature of the shock wave. A more detailed examination of compressibility, transonic flow and their impact on airfoil performance is provided in section 2.2. The following literature is available regarding the effects of compressibility on wind turbine performance.

Studies on compressibility assessments

The effects of compressibility on wind turbine performance become noticeable even under moderate conditions, well before the onset of shock waves. Wood, 1997, presents one of the earliest studies on the effects of compressibility on small HAWT operating, hypothesising that these effects would likely occur due to operation at high tip speed ratios (TSRs). The study aimed to explore the use of shock stall, the shock-wave-induced separation of the blade's boundary layer, as a passive means of overspeed protection. The aerodynamic performance of a small HAWT with a NACA 0012 airfoil was evaluated computationally using a BEM theory-based model, incorporating the Prandtl-Glauert compressibility correction factor to the airfoil's 2D lift and drag characteristics. More recently, Yan and Archer, 2018, also used BEM with an incorporated the Prandtl-Glauert correction to assess the effects of compressibility for the NREL-5MW Reference Offshore Wind Turbine in terms of its thrust and power coefficients, when operating within and outside its rated design conditions.

The following studies have used CFD RANS simulations with a validated set-up, assessing compressibility effects on the NREL-5MW Reference Offshore Wind Turbine performance, with a rated wind speed of 11.4m/s and a maximum TSR of 7 at rated conditions (Jonkman et al., 2009). Yan and Archer, 2018, presented an assessment of the variable-density effects by using an `OpenFoam` based solver, and conducting a 3D compressible unsteady RANS simulation of a single and two turbine configuration, comparing the results with an incompressible simulation. Similarly, Campobasso et al., 2018, investigated the existence and impact of compressibility effects by using the compressible Navier Stokes CFD Optimized Structured multi-block Algorithm (`COSA`) code, the incompressible `NREL FAST` software (predecessor of `OpenFAST`), and incompressible simulation in `FLUENT` simulation to analyse the FOWT under an imposed pitching motion.

The following studies have used CFD with a validated set-up to assess the effect of compressibility on the IEA 15 MW Reference Offshore Wind Turbine performance, with a rated wind speed of 10.59m/s and a maximum TSR of 9 (Gaertner et al., 2020). Cao et al., 2023 used an incompressible, and a compressible RANS solver to compare the aerodynamic characteristics of the wind turbine and wake vortex development at speeds of 7 and 10.59 m/s, at a TSR of 9. Mezzacapo et al., 2023 presents a blade-level unsteady and compressible RANS simulation using `OpenFoam`.

While previous studies focused on the potential compressibility effects for large wind turbines, De Tavernier and Von Terzi, 2022, presents unique research on the IEA 15 MW Reference Offshore Wind Turbine performance using `OpenFAST`, aiming 1) To determine which operational conditions give rise to local supersonic speeds within the design space and in off-design conditions, 2) To determine whether and how often these occur, and 3) To assess how sensitive the conditions are environmental and turbine-specific parameters. This study is the first to be motivated by conditions that may allow the tip to reach local supersonic speeds. For the first time, the threshold between subsonic and supersonic flow over the FFA-W3-211 airfoil, used in the tip region of the blade, was determined using `XFOIL`, with the Prandtl compressibility correction, for different combinations of the inflow Mach number and angles of attack (See Figure 2.4). The sonic-supersonic was derived by comparing the critical pressure coefficient to the lowest pressure coefficient over the airfoil. The operating Mach number and angle of attack conditions in `OpenFAST` for the wind turbine airfoil section at position r/R = 0.97 was compared to the supersonic envelope to determine the presence of supersonic flow.

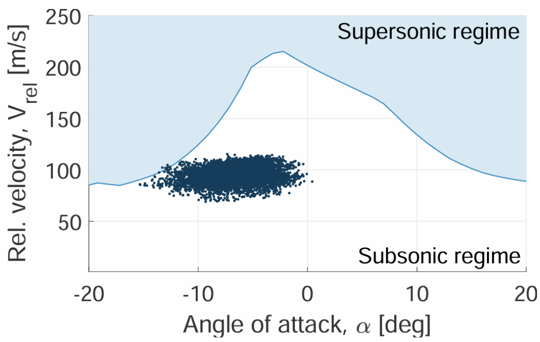

Figure 2.4: Operational conditions of IEA15 MW turbine at r/R = 0.97 in normal turbulent wind of class A at 25m/s. The supersonic boundary is derived for the tip-airfoil FFA-W3-211 at $Re = 10 \times 10^6$ (De Tavernier & Von Terzi, 2022)

Compressibility over the wind turbine blade tip region

The available literature consistently identified that compressibility effects manifest predominantly in the tip region of the blades, where the relative Mach number is the highest, bringing the flow closer to the compressible regime. The incompressible and compressible CFD results from Yan and Archer, 2018, for a single turbine demonstrate that these effects originate near the blade tips, however, they also affect the entire wake by lowering the wind speed deficit and turbulence. Campobasso et al., 2018 hypothesize that compressibility effects at the tip cause the differences between compressible and incompressible CFD results, as the instantaneous Mach number at the outboard part of the blades exceeds 0.4 when the tower experiences the maximum induced velocity from its pitching motion. Cao et al., 2023 observed that variations in pressure and density become more pronounced toward the outer portions of the blade, particularly near the leading edge. It was verified that the outboard region corresponds to where the most power is generated and where the largest Mach numbers, and thus compressibility effects, are predicted. Additionally, wake analysis supports the claim that compressibility manifests in the tip region and propagates downstream in the wake. Mezzacapo et al., 2023, further corroborates these results, identifying significant density variations at the suction side of the tip region of the IEA 15 MW offshore wind turbine blades, with the maximum Mach number occurring close to the leading edge. For the same turbine model, De Tavernier and Von Terzi, 2022 identifies that, in normal operation, it is the outboard 7.5% of the blade that is at risk of experiencing supersonic flow over the blades (See Figure 2.5). The collective findings across these studies indicate that the tip region is the critical area for compressibility effects in wind turbines, corresponding to a region with the highest Mach number, pressure, and density variations.

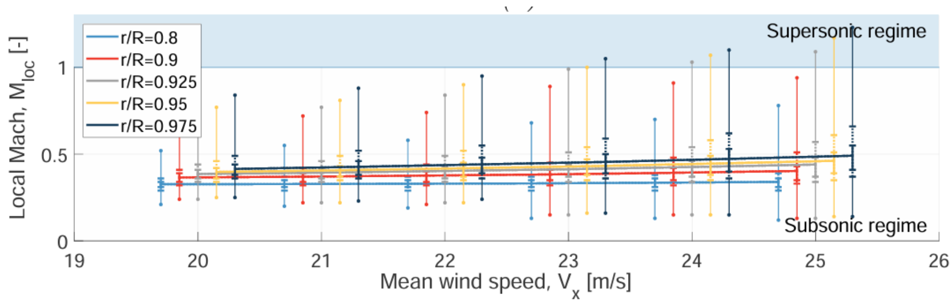

Figure 2.5: Locally achieved Mach number for different mean inflow conditions at various spanwise locations. 25-75 percentile, 10-90 percentile and the min/max visualized. De Tavernier and Von Terzi, 2022

Effects on aerodynamic performance

Amongst the results from Wood, 1997, there are significant performance reductions in the power coefficient at a freestream speed of 30m/s. Results for $V_\infty = 30m/s$ with λ=5 showed a significant reduction in the power coefficient, whereas the one at $V_\infty = 10m/s$ with λ=12 did not, despite having a similar M_{tip}. With this, Wood also demonstrates that wind turbine performance is not just dependent on M_{tip} Wood, 1997. Yan and Archer, 2018 determined a strong TSR dependency of compressibility effects using BEM and corrections of the aerodynamic coefficients. For normal operating conditions of the NREL 5MW turbine, power production was lowered by 8% from incompressible to compressible flow. At higher wind speeds and larger TSR values power losses exceeded 20% and reached as high as 50%. Conversely, the thrust force was found to increase. In the same study, the CFD results to assess the variable density effects also indicated reduced performance from incompressible to compressible flow, by 3% for a simulation conducted at $V_\infty = 15m/s$ with λ=5.58, and by 8% for a simulation conducted at $V_\infty = 15m/s$ with λ=8.37. Wake analysis results indicated the compressible wake has higher velocities, but up to 15% lower Turbulent Kinetic Energy (TKE), with variations propagating from the blade tips, and a strong dependence on the TSR. The results from Campobasso et al., 2018 have presented a contrasting effect, where the compressible CFD analysis resulted in a peak power 20% higher than its incompressible counterpart, and 9% higher than the `NREL FAST` incompressible solver result, at rated turbine conditions. Investigations by Cao et al., 2023, indicate that compressibility effects increased the normal and tangential forces along the tip region of the blade under rated conditions. For rated conditions, the compressible CFD simulation's torque was at most 11.07 % higher than the incompressible solution. These findings outline the significant impact compressibility can have on the aerodynamic efficiency of wind turbines, particularly at higher wind speeds and operating TSR. Despite the diverse findings and still limited understanding, it is undeniable that there is an influence of the compressibility of rotor aerodynamics and performance.

Prevalence of compressible and transonic flow conditions

The operational conditions under which compressibility effects may become significant are relatively rare but significant, particularly in large wind turbines operating at high tip speeds and wind velocities. Aditya et al., 2024, presents one of the few studies conducted on off-design conditions, stating that for the NREL 5MW wind turbine, it is rare to operate at a windspeed larger than $15m/s$, and TSR larger than 12, implying that the conditions at which compressibility effects are noticeable are infrequent. Wood, 1997, identified that the windspeed had to be around $30m/s$ to trigger a significant reduction in optimum performance, a rare operating condition for wind turbines. Off-design conditions are an important aspect of offshore wind turbines, as the operating environment can vary drastically. Previously it was mentioned that the presence of turbulence, wind gusts, or blade/turbine deflections may cause a significant increase in the velocity experienced by the blades. The results from De Tavernier and Von Terzi, 2022, show local supersonic conditions appearing near cut-out wind speeds of around 25 m/s, while this may already occur at lower speeds in off-design conditions. For extreme operating conditions, supersonic flow was identified to occur for approximately 15 seconds in a 10-minute interval, hinting towards an intermittent and infrequent development of supersonic conditions. While these may be relatively rare and brief, it is unknown how the flow reacts entering the conditions, what and how transonic phenomena develop, and what their immediate effect on performance and loading is. Given that transonic flow conditions are more extreme and rare compared to general compressible flow, the additional loads generated during brief transonic conditions may be easily overlooked in wind turbine design. However, these forces will inevitably affect the turbine's structural integrity over its lifetime.

Building on the understanding of how compressible and transonic flow conditions emerge in wind turbines, the available literature has explored the effect of compressibility on power generation, linking variations in performance to changes in flow field density and airfoil performance near the tip region of the blade, where effects are most prominent. In more severe and infrequent conditions, transonic flow introduces unique challenges. While research into localized supersonic flow over turbines is still emerging, it is crucial to ensure the aerodynamic performance and structural integrity of modern and future wind turbines throughout their lifetimes. subsection 2.1.1 and subsection 2.1.2 have already demonstrated the significant influence of airfoil design and performance on overall turbine performance. Therefore, a comprehensive understanding of compressible and transonic flow effects over wind turbines is best achieved from a preliminary understanding at a wind turbine airfoil level. To this end, the focus is shifted entirely on airfoil performance, were section 2.2 presents a detailed exploration of the fundamental principles, associated phenomena and effects of compressible and transonic flow on airfoils.

2.2. Compressible and transonic aerodynamics of airfoils

As highlighted by subsection 2.1.3, compressibility and transonic flow effects present significant challenges for wind turbine performance. This section provides a detailed exploration of compressible and transonic flow principles needed to understand their impact on turbine design and performance.

2.2.1. Basic principles

As discussed briefly in subsection 2.1.3, the Mach number allowed to define flow speed regimes, being subsonic when $M < 1$, transonic when $M \approx 1$, supersonic when $M > 1$, and hypersonic when $M > 5$. Transonic flow is the regime centred around sonic conditions $M = 1$, characterized by the simultaneous presence of subsonic and supersonic regions. The reason for the effects of compressibility being considered non-negligible beyond $M > 0.3$ will be explained.

An important concept in compressible flows is entropy, a thermodynamic state function describing the state of order of a fluid. A flow which is gradually compressed, and later gradually expanded to attain the original flow condition is said to have undergone a reversible process, which conserves the level of entropy. If, in addition to being reversible, the flow is assumed to be adiabatic (Negligible heat transfer in and out of the fluid) and follows the behaviour of an ideal gas, then it is referred to as isentropic flow.

An ideal gas is modelled by the ideal gas equation, Equation 2.16, and the thermodynamic energy relations for a calorically perfect gas, Equation 2.17.

$$p = \rho R T \tag{2.16}$$

$$c_p - c_v = R, \qquad \gamma = c_p/c_v \tag{2.17}$$

The flow around an airfoil operating beyond M_∞ > 0.3 may be assumed to be isentropic, and experiences variations in pressure, temperature and density, which are related to the local Mach number M by Equation 2.18, Equation 2.19 and Equation 2.20 respectively. Here, the subscript t refers to the total quantity of the variable, namely the condition achieved by isentropically decelerating the flow to rest.

$$\frac{p}{p_t} = \left(1 + \frac{\gamma - 1}{2} M^2\right)^{\frac{-\gamma}{\gamma - 1}} \tag{2.18}$$

$$\frac{T}{T_t} = \left(1 + \frac{\gamma - 1}{2} M^2\right)^{-1} \tag{2.19}$$

$$\frac{\rho}{\rho_t} = \left(1 + \frac{\gamma - 1}{2} M^2\right)^{\frac{-1}{\gamma - 1}} \tag{2.20}$$

Based on Equation 2.20, the density deviates by more than 5% from stagnation conditions for Mach numbers exceeding 0.3. Therefore, compressibility effects are no longer negligible and should be taken into account.

As flow travels over the curved surface of an airfoil, it accelerates, generally reaching its highest velocity close to the region of minimal pressure. Consequently, the thermodynamic variables vary over the airfoil surface. The pressure at the surface of the airfoil is a variable of particular interest, as it provides insights into the loading distribution and boundary layer development. The pressure distribution over the airfoil is generally expressed by the non-dimensional pressure coefficient, c_p, defined by Equation 2.21.

$$c_p = \frac{p - p_\infty}{\frac{1}{2}\rho V_\infty^2} \tag{2.21}$$

In subsection 2.1.3, the emergence of compressible and transonic flow, and their effects on wind turbine performance was explored. Previous literature presented using BEM theory accounted for compressibility effects using the well known Prandtl-Glauert correction on the pressure, lift and drag coefficients (De Tavernier & Von Terzi, 2022; Wood, 1997; Yan & Archer, 2018). The correction is defined by Equation 2.22, and depends only on the freestream Mach number, M_∞. This correction is based on a linearized perturbation velocity potential using subsonic theory and is limited to thin airfoils at small angles of attack. The validity and limitations of this correction in transonic conditions will be discussed in the following section.

$$\begin{aligned} c_{p,c} &= \frac{C_{p,i}}{\sqrt{1 - M_\infty^2}} \\ c_{l,c} &= \frac{C_{l,i}}{\sqrt{1 - M_\infty^2}} \\ c_{d,c} &= \frac{C_{d,i}}{\sqrt{1 - M_\infty^2}} \end{aligned} \tag{2.22}$$

As the inflow Mach number increases, the local flow velocities over the airfoil also increase. The inflow Mach number at which the local flow first reaches sonic conditions over any point on the airfoil is known as the critical Mach number, M_{cr}. A straightforward method to estimate the critical Mach number for an airfoil is based on the determination of the critical pressure coefficient, $C_{p_{\text{crit}}}$, as defined by Equation 2.23.

$$c_{p_{\text{crit}}} = \frac{2}{\gamma M_\infty^2} \cdot \left(\left[\frac{1 + \frac{1}{2}(\gamma - 1) M_\infty^2}{1 + \frac{1}{2}(\gamma - 1)} \right]^{\frac{\gamma}{\gamma - 1}} - 1 \right) \tag{2.23}$$

The critical pressure coefficient defines the pressure coefficient at which the local flow first reaches sonic conditions for a given freestream Mach number. As shown in Equation 2.23, this relation is independent of airfoil geometry, allowing it to be used to determine if an airfoil will experience supersonic flow. By comparing the minimum pressure coefficient on the airfoil surface to the critical pressure coefficient, one can assess whether any part of the flow exceeds the sonic condition. This means that the critical Mach number depends on the airfoil's geometry and the flow conditions, such as the angle of attack. Thicker airfoils, like those used in wind turbine applications, generally feature lower values for the critical Mach number in comparison to thinner airfoils used in aviation, meaning these are more susceptible to the emergence of supersonic flow.

Transonic shock formation over airfoils

When an airfoil is exposed to a freestream Mach number greater than its critical Mach number, it will develop a region of supersonic flow. The supersonic region is separated from the surrounding subsonic flow by a boundary known as the sonic line or sonic boundary. Following the discussion provided by Babinsky and Harvey, 2011, the convex curvature over the airfoil generates expansion waves that further accelerate the flow. The expansion waves interact with the sonic boundary, reflecting back as compression waves of equal strength. Compression waves within the sonic boundary merge downstream, forming an abrupt discontinuity referred to as a shock wave. A normal or near-normal shock wave terminates the supersonic flow region, decelerating the flow abruptly and interacting with the boundary layer. The flow is most affected close to the surface, with the skin friction decreasing rapidly and the boundary layer-shape factor increasing rapidly. Figure 2.6 illustrates the formation of a shock wave over an airfoil in transonic conditions, resulting in transonic Shock Wave and Boundary Layer Interaction (SWBLI).

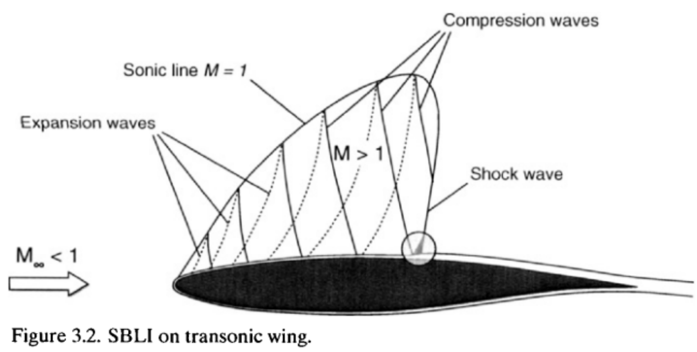

Figure 2.6: The development of supersonic flow region over an airfoil, terminated by a near-normal shock (Babinsky & Harvey, 2011)

The shock discontinuity is a non-isentropic phenomena with non-negligible viscous interaction and irreversibility. The isentropic equations fail to model the flow across the shock wave. Instead, the flow variables are determined by the so-called Rankine-Hugoniot normal shock relations, provided here for completeness. The change in the Mach number across a normal shock is defined by Equation 2.24.

$$M_1^2 = \frac{(\gamma - 1)M^2 + 2}{2\gamma M^2 - (\gamma - 1)} \tag{2.24}$$

The changes in the pressure, temperature and density over a normal shock wave are determined by Equation 2.25, Equation 2.26, Equation 2.27, where the changes in total pressure for each variable are also defined.

$$\frac{p_1}{p_0} = \frac{2\gamma M^2 - (\gamma - 1)}{\gamma + 1}, \qquad \frac{p_{t_1}}{P_{t_0}} = \left[\frac{(\gamma+1)M^2}{(\gamma-1)M^2+2}\right]^{\frac{\gamma}{\gamma-1}} \left[\frac{(\gamma+1)}{2\gamma M^2 - (\gamma-1)}\right]^{\frac{1}{\gamma-1}} \tag{2.25}$$

$$\frac{T_1}{T_0} = \frac{\left[2\gamma M^2 - (\gamma-1)\right]\left[(\gamma-1)M^2+2\right]}{(\gamma+1)^2 M^2}, \qquad \frac{T_{t_1}}{T_{t_0}} = 1 \tag{2.26}$$

$$\frac{\rho_1}{\rho_0} = \frac{(\gamma+1)M^2}{(\gamma-1)M^2+2} \tag{2.27}$$

The strength of the shock wave is directly affected by the size of the supersonic region and the local Mach number immediately before the shock, which is linked to the freestream Mach number, airfoil shape, and the angle of attack. These directly impact the aerodynamic loading, especially regarding the airfoil's drag. The Mach number at which the increase in the drag becomes significant is referred to as the drag-divergence Mach number, M_{dd}. Contrary to the drag, generally the lift first increases with increasing Mach number. The increased shock strength when increasing the Mach number leads to more pronounced effects of flow separation, which then causes a decrease in the lift coefficient. An illustration of the effects of the Mach number on the drag is shown by Figure 2.7.

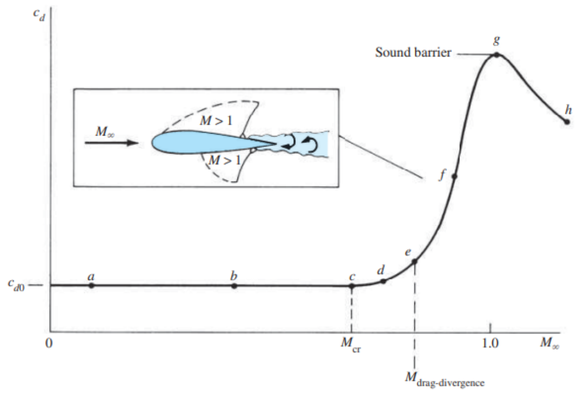

Figure 2.7: The effect of the Mach number on airfoil drag (Anderson, 2011)

There are two mechanisms through which a shock may lead to an increase in drag (Babinsky & Harvey, 2011). The first mechanism is related to the drop in total pressure in the wake due to the shock, otherwise known as 'wave drag'. The greatest losses in stagnation pressure occur near the airfoil surface, where the shock is strongest. The second mechanism is associated with the additional drag generated by shock-induced separation. Both the wave drag and flow separation manifest as pressure drag, as these alter the pressure distribution over the airfoil. The interaction of the shock and the boundary layer affects the state of the boundary layer, and thus flow separation may contribute to greater viscous drag as well.

2.2.2. Shock Wave - Boundary Layer Interaction

Any boundary layer would separate if subjected to the almost infinite pressure gradient over a shock wave, if this were extended to the wall. In reality, the shock wave and boundary layer interact in a way that dissipates the effects of the shock wave gradually over a larger region. A shock wave can induce flow separation via two mechanisms (Babinsky & Harvey, 2011).

1. Through a significant increase in the adverse pressure gradient over the boundary layer at the shock location, resulting in a local separation of the boundary layer that may reattach downstream or, for sufficiently strong shocks, extend down to the trailing edge.

2. The thickening of the boundary layer at the shock location, makes it more sensitive to adverse pressure gradients, which is more likely to lead to boundary layer separation

When the separation extends towards the trailing edge, this phenomenon is commonly known as "shock stall," as it involves a sudden decrease in lift and a sharp rise in drag. According to Pearcey, 1955, transonic airfoil separation may be classified into Type A and B, which exhibit distinct behaviours when increasing the shock strength, as illustrated by Figure 2.8. These models capture the two mechanisms of transonic flow separation previously explained.

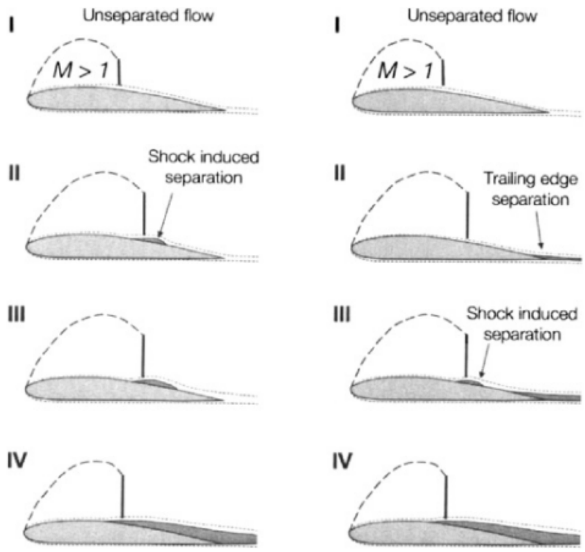

Figure 2.8: Transonic flow separation characterization (Pearcey, 1955). *Left:* Type 'A', Separation originates at the shock. *Right:* Type 'B', Separation originates at the trailing edge.

The surface curvature where shocks manifest over an airfoil is relatively small. Therefore, the flow can be assumed to be normal to the shock, and the interaction between a normal shock and the boundary layer becomes the most relevant to study. The interaction between a normal SWBLI at the so-called 'shock foot' can be characterised as weak or strong (Babinsky & Harvey, 2011), both of which manifest in type A and type B transonic flow separation.

Following the discussion provided by Babinsky and Harvey, 2011, a weak SWBLI exhibits no flow separation at the shock foot. The sonic line divides the supersonic and subsonic regions of the boundary layer, where pressure information can propagate upstream within the subsonic region. The supersonic region is stretched ahead of the shock, causing the boundary layer to thicken, thus forming compression waves that deflect the flow accordingly. The compression waves intersect along the normal shock outside the boundary layer. Closer towards the wall, the compression waves effectively allow the flow to be isentropically compressed, imposing a gradual shock-induced pressure rise along the stream-wise distance, which reduces the pressure gradient experienced by the BL, and permits it to remain attached. With decreasing wall distance, the shock wave reduces to almost a sonic wave, and the losses in stagnation pressure are reduced. The reduction in stagnation pressure losses across the shock foot is due to viscous interaction, implying that inviscid solvers are prone to overpredictions in shock losses and, thus, wave drag. This interaction can indirectly cause flow separation due to the thickening of the boundary layer, as a thicker boundary layer is more sensitive to adverse pressure gradients and, thus, separation. The topology of a weak SWBLI in equilibrium conditions is illustrated in Figure 2.9.

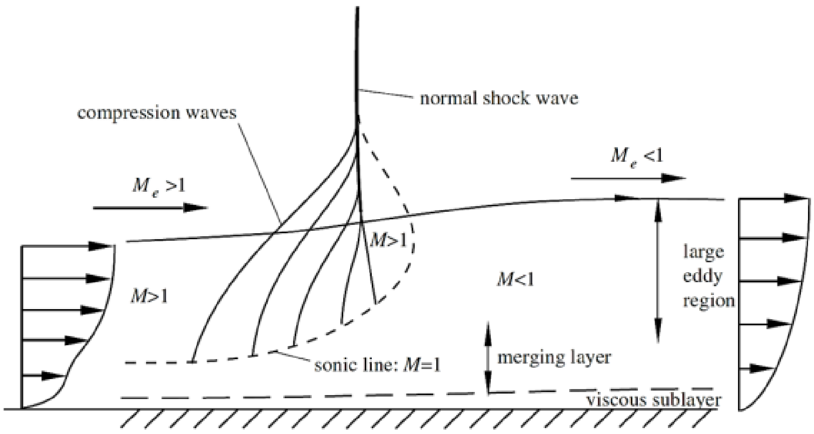

Figure 2.9: Topology of a weak SWBLI (Moulden, 1984)

On the other hand, the strong SWBLI exhibits a shock that is strong enough to separate the boundary layer at the shock foot, as shown by Figure 2.10. The boundary layer is displaced at the separation point, which causes the compression waves to form and coalesce into an oblique shock outside the boundary layer edge. A second shock develops downstream to incorporate the pressure increase due to the main normal shock, intersecting the other shock at the triple-point. The shock configuration is commonly referred to as the lambda (λ) - shock structure. The boundary layer then usually attaches downstream due to the. For turbulent boundary layers over a flat plate, Babinsky and Harvey, 2011 states that the onset of shock-induced separation occurs for free stream Mach numbers $1.3 < M_\infty < 1.35$.

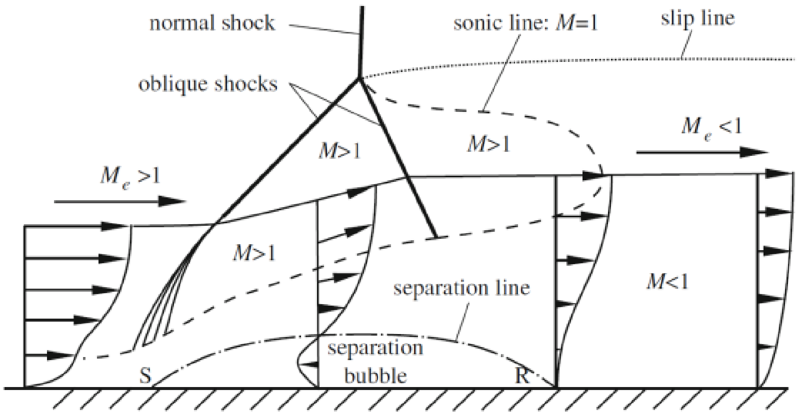

Figure 2.10: Topology of a strong SWBLI (Vos & Farokhi, 2015)

An additional distinction is made between laminar and turbulent SWBLI, which distinguishes the state of the boundary layer before the interaction. Around 1950, Gamble, 1951 conducted one of the first experiments to observe the peculiar effect of transonic SWBLI on an airfoil with free and fixed transition. As summarized by Elsenaar, 1997, during these experiments, the addition of the transition strip resulted in flow separation near the rear of the airfoil, a behaviour absent in the case of free transition. This result was surprising, as it was generally believed that a turbulent boundary layer is more resistant to separation. The flow patterns observed were sketched for a laminar boundary layer and turbulent boundary layer interaction, as shown by Figure 2.11.

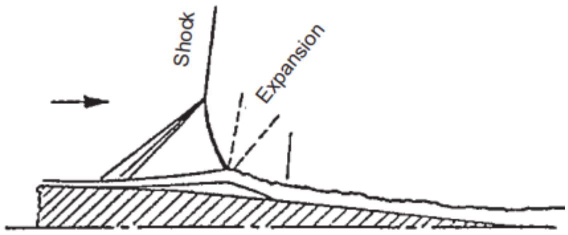

(a) Laminar boundary layer

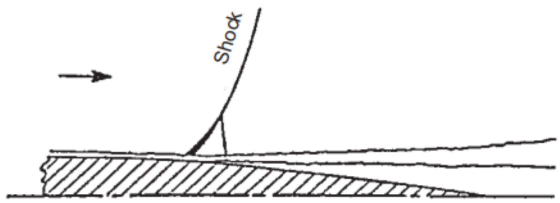

(b) Turbulent boundary layer

Figure 2.11: Flow patterns for laminar and turbulent separated boundary layer interaction (Haines et al., 1957)

Since the observations over half a century ago, the differences in turbulent and laminar SWBLI are now more understood in a qualitative sense, for which Babinsky and Harvey, 2011 provides a good description. Intuitively, less-full laminar boundary layer profiles separate easily, however, these also experience the largest degree of shock-smearing (breakdown of the shock into compression waves at the foot), and thus reduced adverse-pressure gradients. Fuller turbulent boundary layer profiles, in contrast, experience a lesser degree of shock-smearing, and thus greater adverse-pressure gradients. The discussion ends with suggesting that compared to incompressible flow separation, the sensitivity to separation in transonic interactions to boundary layer shape is reduced.

2.2.3. Transonic buffet

Generally, small local shock-induced separation does not generate significant performance decrements. However, trailing edge separation is the reason for significant increases in drag and losses of lift. Furthermore, in conditions where the flow is completely separated between the shock and the trailing edge, the resulting flow unsteadiness and its development downstream can start and sustain a feedback loop between disturbances in the flow and the shock wave's location and strength. This phenomenon is known as transonic buffeting and is described by an oscillation of a shock wave over the suction side of the airfoil. The periodic changes in the aerodynamic forces, and resultant fatigue due to transonic buffeting may pose a risk for wind turbine blade tips operating in transonic conditions. Therefore, it is crucial to characterize and quantify its impact on the aerodynamic loading.

Classification and physical mechanisms

Hilton and Fowler, 1947, conducted the first research on transonic buffet almost 8 decades ago. The development of high-speed aviation aircraft was a major interest during the 1940s, prompting the study of transonic aerodynamics of aircraft. It comes as no surprise that the early understanding of transonic buffet was developed under the context of aviation studies. Lee, 2001 reviews the early experimental and numerical studies work aimed to determine the physical mechanisms of transonic buffeting. Building upon this review is the review by Giannelis et al., 2017, which outlines recent developments in the understanding of transonic buffeting.

The experimental and numerical work has culminated in identifying two types of transonic buffet, namely

- Type I: Transonic shock buffet at zero incidence on biconvex sections, including shock oscillations on both the pressure and suction sides of an airfoil.
- Type II: Transonic shock buffet at a non-zero incidence on modern supercritical airfoils, involving an oscillating shock on the suction side of the airfoil.

The investigations from Mabey, 1981, and Gibb, 1990, have led to the developing of a working model for Type I buffet. Both have proposed being able to predict the onset of the transonic buffet by assessing the Mach number ahead of the shock, as a Type I buffet required a strong SWBLI.

In the context of current research on transonic flow over wind turbines, a review of Type II buffet is more relevant, as the wind turbine tip generally operates at non-zero angles of attack. Therefore, the following sections focus on the Type II buffet. Tijdeman, 1977 presents three classifications of the Type II buffet, characterised by experimental work on the NACA 64A006 airfoil with sinusoidal flap deflections. These shock oscillation modes have been also identified for stationary airfoils at certain operational conditions Lee, 2001. The following descriptions have been taken from the review provided by Giannelis et al., 2017. An illustration of these different oscillations is given by Figure 2.12.

- Type A: Represented by near sinusoidal shock oscillations across the upper surface of the aerofoil, for which the shock is present throughout the entire buffet cycle but varies in strength, with maximum shock strength achieved during the upstream excursion.
- Type B: Resembles Type A; however, the magnitude of shock strength variation is considerably larger, resulting in a disappearance of the shock during the downstream excursion.
- Type C: Qualitatively distinct from the preceding modes. The shock travels upstream, initially strengthening and then weakening, but continuing to move forward, eventually propagating forward into the oncoming flow as a free shock wave.

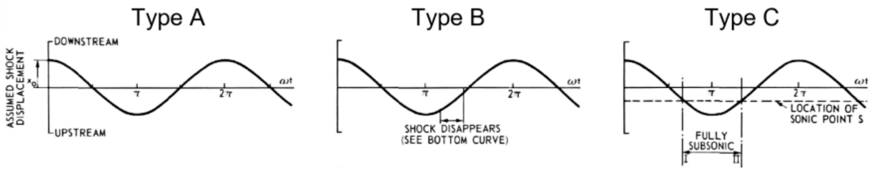

Figure 2.12: Classifications for the Type II transonic buffet into types A, B and C, as distinguished by Tijdeman, 1977

Despite numerous experimental and numerical studies available, the physical mechanism of Type II buffet is still to be determined, with several authors proposing different flow physics (Crouch et al., 2009; Lee, 1990; Pearcey, 1958; Pearcey & Holder, 1962; Raghunathan et al., 1998). Lee's model has resulted in good predictions of the buffet frequency for several airfoils, but poorer estimates for others (Giannelis et al., 2018).

The onset of transonic buffeting

Across different airfoil investigations, the onset of transonic buffeting depends on the angle of attack, Mach number and Reynolds number. The results of an extensive study on static and dynamic pressure measurements on the NACA 0012 airfoil by McDevitt and Okuno, 1985, indicate that the minimum angle for the onset of transonic buffet decreases with increasing freestream Mach number. These simulations were conducted at freestream Mach numbers 0.7 < M_∞ < 0.8, at Reynolds numbers between 1 and 14 million. These observations are in accordance with the findings of a recent numerical study by Giannelis et al., 2017, which employed URANS simulations on the OAT15A airfoil to characterize the influence of the Mach and angle of attack on the characteristics of transonic buffeting.

Buffeting characteristics

An observation of Giannelis et al., 2018, is that transonic buffeting at onset closely resembles the Type A buffet, however, it evolves into a combination of type A and C oscillations at higher angles of attack. At angles of attack beyond the onset of transonic buffeting, where the airfoil is generally stalled, a non-linear variation in the aerodynamic coefficients was observed. Furthermore, the shock oscillations at $M_\infty \geq$ 0.56 exhibited intermittent separation and reattachment of the shear layer downstream of the shock. At lower Mach numbers, separation extended from the shock foot towards the trailing edge instead, suggesting a strong characteristic dependency on the Mach number.

The spectral contents of the transonic buffeting phenomenon are characterized by a narrow-band frequency contribution and have been investigated in several numerical and experimental settings. The strouhal number, St, is a useful non-dimensional parameter that describes oscillatory flow mechanisms. An oscillatory flow mechanism's frequency, f, may be non-dimensionalised using Equation 2.28, where the characteristic length scale, L, is typically the airfoil's chord length, and the characteristic velocity, V, is the freestream velocity.

$$St = \frac{fL}{V} \tag{2.28}$$

As stated by D'Aguanno, 2023, the results of several experimental (Hartmann et al., 2013; Jacquin et al., 2009; McDevitt & Okuno, 1985) and numerical studies(Deck, 2005; Giannelis et al., 2018; Iovnovich & Raveh, 2012; Thiery & Coustols, 2006) support the claim that the peak frequency for transonic buffeting is somewhere in the range between $0.05 \leq St \leq 0.08$. However, these studies are conducted on normal or supercritical airfoils, and there is no guarantee that a wind turbine airfoil will display similar behaviours.

As can be expected based on the difference in laminar and turbulent boundary SWBLI, the characteristics of the transonic buffet also change depending on this interaction (Moise et al., 2023). A comparison between Large Eddy Simulations (LES) on the NACA 0012 airfoil at Re = 5 million, M = 0.7-0.8, revealed, among many results, that buffet amplitude was reduced in fixed-transition simulations. Furthermore, the buffet frequency and global dynamic behaviors were observed to be similar in both simulations.

2.2.4. State-of-the-art research for wind turbine airfoils in transonic flow

As mentioned in section 2.1, wind turbine airfoils at the tip are significantly different from those in aviation, in terms of their geometry and operational conditions. Thus, one can expect variations in how transonic flow effects develop and manifest over them. De Tavernier and Von Terzi, 2022 revealed that local supersonic flow appears near the cut-out speed of wind turbines, at which point the blades are pitched out to maintain rated power and lower the aerodynamic loads experienced. The blade pitch reduces the angle of attack experienced by the tip region, leading to transonic flow developing while the airfoil operates at negative angles of attack. These unique operational conditions and the novelty of transonic flow over wind turbines are reflected in the limited amount of literature on wind turbine airfoils in or close to transonic conditions.

Available literature

Hossain et al., 2013 presents a numerical analysis of compressible flow around the NREL phase VI wind turbine blade airfoil S809, at a Mach no. M = 0.8 for angles of attack between 0° and 10°. Even though the study by Hossain et al., 2013, was conducted at a free-stream Mach number of 0.8, which may be too high to be of relevance for current wind turbine operational regions at the tip, and for positive angles of attack, the results provide valuable insights into the formation and propagation of shock waves around wind turbine airfoils. The airfoil features a relative thickness of 21%, which is comparable to that of typical airfoils used at the blade tip. The commercial CFD code `ANSYS FLUENT` was used to determine the pressure coefficient, lift and drag coefficients.

Sørensen states it is difficult to compare the compressible and incompressible solutions for a full-size 3D rotor CFD simulation because compressibility also affects the rotor induction. To bypass this issue, Sørensen et al., 2018, presents a 2D numerical analysis of compressible flow around the DU91-W2-250 airfoil, scaled to have a relative thickness of 24%. study of compressibility effects in a full 3D rotor CFD simulationThe lift coefficient, drag coefficient and pressure distribution results from separate RANS simulations using the compressible `FLOWer` solver, the incompressible `EllipSys2D` solver, and a compressible version of the `EllipSys2D` are compared between M_∞ = 0 to 0.5. Additionally, the validity of compressibility corrections is assessed.

The work from De Tavernier and Von Terzi, 2022 has been previously described in subsection 2.1.3, as it presented a unique analysis of the conditions for which transonic flow occurred over the IEA 15MW Reference Wind Turbine using `OpenFAST` and `XFOIL`. The tip region, which uses the FFA-W3-211 airfoil, was demonstrated to operate in transonic conditions, motivating the experimental investigation on the occurrence of transonic flow effects on the FFA-W3-211 airfoil by Aditya et al., 2024. To the authors' knowledge, this presents the first experimental assessment of transonic flow over a wind turbine airfoil. The investigation is carried out for $M_\infty = 0.5$ and 0.6, for the AoAs of -6° and -10°, in free-transition. These operational conditions were chosen based on the supersonic threshold derived by De Tavernier and Von Terzi, 2022. The flow field around the airfoil was analysed using the Schlieren and Particle Image Velocimetry (PIV) techniques.

Two recent numerical studies continued the work of assessing the transonic envelope of the FFA-W3-211 airfoil, derived by De Tavernier and Von Terzi, 2022, and its performance under steady and unsteady conditions. The work of M. Vitulano et al., 2024, features unsteady RANS (URANS) CFD simulations

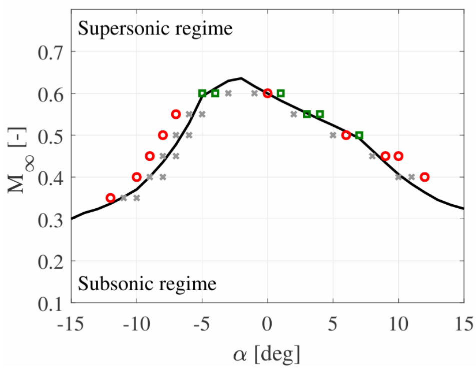

Figure 2.13: Subsonic-supersonic boundary for the FFA-W3-211 wind turbine tip airfoil (using Xfoil): configurations selected for URANS threshold (grey crosses), configurations in which a supersonic regime is established (red circles), and configurations in which shock waves appear (green square). Results shown for $Re = 1.8 \times 10^6$ (M. Vitulano et al., 2024)

using OpenFOAM and XFOIL simulations at Re = 1.8 and 9 million, to establish when transonic flow occurs, for combinations of M_∞ and α, during steady conditions. The lower Reynolds number is in the order for which wind turbine airfoil polars are typically determined experimentally. The latter value is closer to the full-scale wind turbine operating conditions at the tip. The first set of simulations result in a supersonic envelope similar to the one developed by De Tavernier and Von Terzi, 2022 using XFOIL and a separate one derived using CFD simulations (See Figure 2.13). The second set of simulations aimed to characterize the behaviour while entering and leaving subsonic and supersonic regimes in an unsteady pitching motion. The airfoil was simulated in a sinusoidal pitching motion at M = 0.35, Re = 9 million, characterized by a mean angle of -10°, an amplitude of 5°, and different values for its frequency, expressed in terms of the reduced frequency $k = \pi fc/V_\infty$ = 0.4, 0.5, 0.6. M. C. Vitulano et al., 2024, presents an analysis of the transonic features of the airfoil, using the tool XFOIL with the Prandtl-Glauert correction, and a URANS CFD simulation using OpenFOAM. Once again, the supersonic envelopes for both approaches are presented, URANS CFD simulations are conducted at configurations close to the sonic-supersonic boundary, to confirm the presence of supersonic flow and shock waves. The previous studies on the FFA-W3-211 airfoil are unique in analysing its behaviour at negative angles of attack, as these conditions are relevant to the actual operating conditions of the blade tip when transonic flow is expected.

Compressibility effects, and corrections for wind turbine airfoils

Sørensen et al., 2018 states that compressibility will generally increase the adverse pressure gradients over the airfoil, resulting in a thicker boundary layer and premature separation. The results find a good agreement between the linear region of the $c_l - \alpha$ polar, namely for -8° < α < 8° for results using the Pranftl-Gluert compressibility correction. However, the study revealed that simple compressibility corrections, such as the Prandtl-Glauert correction, are not sufficient outside of the linear region, where stall and viscous effects are strong. These conclusions are validated for positive angles of attack only. The discrepancy between the incompressible and compressible solutions relative to the compressible solution increased with increasing Mach number, reaching a maximum of -14% for the lift and -18% for the drag. The discrepancies were reduced to a maximum of 6% and -6% respectively, after applying the Prandtl-Glauert correction. The correction is seen to over-correct the coefficients at low angles of attack, and under-correct for higher angles of attack. The investigation indicates that the discrepancy is greatly due to the differences in the pressure and skin friction distributions over the airfoil, which have shown to be limited for Mach numbers below 0.3 but already significant for Mach numbers around 0.5. Given that transonic flow over wind turbines is likely to occur in the tip region at negative angles of attack and for free-stream Mach numbers around and potentially beyond 0.3, the limitations of the Prandtl-Glauert correction in assessing the effects of compressibility, and even more so, transonic flow over an airfoil, highlight the need for alternative assessment methods that do not rely on simple corrections. More accurate corrections may be achieved using the Karman-Tsien and the Laitone corrections.

The conclusions for the accuracy of the compressibility corrections are corroborated by the findings from M. C. Vitulano et al., 2024 for the derived supersonic-sonic boundary using XFOIL with the Prandtl-

Glauert correction and `OpenFast`, as these displayed a mismatch that grew for large angles of attack, and high Mach numbers. At the same Mach number, URANS predicted the onset of transonic flow at slightly smaller AoAs. For a wind turbine operating beyond rated speeds and with the blades pitched to maintain rated power, thus making the tip operate at negative angles of attack, URANS simulations suggest a larger safety margin. The inverse holds for turbines operating below-rated wind speeds.

Shock wave formation and boundary layer interaction

Across various studies on transonic flow over wind turbine airfoils, supersonic flow has been identified under several operating conditions, with some cases leading to the development of shock waves and shock-induced boundary layer separation. The results from Hossain et al., 2013, indicate the presence of two shock waves, one on the top and one on the bottom side of the airfoil, for all considered AoAs. Near the shock regions, the pressure distribution, Mach number distribution, and temperature distribution along the airfoil are shown to vary substantially. An analysis of the streamlines and of the turbulent viscosity contours led to the observation of flow separation after the shock, starting at an angle of attack α = 8°, suggesting a strong boundary layer interaction. Given that RANS simulations yield mean-flow solutions, a temporal analysis of the shock is not possible.

The experimental results from Aditya et al., 2024 confirm the presence of supersonic flow over the free-transition suction-side of the FFA-W3-211 airfoil for some conditions at negative AoAs where this was expected according to the supersonic envelope developed by De Tavernier and Von Terzi, 2022, however, findings also show that the mean flow barely reached a local Mach number of 1 for a free-stream M =0.5 and α =-6° in which supersonic flow was predicted based on the supersonic envelope. This is likely due to the uncertainty introduced by the compressibility corrections used in `XFOIL` to calculate the sonic-supersonic boundary, and having conducted the experimental measurements close to the derived sonic-supersonic boundary conditions. Upon inspecting individual PIV frames, supersonic flow was found to occur intermittently for a very small region in 10-30% of the total frames. For the most drastic case at M = 0.6 and α = -10°, the mean flow reaches supersonic speeds, extending from 5-35% of the chord. An analysis of the standard deviation in the Mach number field suggests the presence of an oscillating shock between 15-35% of the chord, confirmed later by an analysis of instantaneous PIV and Schlieren images, from which the shock is observed between 20% to 35% of the chord. Similarly, the presence of an unsteady separation of the shear layer due to the shock, extending downwards from 20-30% of the chord, was also identified and confirmed. The PIV and Schlieren measurement techniques successfully identified shock waves and their interactions with the boundary layer, triggering the onset of separation. While the acquisition frequency of the PIV measurements was sufficient to detect the presence of moving shock waves and shock intermittency, this was too low for calculating the characteristic frequencies of the shock movement or analyzing its temporal development.

Similarly to the experimental results, the URANS simulation results from M. C. Vitulano et al., 2024 identified supersonic flow where expected according to the supersonic envelope developed by De Tavernier and Von Terzi, 2022, however, no supersonic flow was observed for a few scenarios in which it was expected. An analysis of the Mach number field showed the presence of a shock wave very close to the leading edge for simulations at α =-15° and α = 15°, for M = 0.4, and Re = 9 million.

As described by numerical and experimental studies, supersonic flow and shock wave formation are identified, with the experimental results suggesting the presence of moving and intermittent shocks. Additionally, the results from these studies have shown to have a strong dependency on the angle of attack, the inflow Mach number and the Reynolds number, subjects treated in the following sections.

Influence of the angle of attack

Across studies, steeper angles of attack have been demonstrated to vary the size, shape and location of the region experiencing supersonic flow along the airfoil. The flow is prone to shock formation at steeper angles of attack, due to the increased acceleration caused by the steeper pressure gradients.

Hossain et al., 2013, found that both c_L and c_D both increase with increasing alpha in the range of 0° $\leq \alpha \leq$ 10°, with significant rise occurring after α =8°. Surprisingly, this coincides with the onset of shock-induced separation, which was observed to occur more rapidly as the AoA increases. This is corroborated by the results from Aditya et al., 2024, which showed that the experiment at M =0.6 and α = -6° displayed less signs of separation compared to the case at M =0.6 and α = -10°, where a strong region of unsteady flow separation and an unsteady shear layer was observed. These results suggest that shock-induced separation is more likely to occur at higher angles of attack.

Across studies, supersonic regions, and shockwave characteristics have been seen to vary with the angle of attack. For the two shockwaves identified by Hossain et al., 2013, the top shocks shift from $x/c \approx 0.51$ to $x/c \approx 0.33$ for an increase in the angle of attack from 0° to 10°. Conversely, the position of the bottom shocks shifted from $x/c \approx 0.42$ to $x/c \approx 0.68$ for an increase in the angle of attack from 0° to 9°. Variations in aerodynamic loading are strongly linked with the associated change in the pressure distribution due to the position and strength of the shock waves. These findings are consistent with the experimental results from Aditya et al., 2024 where the sonic line along the bottom of the airfoil is seen to move upstream and vary in shape and size for a steeper variation in the AoA from -6° to -10°. This was found by mapping the probability of sonic flow over the flow field, for all frames, and denoting the contour corresponding to a probability of 0.5 as the sonic line. The shape of the approximate supersonic region has been observed to change with AoA, being flatter (maximum $y/c \approx 0.18$) and more elongated (x/c ranging from 5% to 35%) for α=−6°, compared to α=−10° where the region extends to $y/c \approx 0.2$ and $x/c \approx$ 2% − 25%.

Analysing the results for the subsonic-supersonic boundary derived for the FFA-W3-211 airfoil in `XFOIL` and URANS CFD simulations by M. C. Vitulano et al., 2024, it is apparent that, for small AoAs $|\alpha| < 5°$, local supersonic flow is predicted to occur for Mach values from $M \geq 0.55$. For steeper AoAs, $|\alpha| >$ 10°, local supersonic flow is predicted to occur for lower Mach values $M \geq 0.4$.

The results of the unsteady simulation by M. Vitulano et al., 2024, indicate that during downstroke motion (Moving into the transonic regime), transonic flow occurs later at α = −14.02° for k=0.4, α = −14.25° for k=0.5, and α = −14.36° for k=0.6, while this is at α = -10.8 in steady conditions. Considering upstroke (Moving away from the transonic regime), transonic flow is delayed until α = −9.93° for k=0.4, α = −9.72° for k=0.5, and α = −9.39° for k=0.6. Effectively, it has been observed that for increased reduced frequencies, the transonic regime expands. Additionally, a hysteresis is observed in the lift and drag coefficients, more pronounced in the drag and expanding with higher reduced frequencies.

Influence of the free-stream Mach number

The inflow Mach number has been observed to play a key role in supersonic flow development and the emergence of shock waves. The experimental simulations at α =-10° from Aditya et al., 2024, show a significant difference in the flow behaviour between M = 0.5 and M = 0.6. Despite local supersonic flow being predicted to occur for both configurations, the simulation at M = 0.6 displayed a greater mean flow Mach number, suggesting the presence of a shock wave, with 100% of PIV frames containing sonic conditions. On the other hand, the simulation at M = 0.5 barely reached supersonic conditions in a mean sense, with 10-35% of the total PIV frames attaining sonic conditions. These findings are consistent with the results of the URANS CFD simulations from M. C. Vitulano et al., 2024. Here, the results indicate that an increase in the Mach number results in the emergence of supersonic flow, and shock waves, even for modest AoAs. However, shock waves were absent at low inflow Mach numbers, even for large AoAs.

M. C. Vitulano et al., 2024 analyzed the skin friction coefficient, observing that in the case of flow separation, the separated region becomes smaller, and its point of separation moves aft with increasing inflow Mach number.

Influence of the Reynolds number

The influence of the Reynolds number has been confirmed to play a role in the accuracy of the Prandtl-Glauert compressibility correction. The discrepancy in the compressible and corrected incompressible results from Sørensen et al., 2018 was demonstrated to depend strongly on the Reynolds number, with larger Reynolds numbers in the order of 14 million being beneficial for the accuracy of the compressibility correction. At the high Reynolds numbers that are experienced by wind turbines, the corrections to the lift and drag allowed the corrected results to be within 2.5% per cent of the compressible results, for Mach numbers up to 0.3. However, even for high Reynolds numbers, the corrections are insufficient beyond Mach 0.3. These conclusions are consistent with the comparison between the subsonic-supersonic boundary derived for the FFA-W3-211 airfoil using `XFOIL` and URANS CFD simulations made by M. C. Vitulano et al., 2024, where even for Re = 9 million, there was a significant discrepancy in the predicted boundary at low angles of attack, due to the high Mach number required to achieve local supersonic flow. Slight discrepancies were also observed for the boundary region near M =0.3, where large angles of attack are required for the presence of local supersonic flow. These observations support the findings that the Prandtl-Glauert compressibility correction becomes inaccurate due to the effects of viscosity and stall, as discussed previously in the results of Sørensen et al., 2018.

The Reynolds number has also been found to play a critical role in the emergence of supersonic flow over the FFA FFA-W3-211 airfoil. For both the subsonic-supersonic boundaries derived using `XFOIL` and URANS CFD simulations, M. C. Vitulano et al., 2024 observed that an increase in the Reynolds number encourages the emergence of local supersonic flow conditions. The effect is apparent for larger AoAs, where the boundary shifts the most. The analysis for URANS CFD configurations close to the subsonic-supersonic boundary showed that an increased number of configurations developed shock waves when increasing the Reynolds number.

The simulation results at α = -15° and 15° for the lower Reynolds number, Re = 1.8 million, confirm that shock waves emerged with increasing inflow Mach number, however, only for α = -15°. Local supersonic conditions were observed near the leading edge for α = 15, however, a smooth sonic pocket indicates that the flow is accelerated sufficiently gradually to prevent shock formation. thus supporting the conclusion that supersonic flow is a necessary, but not sufficient, condition for shock wave formation. At the higher Reynolds number Re = 9 million, the local Mach number reaches values as high as M = 1.36, for α = 15°, for which density gradients around the region were identified. Apparently, the pressure drop does not lead to subsonic conditions after the first supersonic region, resulting in another supersonic pocket developing shortly downstream. For the case at α = -15°, the local Mach number reaches a maximum value of 1.48, for which a single shock was identified.

Summary of Transonic Flow Effects on Wind Turbine Airfoils

The state-of-the-art research on wind turbine airfoils operating in transonic flow has revealed specific circumstances that lead to the emergence of transonic flow and shock waves. Both numerical and experimental studies have shown that the formation and characteristics of these shocks are influenced by factors such as the inflow angle of attack, Mach number, and Reynolds number. Although shock wave-associated phenomena like boundary layer interaction (shock-induced buffeting and separation) have been documented, the direct impact of these effects on the aerodynamic performance of airfoils, specifically in terms of lift and drag coefficients, remains underexplored. Given the importance of airfoil performance in wind turbine power generation and integrity, as discussed in section 2.1, it is important to quantify these effects for the design of modern and future turbines.

Sørensen et al., 2018, has addressed the limitations of compressibility corrections under conditions in which transonic flow is expected over the tip of wind turbine blades, namely for airfoils operating outside their linear range, and at inflow Mach numbers higher than 0.3. Many existing studies have relied on tools that depend on compressibility corrections, thus, introducing a degree of uncertainty in their results. Numerical studies for this topic have relied on URANS CFD simulations; however, M. C. Vitulano et al., 2024, has highlighted and acknowledged the limitations in their ability to accurately capture transonic flow phenomena, especially shock waves. This is due to the inherent assumptions and modelling of turbulent flow, and its interaction with shocks.

On the other hand, experimental work on wind turbine airfoils in transonic conditions remains limited. New experimental studies in this area would provide valuable data for validating numerical simulations and offer a deeper understanding of the real aerodynamic behaviours under transonic conditions. Furthermore, experiments may provide additional insights that are challenging to resolve through numerical models due to their limitations. section 2.3 will explore various experimental methods that may be employed to study the effect of transonic flows for wind turbine airfoils.

2.3. Experimental measurement techniques

As discussed in subsection 2.1.2, experimental testing of wind turbine airfoils is a critical step in predicting wind turbine performance. This testing is conducted in wind tunnel facilities, where the aerodynamic characteristics of a scaled-down airfoil model can be systematically investigated.

2.3.1. Wind tunnel facilities

Subsonic wind tunnels use a large fan to accelerate air to a steady subsonic free stream within the test section. In closed-circuit wind tunnels, the airflow is recirculated, whereas in open-circuit tunnels, the air is expelled into the atmosphere. An example of the latter is the Open Jet Facility (OJF) at the Aerodynamics Laboratory of Delft University of Technology (TU Delft), The Netherlands.

Fan-driven wind tunnels are effective up to velocities of approximately 110m̃/s, beyond which the power requirements make it impractical. To reach higher speeds, a converging-diverging duct is used instead. Transonic and supersonic wind tunnels operate in one of the following configurations:

1. **Blow-down:** Pressurised air stored in a high-pressure vessel is released, accelerating through the test section before being expelled into the atmosphere.
2. **Indraft:** A vacuum chamber downstream of the test section draws air through the test section, accelerating it to the desired velocity.
3. **Blow-down/Indraft Combination:** A hybrid configuration utilizing both pressurised air supply and vacuum suction to achieve the desired flow conditions.

Given these constraints, the investigation of the transonic performance of an airfoil must be conducted in a transonic wind tunnel employing one of these operating principles.

For airfoil performance, it is important to quantify the aerodynamic loads, pressure distribution, boundary layer development, and flow behaviour around the airfoil, especially under the effect of compressibility. By analysing these factors under varying operational conditions such as angle of attack, Mach number, and Reynolds number, aerodynamicists can gain valuable insights to understand airfoil performance and optimise design. This section discusses several techniques that have been considered suitable to visualize the flow field and obtain pressure and aerodynamic load measurements for an airfoil operating in transonic conditions.

2.3.2. Flow-field measurements

Flow-field measurements are essential to understanding the interaction between the airfoil and the incoming flow, manifested through various phenomena such as boundary layer development, flow separation, wake development, shock waves, etc. To understand this interaction, it is important to measure key variables from the flow field, such as pressure, temperature, density, and velocity. From these, other flow characteristics of interest may be derived, such as the Mach and Reynolds numbers.

Velocity measurements are common among flow-field measurements. This may be measured in a wind tunnel facility indirectly from pressure measurements (Tropea et al., 2007). Here, a focus is made on other techniques, starting with anemometry-based techniques. Anemometry-based techniques rely on directly measuring the velocity vector field. Well-researched anemometry-based techniques that have been applied in investigating transonic flow around aerodynamic objects include Laser Doppler Anemometry (LDA), Hot Wire/Film Anemometry, and Particle Image Velocimetry (PIV). For further details about these techniques, refer to Tropea et al., 2007 and Ristić et al., 2004, from which the following descriptions have been obtained.

Laser Doppler Anemometry

LDA is a particle-based technique that assesses the velocity of tracer or seed particles travelling along the flow, assuming these accurately represent the flow velocity at a specified location. Tracer particles must possess suitable mechanical and scattering properties, such as being capable of following the flow and scattering sufficient light for detection. They should also be non-contaminant and safe for use in a wind tunnel environment. The LDA technique has different modes of operation, including the reference beam, and the crossed beam 'or 'fringe' setups, the later of which provides a greater signal intensity. Both of these setups involve illuminating the tracer particles with a monochromatic, coherent, and collimated laser beam. The scattered light from these particles is then captured by a photodetector. The photodetector converts the scattered light signal into an electrical signal, which is analyzed to determine the Doppler frequency shift. This frequency shift is directly related to the velocity of the tracer particles. This technique requires no calibration, just an accurate setup, offering high spatial resolutions.

Hot Wire/Film Anemometry

HWA is a thermal anemometry technique used to quantitatively assess the velocity and temperature fluctuations at a specified location, particularly in turbulent flows. The setup consists of a probe with a thin metallic wire heated by a continuous electrical current due to the Joule effect. As the probe is introduced to the flow, the heat transfer between the wire and the fluid is influenced by both flow velocity and temperature. The HWA technique has different modes of operation, including the Constant Temperature Anemometer (CTA), or a Constant Current Anemometer (CCA), each providing different electrical responses to changes in fluid velocity. Calibration is required to establish a relationship between the anemometer output voltage and the velocity magnitude. The calibration is sensitive to the temperature at which the probe is calibrated. This technique can be suitable for supersonic flows, offering high temporal resolution, and is capable of capturing velocity signals up to several kHz at specific points in the flow.

Particle Image Velocimetry

Similar to LDA, PIV is a particle-based technique used to measure flow-field velocity by measuring the displacement of tracer particles in a short time interval. The tracer particles must meet criteria similar to those used in LDA, such as appropriate mechanical and light scattering properties. The PIV setup involves a laser sheet, created by a pulsating light source, that illuminates a thin plane of the flow, providing a defined measurement area. As the particles move through this illuminated plane, they scatter light. A high-speed camera captures two images of the illuminated particles at short time intervals. These images are processed into multiple interrogation windows. By correlating the particle displacements between image pairs within each window, the average velocity components along the plane are determined. This analysis yields detailed velocity vectors for the entire plane, which allows PIV to capture instantaneous flow structures, making it suitable for studying complex flow phenomena such as shock waves. However, its temporal resolution is limited by the capabilities of the laser and camera systems.

A summary of the advantages and disadvantages of LDA, HWA, and PIV techniques is presented in Table 2.1. key criteria include

Table 2.1: Comparison of velocity measurement techniques: LDA, HWA, PIV

Technique / Criteria	**LDA**	**HWA**	**PIV**
Intrusiveness	Low	High	Low
Velocity components	Up to 3 components	Magnitude only	Up to 3 components
Whole field measurement	No	No	Yes
Temporal resolution	Good	Best	Limited by equipment
Calibration	Not required	Complex	Simple
Optical access	Required	Not Required	Required

Light transmission-based methods rely on capturing the change in fluid density generated by aerodynamic effects and the resultant flow inhomogeneity, through which light refracts differently as it travels across. These become interesting when analysing compressible phenomena. A relationship between the refractive index of a fluid and its density is defined by the Clausius–Mosotti equation. For gases, this is expressed by the Gladstone-Dale equation, shown by Equation 2.29, where K is the Gladstone-Dale constant.

$$n - 1 = K\rho \tag{2.29}$$

The relationship between variations in fluid density and the refractive index is linear. As a result of variations in the refractive index, light is deflected in the direction of increasing refractive index/density. For compressible flows, the density is a function of the Mach number; thus, from the resulting refraction of light rays, it is possible to deduce information about the flow Mach number. Well-researched transmission-based techniques that have been applied in measuring the flow around aerodynamic objects include shadowgraphy, schlieren, and interferometry. For further details about these techniques, refer to Tropea et al., 2007 and Ristić et al., 2004, from which the following descriptions have been obtained.

Shadowgraphy
This technique provides a qualitative measure of the second derivative of the density field. The setup for this technique is simple, requiring an incoherent diverging light source to be transmitted as parallel rays through the test section containing the model. Aerodynamic effects present around the model subjected to an incoming flow create variations in the fluid density and deflect the incoming light rays, creating shadow patterns. The inhomogeneous density field can be observed in the shadow patterns at a plane behind the model, which is the point of focus for images. Reconstructing the density field from Shadowgraphy images requires integrating the measured double derivative twice, which may introduce significant errors, and thus, quantitative shadowgraphy is rare in practice. Shadowgraphy is very commonly used for analysing compressible flows and shock waves.

Schlieren
This technique provides a qualitative measure of the first derivate of the density field. The setup for this technique is simple and comparable to shadowgraphy, however, the flow is now the focus of the image. After light passes through the test section, it is focused by a lens onto a point where a knife edge is placed. The knife-edge blocks some of the deflected light rays, specifically those travelling in a certain direction that would otherwise reach the detector. By blocking these rays, the image becomes more sensitive to specific density gradients. Similarly to shadowgraphy, this technique is commonly used for analysing compressible flows and shock waves.

Interferometry
This technique provides a qualitative measure of the density field. The setup is complex, requiring the use of an interferometer to measure the change in phase of the light rays travelling across the test section. The resulting visible pattern displays the interference of light rays and provides iso-lines of the refractive index/density. Two common methods are the reference beam interferometry and shearing interferometry. This technique is suitable for analysing compressible flows.

2.3.3. Pressure and aerodynamic load measurements

Pressure measurements are important to derive other thermodynamic flow field properties, such as temperature, but may also help in determining the aerodynamic loads acting on the airfoil. From the previous sections, there have been different concepts related to pressure, namely static pressure, total pressure and dynamic pressure, which are defined as follows

- Static pressure: The force per unit area exerted by the random motion of the molecules in a fluid
- Total pressure: The pressure that results by isentropically decelerating the flow to rest
- Dynamic pressure: The kinetic energy per unit volume of the fluid

A pressure transducer is the device responsible for measuring pressure. The accuracy of the measurement depends heavily on the sensitivity of the transducer. When experimenting with airfoils, total and static pressure measurements around the flow field can be taken using pitot and static pressure probes, or one that combines both as a pitot-static probe connected to pressure transducers. A long, slender tube with a round tip is generally used for subsonic and transonic flows, while one with a sharp tip is used for supersonic flows. In some conditions, shock waves may develop over the probes, altering the pressure field significantly, and thus the readings obtained. The probe design must take these effects into account. One of the disadvantages of pressure probes is their intrusion on the flow, and their limitation to point-wise measurements.

Static pressure measurements at the airfoil surface are commonly obtained using wall tapping, which involves small pressure orifices connected to pressure transducers. By installing multiple pressure taps across the surface of the airfoil, a detailed pressure distribution can be mapped. This distribution may provide valuable insights into boundary layer development and loading distribution, and the pressure data can be integrated to estimate the aerodynamic loads. One disadvantage of this method is that it is intrusive, which can disturb the local flow and impact measurement accuracy. Additionally, the spatial resolution is limited by the placement and number of pressure taps, and installation becomes particularly challenging with small-scale airfoil models used in transonic wind tunnels.

Aerodynamic loads may be determined through a force balance. The two groups of balances include internal and external balances. Detailed descriptions of their working principles are available within Tropea et al., 2007. Other methods to calculate the airfoil drag involve the use of a wake rake to capture the total pressure deficit in the wake, which is proportional to the airfoil drag.

More recently, several studies at the Delft University of Technology have explored a non-intrusive integral aerodynamic load determination method for airfoils through the reconstruction of the pressure field using the velocity data from PIV measurements(D'Aguanno, 2023; D'Aguanno et al., 2025; Ragni et al., 2009; B. W. Van Oudheusden et al., 2007; B. Van Oudheusden, 2008; B. Van Oudheusden et al., 2006). B. Van Oudheusden et al., 2006 provides the methodology to characterise the loads over a low-speed airfoil, using isentropic flow relations to determine the pressure field, and a control volume approach to determine the loads. D'Aguanno et al., 2025; Ragni et al., 2009; B. W. Van Oudheusden et al., 2007 later expanded the method to compressible flow applications, including flows with shock waves. Through a manipulation of the momentum equation, an expression for the derivative of the pressure in terms of the local flow velocity may be used to reconstruct the pressure field in regions where the isentropic flow assumption, such as near shock waves, and in viscous shear layers like the boundary layer and the wake. The pressure reconstruction method relies on the integration of the inferred pressure gradient field. Studies have shown that PIV-based load estimation for airfoils in transonic conditions is feasible, offering the advantages of being non-intrusive, directly correlating aerodynamic loads with flow features, and providing higher spatial resolution, greater flexibility, and simplicity compared to pressure taps and balance systems. The details of this non-intrusive load determination method are saved for chapter 4.

This section discusses various experimental techniques considered for analysing a wind turbine airfoil in compressible and transonic conditions. The previous sections have outlined the key role of airfoil performance in the aerodynamic performance and loading of wind turbines. The literature review identifies a clear knowledge gap in experimental work regarding the effects of compressibility at the wind turbine and wind turbine airfoil level, particularly in transonic conditions where compressible phenomena may become severe. The motivation of this thesis is to understand the effects of compressibility at a scaled-down wind turbine airfoil level, with the hope of building a foundation to later understand these effects at the full-scale wind turbine level. Given the recent advancements in the transonic performance of wind turbine airfoils, this thesis will move forward with an experimental investigation of the effect of compressibility on the FFA-W3-211 airfoil. The Schlieren and PIV techniques are chosen to provide instantaneous and time-averaged flow field data. The pressure reconstruction technique will be used to inffer the pressure field from PIV velocity data, from which the aerodynamic loads are determined via a non-intrusive determination method.

3
Experimental setup

This chapter presents a detailed description of the experimental setup carried out at the TST-27 Transonic/Supersonic wind tunnel at TU Delft, The Netherlands, to investigate and gather accurate and repeatable results on the performance of the FFA-W3-211 airfoil in compressible and transonic conditions. The chapter begins with an overview of the wind tunnel facility used for the testing, followed by descriptions of the various flow visualisation and measurement techniques employed, including oil flow visualisation, Schlieren imaging, and Particle Image Velocimetry (PIV). Finally, the specific testing conditions for each campaign are presented.

3.1. Wind tunnel facility

All experimental data presented in this thesis has been acquired at the TST-27 Transonic/Supersonic wind tunnel at TU Delft, The Netherlands. A picture of the TST-27 wind tunnel is provided in Figure 3.1, followed by a technical drawing around the test section shown in Figure 3.2.

Figure 3.1: TST-27 Transonic/Supersonic wind tunnel at TU Delft

A limitation on the run time is imposed by the amount of pressurized air available in the pressure vessel, making the TST-27 a blow-down intermittent wind tunnel. The test section measures 280 mm wide and has a variable height ranging between 250 to 270 mm, depending on the Mach number used for testing. The subsonic test Mach numbers, ranging from 0.5 to 0.85, are controlled using a variable choke section in the outlet diffuser. The supersonic test Mach numbers, ranging from 1.15 to 4.2, are controlled by a continuously variable throat and flexible upper and lower nozzle walls. The maximum unit Reynolds number varies from 38 million per meter in the transonic range to 130 million per meter at Mach = 4.

3.1.1. TST-27 Components

As summarized in detail by van Rijswijk, 2012, the tunnel may be divided into 9 components. Figure 3.2 illustrates the first 7 components of the TST-27.

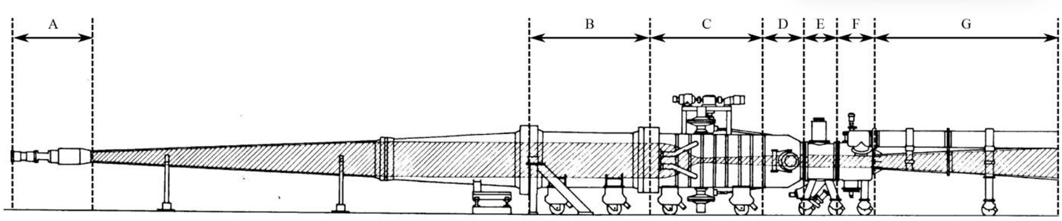

Figure 3.2: TST-27 Transonic/Supersonic wind tunnel components technical drawing (Blume, 2007)

(A) **Control Valve:** The control valve regulates the amount of pressurized air coming from the pressure vessel to the wind tunnel.

(B) **Settling Chamber:** The settling chamber reduces the turbulence intensity in the air through several meshes. This features a built-in input nozzle designed for particle injection during PIV experiments. The pressure can be set between 1.5 to 4 bar.

(C) **Nozzle:** The nozzle is equipped with flexible walls that can be adjusted to generate supersonic flow conditions, achieving Mach numbers of up to 4.

(D) **Test Section:** The test section measures 280 mm wide and has a variable height ranging between 250 to 270 mm, depending on the Mach number used for testing. Interchangeable windows with polished surfaces allow for optical measurement techniques like Schlieren and PIV.

(E) **Interchangeable Sections:** Three interchangeable sections are available, including 1) a solid wall section with an angle-of-attack mechanism and model support, 2) a slotted wall section to be used in combination with the solid wall section only in transonic conditions, and 3) the XYZ section which allows a wake rake to be mounted downstream of the model. The solid wall section has been used for all experiments conducted.

(F) **Second Throat:** The throat houses the rods and wing used as a choke system for transonic tunnel control. More details in subsection 3.1.2. Two external pipes are connected to this section: one functions as a bleed valve for flow regulation, and the other serves as a safety valve to prevent overpressure.

(G) **Diffuser:** A divergent section stabilizes the shock wave, reducing flow velocity to subsonic levels before ejection into the atmosphere.

(H) **Ejector:** Outside of the laboratory, the ejector is used to reduce the pressure in the test section during starting and stopping of the wind tunnel by blowing pressurized air through a venturi. This way, the forces on the model and its mounting parts are reduced during start and stopping of the wind tunnel. By lowering the pressure in the test section the settling chamber pressure can be reduced at the same pressure ratio, allowing for lower Reynolds number testing.

(I) **Silencer:** The silencer is integrated into the end section of the wind tunnel, which reduces the noise of the high-velocity flow before it exits into the atmosphere.

3.1.2. Transonic Mach number control

As previously stated, the TST-27 wind tunnel is able to run at transonic and supersonic conditions, featuring two variable area throats. A_{t1}, upstream of the test section, and A_{t2}, downstream as illustrated in Figure 3.3.

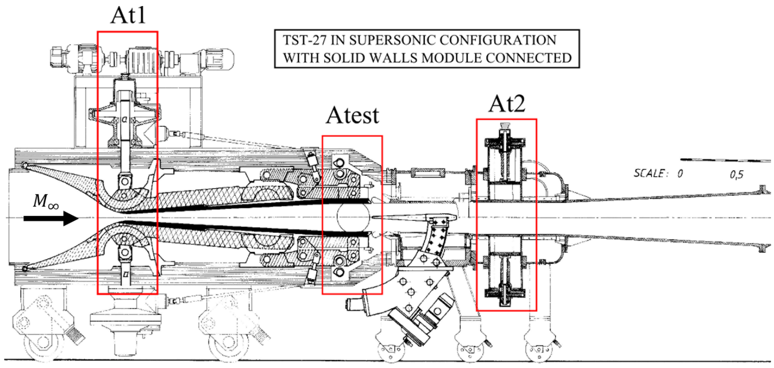

Figure 3.3: TST-27 with solid wall and slotted wall configuration (Blume, 2007), with sections of interest marked by A_{t1}, A_{test} and A_{t2} (van Rijswijk, 2012)

Both transonic and supersonic conditions are generated based on the principle of the area-Mach relation to control the Mach number in the test section. Here a focus is made on the mechanism for transonic Mach number control. Theoretically, the transonic control of the Mach number in the test section can be achieved through variations in the first throat positioning. In practice, however, the first throat is set to a fixed position, such that $A_{t1} > A_{t2}$, and thus the flow attains sonic conditions (M = 1) at the second throat location $A_{t2} = A^*$. The sonic conditions downstream of the test section prevent external atmospheric disturbances from affecting the test section.

A blockage to the flow to vary the ratio A_{t1}/A_{t2} is necessary to change the Mach number in the test section according to the subsonic solution of the area-Mach relation. This is achieved by eight biconvex rods (coarse setting) and a wing (fine tuning), as shown in Figure 3.4. Lowering the rods into the flow decreases A^*, increasing the Mach number in the test section, while raising them has the opposite effect. This mechanism provides greater accuracy and controllability compared to variations in the first throat area. A more detailed description of the mechanism is provided in van Rijswijk, 2012.

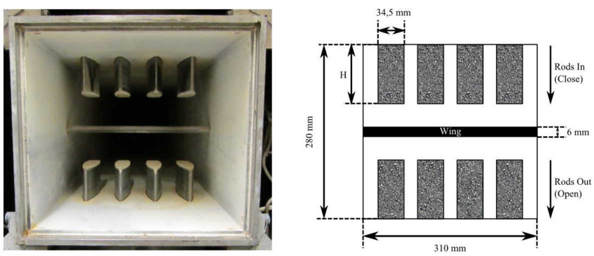

Figure 3.4: Transonic choke mechanism, featuring biconvex rods and a wing located in the second throat of the TST-27 (van Rijswijk, 2012)

3.2. Blockage correction

The airfoil model and its wake reduce the effective cross-sectional area in the test section and at the second throat, A^*. This reduction alters the effective Mach number in the test section, leading to increased local velocities and altered aerodynamic performance compared to free-stream conditions in unbounded flow. An important aspect of experimental testing is accounting for the effect of blockage. Factors influencing blockage include the model's size, shape, orientation, and the dimensions of the test section.

When presenting aerodynamic coefficients derived in this thesis, the blockage corrections proposed by Herriot, 1947 are applied. The corrections are based on the width of TST-27, B [m], height of the TST-27, H [m], airfoil chord, c [m], thickness to chord ratio, t/c [-], span of the wing model, s [m], cross-sectional area of the tunnel, C [m^2], area on which the drag coefficient is based on, S [m^2] and the shape parameter λ (0.2356 for the NACA0012 airfoil, 0.3795 for the FFA-W3-211 airfoil).

The solid model blockage factor, k_w, is modelled by the parameters K_2 and τ as

$$
\begin{aligned}
K_w &= \frac{1}{(1-M_\infty^2)^{1.5}}\frac{K_2\tau 2sct}{C^{1.5}}\\
K_2 &= \frac{\pi^{1.5}}{16}\frac{\lambda}{t/c}\\
\tau &= 0.5\left(\frac{B/H}{\pi}\right)^{1.5}\frac{4}{B/H}\frac{\pi^2}{6}+\frac{1}{(B/H)^2};
\end{aligned}
\tag{3.1}
$$

The wake blockage, k_{wk}, is modelled as

$$
K_{wk} = \frac{1}{(1-M_\infty^2)^{1.5}}\frac{K_2\tau(2sct)}{C^{1.5}}
\tag{3.2}
$$

The correction to the drag coefficient due to the wake pressure gradient is expressed as

$$
\Delta_{c_d} = \frac{1+0.4M_\infty^2}{(1-M_\infty^2)^{1.5}}\frac{K_2\tau(2sct)c_d}{C^{1.5}};
\tag{3.3}
$$

The aerodynamic coefficients and freestream quantities are then corrected according to

$$
\begin{aligned}
K &= K_w + K_{wk}\\
c_{l,corr} &= c_l/(1+(2-M_\infty^2)*K)\\
c_{d,corr} &= c_d(1-(2-M_\infty^2)K-\Delta_{c_d})\\
Re_{\infty,corr} &= Re_\infty(1+(1-0.7M_\infty^2)K)\\
M_{\infty,corr} &= M_\infty(1+(1+0.2M_\infty^2)K)
\end{aligned}
\tag{3.4}
$$

Unless otherwise specified, all results reported are presented under the uncorrected freestream Mach number.

3.3. Airfoil geometry and experimental models

As will become evident throughout this chapter, all experimental models were tested in both a nominal configuration (with the positively cambered surface facing upwards) and an inverted configuration (with the positively cambered surface facing downwards). In the nominal configuration, a negative angle of attack is achieved by tilting the airfoil chord line downward relative to the flow, whereas in the inverted configuration, it is achieved by tilting the chord line upward. Since only negative angles of attack were examined, flow field results are presented based on the inverted configuration, including those for symmetric airfoil tests. Hereafter, the positively cambered side is referred to as the ”lower surface” or ”pressure surface,” while the opposite side is designated as the ”upper surface” or ”suction surface.”

3.3.1. The FFA-W3-211 airfoil

The FFA-W3-211 airfoil (see Figure 3.5) is part of the FFA-W3 airfoil family, having a relative thickness $t/c = 21.1\%$, and a trailing edge thickness of 0.262%c. There are two reasons for choosing this specific wind turbine airfoil: first, it is relevant to the study of transonic flow over wind turbines, as this is used in the outboard tip region (r/R ≥ 0.98) of the newest reference offshore wind turbines (Jonkman et al., 2009; Zahle et al., 2024), where compressible and transonic flow conditions have been identified; second, studies conducted at TU Delft have begun assessing its compressible and transonic performance characteristics (Aditya et al., 2024; M. C. Vitulano et al., 2024; M. Vitulano et al., 2024), providing a foundation for this research to build upon.

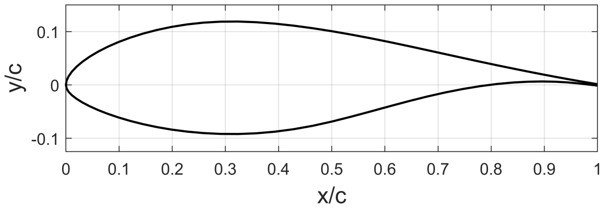

Figure 3.5: FFA-W3-211 airfoil geometry presented in its nominal configuration

A straight-wing model of the FFA-W3-211 airfoil with 67mm chord length has been used to gather results to answer the main research objectives. Unless otherwise specified, all experimental settings documented in this chapter are specific to this model. Another straight-wing model of the FFA-W3-211 airfoil with a chord of 50 mm has been used to gather results to quantify the blockage effects. Both experimental models feature a smooth surface finish, coated with a thin layer of non-reflective paint to minimise issues with light reflections during imaging. The nominal or inverted configuration of the model is set by mounting the airfoil in its standard or flipped orientation within the wind tunnel.

Wind turbine airfoils operate under turbulent conditions, such as those generated by harsh weather conditions, irregular terrains, wind gusts, the wake of other turbines, etc. By tripping the flow over the airfoil via a transition strip, the flow more accurately resembles the desired boundary layer behaviour despite low test Reynolds Numbers. A 2mm wide transition strip at a chord-wise location x/c = 5% (see Figure 3.6) is placed to promote transition over the suction surface.

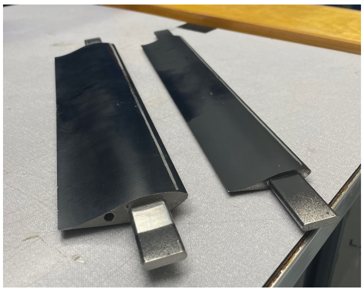

Figure 3.6: FFA-W3-211 airfoil models, left: 67mm chord, right: 50mm chord, with a transition strip on the suction surface at a chord-wise location x/c = 5%

The transition strip is fabricated using double-sided tape embedded with carborundum 400 particles as the tripping agent. Carborundum 400 particles have successfully been applied as a tripping agent in previous experimental transonic aerodynamic airfoil studies (D'Aguanno, 2023). The proper functioning of the transition strip was verified through oil flow visualisation experiments on the 67mm airfoil model, a technique that will be briefly introduced in the following section.

3.3.2. The NACA 0012 airfoil

The NACA 0012 airfoil (see Figure 3.7) belongs to the NACA 4-series airfoil family, featuring a relative thickness of $t/c = 12\%$ and a symmetric profile. This airfoil was selected to verify the aerodynamic load calculation method due to the available studies for its aerodynamic load in transonic conditions.

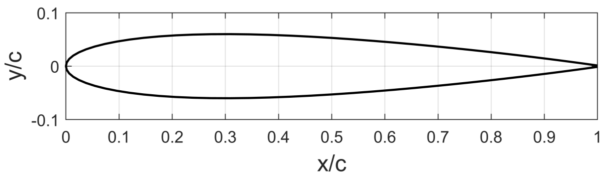

Figure 3.7: NACA 0012 airfoil geometry

The experimental model of the NACA 0012 airfoil is a straight wing (see Figure 3.8) featuring a chord length of 100mm and no transition strip. This is due to the availability of experimental data with a free transition, for which the addition of a transition strip can be avoided. The model features a smooth metallic surface finish, which did not create significant light reflection issues during imaging.

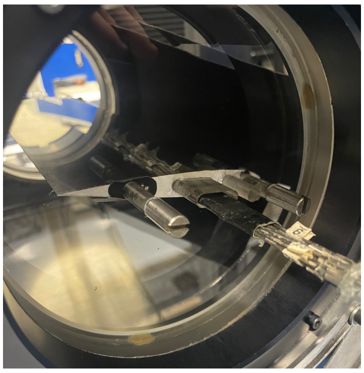

Figure 3.8: NACA 0012 airfoil model with a chord of 100mm, mounted inside the wind tunnel

3.4. Schlieren technique

As described briefly in section 2.3, Schlieren is a light transmission-based technique used to determine the first derivative of the density field around the aerodynamic model, commonly used to analyze compressible flows and shock waves.

Schlieren was chosen as a preliminary method to visualize and qualitatively analyze the flow field around the airfoil model, including shock waves, separation characteristics, and dynamics. The main advantages of this technique are its straightforward setup and relatively low data processing requirements, which allowed numerous experiments that offered a large coverage of the testing conditions. The results, can be used to identify regions of interest and optimize both the testing conditions and experimental setup for subsequent quantitative analysis methods that require more detailed measurements.

3.4.1. Working principles of Schlieren

German chemist and physicist August Toepler is credited with introducing the Schlieren method, as described by the review of Settles, 2001. The working principles of Schlieren will be described based on the Toepler Schlieren method.

The Toepler Schlieren setup consists of several optical components that work together to visualise flow features. The light source, optical elements, knife edge, and image recorder collaborate to form a precise image of the flow field within the test section. An example of such a setup is presented in Figure 3.9. First, Light from a typically non-monochromatic, incoherent point source is focused by a convex lens. A pinhole placed at the focal point may be used to define the beam radius, A. The light beam is collimated by a convex lens or concave mirror before passing through the test section. Upon exiting, a concave mirror or lens (referred to as the schlieren head) refocuses the beam to a point, where a knife edge (perpendicular to the light beam) at the focal plane selectively blocks deflected light rays normal to its orientation. The remaining light beam, with size $A' < A$, can then be focused by a final converging lens onto the recording plane, forming an image of the test object and flow features. In the absence of refractive index variations within the test section, the recording plane is uniformly illuminated, with reduced intensity as A' is decreased.

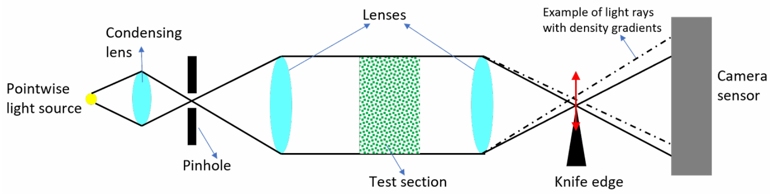

Figure 3.9: Toepler Schlieren configuration. Sketch by D'Aguanno, 2023

For simplicity of explaining the method, only refractive index variations in the y-direction will be considered to be present within a test section medium, and a horizontal knife's edge orientation is considered (parallel to the x-direction), making the setup sensitive to light ray deflections in the vertical y-direction. Light rays traversing the test section in the z-direction, $z_0 \leq z \leq z_1$, experience a deflection angle, ϵ, which depends on the spatial variation in refractive index. By combining the ray equation of deflection and acceleration, assuming a small deflection angle and ray displacement normal to the z-direction, an expression can be derived for the ray's deflection angle due to refractive index variations in the y-direction, which can be related to density variations through the Gladstone-Dale equation. Here, it is assumed $n \approx 1$ for air, as K_{air}=$2 \cdot 10^{-4}\mathrm{m}^3\mathrm{kg}^{-1}$.

$$\epsilon_y = \frac{\partial y}{\partial z} = \int_{z_0}^{z_1} \frac{\partial n}{\partial y} dz = K \int_{z_0}^{z_1} \frac{\partial \rho}{\partial y} dz \tag{3.5}$$

A horizontal knife edge, as shown by Figure 3.9, effectively blocks light rays deflected in the negative y-direction intersecting with the edge. Meanwhile, rays that are either undeflected, minimally deflected, or deflected upward pass through without obstruction. This configuration makes the setup sensitive to density variations in the vertical direction, $\frac{\partial \rho}{\partial y}$. Conversely, a vertical knife edge orientation would increase the sensitivity to density variations in the horizontal direction, $\frac{\partial \rho}{\partial x}$.

To better understand the link between density variations and image intensity changes, let a' represent the height of the undisturbed (under the effect of no refractive index variations) light source image with intensity I_0 at the knife-edge plane. The ratio of the undisturbed to disturbed light source image, resulting from a shift d in the undisturbed image source height due to the deflection of light rays by the refractive index gradient in the test section, can be calculated as shown in Equation 3.6, assuming a small deflection angle ϵ_y.

$$\frac{I}{I_0} = \frac{a' + d}{a'} = 1 + \frac{f \tan(\epsilon_y)}{a'} = 1 + \frac{f \epsilon_y}{a'} \tag{3.6}$$

Where f is the focal length of the Schlieren head. By substituting the expression for the light ray's deflection angle, given in Equation 3.5, into Equation 3.6, and rearranging to solve for the intensity variation $\Delta I = I - I_0$, the following result is obtained.

$$\frac{\Delta I}{I_0} = \frac{f}{a'} \int_{z_0}^{z_1} \frac{\partial n}{\partial y} dz = \frac{fK}{a'} \int_{z_0}^{z_1} \frac{\partial \rho}{\partial y} dz \tag{3.7}$$

Considering a vertical knife edge, the following expression is obtained.

$$\frac{\Delta I}{I_0} = \frac{f}{a'} \int_{z_0}^{z_1} \frac{\partial n}{\partial x} dz = \frac{fK}{a'} \int_{z_0}^{z_1} \frac{\partial \rho}{\partial x} dz \tag{3.8}$$

This result shows that variations in the density field around an aerodynamic object can be detected as changes in the refractive index, which manifest as intensity variations in the image formed at the recording plane.

Assuming a fixed focal length f of the Schlieren head, the sensitivity to density gradient variations can be enhanced by adjusting a', which is controlled by the position and extent of the knife edge. A balance must be achieved between achieving sufficient image intensity and maintaining sensitivity to density gradients through an adjustment of the knife edge. A horizontal knife edge favors the visualization of density gradients along the shear layer, boundary layer, and separation region. A vertical knife edge, on the other hand, is more suited for visualizing shock waves and pressure waves.

3.4.2. Schlieren setup

To reduce typical optical aberrations found in Schlieren setups such as astigmatism and coma, a z-configuration Schlieren setup is used (See Figure 3.10). The key difference between this setup and a Toepler setup lies in the use of two parabolic mirrors arranged in a ”Z” configuration, which work together to generate collimated light through the test section.

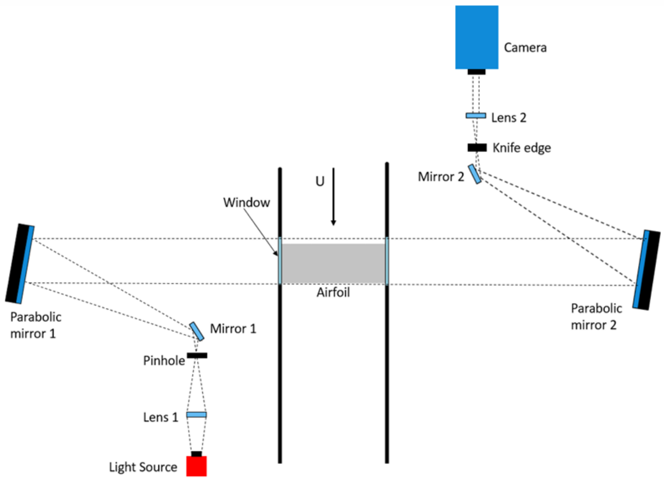

Figure 3.10: Z-configuration Schlieren setup featuring a light source, lenses, a pinhole, mirrors, a knife edge and a camera. Sketch done by D’Aguanno, 2023

A white Light Emitting Device (LED) light bulb provides a constant, uninterrupted light source for the setup. The pinhole diameter is set to 2 mm, producing a light beam that generates suitable contrast in the image at the recording plane. This ensures clear visualisation of the refractive index variations within the test section. The knife edge is positioned in a horizontal configuration to enhance the visualisation of density variations along the wake and separated flow regions.

The imaging system used in this experiment consists of a Photron Mini AX100 camera. The imaging sensor can deliver a 1-megapixel resolution (1024 $\times$ 1024 pixels) at an acquisition frequency of 4000 Hz, with a minimal exposure time of 1.05 μs. The camera was initially operated at an acquisition frequency of 2500Hz, followed by 6200Hz, and a final frequency of 7200Hz by cropping the sensor, with an exposure time of $25\mu\mathrm{s}$. The camera’s field of view (FOV) is enough to capture the entire airfoil model within the frame.

3.5. Particle Image Velocimetry technique

As described briefly in section 2.3, PIV is a particle-based technique used to determine the flow-field velocity by measuring the displacement of seeding particles within a specific flow region over a short time interval.

Planar PIV was chosen as the main quantitative analysis technique for this research due to its significant advantages across several key criteria, as outlined in Table 2.1. Firstly, it is a non-intrusive measurement technique crucial in studying sensitive phenomena developing over the airfoil, such as shock waves. Secondly, planar PIV setups can simultaneously measure two velocity components, making it effective for capturing complex flow patterns in two-dimensional experimental simulations. Additionally, PIV provides whole-field measurements, allowing an analysis of the flow dynamics across the region of interest. The laser source and camera equipment available at the wind tunnel facility allow a high-speed PIV frame acquisition rate, and thus it can capture rapidly changing flow phenomena, such as shock wave dynamics. Lastly, PIV requires a relatively straightforward calibration process.

3.5.1. From instantaneous snapshots to velocity fields

The following section details the procedure to determine the velocity field from the raw images captured by the imaging system. At the core of the planar PIV technique are three key components: The presence of seeding particles in the flow, the illumination of the seeding particles, and the imaging of the seeding particles (See Figure 3.11).

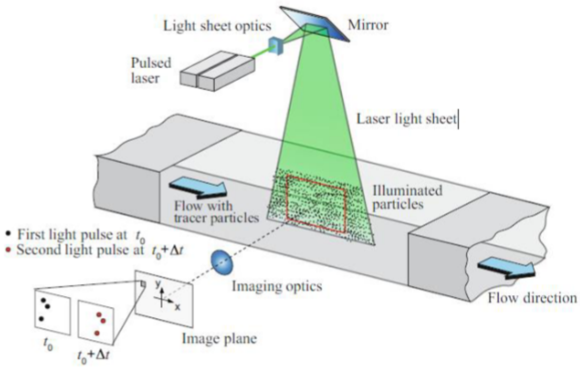

Figure 3.11: The three key components of PIV, seeding particles in the flow, their illumination and their imaging. Image provided by Raffel et al., 2018

Considering a successful PIV setup, a single PIV image (See Figure 3.12) represents an instantaneous snapshot, at a time $t = t_0$, capturing the illuminated seeding particles within the region of interest. The imaging sensor consists of an array of M by N pixels. For each pixel, incoming photons are converted into an electric charge, which is then processed through a charge-to-voltage conversion, which is subsequently digitized to form the recorded image. In this way, illuminated particles are represented as areas of higher pixel intensity in the image. A second snapshot captured at $t = t_0 + \Delta t$ provides information on particle displacement over the time interval Δt.

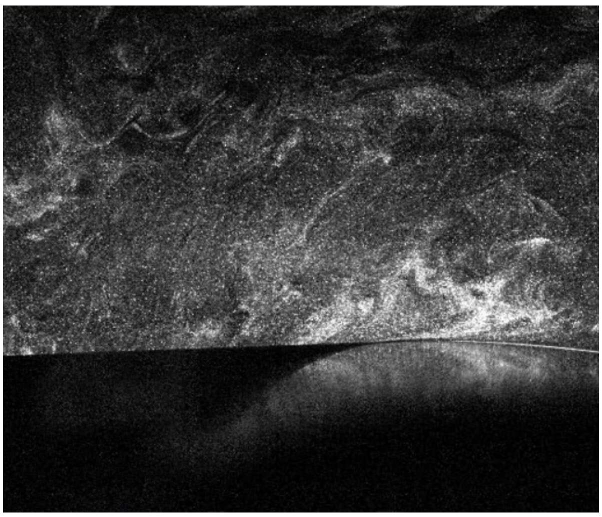

Figure 3.12: Instantaneous PIV snapshot displaying the illuminated particles in the laser sheet plane

The first step in determining the velocity field is to divide the imaging region into so-called interrogation windows. The aim is to determine the averaged velocity components, for all individual interrogation windows considered. For each interrogation window, the most probable particle displacements along the $x-$ and $y-$ direction of the wind tunnel reference frame (See Figure 3.2), Δx_{max} and Δy_{max} respectively, are determined as the resulting maxima when computing the two-dimensional cross-correlation between two consecutive instantaneous PIV snapshots. The two-dimensional cross-correlation function is defined by Equation 3.9, where Δx and Δy represent the considered two-dimensional shift between image pairs, and $I(x, y)$ and $I'(x, y)$ represent the snapshot intensity field at times t_0 and $t_0 + \Delta t$ respectively.

$$\phi(\Delta x, \Delta y) = \sum_{i=1}^{M}\sum_{j=1}^{N} I(x, y) \cdot I'(x + \Delta x, y + \Delta y) \tag{3.9}$$

Given that the time interval between consecutive PIV snapshots is Δt, the velocity components u and v, corresponding to the x- and y-directions, respectively, are determined using Equation 3.10.

$$u = \Delta x_{max}/\Delta t, \qquad v = \Delta y_{max}/\Delta t \tag{3.10}$$

After applying this procedure to all interrogation windows, the two-dimensional instantaneous velocity field around the airfoil is obtained. The temporal evolution of the velocity field can be resolved by processing successive PIV image pairs, enabling further analysis of the flow dynamics.

3.5.2. PIV setup

This section describes the PIV setup, including the seeding system, laser system and laser sheet formation optics, and the optics system, all of which are common to all PIV measurements throughout the campaign. The PIV setup, highlighting the seeding of the flow, the laser and camera systems are illustrated in Figure 3.13.

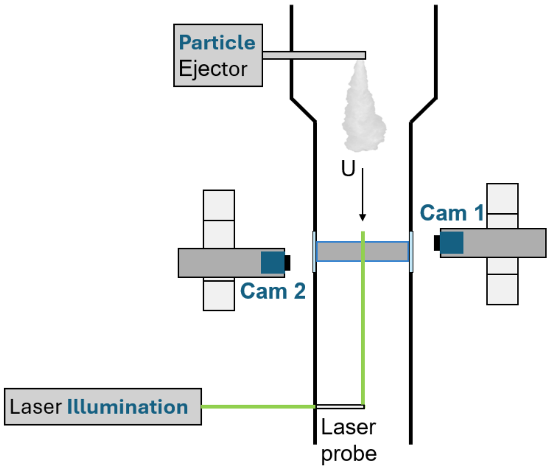

Figure 3.13: Illustration of the seeding introduced in the settling chamber, the laser setup downstream of the airfoil, and camera 1 capturing the LE of the airfoil, while camera 2 captures the TE region.

Seeding system

The seeding system used in the experiments consists of a seeding generator, seeding rake, and seeding particles. The PIVTEC Aerosol Generator PivPart45 seeding generator has been used for this experiment, with an output particle size of 0.9 μm. To incorporate the seeding particles into the flow, the seeding generator is connected to the seeding rake, and placed within the settling chamber of the wind tunnel. The seeding system includes 45 high-precision brass Laskin nozzles to control seeding density. All 45 nozzles were used throughout the experiments to ensure sufficient seeding density.

As briefly stated in section 2.3, the choice of seeding particles is crucial for a good PIV experimental setup. The seeding particles must possess adequate mechanical and scattering properties, and be non-contaminant and safe for use in a wind tunnel environment.

The flow tracing capabilities of the seeding particles are quantified by the particle Stokes number, S_k, defined as the ratio between the particle response time, τ_p, and the flow response time,τ_f, as shown by Equation 3.11.

$$S_k = \frac{\tau_p}{\tau_f} \tag{3.11}$$

Low S_k values A good compromise between practicality and tracing accuracy can be achieved for S_k < 0.1 (Samimy & Lele, 1991; Tropea et al., 2007), where the tracing error falls within 1%. The discontinuity in the velocity flow field at the shock yields a region where $S_k >> 1$, for which a suitable choice for seeding particles which minimises this effect is of great importance. Due to their lower response time, good flow-tracing capabilities are easier to achieve with smaller particles; however, they scatter less light. Therefore, a balance must be found to optimise the PIV setup.

The experiments in this thesis make use of DEHS seeding particles (Di-Ethyl-Hexyl-Sebacat), as their flow-tracing performance across shocks has been investigated by Ragni et al., 2011 in experiments at the TST-27, calculating a particle response time in the order of $\tau = 2\mu s$. More recently, the work by D'Aguanno, 2023, calculated a particle response time of 2.1 μs, and provides results for successful flow tracing capabilities in a transonic PIV campaign.

Laser system

The experiments use the Quantronix Darwin Duo 527-80-M laser. This is a dual oscillator/single head, high repetition rate, diode-pumped Nd:YLF(Neodymium doped:Yttrium Lithium Fluoride gain medium) laser designed for, and commonly used in PIV setups. Two identical and independent oscillators within a single head provide complete control over pulse separation and energy, generating temporally and spatially matched pulses at a wavelength of 527 nm, pulse duration of <230 ns, pulse repetition rate between 0.1-10 kHz, and total pulse energy of 50 mJ.

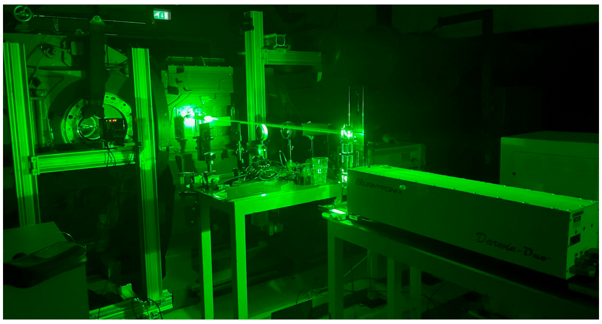

Figure 3.14: PIV laser setup

The pulse repetition rate used to conduct the high-speed acquisition PIV measurements in this thesis was determined from the results of the Schlieren campaign, which suggested that an image pair acquisition frequency of 2500Hz was adequate to capture instances of the transonic buffet cycle frequencies estimated in the order of 1000 Hz.

A laser probe designed by F.J. Donker Duyvis (Donker Duyvis, 2005) is used to generate a laser sheet of approximately δ_{ls} = 2mm thickness on the streamwise-vertical plane near the mid-span location along the airfoil model. The mid-span location is optimal for PIV measurements, as it minimizes the influence of wind tunnel walls on the flow field. The laser probe, as shown by Figure 3.15 is introduced downstream of the airfoil model through the side wall of the wind tunnel.

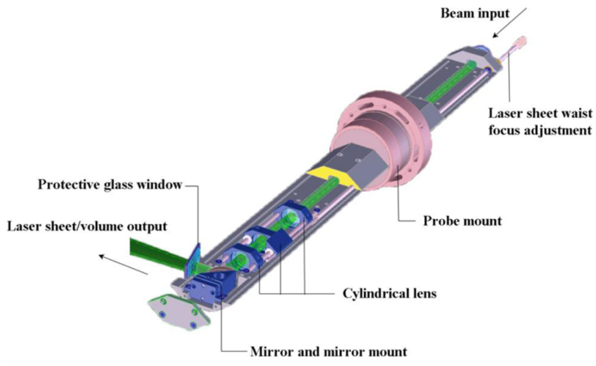

Figure 3.15: PIV laser probe

The airfoil model obstructs the laser sheet, creating a 'shadow region' where no seeding particles can be illuminated. With a fixed laser probe setup, the extent of this shadow region depends on the angle of attack, model geometry and orientation. The aerodynamic load determination technique used in this thesis relies on flow field data around the airfoil model.

Optics system

The optics system is modeled in advance of its setup. The derivation of the equations used are omitted, and may be found in literature. For the imaging system, the distance between the object which is being imaged (airfoil model), d_o, and its image incident on the camera lens,d_i, is related via the thin-lens equation. Here, f is the focal length of the imaging lens used.

$$\frac{1}{f} = \frac{1}{d_i} + \frac{1}{d_o} \tag{3.12}$$

The magnification factor is the ratio between the sensor size and the object size.

$$M = \frac{\text{Sensor size}}{\text{Object size}} = \frac{d_i}{d_o} \tag{3.13}$$

Introducing the aperture of the lens d, this is expressed together with the focal length as the f-stop parameter, $f_\#$. The lens aperture controls the amount of light incident on the lens.

$$f_\# = f/d \tag{3.14}$$

The imaging of seeding particles is not only based on their geometry, but also by light diffraction. The particle diameter d_τ is expressed as a function of its geometric diameter d_p, and the effect of diffraction d_{diff}. Here, λ refers to the light wavelength used by the laser system.

$$d_\tau = \sqrt{(Md_p)^2 + d_{diff}^2}, \qquad d_{diff} = 2.44(1+M)f_\# \tag{3.15}$$

The depth of field, which is physically described as the region in focus in the image, is expressed as

$$\delta_z = 4.88\lambda f_\#^2 \left(\frac{M+1}{M}\right)^2 \tag{3.16}$$

A good PIV setup is achieved through a well-defined correlation peak, as this helps capture the most likely displacement. A particle diameter of $d_\tau \gtrsim 2{-}3$px is generally considered a good size to distinguish particles in PIV frames and improve the accuracy of the cross-correlation. Ideally, all imaged particles should be in sufficient focus, and the depth of field d_τ is generally desired to be greater than the width of the laser sheet. Details on the imaging characteristics for FOV$_1$ and FOV$_2$ are provided in Table 3.1 and Table 3.2.

Table 3.1: Optics setup details for FOV$_1$, for the different airfoil model experiments.

Experiments/ Parameter	M [-]	$f_\#$ [-]	d_τ [px]	δ_z/δ_{ls} [-]
FFA-W3-211 (67mm)	0.34	8	2	1.27
FFA-W3-211 (50mm)	0.34	8	2	1.27
NACA 0012 (100mm)	0.26	8	2.52	1.97

Table 3.2: Optics setup details for FOV$_2$, for the different airfoil model experiments.

Experiments/ Parameter	M [-]	$f_\#$ [-]	d_τ [px]	δ_z/δ_{ls} [-]
FFA-W3-211 (67mm)	0.34	8	2.6	2
FFA-W3-211 (50mm)	0.34	8	2.6	2
NACA 0012 (100mm)	0.27	8	2.44	1.86

The imaging system used in all experiments consists of two Photron Mini AX100 cameras with a 105mm focal lens attached. An individual imaging sensor can deliver a 1-megapixel resolution (1024 $\times$ 1024 pixels) at an acquisition frequency of 4000Hz, with a minimal exposure time of 1.05 μs. All PIV data was acquired at 2500 Hz in double frame mode (δ t = 2.84 μs) by cropping the sensor to a resolution of 1024 $\times$ 864 pixels. A greater acquisition frequency is possible, but at the cost of a smaller FOV. Given the limitations in acquisition frequency and the high transonic buffet cycle frequency, the PIV measurements are not able to resolve it entirely in time. The exposure time was constrained to be 196 $\mu\mathrm{s}$.

As the laser sheet setup suggested, the streamwise-vertical measurement plane is near the mid-span location along the airfoil model. Two cameras were placed opposite each other, on opposite sides of the wind tunnel test section. The cameras were positioned at opposite sides because their width did not allow overlapping fields of view when mounting them side-to-side, which is necessary to merge the velocity field data.

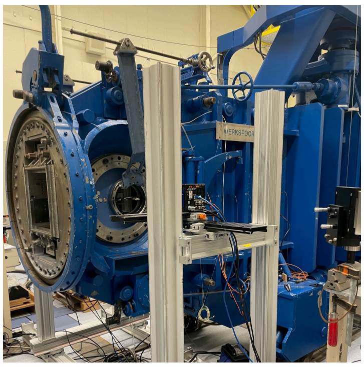

(a) FOV$_1$ setup

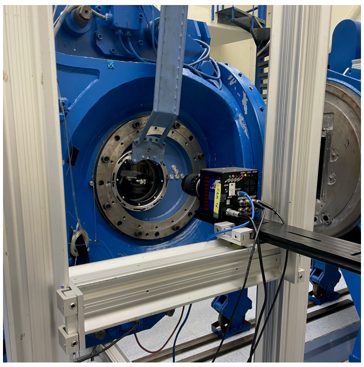

(b) FOV$_2$ setup

Figure 3.16: PIV camera setup

Camera 1 captures the leading-edge (LE) field of view (FOV$_1$) of the measurement plane, while Camera 2 captures the trailing-edge (TE) FOV$_2$. Although ideal FOVs were estimated beforehand based on the inverted model configuration of the FFA-W3-211 model with 67mm chord length, in practice, FOV$_1$ had dimensions of approximately $88\% \times 74\%$ of the chord, while FOV$_2$ measured approximately $80\% \times 67\%$ of the chord. FOV$_1$ begins at a position located at the LE plus 22% of the chord length, whereas FOV$_2$ is positioned starting at an approximate spanwise location of 55% of the chord, resulting in an overlap region between FOVs of about 11% of the chord. The FOV heights were chosen to ensure the visibility of both sides of the airfoil model during testing, creating a minimum $30\%c$ overlap between nominal and inverted configuration runs. The same camera setup was used for the experiments on the scaled-down model. Details on the imaging characteristics for FOV$_1$ and FOV$_2$ are provided in Table 3.1 and Table 3.2.

For the experiments on the NACA 0012 airfoil, FOV$_1$ had dimensions of approximately $79\% \times 67\%$ of the chord, while FOV$_2$ measured approximately $75\% \times 63\%$ of the chord.FOV$_1$ begins at a position located at the LE plus 14% of the chord length, whereas FOV$_2$ is positioned starting at an approximate spanwise location of 56% of the chord, resulting in an overlap region between FOVs of about 9% of the chord. The FOV heights were chosen to ensure the visibility of both sides of the airfoil model during testing, creating a minimum $38\%c$ overlap between nominal and inverted configuration runs. Details on the imaging characteristics for FOV$_1$ and FOV$_2$ are provided in Table 3.1 and Table 3.2.

For each angle of attack, experiments were conducted in both nominal and inverted model configurations under identical operational conditions. This minimises the effective shadow region and increases the measurable flow field region. Ideally, the size and positioning of FOV$_1$ and FOV$_2$ relative to the airfoil model should be identical between nominal and inverted runs. However, minor variations are inevitably present in practice. An estimate of the total FOV when combining the FOVs from the nominal and inverted airfoil configuration for the FFA-W3-211 airfoil model was determined prior to all experiments, as shown by Figure 3.17.

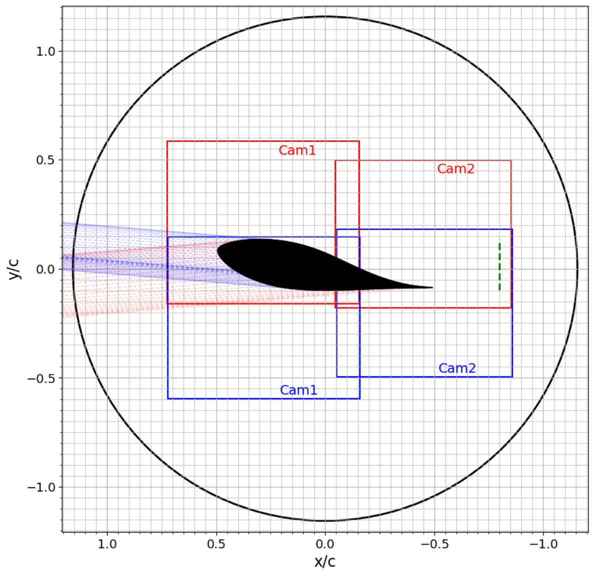

Figure 3.17: Effective FOV around the FFA-W3-211 airfoil, estimated for the two cameras and both airfoil configurations at an angle of attack of $\alpha = 10°$. Red corresponds to the inverted configuration, while blue corresponds to the nominal configuration FOVs. The estimated shadow region is visualised as the shaded red and blue region ahead of the airfoil.

When unifying all FOV data, the effective shadow region is the overlap between the nominal and inverted shadow regions, where no flow field data can be derived due to the laser sheet being blocked by the airfoil model. In practice, the three-dimensionality of all airfoil models introduces additional obstructions in the recorded images, further reducing the measurable flow field area near the lower edge of the FOV in the inverted configuration and the upper edge in the nominal configuration.

Synchronization system

The cameras and laser are synchronised using the DaVis software in combination with the Programmable Timing Unit (PTU X) from LaVision. The operation of the PTU X as a high-speed triggering device is known as the LaVision High-Speed Controller, which is essential due to the high temporal accuracy required to synchronise all components. This system ensures that both cameras receive precisely timed trigger signals, enabling the capture of synchronized image pairs. Simultaneously, the laser receives a corresponding trigger signal that controls both oscillators, ensuring consistent illumination for all snapshots. The PTU X in operation is shown in Figure 3.18, where its high-speed function is indicated by a flashing light.

Figure 3.18: Programmable Timing Unit in charge of synchronising the camera and laser input trigger signals

Image spatial calibration

The calibration of all FOVs is performed with the help of a calibration objects (See Figure 3.19). The calibration objects consist of a 3d-printed element that following the shape of the airfoil surface. Graph paper is adhered to each of the calibration element sides. By placing the calibration object on top of the airfoil model, as shown in Figure 3.20, the images are calibrated by selecting two points with a known distance between each other. The origin for FOV_1 is set to the LE. while the origin of FOV_2 is set to the TE. A visible point to both FOVs is marked. Its coordinates are required to derive the shift between both FOVs, used to merge the data from both FOVs to a unified FOV. More details on the merging process are provided in chapter 4.

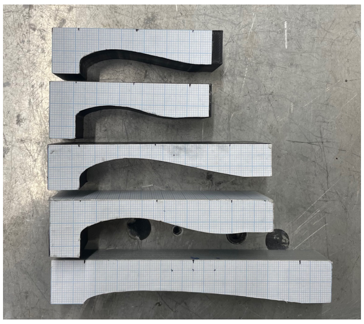

Figure 3.19: Calibration objects used for all airfoil models tested

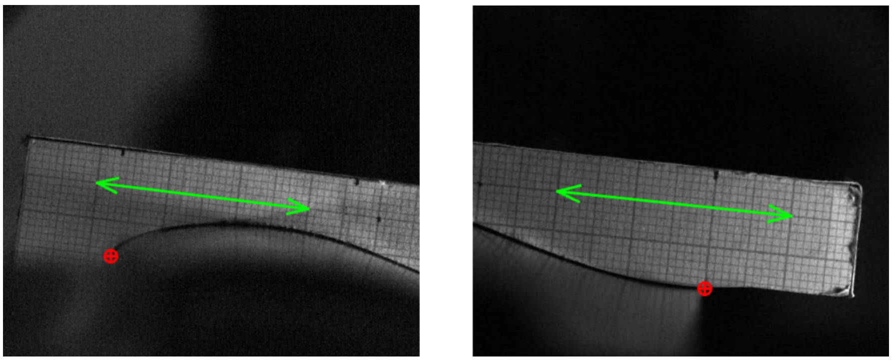

(a) Calibration of FOV_1 **(b)** Calibration of FOV_2

Figure 3.20: Calibration of the inverted FOVs using the calibration object, using two points with a known distance. The origin for FOV_1 is set to the LE. The origin of FOV_2 is set to the TE. A visible point to both FOVs is marked.

3.6. Testing conditions

Investigating the effects of compressibility on the loading and flow field characteristics of the FFA-W3-211 airfoil requires data at various combinations of the freestream Mach number and angles of attack. Experimental and numerical campaigns on the FFA-W3-211 airfoil under transonic conditions have been documented in the works of Aditya et al., 2024; De Tavernier and Von Terzi, 2022; M. C. Vitulano et al., 2024; M. Vitulano et al., 2024, as outlined in the literature study in subsection 2.2.4. The results presented by Aditya et al., 2024 for the subsonic-supersonic boundary (see Figure 3.21), derived from the URANS CFD and `XFOIL` simulations for $Re_c = 1.8$ million (M. C. Vitulano et al., 2024), along with the experimental work conducted at $M_\infty = [0.5, 0.6]$ and $\alpha = [-6, -10]$ (Aditya et al., 2024), have influenced the freestream Mach number and angle of attack combinations chosen as test conditions for the current research.

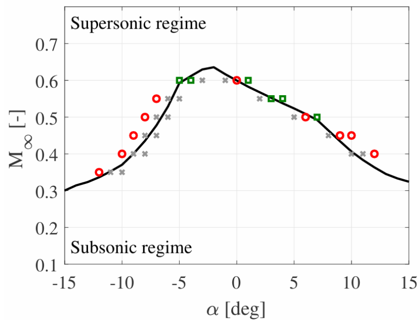

Figure 3.21: Subsonic-supersonic boundary for the FFA-W3-211 wind turbine tip airfoil (using Xfoil) at Re_c= 1.8 million: configurations selected for URANS threshold (grey crosses), configurations in which a supersonic regime is established (red circles), and configurations in which shock waves appear (green square) (M. C. Vitulano et al., 2024).

With this in mind, freestream Mach numbers of M_∞ = 0.5, 0.55, 0.6, and 0.65 have been considered in experiments. The lower limit of the Mach number range was dictated by the wind tunnel's capabilities, while higher Mach numbers were deemed unsuitable for current wind turbine studies. The wind tunnel facility, when operating in transonic conditions, supplies air to the settling chamber at a nominal stagnation pressure of 2 bar. However, during the experimental campaign, a calibration issue in the pressure sensor revealed that the actual stagnation pressure was 1.8 bar. Therefore, a stagnation pressure of $p_{t,\infty} = 1.8$ bar is considered for all experiments. The total temperature in the settling chamber is measured to be $T_{t,\infty}$ = 288.15K.

From the stagnation conditions the freestream temperature,T_∞, speed of sound, a_∞, velocity, U_∞, pressure, p_∞, density ρ_∞, and Reynolds number, Re from the equations below. The freestream dynamic viscosity, μ_∞, has been calculated according to Sutherland's formula under the assumption of standard air.

$$T_\infty = T_{t,\infty}\left(1+\frac{\gamma-1}{2}M_\infty\right)^{-1}$$

$$a_\infty = \sqrt{\gamma R T_\infty}$$

$$U_\infty = M_\infty a_\infty$$

$$p_\infty = p_{t,\infty}\left(1+\frac{\gamma-1}{2}M_\infty\right)^{\frac{-\gamma}{\gamma-1}}$$

$$\rho_\infty = \frac{p_\infty}{RT_\infty}$$

$$Re_{c,\infty} = \frac{\rho_\infty U_\infty c}{\mu_\infty}$$

The freestream conditions in Table 3.3 and Reynolds number in Table 3.4 apply to all experiments conducted on the FFA-W3-211 airfoil model with 67mm chord, the scaled down version, and the NACA0012 airfoil model. As indicated by the blockage corrections, the contribution due to the wake blockage accounts for the drag coefficient.

Table 3.3: Freestream conditions and Reynolds number (million) for all conditions and models tested.

M_∞	T_∞ [K]	a_∞ $[\mathrm{ms^{-1}}]$	U_∞ $[\mathrm{ms^{-1}}]$	p_∞ [Pa]	ρ_∞ $[\mathrm{kgm^{-3}}]$	μ_∞ $[\mathrm{kgm^{-1}s^{-1}}]$
0.5	274.43	332.0	166.03	151743	1.926	1.742×10^{-5}
0.55	271.71	330.41	181.73	146549	1.879	1.728×10^{-5}
0.6	268.80	328.64	197.18	141120	1.829	1.714×10^{-5}
0.65	265.70	326.74	212.38	135509	1.777	1.698×10^{-5}

In Table 3.4, an informative estimate for the corrected freestream Mach number and Reynolds number is presented in parentheses for the experiments on the FFA-W3-211 airfoil with 67mm. These are calculated by neglecting the wake blockage contribution. As a result, a corrected value can be associated with all cases tested at the same freestream Mach number. A more accurate correction would account for wake blockage effects; however, this results in an individual correction for each test case.

Table 3.4: Reynolds number (million) for all conditions and models tested. An estimate for the corrected quantities for blockage effects is shown in parentheses for the FFA-W3-211 experiments.

Mach number	$Re_{c,\infty}$ (FFA67)	$Re_{c,\infty}$ (NACA0012)	$Re_{c,\infty}$ (FFA50)
0.5 (0.51)	1.26 (1.29)	-	0.94
0.55 (0.57)	1.35 (1.38)	-	-
0.6 (0.62)	1.42 (1.45)	2.12	1.06
0.65 (0.68)	1.49 (1.53)	-	-

3.6.1. Schlieren campaign

For a 1-week Schlieren experimental campaign focused on a preliminary flow field study prior to quantitative analysis, testing was conducted across a broad range of conditions surrounding the subsonic-supersonic boundary (see Figure 3.21). The testing matrix included five angles of attack: $-4°$, $-6°$, $-8°$, $-10°$, and $-11°$, at four different freestream Mach numbers: M_∞ = 0.5, 0.55, 0.6, and 0.65. Only negative angles of attack were examined, as these reflect typical conditions encountered at the blade tip (De Tavernier & Von Terzi, 2022), with $\alpha = -11°$ selected for its potential to yield interesting post-stall behavior. Testing conditions at $M_\infty = 0.5$ for $\alpha = -4°$, $-6°$, and $-8°$, as well as at $M_\infty = 0.55$ for $\alpha = -4°$, were omitted due to the availability of Schlieren data or the expectation of no significant flow features of interest. Table 3.5 presents the full set of testing conditions for the FFA-W3-211 airfoil model with a 67mm chord length and free transition.

Table 3.5: Schlieren test matrix for the FFA-W3-211 airfoil model with 67mm chord and free transition

Run	α [°]	M_∞ [-]
1	-11	0.5
2	-11	0.55
3	-11	0.6
4	-11	0.65
5	-10	0.55
6	-10	0.6
7	-10	0.65
8	-8	0.55
9	-8	0.6
10	-8	0.65
11	-6	0.55
12	-6	0.6
13	-6	0.65
14	-4	0.6
15	-4	0.65

Similarly, Table 3.6 presents the complete set of testing conditions for the FFA-W3-211 airfoil model with a 67mm chord length and a fixed transition at x/c = 5%. The data obtained from this configuration provided insights into the impact of transition location on the flow field characteristics, contributing to an understanding of the airfoil's behaviour under various testing conditions. The Schlieren results for the fixed transition configuration were essential to define the experimental setup and testing conditions for the subsequent PIV study.

Table 3.6: Schlieren test matrix for the FFA-W3-211 airfoil model with 67mm chord and fixed transition at x/c = 5%

Run	α [°]	M_∞ [-]
16	-4	0.6
17	-4	0.65
18	-6	0.55
19	-6	0.6
20	-6	0.65
21	-8	0.55
22	-8	0.6
23	-8	0.65
24	-10	0.5
25	-10	0.55
26	-10	0.6
27	-10	0.65
28	-11	0.5
29	-11	0.55
30	-11	0.6
31	-11	0.65

3.6.2. Oil flow campaign

Following the completion of the Schlieren runs for the FFA-W3-211 airfoil with free transition, the effectiveness of the transition strip was assessed through four runs in an oil flow visualization campaign. As previously described, a fabricated transition strip using carborundum 400 as the tripping agent was applied to one half of the airfoil span, while the other half remained with free transition. The runs were selected as a combination of two angles of attack: -4° and -11°, at two different freestream Mach numbers: M_∞ = 0.5 and 0.6. Table 3.7 presents the complete set of testing conditions for the FFA-W3-211 airfoil model with a 67mm chord length, where half of the model span featured a fixed transition at $x/c = 5\%$, while the remaining span had a free transition.

Table 3.7: Oil flow test matrix for the FFA-W3-211 airfoil model with 67mm chord. Half model span with fixed transition at x/c = 5%, and remaining span with free transition.

Run	α [°]	M_∞ [-]
1	-6	0.6
2	-6	0.6
3	-10	0.5
4	-10	0.5

3.6.3. PIV campaign

For a 2-week PIV experimental campaign focused on a quantitative flow field study after the quantitative analysis provided by the schlieren campaign, testing was conducted across a broad range of conditions of interest identified during the schlieren campaign. The testing matrix included five angles of attack: $-4°$, $-6°$, $-8°$, $-10°$, and $-11°$, at four different freestream Mach numbers: M_∞ = 0.5, 0.55, 0.6, and 0.65. Testing conditions at $\alpha = -6°$ and $-10°$ were the only cases examined at $M_\infty = 0.65$, selected to quantify the effects of higher Mach numbers. Table 3.8 presents the complete set of testing conditions for the PIV experiments conducted on the FFA-W3-211 airfoil model with a 67mm chord length.

Table 3.8: PIV test matrix for the FFA-W3-211 airfoil model with 67mm chord

Run ID	α [°]	M_∞ [-]	Configuration
1	-10	0.6	Inverted
2	-10	0.55	Inverted
3	-10	0.5	Inverted
4	-10	0.65	Inverted
5	-8	0.6	Inverted
6	-8	0.55	Inverted
7	-8	0.5	Inverted
8	-6	0.5	Inverted
9	-6	0.55	Inverted
10	-6	0.6	Inverted
11	-6	0.65	Inverted
12	-4	0.6	Inverted
13	-4	0.55	Inverted
14	-4	0.5	Inverted
15	-11	0.5	Inverted
16	-11	0.55	Inverted
17	-11	0.6	Inverted
18	-11	0.5	Nominal
19	-11	0.55	Nominal
20	-11	0.6	Nominal
21	-10	0.5	Nominal
22	-10	0.55	Nominal
23	-10	0.6	Nominal
24	-10	0.65	Nominal
25	-8	0.5	Nominal
26	-8	0.55	Nominal
27	-8	0.6	Nominal
28	-6	0.5	Nominal
29	-6	0.55	Nominal
30	-6	0.6	Nominal
31	-6	0.65	Nominal
32	-4	0.5	Nominal
33	-4	0.55	Nominal
34	-4	0.6	Nominal

A separate PIV campaign using the scaled-down model of the FFA-W3-211 airfoil was performed to assess the impact of wind tunnel blockage. The testing matrix included two angles of attack, $-4°$ and $-10°$, at freestream Mach numbers of M_∞ = 0.5 and 0.6. These conditions were selected to ensure that blockage effects could be evaluated under significantly different aerodynamic conditions. Table 3.9 presents the complete set of testing conditions for the PIV experiments conducted on the FFA-W3-211 airfoil model with a 50mm chord length.

Table 3.9: PIV test matrix for the FFA-W3-211 airfoil model with 50mm chord

Run ID	α [°]	M_∞ [-]	Configuration
35	-10	0.5	Inverted
36	-10	0.6	Inverted
37	-4	0.5	Inverted
38	-4	0.6	Inverted
39	-10	0.5	Nominal
40	-10	0.6	Nominal
41	-4	0.6	Nominal
42	-4	0.5	Nominal

A final PIV campaign using the NACA 0012 airfoil was performed to provide results that verify the aerodynamic load calculation method used in this thesis (More on the aerodynamic load calculation in chapter 4. Table 3.10 presents the complete set of testing conditions for the PIV experiments conducted on the NACA 0012 airfoil model.

Table 3.10: PIV test matrix for the NACA 0012 airfoil model

Run ID	α [°]	M_∞ [-]	Configuration
43	-10	0.6	Nominal
44	-8	0.6	Nominal
45	-6	0.6	Nominal
46	-10	0.6	Inverted
47	-8	0.6	Inverted
48	-6	0.6	Inverted

4 Data processing and analysis

This chapter presents the different ways in which data from Schlieren and PIV have been processed and analysed. section 4.1 documents the spectral analysis performed on the Schlieren data. section 4.2, section 4.1, and section 4.4 document the pre-processing of PIV data, mean flow and phase-averaged analysis considerations. Their results are part of the results section of this thesis. Lastly, section 4.5 provides a motivation for the estimation of the aerodynamic load uncertainty.

4.1. Spectral Analysis using Schlieren data

The buffet oscillation frequency for cases with a clear transonic buffet cycle has been estimated both visually and through a spectral analysis of Schlieren images. Regions with high-density gradients, such as shock waves, are visually identified by the contrast in the image, as the light intensity incident at each pixel is converted into a representative numerical value which can be further analyzed (both visually and numerically).

The first step in the analysis involves selecting the positions of 3 to 5 analysis windows, from which the spectral contents are computed based on the Schlieren data within each window. Using the numerical data from all pixels within each window, the average light intensity is computed for every instantaneous frame. This results in a time series representing the variations in average intensity within each window, which is expected to be a rather noisy signal. When defining a window within the oscillation region of the shock wave, the window intensity signal will vary according to the position of the shock wave. This is illustrated in Figure 4.1, from which it is understood that the window's average intensity signal is higher in frames where the shock wave is not captured within the window (right) and lower when it is (left).

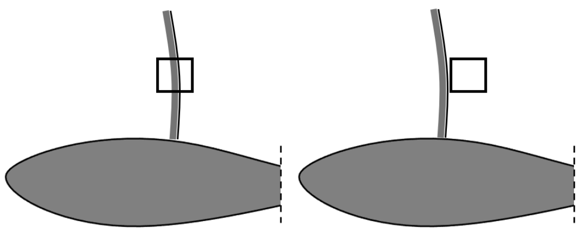

Figure 4.1: Illustration of a window used to obtain a time series for the average light intensity. Variations in window average intensity are due to the presence of an oscillating shock wave and the static window location.

An estimate of the Power Spectral Density (PSD) of the window average light intensity signal is obtained through MATLAB's `pwelch` function. In this way, the frequency of the shock wave oscillation is derived from the variations in the instantaneous average light intensity in the window.

The shadow region created by the shock's strong density gradient is on the order of, at most, $\sim$10 px wide, and is observed to oscillate within an extent of $\gtrsim 30\%c$ during the buffet cycle. The optimal window width must ensure that it is not too wide, such that the shadow region is always captured and no signal variations are observed, but wide enough that the shadow region is captured. Taking this considerations into account, the window dimensions were chosen to be 11$\times$11 pixels (width $\times$ height).

Besides varying the window dimensions and their ability to adequately capture the shadow region of the shock wave, multiple windows are defined in different locations within the flow field to verify the results. For all analyses, additional windows defined in locations such as the free stream, shear layer, and wake, serve to identify the spectral contents related to the transonic buffet phenomena alone and verify agreement between windows within the shock's oscillatory region.

4.2. Pre-processing of PIV velocity data

The raw PIV data is first preprocessed to obtain the velocity fields using the software `DaVis`. The sliding background subtraction filter with a window size of 8px was applied to remove local background intensity variations, improving the contrast of seeding particles. This works well for local corrections needed near the airfoil surface, which sometimes displayed significant reflections from particles stuck to the surface.

Cross-correlation was performed on an initial square interrogation window with size 64$\times$64 px and an overlap of 50%, followed by two passes with a window size of 32$\times$32 px and 75% overlap. This follows from the choices made during a previous PIV experimental campaign on the same airfoil (Aditya et al., 2024). The coarse initial pass, with 50% overlap, results in a rough velocity estimate for a relatively large region at a better spatial resolution than when using non-overlapping windows. The final two passes with 75% overlap allow for a more refined and localised determination of the displacement, further increasing the spatial resolution to a final value of 0.5mm. The lack of edges in the circular windows used in the final passes minimises the alignment bias from square windows, leading to a more accurate determination of the displacement in regions with curved or rotational flow, such as in the airfoil's wake. Carrying out the cross-correlation for all FOVs in both inverted and nominal airfoil model configurations for each test condition results in 4 different velocity FOVs (Each containing a velocity in x and y-direction, for a total of 8 velocity fields), two for each configuration. The next step is to merge these fields to obtain the velocity field around the airfoil. All subsequent data processing is performed using the software `Matlab`.

The 4 velocity FOVs available for every test condition, together, define the velocity field around the airfoil. The velocity data in FOVs belonging to the same model configuration is merged in the instantaneous sense, as they are synchronized in time. The result is the merged u and v velocity fields for the nominal model configuration and u and v velocity fields for the inverted model configuration. The merging process between these is then only possible in the time-averaged sense, as their measurements are not synchronised in time.

Considering four FOVs, and the calibration process previously described, each FOV has data on a grid with an origin defined at either the LE or TE of the airfoil, depending on which one is visible. By defining a point, P, along the calibration object and visible to both inverted FOVs, all FOV grids are translated to align their origin and orientation with Inverted FOV$_1$. This is illustrated by Figure 4.2.

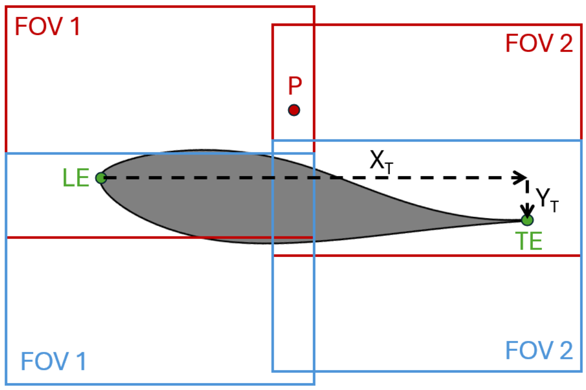

Figure 4.2: FOV grid translation into the grid of inverted FOV 1, using a reference point, P, common to both inverted FOVs. Inverted FOVs are coloured in red, Nominal FOVs coloured in blue.

The relative shift between inverted FOV$_1$ and FOV$_2$, X_T and Y_T, is calculated from the coordinates of point P expressed in both inverted FOV grids. Here, the subscript numbers '1' or '2', and the subscript text 'inv' or 'nom' distinguish all FOVs.

$$\begin{aligned} X_T &= x_{p,1,inv} - x_{p,2,inv} \\ Y_T &= y_{p,1,inv} - y_{p,2,inv} \end{aligned} \tag{4.1}$$

Nominal and Inverted FOV$_1$ share the same origin but with different orientations. Similarly, Nominal and Inverted FOV$_2$ share the same origin, with different orientations. The following transformations ensure all FOV data are expressed in the same coordinate system of Inverted FOV$_1$. Here, the subscript 's' refers to the shifted coordinate system,

$$\begin{aligned} x_{1,inv,s} &= x_{1,inv} \ , & y_{1,inv,s} &= y_{1,inv} \\ x_{2,inv,s} &= x_{2,inv} + X_T \ , & y_{2,inv,s} &= y_{2,inv} + Y_T \\ x_{1,nom,s} &= x_{1,nom} \ , & y_{1,nom,s} &= -y_{1,nom} \\ x_{2,nom,s} &= x_{2,nom} + X_T \ , & y_{2,nom,s} &= -y_{2,nom} + Y_T \end{aligned} \tag{4.2}$$

The velocity data is now expressed in the Inverted FOV$_1$ coordinate system, with origin at the LE of the airfoil, yet remains defined in non-overlapping grids. A global grid is defined with uniform spacing in the order of the original gridded data. All velocity data across different FOVs is linearly interpolated to the global grid. Velocity data is available twice at grid points in the overlap region between the inverted FOVs. In this region, the data is merged using a linear weighting function, defined only within the overlap region as illustrated by Figure 4.3. Similar weight functions are employed to merge nominal FOVs. and to merge the nominal and inverted data.

(a) Weighting function for inverted FOV$_1$

(b) Weighting function for inverted FOV$_2$

Figure 4.3: Linear weighting functions for FOV$_1$ (left) and FOV$_2$ (right) used to merge the velocity data defined in the inverted FOVs. Blue represents a weight of 1, white represents a weight of 0, and intermediate weights are shown in the overlapping region.

After merging the inverted and nominal FOVs into two global fields (one nominal and another inverted), the mean u and v velocity fields are computed for each configuration, along with the standard deviation at each grid point. A basic outlier detection method is applied to the u and v components, discarding instantaneous velocity data that deviate by more than four standard deviations from the local mean. The remaining velocity data is averaged, and the resulting inverted and nominal mean u and v fields are combined to obtain unified mean velocity fields spanning all FOVs.

4.3. Mean flow field analysis

With the availability of the instantaneous and mean velocity fields, the mean/instantaneous temperature and Mach number fields can be calculated. By assuming a constant total enthalpy in the flow, the static temperature is expressed in terms of the local velocity magnitude. $V = \sqrt{u^2 + v^2}$ using Equation 4.3. Assuming no significant heat transfer and a steady flow, the adiabatic flow assumption is reasonable even in viscous regions (White, 1991).

$$\frac{T}{T_\infty} = 1 + \frac{\gamma - 1}{2} M_\infty^2 \left(1 - \frac{V^2}{V_\infty^2}\right) \tag{4.3}$$

The local Mach number is calculated via Equation 4.4

$$M = \frac{V}{a} = \frac{V}{\sqrt{\gamma R T}} \tag{4.4}$$

In addition, the Reynolds stress field is calculated from the instantaneous and mean inverted and nominal velocity fields, later merged into a unified field. Here n refers to the total number of frames, and the mean fields are represented by the overline notation.

$$\begin{aligned}
\overline{u'u'} &= \frac{1}{n} \sum (u - \bar{u})(u - \bar{u}) \\
\overline{u'v'} = \overline{v'u'} &= \frac{1}{n} \sum (u - \bar{u})(v - \bar{v}) \\
\overline{v'v'} &= \frac{1}{n} \sum (v - \bar{v})(v - \bar{v})
\end{aligned} \tag{4.5}$$

4.3.1. Separated flow and supersonic flow criteria

The separated flow and supersonic flow characteristics are of great interest for analyzing the mean flow field of all test conditions. For separated flow, a simple yet meaningful criterion is used. This thesis defines an estimate for the separated flow region as regions with a negative u velocity component ($u < 0$). The number of data points satisfying the criterion are then multiplied by the grid point area, arriving at a metric for the separated flow area.

With this criterion, the following analysis on separated flow is possible.

- A metric for the separated area of the mean flow field, $A_{sep,mf}$, is determined by applying the separated flow criterion to the mean u-velocity flow field.
- A metric for the instantaneous separated area of the flow field in frame i, $A_{sep,i}$, is determined by applying the separated flow criterion to the instantaneous u-velocity flow field.
- A metric for the mean separated area, $\overline{A}_{sep}$, is determined by averaging $A_{sep,i}$ in time.
- A metric for the separated flow probability in the flow field, $P_{sep}(x, y)$, is determined by applying the metric to all PIV frames, summing the instances of separation over time, and dividing by the total number of frames available. This results in a spatial distribution of flow separation.

For supersonic flow, this thesis defines a supersonic flow region with a local Mach number greater than 1 (M > 1). The data points satisfying the criterion are then multiplied by the grid point area, arriving at a metric for the supersonic flow area.

With this criterion, the following analysis on supersonic flow is possible.

- A metric for the supersonic area of the mean flow field, $A_{sup,mf}$, is determined by applying the supersonic flow criterion to the mean Mach number flow field.
- A metric for the instantaneous supersonic area of the flow field in frame i, $A_{sup,i}$, is determined by applying the supersonic flow criterion to the instantaneous Mach number flow field.
- A metric for the mean supersonic area, $\overline{A}_{sup}$, is determined by averaging $A_{sup,i}$ in time.
- A metric for the supersonic flow probability in the flow field, $P_{sup}(x, y)$, is determined by applying the metric to all PIV frames, summing the instances of supersonic flow over time, and dividing by the total number of frames available. This results in a spatial distribution of supersonic flow.

4.3.2. Pressure field reconstruction

In isentropic flow regions sufficiently distant from the airfoil, the static pressure can be expressed in terms of velocity magnitude, V, as shown in Equation 4.6.

$$\frac{p}{p_\infty} = \left(1 + \frac{\gamma - 1}{2} M_\infty^2 \left(1 - \frac{V^2}{V_\infty^2}\right)\right)^{\frac{\gamma-1}{\gamma}} \tag{4.6}$$

Near regions where isentropic flow assumptions break down, such as shock waves and the airfoil wake, the differential form of the momentum equation from the Navier-stoke equations is used as a direct link between the velocity and pressure in the flow field. The differential momentum equation for compressible flow in conservative form is shown in Equation 4.7, where $\vec{V}$ is the velocity vector, μ is the dynamic viscosity of the fluid, and $\vec{F}$ is the external force vector.

$$\frac{\partial(\rho\vec{V})}{\partial t} + \nabla(\rho\vec{V}\vec{V}) = -\nabla p + \mu\nabla^2\vec{V} + \rho\vec{F} \tag{4.7}$$

The acceleration term, $\frac{\partial\vec{V}}{\partial t}$, viscous term, $\mu\nabla^2\vec{V}$, and external force term, $\rho\vec{F}$, are discarded by assuming, steady flow, an absence of external forces, and neglecting the contribution of viscous terms, resulting in the conservative formulation Equation 4.8.

$$\nabla(\rho\vec{V}\vec{V}) = -\nabla p \tag{4.8}$$

Through the definition of the material derivative $\frac{Dq}{Dt} = \frac{\partial q}{\partial t} + (V \cdot \nabla)q$ for a quantity q, the non-conservative formulation is expressed as shown in Equation 4.9. Both the conservative and non-conservative formulations represent the same momentum conservation law, but they differ in how quantities are conserved across the domain, especially once the equations are used in a discretized domain. More on this later.

$$\rho(\vec{V} \cdot \nabla)\vec{V} = -\nabla p \tag{4.9}$$

Introducing the Reynolds averaging approach, a time-varying quantity q is decomposed into its time-averaged mean $\overline{q}$ and a fluctuating component, q', referred to as Reynolds decomposition.

$$q(t) = \overline{q} - q'(t) \tag{4.10}$$

Applying Reynolds averaging to the conservative formulation, re-writing the density gradient as a gradient in the pressure and temperature, and dividing by the static pressure results in the conservative expression for the pressure gradient, Equation 4.11, written elegantly using tensor notation.

Conservative Formulation

$$-\frac{1}{p}\frac{\partial p}{\partial x_i} - \frac{1}{p} \cdot \frac{1}{RT}\frac{\partial p}{\partial x_j}\left[\bar{u}_i\bar{u}_j + \overline{u_i'u_j'}\right] = \frac{1}{RT}\left[\frac{\partial}{\partial x_j}\left(\bar{u}_i\bar{u}_j + \overline{u_i'u_j'}\right) - \frac{1}{T} \cdot \frac{\partial T}{\partial x_j}\left(\bar{u}_i\bar{u}_j + \overline{u_i'u_j'}\right)\right] \tag{4.11}$$

Applying Reynolds averaging to the non-conservative formulation, smartly substituting the result of the Reynolds averaged continuity equation into the expansion terms (to operate on terms of the form $\overline{x'x'}$), re-writing the density gradient as a gradient in the pressure and temperature and dividing by the static pressure results in the non-conservative expression for the pressure gradient, Equation 4.12, written elegantly using tensor notation.

Non-Conservative Formulation

$$-\frac{1}{p}\frac{\partial p}{\partial x_i} - \frac{1}{p}\frac{1}{RT}\frac{\partial p}{\partial x_j}\overline{u_i'u_j'} = \frac{1}{RT}\left[\bar{u}_j\frac{\partial \bar{u}_i}{\partial x_j} + \frac{\partial}{\partial x_j}\left(\overline{u_i'u_j'}\right) - \frac{1}{T}\frac{\partial T}{\partial x_j}\overline{u_i'u_j'}\right] \tag{4.12}$$

The full derivation of these expressions has been omitted for simplicity. In the derivations, the ideal gas law is used to re-write the density gradient as shown in Equation 4.13.

$$\begin{aligned}\frac{\partial \rho}{\partial x_j} &= \frac{\partial p}{\partial x_j}\cdot\frac{1}{RT} + \frac{p}{R}\cdot\frac{\partial}{\partial x_j}\left(\frac{1}{T}\right)\\ &= \frac{1}{RT}\left(\frac{\partial p}{\partial x_j} - \frac{p}{T}\frac{\partial T}{\partial x_j}\right)\end{aligned} \tag{4.13}$$

While Equation 4.3 in combination with the ideal gas law has been used to express the term $\frac{\rho}{p} = \frac{1}{RT}$ in terms of the local velocity magnitude.

$$\frac{\rho}{p} = \frac{1}{RT} = \frac{\gamma M_\infty^2}{V_\infty^2 + \frac{\gamma-1}{2}M_\infty^2(V_\infty - V^2)} \tag{4.14}$$

The pressure gradient terms in both conservative and non-conservative expressions are written more conveniently using the fact that

$$\frac{\nabla p}{p} = \nabla \ln(p) \tag{4.15}$$

The variables used in these Reynold-averaged expressions are the mean pressure field, $p = \overline{p}$, and mean velocity magnitude field, $V = \overline{V}$, both a function of space.

As a result, the pressure gradients needed to reconstruct the mean pressure field can be determined by solving the conservative or non-conservative linear set of equations, Equation 4.11 or Equation 4.12, with or without the addition of the turbulent stresses. Unless otherwise specified, the results of this thesis use a pressure determination method based on the conservative formulation with added turbulent stresses. This follows from its ability to correctly propagate the flow information during the integration across different flow regions. According to a study on the performance of these formulations, the conservative formulation can return a pressure rise over shocks that is in agreement with shock theory, while the non-conservative formulation returns the isentropic pressure (B. Van Oudheusden, 2008). This is of great importance when the mean flow field captures prominent shock over the airfoil, such as in a shock-wave-phase-averaged flow analysis (An analysis to be discussed later).

A numerical spatial integration method similar to the one used by Baur, 1999 and B. Van Oudheusden, 2008, has been adopted to solve for the logarithmic pressure gradient field by prescribing isentropic pressure boundary conditions in what is considered to be the 'freestream'. The pressure is separately reconstructed on the inverted and nominal fields and then merged to a unified mean pressure field, similar to the process performed on the velocity fields. For the inverted field, the presence of shock waves and a wide wake resulted in the defining the 'free stream' as the union of regions satisfying $y/c \gtrsim 30\%$ and $x/c \lesssim 8\%$. For the nominal field, the 'freestream' is defined as the union of regions satisfying $y/c \lesssim -30\%$ and $x/c \lesssim 73\%$. In these 'freestream' regions, the pressure is determined directly from the velocity magnitude through Equation 4.6, and the pressure in the rest of the domain is determined from the pressure integration scheme chosen. The regions are visualized in Figure 4.4 for the case at $\alpha = -10°$, in both inverted and nominal fields.

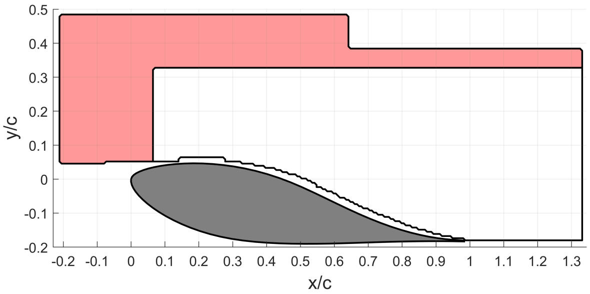

(a) The isentropic region shaded in light red.

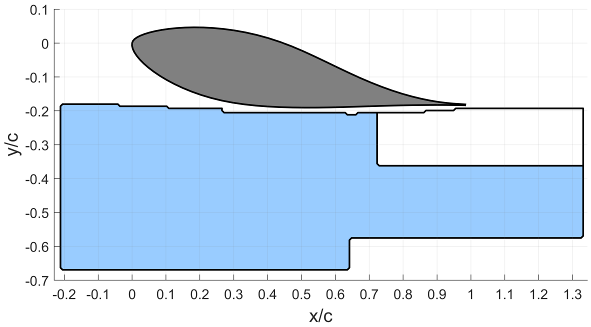

(b) The isentropic region shaded in light blue.

Figure 4.4: Nominal (right) and inverted (left) field regions for which the flow is assumed to be isentropic. The unshaded domain describes the region in which the pressure-integration scheme is used. Green markers define the start of the integration front

The spatial integration method marches through space, determining the pressure field by using the pressure information of all neighboring points in which the pressure has been previously prescribed or computed. The unknown pressures are an equally weighted average of all neighboring contributions. The pressure integration scheme uses a minimum number of neighbors $N_{min} = 4$ to propagate the pressure at the unknown data points, thus propagating outward from the green markers in Figure 4.4. When the propagation front features no point with N_{min} neighbors, this continues propagating into unknown data points with a minimum of $N_{min} - 1$ available neighbors. The propagation of pressure information for the inverted field starting with $N_{min} = 4$ is illustrated by Figure 4.5.

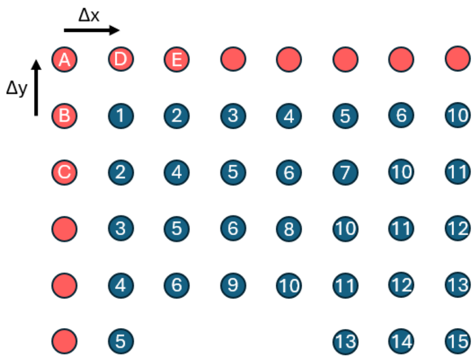

Figure 4.5: Propagation of pressure field across the integration domain, starting with a minimum number of required neighbors $N_{min} = 4$. Red grid points represent the boundary conditions, while blue grid points represent the integration domain. Grid point numbering represent the order in which these are determined

Here, the first point in the integration domain to be filled is numbered '1', with contributions from 5 neighboring points, A, B, C, D, and E.

$$
\begin{aligned}
p_1 = \frac{1}{5}\Bigg[& \left(p_A + \frac{\partial p}{\partial x}_A \Delta x - \frac{\partial p}{\partial y}_A \Delta y\right) + \left(p_B + \frac{\partial p}{\partial x}_B \Delta x\right) \\
& + \left(p_C + \frac{\partial p}{\partial x}_C \Delta x + \frac{\partial p}{\partial y}_C \Delta y\right) + \left(p_D - \frac{\partial p}{\partial x}_D \Delta y\right) \\
& + \left(p_E - \frac{\partial p}{\partial x}_E \Delta x - \frac{\partial p}{\partial y}_E \Delta y\right)\Bigg]
\end{aligned} \tag{4.16}
$$

4.3.3. Aerodynamic load calculation

The TST-27 wind tunnel lacks an integrated force balance, and the FFA-W3-211 airfoil model is not fitted with static pressure probes along its surface, which would otherwise allow for an estimate of aerodynamic loads through the integration of the pressure distribution. Consequently, an alternative method for calculating aerodynamic loads has been adopted, which relies on reconstructing the pressure field from the velocity field data obtained through Particle Image Velocimetry (PIV).

An integral momentum conservation formulation is applied over a control volume around the airfoil, where the concept of Reynolds averaging will be applied to the Navier-Stokes momentum equation to formulate an expression for the mean aerodynamic loads acting on the airfoil. A fixed control volume in space and time is considered, illustrated in Figure 4.6

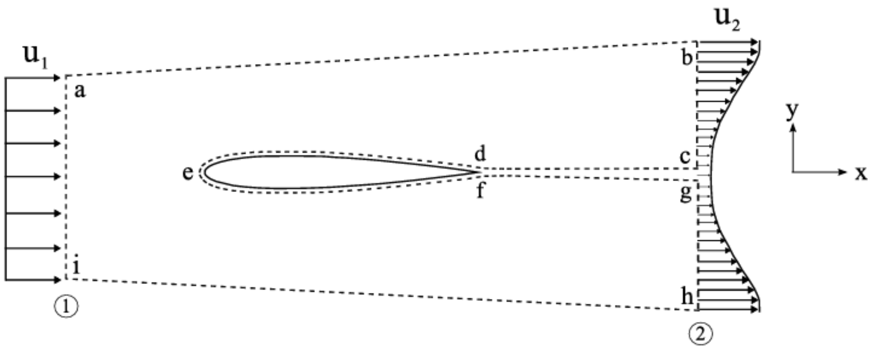

Figure 4.6: Control volume considered for the integral momentum conservation (Anderson, 2011)

Applying the conservation of momentum in integral form over the control volume V bounded by the contour S, assuming a steady two-dimensional flow, neglecting the contribution from body forces and neglecting the contribution from viscous terms results in

$$\iint_S \rho\left(u_j n_j dS\right) u_i = -\iint_S p n_i dS \tag{4.17}$$

The integral is expanded to indicate the contributions from segments a-i. The force acting on segments dc and fg are equal and opposite, so these cancel out. The force at the airfoil surface def applied by the fluid on the airfoil, R, is equal and opposite to the reaction force exerted by the airfoil on the fluid. To calculate the aerodynamic force R, the expansion terms over segment def are written out explicitly, as shown below. Here, the momentum flux term over the segment def is zero, as this is a solid boundary.

$$\iint_{abhi} \rho\left(u_j n_j dS\right) u_i + \cancelto{0}{\iint_{def} \rho\left(u_j n_j dS\right) u_i} = -\iint_{abhi} p n_i dS - \iint_{def} p n_i dS$$

$$\iint_{abhi} \rho\left(u_j n_j dS\right) u_i = -\iint_{abhi} p n_i dS - \underbrace{\iint_{def} p n_j dS + \iint_{def} \tau_{ij} n_j dS}_{=-R_i}$$

$$R_i = -\oint_{abhi} \rho\left(u_j n_j dS\right)\left(u_i - U_{\infty,i}\right) - \oint_{abhi} p n_i dS$$

In the last equation, a correction for mass conservation is included by subtracting a force equivalent to the mass flux multiplied by the freestream velocity. This correction increases the robustness of the result, and is allowed as its integral over segment def is zero. Applying Reynolds averaging yields the time-averaged aerodynamic force acting on the airfoil, relating the mean aerodynamic load to an integral of flow field variables over the contour $abhi$.

$$R_i = \iint_{abhi} \left[-\rho\left(\bar{u}_i \bar{u}_j - U_{\infty,i} \bar{u}_j\right) n_j - \rho\left(\overline{u_i' u_j'}\right) n_j - \bar{p} n_i\right] dS \tag{4.18}$$

The contour integral is taken on the boundary illustrated by Figure 4.7, paying attention to the orientation of the boundary-normal vectors and the integral orientation. The vertical extent of the contour is defined by the upper boundary at $y/c \approx 30\%c$ and the lower boundary at $y/c \approx -40\%c$, while the left and right boundaries are defined at $x/c \approx -15\%c$ and $x/c \approx 120\%c$. contour data in the shadow region of the freestream is interpolated from the available data.

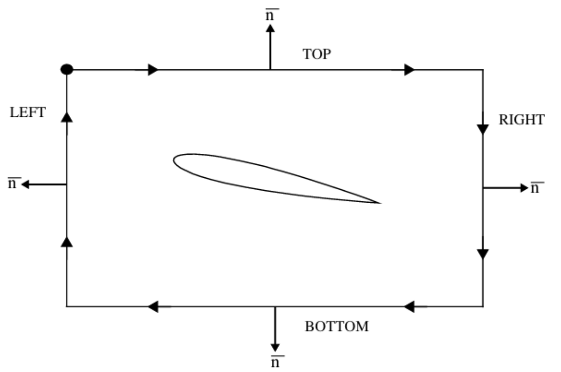

(a) Contour boundaries, integration orientation, and normal vector to each boundary.

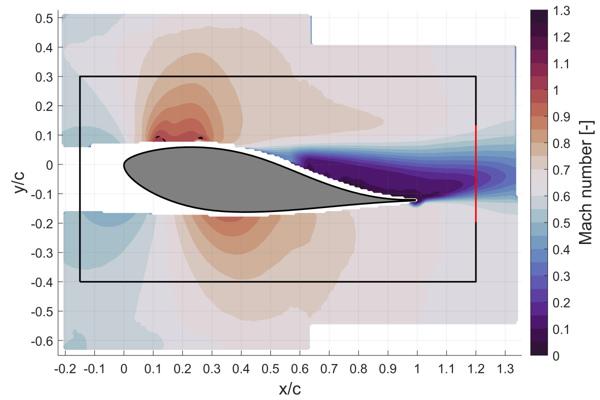

(b) Visualization of the contour by the solid black lines. The red line represents the line used to determine the wake-based drag coefficient.

Figure 4.7: Contour shape and boundary

Expanding the expression in the cartesian frame of reference along the y-direction, yields the expression for the time-averaged lift force per unit span, dL, as a function of the velocity components u and v. Similarly, it is possible to obtain the time-averaged drag force per unit span. These expressions are evaluated along the entire contour boundary to derive the integral aerodynamic loads.

$$dL = \bar{\rho}(\bar{u}\bar{v})dy - \rho(\bar{v}\bar{v})dx + \rho(\bar{u'}\bar{v'}) - \rho(\bar{v'}\bar{v'}) - \bar{p}dx \tag{4.19}$$

$$dD = \bar{\rho}\bar{u}(\bar{u} - U_\infty)dy - \rho\bar{v}(\bar{u} - U_\infty)dx + \rho(\bar{u'}\bar{u'}) - \rho(\bar{u'}\bar{v'}) + \bar{p}dx \tag{4.20}$$

The lift term is expected to be dominated by the pressure contribution, while the drag term is dominated by the momentum flux contribution. Despite the mass conservation correction, evaluating the contour integral can result in the accumulation of errors and uncertainties derived from the PIV measurement data and the pressure integration scheme. Following the discussion from B. Van Oudheusden et al., 2006, these errors and uncertainties may lead to violations in the integral mass conservation over the contour, which particularly affects the drag load estimation as it is a small quantity. For this reason, the drag is also calculated from the momentum deficit in the wake, based on the approach by Jones, 1936, with an adaptation to account for compressibility effects. The derivation is omitted and may be found in Bannink, 1987, however, a brief conceptual description of the approach is presented.

Three locations in the freestream direction are considered in the derivation of the expression. the freestream or undisturbed flow (∞), the near-wake (2) and the far-wake (1). It is assumed that the pressure has recovered in the far-wake to the freestream value, therefore this can be neglected in the derivation of the drag from the momentum equation, obtaining

$$D = \int \rho u_1 (U_\infty - u_1) dy_1 \tag{4.21}$$

The optical access in the wind tunnel does not allow for measurements in the far-wake (1), and is limited to those in the near wake (2). The following assumptions are made to relate the far-wake quantities to those in the near-wake.

- The continuity equation is valid, assuming only a horizontal velocity component (one-dimensional flow)
- The total enthalpy is constant, leading to a constant total temperature.

- The total pressure along the streamlines within the wake is conserved.
- The flow may be assumed to be homentropic

Employing these assumptions and substituting the variables in the far-wake for those measured/ inferred in the near wake results in the expression for the drag coefficient, Equation 4.22

$$c_d = 2\int_{y_2}^{y_1} \left(\frac{p_2}{p_\infty}\right)^{\frac{1}{\gamma}} \left(\frac{p_{t,2}}{p_{t,\infty}}\right)^{\frac{\gamma-1}{\gamma}} \sqrt{\frac{\left(\frac{p_2}{p_{t,2}}\right)^{\frac{\gamma-1}{\gamma}}}{\left(\frac{p_\infty}{p_{t,\infty}}\right)^{\frac{\gamma-1}{\gamma}}}} \left[1 - \sqrt{\frac{\left(\frac{p_\infty}{p_{t,2}}\right)^{\frac{\gamma-1}{\gamma}}}{\left(\frac{p_\infty}{p_{t,\infty}}\right)^{\frac{\gamma-1}{\gamma}}}}\right] d\left(\frac{y}{c}\right) \tag{4.22}$$

This expression requires the static and total pressure field to be resolved in the near-wake of the airfoil. The previous section described how the mean pressure field is inferred from PIV velocity data. The integral is evaluated at a distance $x/c \approx 120\%$, considering part of the wake were there is a loss in total pressure.

4.4. Phased-averaged flow field analysis

4.4.1. Shock wave identification

The analysis of shock waves requires the identification of these in instantaneous PIV frame data. Different approaches for shock-wave detection approaches exist in numerical simulations, for example, through an analysis of the Mach number or the pressure field, as these display high gradients at the shock front. In this thesis, a shock front detection algorithm is used to detect shock waves and their location based on the instantaneous Mach number field. This is best explained through the detection of a shock wave visualized in Figure 4.8.

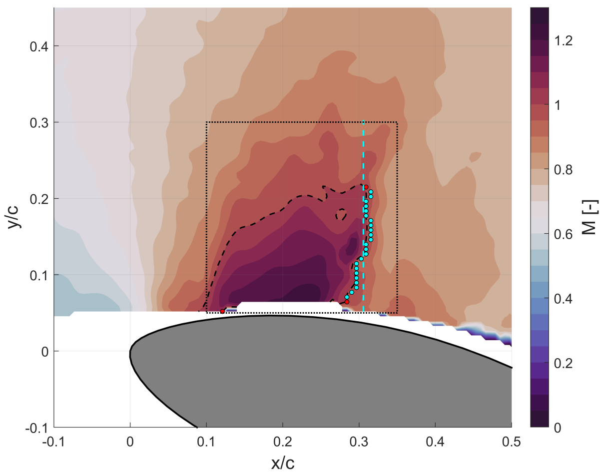

Figure 4.8: Shock wave detection algorithm within the search region (Dotted box). All markers represent the boundary between supersonic and subsonic flow. Only cyan markers satisfy all requirements to be considered part of the front. The cyan line represents the derived shock location.

The following steps describe the algorithm used to detect shock waves from instantaneous Mach number fields. All choices, distinguished below in parenthesis, were carefully verified through an analysis of the shock waves detected in two different test conditions.

1. For all grid rows within the search region (Dotted box in Figure 4.8), the potential shock front is defined as the location in which flow last changes from supersonic ($M > 1$) to subsonic ($M < 1$) conditions. These are visualized by all the markers.
2. A Mach number threshold is defined at each potential shock-front point. Only those whose ($n_{us} = 3$) upstream neighboring points satisfy ($M_{sup} > 1$) and whose ($n_{ds} = 4$) downstream neighboring points satisfy ($M_{sub} < 0.98$) are considered. This can be seen as a requirement on the shock wave strength and extent.

3. The mean chord-wise location of each remaining shock front point, $x_{fro,j}$, is gathered, from which the mean location and standard deviation are computed. Only points within (2) standard deviations from the mean are further considered. The algorithm stops and continues assessing the next frame if the standard deviation is greater than (13), or if the number of remaining shock front points fall under ($n_{sho} < 8$).
4. Data points that do not meet any of the previous requirements are colored red in Figure 4.8, remaining data points are colored in cyan. The instantaneous shock wave location is defined as the mean of the remaining shock front points $x_{sho,i} = \bar{x}_{fro,j}$.

A verification through the sensitivity of the shock-detection algorithm to changes in M_{sub} and n_{sho} is conducted for a fixed choice of $n_{us} = 3$ and $n_{ds} = 4$, and other choices as stated previously. For this, the instantaneous FFA-W3-211 airfoil PIV data at the test conditions ($\alpha = -6°$,$M_\infty = 0.65$) and ($\alpha = -10°$,$M_\infty = 0.65$) was considered .The number of PIV frames with detected shock waves divided by the total number of frames, expressed as by percentage P_{sho}, and its sensitivity to M_{sub} and n_{sho} is illustrated in Figure 4.9.

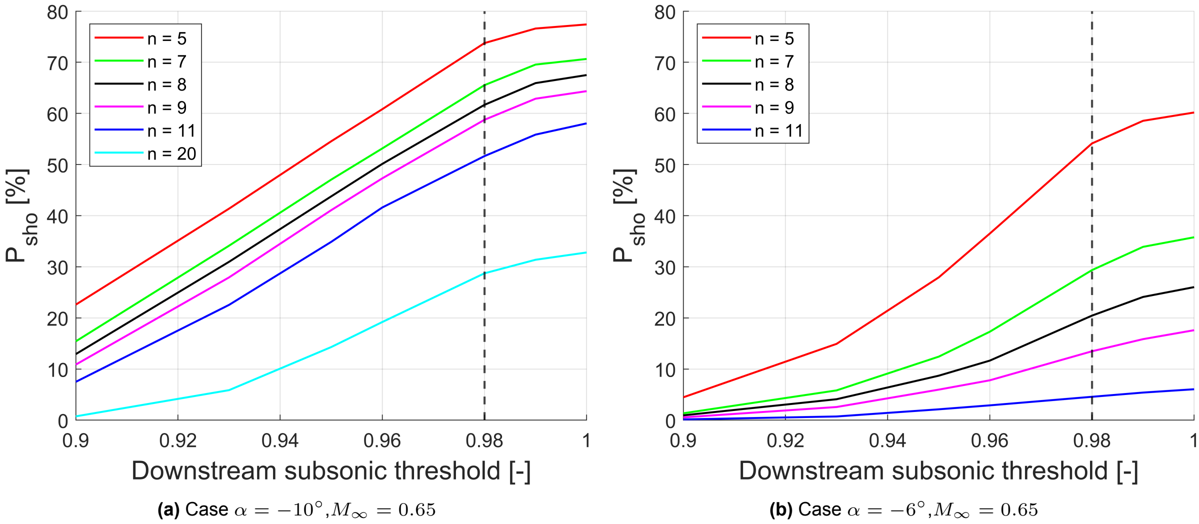

Figure 4.9: Sensitivity of the percentage of frames with a detected shock wave to the choice of M_{sub} and n_{sho}, for the cases $\alpha = -6°$,$M_\infty = 0.65$ (right) and $\alpha = -10°$,$M_\infty = 0.65$ (left)

As expected, increases in n_{sho}, and decreases in M_{sub} reduce the number of PIV frames with shock waves detected. The choice of $M_{sub} = 0.98$ and n_{sho} is motivated to remain conservative in detecting shock waves. With this choice, it is preferred to avoid detecting a shock wave where it should not be detected.

4.4.2. Phase-definition

Having characterised each PIV frame with a shock (or no shock) and its location, a phase-averaged approach is defined to analyze test conditions that develop a clear transonic buffet cycle.

Similar to the work of D'Aguanno, 2023, four buffet phases are defined. Shock wave at its most upstream position (1), shock wave during its downstream movement (2), shock wave at its most downstream position (3), shock wave during its upstream movement (4). In addition, all frames for which no shock is detected are distinguished as the phase 'No shock'. The shock wave position distinguishes between phases 1 and 3. Both instantaneous shock wave position $x_{sho,i}$ and separated area $A_{sep,i}$ distinguish between phases 2 and 4, where it is assumed that a correlation exists between the separated area and the shock's upstream and downstream movements.

It is assumed that the instantaneous flow field can be decomposed into its mean component, a periodic component, and a turbulent component as

$$\vec{u} = \vec{u}_{mean} + \vec{u}_{per} + \vec{u}_{turb} \tag{4.23}$$

The phase-averaged velocity fields, equivalent to the summation of the periodic and mean contributions ($\vec{u}_{phs} = \vec{u}_{mean} + \vec{u}_{per}$), are obtained by computing the mean of all frames belonging to each phase. The same analysis procedures of the mean flow analysis described in section 4.3 can be applied to derive the phase-averaged velocity, Mach number, and pressure fields.

The assumption that there is a correlation between the shock's upstream or downstream movement and the intensity of separated flow is verified and discussed in section 5.4.

4.5. Aerodynamic load uncertainty estimation

An important aspect in the analysis of the aerodynamic loading trends is taking into account the uncertainty in these estimates, especially when discussing trends which may fall within the uncertainty of the method. The uncertainty may be determined following an external approach, or a measurement approach, for which only the later provides for the intermediate quantities required to determine the loads.

Possible sources for the error in PIV velocity

- Particle lag: Near the leading edge or across shock waves, where regions of high flow velocity gradients exist, the seeding particles' response may not accurately capture actual flow velocity due to its delayed response. In this thesis, instantaneous and local corrections to the velocity fields due to particle lag are not considered due to the majority of test conditions displaying no prominent shocks. For the few test conditions with prominent shocks, the particle lag and lack of corrections is expected to result in higher instantaneous velocities determined immediately downstream of the shock. These can be expected to be in the order of $\lesssim 60\mathrm{ms}^{-1}$ (D'Aguanno, 2023), given similar conditions and seeding particles used.
- Particle displacement: It is expected that random errors are in the order of 0.1 pixel (Ragni et al., 2009). Systematic errors introduced by the phenomenon of peak locking are neglected, given imaged seeding particles are well beyond 2-3px in diameter. This has been verified through histograms of the local u and v velocity.
- Calibration procedure: The uncertainty in the scale to pixel displacements to physical displacements introduces a systematic error in the displacement. The repeatability of experiments and calibration procedures allows to estimate the relative uncertainty in the scaling factor to be well within <1%.
- Post processing: These include errors introduced by misalignments in the coordinate system, the interpolation of the velocity into a global unified grid, the merging process in overlapping regions, and errors introduced by the outlier removal method. No quantification is made on these sources of error.
- Aero-optical effects: These are introduced by the blurring of particles due to the refractive index variations in the flow field, and are translated to weaker correlation peaks.
- Temporal errors: These are associated with the uncertainty in the programmable timing unit and the synchronisation of the laser-camera system. These effects have been considered to be negligible.

A wide variety of errors increase the uncertainty of the velocity fields determined from PIV. These are translated to the aerodynamic loads via intermediate quantities such as the pressure. The detailed identification and quantification of all sources of uncertainty, their propagation to the aerodynamic loads via intermediate quantities can easily require an entire scope dedicated to a detailed analysis. Given the scope of this thesis, an simple external approach to determining the uncertainty in aerodynamic loads is followed. Nontheless, a detailed uncertainty assessment of a similar experimental campaign can provide an order of magnitude for the uncertainty when conducting a measurement chain assessment.

4.5.1. Measurement chain uncertainty assessment

This section presents a brief summary of the measurement chain approach that would be required to quantify the uncertainty of the aerodynamic loads and intermediate quantities used in their determination.

Previous experimental campaigns using the momentum contour integral and wake momentum deficit methods to calculate the mean lift and drag loads on the NACA 0012 airfoil under transonic conditions have performed a measurement chain assessment (Ragni et al., 2009). The test conditions for the study were $M_\infty = 0.6$, $T_{t,\infty} = 270\mathrm{K}$, and $p_{t,\infty} = 1.9\mathrm{bar}$. The uncertainty analysis was carried out on the non-conservative pressure formulation with the omission of turbulent stress terms. Its approach is presented, and its results are taken into consideration to discuss the uncertainty of the present study.

Following the uncertainty propagation law, Equation 4.24 , all expressions for which the uncertainty shall be calculated are required to be written out in variables that are independent of each other. With this approach, it is possible to determine the uncertainty of each variable, due to random errors.

$$\Delta F = \sqrt{(\Delta F_{x1})^2 + (\Delta F_{x2})^2 + (\Delta F_{x3})^2 + \ldots} = \sqrt{\sum_{i=1}^{n} (\partial F/\partial x_i)^2 \cdot (\Delta x_i)^2} \tag{4.24}$$

In the propagation of uncertainty, the variables assumed to be uncorrelated include $T_{t,\infty}$, $p_{t,\infty}$, M_∞, M_∞, u, v, $\partial u/\partial x$, $\partial u/\partial y$, $\partial v/\partial x$, $\partial v/\partial y$. To simplify the analysis, the velocity gradients were assumed to be uncorrelated with the velocity.

In Ragni et al., 2009, the error in the velocity field is determined by applying the Root Mean Squared (RMS) to a uniform flow region like the freestream. The uncertainty was determined to be 1% of the velocity, but a more prudent and conservative estimate of 3% is taken.

The freestream variables are expressed in terms of uncorrelated values, with dependencies as summarized below.

$$\begin{aligned} T_\infty &= f(T_{t,\infty},\ M_\infty) \\ V_\infty &= f(T_{t,\infty},\ M_\infty) \\ p_\infty &= f(p_{t,\infty},\ M_\infty) \\ \rho_\infty &= f(T_{t,\infty},\ p_{t,\infty},\ M_\infty) \end{aligned} \tag{4.25}$$

The velocity gradients are expressed in terms of the velocity field.

$$\nabla V = f(u, v) \tag{4.26}$$

Here, the error is dependent on the scheme used to calculate the velocity gradients, and on the grid spacing, introducing a spatial uncertainty field. These errors are evaluated to be even greater than the calculated gradient in the freestream direction in regions close to the shock, where large velocity gradients exist. The finite-difference schemes used by Ragni et al., 2009 include a least-squares scheme, central differences and one-sided schemes, with a grid spacing in the order of $10^{-3}\mathrm{m}$. In the present study, central differences and one-sided schemes are used, with grid spacing in the order of $10^{-3}\mathrm{m}$. As the finite difference schemes used possess a similar error magnitude, and the grid spacing is comparable, the uncertainty in the velocity gradient field is likely of the same order.

The pressure gradients are also expressed in terms of uncorrelated values. The uncertainty analysis of Ragni et al., 2009 showed that the greatest contribution to its uncertainty is from the uncertainty of the velocity gradients. The uncertainty of the pressure gradients in the current study is expected to be greater due to the inclusion of Reynolds stresses in the pressure gradient formulation used.

$$\nabla p = f(T_{t,\infty},\ u,\ v,\ \partial u/\partial x,\ \partial v/\partial x,\ \partial u/\partial y,\ \partial v/\partial y) \tag{4.27}$$

The pressure field is computed directly from either the isentropic definition, or the integration scheme. The uncertainty in pressure at a point is the contribution of the uncertainty in the pressure and pressure gradients at the neighbouring points used for its determination. For this reason, the uncertainty is accumulated along the integration. The result is a spatial uncertainty field for the pressure, which grows larger with greater integration regions. Due to the large domain where the pressure is integrated, it is expected that the current results possess a higher uncertainty level than those of (Ragni et al., 2009).

The aerodynamic loads determined from the momentum contour integral are expressed in terms of uncorrelated variables. Again the inclusion of Reynolds stresses and higher levels of uncertainty expected in the intermediate variables are likely to yield a higher level of uncertainty in the current experiments than for (Ragni et al., 2009).

$$dL, dD = f(T_{t,\infty},\ u,\ v,\ p,\ M_\infty) \tag{4.28}$$

The drag estimated through the wake deficit line integral is expressed in terms of uncorrelated variables. A perturbation analysis performed showed it to be most influenced by the uncertainty in M_∞ and u.

$$c_d = f(T_{t,\infty},\ u,\ v,\ p,\ M_\infty,\ p_{t,\infty}) \tag{4.29}$$

The uncertainty of the aerodynamic loads is dependent not only on the test conditions, but also on the angle of attack. Across $0 \leq \alpha \leq 8$, the analysis concludes in a maximum uncertainty of the contour-based lift coefficient in the order of 0.02. The maximum order of magnitude for the contour-based drag is of the order 0.02. The maximum order of magnitude for the wake-based drag coefficient was of the order 0.002. Given the differences between the referenced study and the current experiments, the expected order of magnitude is likely greater, though it may, at best, be comparable.

4.5.2. External uncertainty assessment

This thesis conducts a simple external uncertainty assessment on the contour-based mean lift and wake-based mean drag coefficients. For the mean lift, this approach consists of varying the vertical extent of the contour. For the mean drag coefficient, this consists of varying the downstream location where the wake integral is performed. This approach indicates the variability of the aerodynamic loads when evaluating the contour integral over different locations, variables and associated uncertainties. The downside of this approach is that uncertainty is essentially treated as a 'black-box', and its contributions are not explicit. The variations in the contour and wake line are illustrated in Figure 4.10.

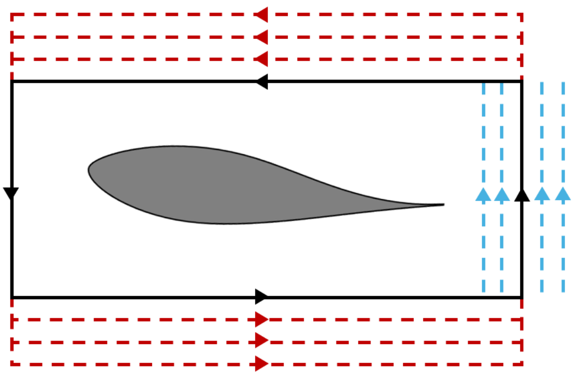

Figure 4.10: Contour variations for the lift coefficient visualised (red). Wake integral variations visualised (blue)

The following contours tabulated in Table 4.1 and Table 4.2 have been defined to test the variability of the mean lift and drag coefficients for the FFA-W3-211 airfoil model experiments.

Table 4.1: Top and bottom boundary locations for the different contours used for the FFA-W3-211 airfoil lift sensitivity study

Contour	$(y/c)_{top}$ [-]	$(y/c)_{bot}$ [-]
1	0.21	-0.31
2	0.24	-0.34
3	0.27	-0.37
4	0.30	-0.40
5	0.33	-0.43

Table 4.2: Wake-deficit x-location used for the FFA-W3-211 airfoil drag sensitivity study

Contour	x/c [-]
1	1.11
2	1.14
3	1.17
4	1.20
5	1.23
6	1.26

The following contours tabulated in Table 4.3 and Table 4.4 have been defined to test the variability of the mean lift and drag coefficients for the NACA 0012 airfoil model experiments.

Table 4.3: Top and bottom boundary locations for the different contours used for the NACA 0012 airfoil lift sensitivity study

Contour	$(y/c)_{top}$ [-]	$(y/c)_{bot}$ [-]
1	0.16	-0.28
2	0.19	-0.31
3	0.22	-0.33
4	0.25	-0.35
5	0.28	-0.38

Table 4.4: Wake-deficit x-location used for the NACA 0012 drag sensitivity study

Contour	x/c [-]
1	1.11
2	1.14
3	1.17
4	1.20
5	1.23
6	1.26

As discussed previously, the lift coefficient results discussed in this thesis are calculated using the contour labeled as 4. The drag coefficient results correspond to the x-location also labelled as 'contour 4'.

5

Results and discussion

The aim of this chapter is to present an analysis of the effects of compressibility on the flow field and aerodynamic performance of the FFA-W3-211 airfoil. To achieve this, the results obtained from the Schlieren and PIV experiments are analysed. The analysis is synthesized across the greater test domain through two distinct and representative angles of attack, $\alpha = -6°$ and $\alpha = -10°$, in the range, M_∞ = 0.5-0.65. The angle $\alpha = -6°$ is representative of a typical operational regime, while $\alpha = -10°$ provides near extreme conditions. Unless otherwise specified, all results and analyses presented are for the FFA-W3-211 airfoil model with $c = 67\text{mm}$ and fixed transition at $x/c = 5\%$. No analysis was carried out on the scaled-down model.

The chapter starts with section 5.1, documenting the steps taken to verify the implementation and results for the pressure reconstruction and aerodynamic load determination methodologies. This is followed by section 5.2, presenting a largely instantaneous analysis of shock waves, their interaction with the boundary layer, and separation. A focus is made on $\alpha = -10°$ and M_∞ = 0.65 due to the extreme conditions observed. section 5.3 then details the flow field development across the (α, M) domain, covering the mean velocity fields, Mach number field, supersonic area, separated area, reconstructed mean pressure field, and extrapolated pressure distribution along the airfoil, all providing a foundation to understand the mean aerodynamic loads. section 5.4 presents a phase-averaged analysis of the transonic buffet cycle identified at $\alpha = -10°$ and M_∞ = 0.65, capturing the distinct phases and flow field developments. The mean aerodynamic loads determined for all cases and documented in section 5.5, including the phase-averaged loads determined for the case with transonic buffet, presenting an interpretation that encompasses the results from all previous sections, as well as the implications on wind turbine loading and performance.

5.1. Verification of the methodology implemented

This section details the verification of the variables calculated to determine the aerodynamic load, including the aerodynamic load itself. A verification of the pressure reconstruction technique and the resulting pressure field is particularly of interest, as this is inferred from the PIV velocity data.

5.1.1. Reconstructed pressure field

CFD RANS simulation data using the software `Ansys`, performed on the FFA-W3-211 airfoil in the conditions $M_\infty = 0.5$, $T_{t,\infty} = 288K$, $p_{t,\infty} = 2.3$bar, $\alpha = -15°$, is used to verify the pressure field reconstruction technique. This is an interesting verification case, as the RANS result features a prominent separated region, and a shock wave over the suction side. The Spalart-Allmaras eddy viscosity model is used to model turbulence. The CFD data fields include u,v,M,T,T_t, p, p_t, and are defined in a non-uniform grid. The only manipulation of the CFD data required to make it suitable to apply the pressure reconstruction algorithm is for it to be specified on a uniform grid. For this, a 2D grid with uniform spacing $\Delta h = 0.3\text{mm}$ is defined, and the CFD data is interpolated.

Following the pressure reconstruction approach outlined in chapter 4, it is necessary to try to limit the discrepancy between the CFD pressure field and the reconstructed pressure field to the pressure integration technique. To achieve this, the inputs to the pressure reconstruction algorithm are the CFD velocity fields u and v. From this, the velocity gradients are calculated, and the gradient of the logarithm pressure field is determined. Outside of the integration domain, and at the boundary, the pressure is taken from the CFD pressure field. In theory, the Reynolds stress components could be derived from the CFD data based on the Boussinesq eddy viscosity assumption, which relates the Reynolds stress tensor to the mean strain rate tensor and the turbulent kinetic energy. Unfortunately, it was not possible to extract the turbulent kinetic energy from the CFD data, and, thus, the pressure reconstruction has been carried out with the omission of the Reynolds stress components.

In Figure 5.1, the reconstructed pressure field, p_{rec}. is compared to the CFD pressure field, p_{cfd}, through the pressure coefficient fields as the criterion $\Delta c_p = (c_{p,rec} - c_{p,cfd})$. This is suitable, as both results are scaled with the same quantities. The results using the conservative and non-conservative schemes are both presented.

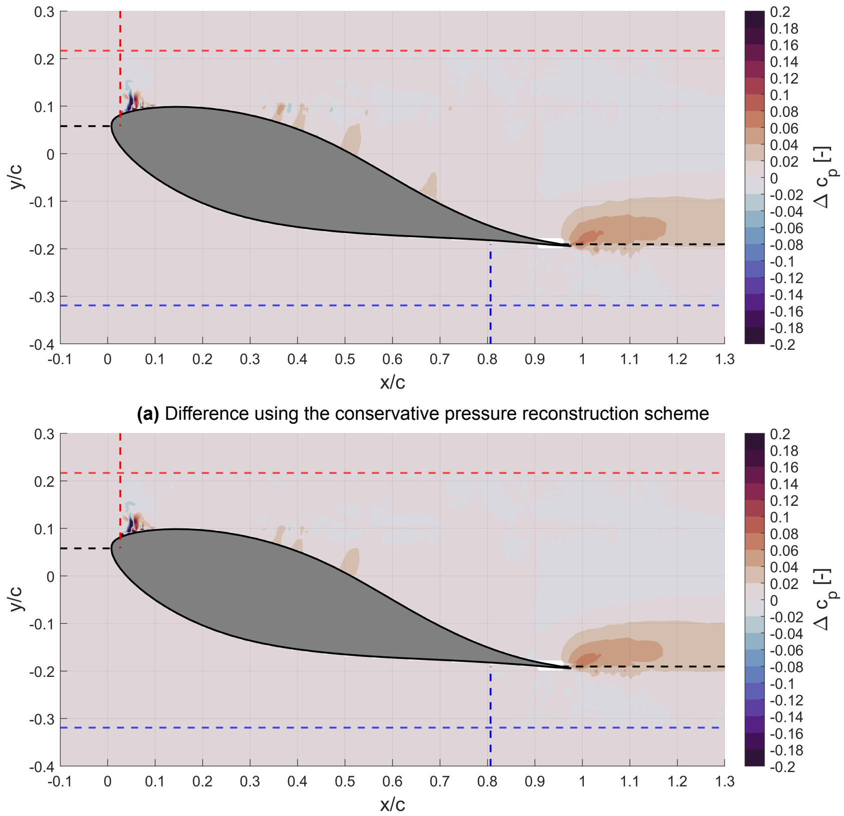

(a) Difference using the conservative pressure reconstruction scheme

(b) Difference using the non-conservative pressure reconstruction scheme

Figure 5.1: Difference between the CFD pressure field and reconstructed pressure field visualised through the difference in the pressure coefficient Δc_p field. Red and blue dashed lines distinguish between the regions where pressure is integrated, as described in chapter 4, for the nominal and inverted FOV distinguished by the black dashed line.

Overall, the pressure reconstruction technique yields a comparable pressure field to the CFD pressure within the integration region. For most of the integration region, the discrepancy in the pressure coefficient fields is of the order $\Delta c_p \approx \pm 0.02 - 0.04$. The discrepancy is most significant close to the shock wave region, reaching values in the order of $\Delta c_p \approx \pm 0.3$. The difference here can be attributed to many factors, like the modelling of the shock wave and turbulence in the CFD simulation, grid spacing, and high velocity gradients. Another region of discrepancy is observed beyond the TE. This is likely due to the absence of the Reynolds stress term in the computation of the pressure field, as their contribution can be expected to be greater in the corresponding region. These results suggest a proper working and implementation of the pressure reconstruction algorithm.

5.1.2. Aerodynamic loading

The verification of the aerodynamic load calculation is performed using the experimental campaign results for the NACA 0012 airfoil, for which additional experimental data is also available in literature (Ragni et al., 2009). The mean flow field velocity, Mach number, and pressure field are provided for completeness in Appendix C. The experiments of this thesis were conducted in what is usually considered to be a negative angle of attack convention. The results from the literature have actually been performed at positive angles of attack. It has been assumed that the lift and drag coefficients display a symmetrical behaviour, as the airfoil is symmetrical.

Following the data processing steps outlined in chapter 4, the aerodynamic loads for the NACA 0012 airfoil model are determined, and tabulated in Table 5.1. The experimental campaign from Ragni et al., 2009 features the same test conditions, pressure reconstruction and aerodynamic load determination methods, offering a good comparison between results. Simulation data using the software `XFOIL` is also tabulated for comparison.

Table 5.1: Comparison of uncorrected lift and drag coefficients for the NACA 0012 airfoil at Mach 0.6. $^{(1)}$ Momentum integral (PIV-based). $^{(2)}$ Load Balance measurement. $^{(3)}$ Simulation (Panel code based). $^{(4)}$ Pressure orifices. $^{(a)}$ Momentum integral (PIV-based). $^{(b)}$ Wake deficit (PIV-based). $^{(c)}$ Wake deficit (Wake rake-based). $^{(d)}$ Simulation (Panel code based).

Source	$\alpha = -6°$		$\alpha = -8°$		$\alpha = -10°$	
	c_l	c_d	c_l	c_d	c_l	c_d
Thesis	-0.8$^{(1)}$	0.038$^{(a)}$ 0.015$^{(b)}$	-1.05$^{(1)}$	0.077$^{(a)}$ 0.074$^{(b)}$	-1.08$^{(1)}$	0.142$^{(a)}$ 0.219$^{(b)}$
Ragni et al., 2009	-0.85$^{(1)}$ -0.78$^{(4)}$	0.062$^{(a)}$ 0.031$^{(b)}$ 0.031$^{(c)}$	-0.96$^{(1)}$ -0.87$^{(4)}$	0.092$^{(a)}$ 0.082$^{(b)}$ 0.088$^{(c)}$	-	-
XFOIL	-0.87$^{(3)}$	0.011$^{(d)}$	-0.96$^{(3)}$	0.027$^{(d)}$	-$^{(3)}$	-$^{(d)}$

The uncorrected aerodynamic coefficient results obtained in the present work are compared with the values reported in literature and from XFOIL simulations, for angles of attack $\alpha = -6°$ and $\alpha = -8°$. At $\alpha = -6°$, the lift coefficient determined by this thesis is in good agreement with the values reported by Ragni et al., 2009, for both PIV-based and pressure orifices-based methods. This thesis predicts a value of $c_l = -0.80^{(1)}$, while literature using the same method predicts a value of $c_l = -0.85^{(1)}$. The results of the pressure orifice method yields a value even closer to this thesis's results, $c_l = -0.78^{(4)}$, with all differences remaining modest. For comparison, `XFOIL` is not significantly far off, predicting $c_l = -0.87^{(3)}$. At $\alpha = -8°$, this thesis predicts a value of $c_l = -1.05^{(1)}$, while literature using the same method predicts a value of $c_l = -0.96^{(1)}$ and the pressure orifice method yields a value of $c_l = -0.87^{(4)}$. A slightly higher difference between sources is observed, but these are still considered to be in good agreement. For comparison, `XFOIL` is also close, predicting $c_l = -0.96^{(3)}$.

For both $\alpha = -6°$ and $\alpha = -8°$, the drag coefficient determined by this thesis shows a noticeable under-prediction from the values reported by Ragni et al., 2009, which, similar to this thesis, also reports values based on two PIV-based methods. Despite the same methods used, noticeable differences are observed: for $\alpha = -6°$, the drag coefficients from the thesis ($c_d = 0.038^{(a)}$ and $0.015^{(b)}$) are both lower than the value from literature ($c_d = 0.062^{(a)}$ and $0.031^{(b)}$) by a factor ~2. When comparing the thesis results to the validation results provided by the wake-rake, $c_d = 0.031^{(c)}$, it is clear that there is a significant deviation. At $\alpha = -8°$ this work predicts $c_d = 0.077^{(a)}$ and $0.074^{(b)}$, and compares once again to values reported in literature $c_d = 0.092^{(a)}$ and $0.082^{(b)}$. The PIV-wake-based drag values, which is the preferred method to report drag, show good agreement. When comparing the thesis results to the validation results provided by the wake-rake, $c_d = 0.088^{(c)}$, it is clear that there is a good agreement with modest deviation. For comparison, the drag coefficient at both angles of attack show significant variation from the validation results, highlighting its limitations.

The reference data from the AGARD AR-138 database is also considered to verify the aerodynamic load calculation. The experiments were conducted in similar Mach and Reynolds number conditions. The results are documented in Table 5.2. All force coefficients are corrected for blockage effects to achieve a valid comparison. The corrected values reported by Ragni et al., 2009 are also included for comparison, as they feature a similar simple model and wake blockage correction procedures.

Table 5.2: Comparison of lift and drag coefficients for the NACA 0012 airfoil at Mach 0.6. [1] Momentum integral (PIV-based). [2] Load Balance measurement. [3] Simulation (Panel code based). [4] Pressure orifices. [a] Momentum integral (PIV-based). [b] Wake deficit (PIV-based). [c] Wake deficit (Wake rake-based). [d] Simulation (Panel code based).

Source	$\alpha = -6^\circ$		$\alpha = -8^\circ$		$\alpha = -10^\circ$	
	c_l	c_d	c_l	c_d	c_l	c_d
Thesis	-0.75[1]	0.035 [a] 0.014[b]	-0.96[1]	0.071[a] 0.068[b]	-1.00[1]	0.130[a] 0.200[b]
Ragni et al., 2009	-0.78[1] -0.71[4]	0.043[a] 0.028[b] 0.028[c]	-0.87[1] -0.79[4]	-[a] 0.072[b] 0.078[c]	-	-
AGARD AR-138	-0.65	0.03	-0.77	-	-	-

At -6°, the corrected lift coefficient of this thesis shows a modest deviation from the AGARD prediction. Once again, the drag coefficient is almost a factor of 2 less than sources from the literature. At -8°, the lift coefficient shows a greater deviation from the AGARD prediction, and no data is unfortunately documented for the drag coefficient.

So far, a descriptive discussion on the results for the aerodynamic coefficients has been provided. To assess the significance of the discrepancy between the results of this thesis and those of the literature, an external uncertainty assessment is carried out on the uncorrected lift and drag coefficients. The variability of the aerodynamic coefficients of this thesis is estimated by varying the contour height used to calculate the lift, and the wake $x-$location to calculate the drag, as described in Table 4.3 and Table 4.4. The results are shown in Table 5.3.

Table 5.3: Sensitivity of the estimated uncorrected lift and drag coefficients to changes in contour/ wake integral definitions according to Table 4.3 and Table 4.4

α	M_∞	$c_{l,1}$	$c_{l,2}$	$c_{l,3}$	$c_{l,4}$	$c_{l,5}$	$c_{d,1}$	$c_{d,2}$	$c_{d,3}$	$c_{d,4}$	$c_{d,5}$	$c_{d,6}$
-6	0.6	-0.79	-0.79	-0.80	-0.81	-0.80	0.014	0.014	0.014	0.014	0.015	0.014
-8	0.6	-1.01	-1.02	-1.03	-1.04	-1.04	0.073	0.070	0.067	0.061	0.063	0.064
-10	0.6	-0.97	-1.00	-1.03	-1.07	-1.06	0.206	0.201	0.196	0.175	0.173	0.186

Based on a conservative estimate of the variability of the lift coefficient, defined as the standard deviation of the variations when varying the contour definition, these are estimated to be of the order $\pm$0.008 for $\alpha = -6^\circ$, $\pm$0.014 for $\alpha = -8^\circ$ and $\pm$0.042 for $\alpha = -10^\circ$. For the drag coefficient, the variability is estimated to be of the order $\pm$0.001 for $\alpha = -6^\circ$, $\pm$0.005 for $\alpha = -8^\circ$, and $\pm$0.014 for $\alpha = -10^\circ$. Recalling the uncertainty of the results from Ragni et al., 2009, this was approximately $\pm$0.02 for the lift coefficient and $\pm$0.002 for the drag coefficient. For this thesis's results, the uncertainty estimate provided by Ragni et al., 2009 is adopted for the results whose present estimated uncertainty falls below it.

Under these considerations, the estimated lift at $\alpha = -6^\circ$ falls closely around the uncertainty of the results from Ragni et al., 2009, and both differ modestly from the AGARD results. On the other hand, the drag coefficient discrepancy between this thesis's results and the literature fall significantly beyond the estimated uncertainty of the results. For $\alpha = -8^\circ$, the results of this thesis are slightly above the uncertainty of the results of Ragni et al., 2009, and considerably above the results from AGARD. Here, the drag discrepancy falls close within the uncertainty estimate from the results in the literature. Thus, the aerodynamic loads have decent agreement with the results in the literature, applying a similar methodology. Nevertheless, there is a non-negligible discrepancy between these. Based on these findings, an analysis of the aerodynamic load trends for the FFA-W3-211 airfoil, across different α, M_∞ test conditions, is valuable when the observed loading trends are sufficiently distinguishable from their estimated uncertainty.

Given the slight different test conditions and methodologies used to extract the aerodynamic loads, a discrepancy between the thesis results and the results from the AGARD data is to be expected. More interesting, is the non-negligible difference between the results of Ragni et al., 2009, which employed the same methodology. Despite conducting a thorough investigation, the exact source of the discrepancy, especially for the drag coefficient at $\alpha = -6°$, remains unknown. For this, some factors which may have had a significant contribution in the discrepancies observed are listed. These are propagated through intermediate variables: from the velocity data to the pressure determination, and ultimately to the aerodynamic load determination.

- **Limited accuracy for angle of attack setting**
  Due to wind tunnel vibrations, the use of a digital inclinometer introduces a mismatch between the angle of attack for nominal and inverted FOV experiments. By inferring the angle from the calibration images, under the assumption that the camera and wind tunnel walls are aligned, it was found that the AoA mismatch between the inverted and nominal runs can be as low as 0.1° and up to 0.7° degrees. For the NACA 0012 experiments, this mismatch was in the order of 0.6°, and while it is not necessarily the absolute mismatch, it provides a indication that the nominal and inverted FOVs might capture slightly different conditions. The differences have been noticeable in the velocity field within overlapping region of the nominal and inverted FOVs, located at the TE of the airfoil. The effects of an angle mismatch between nominal and invited FOVs have not been assessed in this thesis, but may surely be a source of discrepancy through the velocity field.
- **Translational and rotational mismatch between FOVs merging procedures**
  In addition to the mismatch in angle of attack between nominal and inverted runs, all FOV data is expressed in the same coordinate system by assuming only a translation of the different grids. This is only valid if the camera is perfectly aligned with the wind tunnel. As a result, any rotational offset present due to the limited AoA accuracy setting or alignment of the camera with respect to the wind tunnel is not accounted for during calibration and merging procedures. These effects translate into an uncertainty in the spatial location at which the velocity is actually measured at. In the thesis, movements along the x and y direction in the flow field are considered as movements along the first and second dimensions of the grid. With significant rotational offsets, movements along the first and second dimensions of the grid might not accurately correspond to movements along the x and y directions,
- **Sensitivity of load determination method**
  Despite the same methodology and similar experimental setup, there are several choices to make, including the formulation used to determine the pressure gradient, the inclusion of Reynolds stresses, the inclusion of viscous terms, the region of integration, and the integration scheme used. A variation of these factors could not replicate the results from the literature, suggesting the discrepancies observed are more likely related to the velocity field. For the relatively narrow wake generated at $\alpha = -6°$, the drag coefficient estimate is likely more sensitive to errors in the velocity field as well as in grid resolution. In addition to that, the results of Ragni et al., 2009 are better able to resolve the wake deficit through a dedicated FOV with a grid spacing of 0.26mm, compared to the present work with a grid spacing around 0.7mm.

In the presence of a narrow wake such as the one for $\alpha = -6°$, and compared to the wider wakes for steeper angles of attack (See Figure C.3 in Appendix C.), it is suggested that the methodology used to determine the drag coefficient is largely sensitive to the aforementioned errors in the velocity field and limited grid spacing, which propagate into the reconstructed pressure field.

Having conducted the verification of the pressure reconstruction and aerodynamic loading methodology, and acknowledging the modest deviations from results provided in the literature, it is worth mentioning that the results remains in decent agreement and with deviations in the order of what may be expected Ragni et al., 2009. The discrepancy between the uncorrected lift coefficient from this thesis and the pressure orifice data indicate a level of 3% at best and 20% at most. Assuming the result for the drag coefficient at $\alpha = -6°$ is not representative of the correct implementation of the pressure reconstruction and aerodynamic load determination methodologies, the error in the drag estimation is also of the order of 15%. Moving forward into the analysis for the FFA-W3-211 airfoil model, the analysis of aerodynamic loads must also consider their uncertainty, with the aim being to identify significant trends across the test space, rather than focusing on the individual force coefficients themselves.

5.2. Instantaneous flow feature characterization

From here onward, all results discussed are from the experiments conducted on the FFA-W3-211 airfoil model. This section aims to qualitatively describe flow features and their development across the test conditions, highlighting the effects of compressibility across different angles of attack.

5.2.1. Shock Waves, boundary Layer interactions, and separation

Shock waves have been confirmed to be present in various testing conditions, while a shear layer originating around the mid-chord section and extending past the TE of the airfoil has been identified in all of them, independent of shock formation. Below, Figure 5.2 presents snapshots taken during the Schlieren campaign for the selected AoAs and Mach numbers, which illustrate the characteristic flow field features and trends observed across tested conditions.

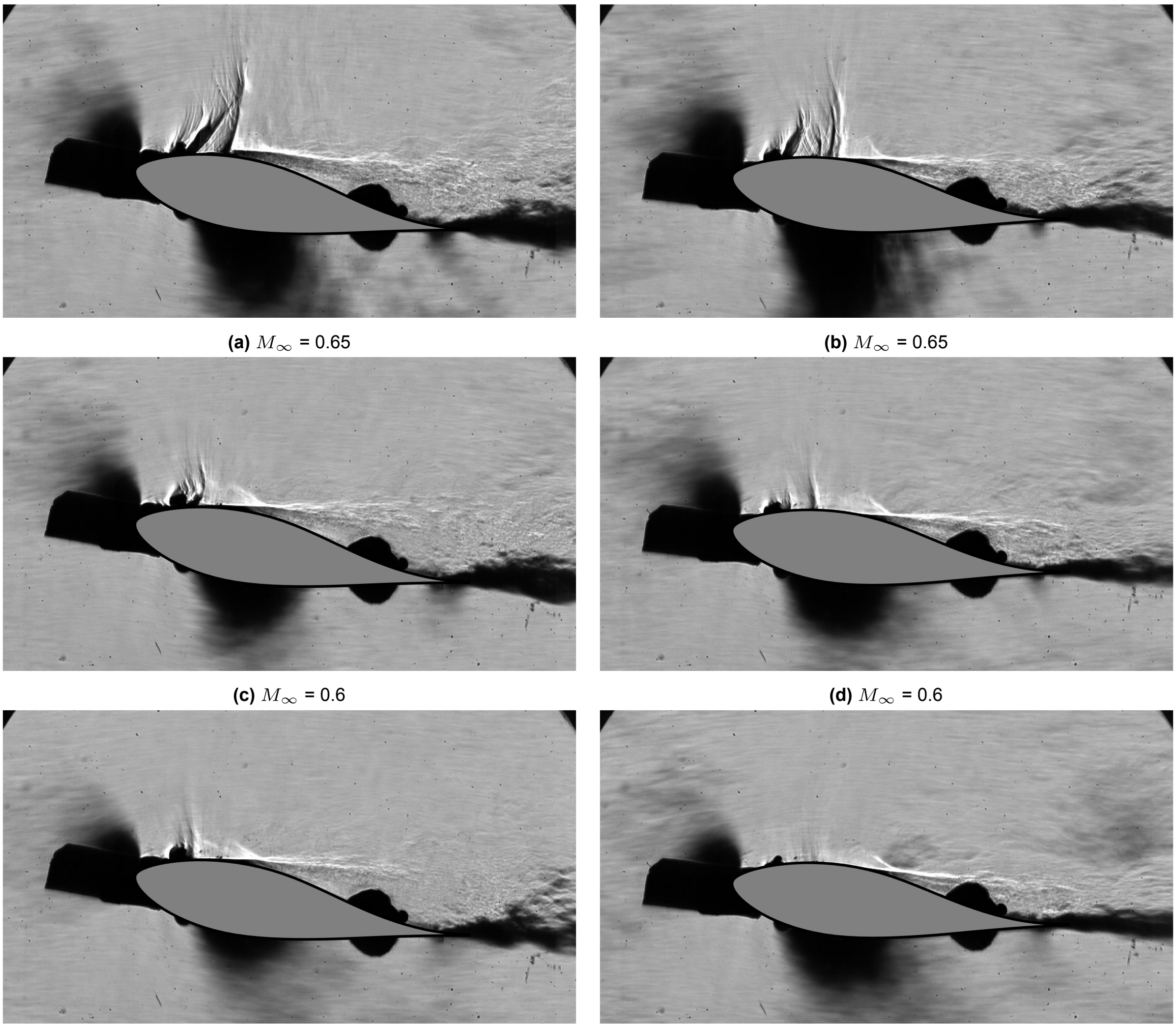

(a) M_∞ = 0.65 **(b)** M_∞ = 0.65

(c) M_∞ = 0.6 **(d)** M_∞ = 0.6

(e) M_∞ = 0.55 **(f)** M_∞ = 0.55

Figure 5.2: Schlieren images for cases at $\alpha = -10°$ (left) and $\alpha = -6°$ (right). Mach number increases from 0.5 (bottom row) to 0.65 (top row).

Further quantitative analysis may confirm the presence of a prematurely separated boundary layer resulting in trailing edge separation and determine its effect on the aerodynamic performance. For now, it is plausible to interpret the shear layer's origin as the boundary layer's point of separation, from which it follows that a significant contribution to the estimated drag will be from pressure drag. In line with the separation characterizations from Pearcey, 1955, all tested conditions closely resemble Type A separation, however, trailing edge separation is already present in the absence of shocks.

Analysing $\alpha = -10°$, it is evident that increasing the Mach number leads to stronger shock waves and reduced shock intermittency. The shear layer is observed to move upstream with increased Mach number, which is in line with the statement from Sørensen et al., 2018, as compressibility generally increases adverse pressure gradients, and thus the boundary layer becomes more susceptible to earlier separation. As mentioned in section 2.2, shock waves influence boundary layer detachment through the abrupt pressure jump and the associated increase in boundary layer thickness, which is likely occurring at the lower end of the tested Mach number range. However, in the case of a strong SWBLI, separation can also occur directly at the shock foot. This is observed to be the case at Mach 0.65, where the shear layer begins at the shock foot, suggesting a case with shock-stall. Similar trends are observed when increasing Mach number at $\alpha = -6°$, however, the data offers an opportunity to study the effects of compressibility at a distinct angle of attack.

Comparing the Schlieren snapshots for cases at $\alpha = -10°$ and $-6°$ in Figure 5.2, and taking into account all other tested conditions reveals that increasing absolute AoA results in the flow becoming more vulnerable to shock wave formation. This is in line with expectations, as steeper absolute AoAs lead to a greater flow acceleration over the suction surface. Again, an upstream movement of the shear layer origin is observed with increased absolute AoA, with this becoming a significant difference at greater Mach numbers, where shock waves become a great influence in boundary layer development. When both angles are compared at the highest Mach number, shock waves exhibit larger oscillations, and SWBLI strengthens as the absolute AoA increases. The consequence is a greater degree of unsteadiness in the detachment of the boundary layer at steeper AoAs.

The unsteady, oscillatory and intermittent nature of shock waves when increasing Mach number and absolute AoA only allows for a largely qualitative description of the average shock location across the test cases, based on Schlieren images. On average, shock waves and the point of separation were located more upstream for steeper AoA. This observation is supported by the same observations made by Sørensen et al., 2018. Increasing the Mach number leads, on average, to a more downstream position of the shock, while it appears to bring the point of separation forward. The later observation is in contrast to the findings of M. Vitulano et al., 2024 from URANS simulations on the same airfoil, for which separation was observed to move downstream with increases in the Mach number.

A later section offers a more quantitative analysis of the separation characteristics. For now, the discussion of shock waves is supported with more quantitative data derived from the PIV measurements, able to provide a measure for the percentage of frames with a shock wave P_{sho}, the mean chord-wise location of the shock wave $\overline{x/c}_{sho}$, and its corresponding standard deviation $\sigma_{\overline{x/c}_{sho}}$. These results are documented in Table 5.4. Due to the need for a shock detection algorithm, these results are indicative, aiming at evaluating significant trends observed across the test conditions.

Table 5.4: Percentage of frames with a detected shock, P_{sho}, mean non-dimensional shock location, $\overline{x/c}_{sho}$, and its corresponding standard deviation, $\sigma_{\overline{x/c}_{sho}}$, for all cases.

AoA [°]	M_∞ [-]	P_{sho} [%]	$\overline{x/c}_{sho}$ [-]	$\sigma_{\overline{x/c}_{sho}}$
-4	0.5	0	-	-
-4	0.55	0	-	-
-4	0.6	0	-	-
-6	0.5	0	-	-
-6	0.55	0	-	-
-6	0.6	0.2	0.28	0.0295
-6	0.65	20	0.26	0.0455
-8	0.5	0	-	-
-8	0.55	0	-	-
-8	0.6	13	0.18	0.0284
-10	0.5	0	-	-
-10	0.55	1.5	0.16	0.0197
-10	0.6	40	0.18	0.0214
-10	0.65	61.7	0.24	0.0527
-11	0.5	0.1	0.16	0.0179
-11	0.55	0.9	0.16	0.0188
-11	0.6	24	0.16	0.0161

The PIV analysis on shock waves indicates a clear emergence of shock waves with increased Mach number and absolute AoA increases. The flow field at $\alpha = -6°$ is characterized by sufficiently prominent shock waves only at M_∞ = 0.65, with a total of $\sim$20.45% frames detecting a shock. In contrast, $\alpha = -10°$ is characterized by probability of $\sim$40% already at M_∞ = 0.6, growing to $\sim$61.675% at M_∞ = 0.65. Taking the results at M_∞ = 0.6, shock waves were, on average, positioned at a chord-wise location of $\overline{x/c}_{sho}$ = 28, 18, 18, 17%c for $\alpha = -6°, -8°, -10°, -11°$, supporting a subtle trend towards more upstream shocks with increased absolute AoAs. Analyzing the trends at $\alpha = -10°$, the average shock location shifts downstream from $x/c \approx$ 18% to 23%c, with an increase in Mach number from 0.6 to 0.65. The increased unsteadiness in shock wave location, as observed in Schlieren images, is reflected by the high standard deviation, $\sigma_{\overline{x/c}_{sho}}$, determined for higher Mach numbers. This measure of unsteadiness doubles from 0.0214 to 0.0527 at $\alpha = -10°$ as M_∞ increases from 0.6 to 0.65.

In addition to analysing shock wave characteristics and their development with increased Mach numbers under different test conditions, this helps identify cases most relevant to studying the effect of shock waves on the mean flow and aerodynamic loads. Four test conditions were chosen to summarise shock wave characteristics using a more informative probability density function for their location, illustrated in Figure 5.3.

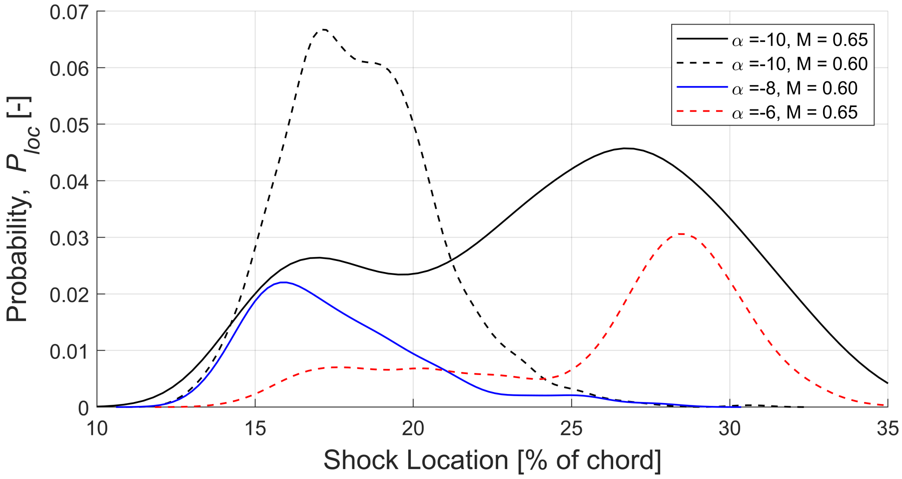

Figure 5.3: Probability density function of the non-dimensional shock wave location, x_{sho}, for cases where a shock develops. The distribution is scaled by the corresponding probability of detecting a shock, P_{sho}.

The most noticeable feature is the large spread of the data for all cases, especially in $\alpha = 0.65$ and $M_\infty = 0.65$. Under these conditions, the shock wave has a significant probability of being located anywhere from 13%c $\lesssim x/c \lesssim 32\%c$, corresponding to a variation up to ~20%c. From a physical point of view, shock wave unsteadiness is, to an extent, inevitable due to the natural unsteadiness arising from SWBLI, turbulent flow separation, and other factors. This case, however, offers an extreme and significant level of unsteadiness. Regarding the effect of compressibility on the flow field and aerodynamic performance, a dedicated analysis of the most extreme conditions observed can prove valuable. For this, the shock wave characteristics and observable time-resolved effects on the flow field at $\alpha = -10°$ and $M_\infty = 0.65$ will be discussed in more detail in the following section.

Visible effects of the transition strip

At high Mach numbers, particularly at larger AoA, a significant variation in image intensity is observed near the location of the strip. Schlieren's results presented in a later section reveal that sonic flow conditions are naturally attained at this location in free transition. For cases with shocks, the effect of the transition strip may be so strong that it locally triggers a small oblique shock wave with immediate reattachment of the boundary layer. This is not strong enough to return the flow to subsonic conditions, as is clear from the secondary, much stronger, normal shock waves.

5.2.2. A case study on transonic buffet

Consecutive Schlieren snapshots of the case at $\alpha = -10°$ at M_∞ = 0.65 reveal a clear transonic buffet cycle with oscillations at a narrow-band frequency. Interestingly, $\alpha = -6°$ did not develop an equally clear and consistent transonic buffet cycle, which could be expected to develop at a higher Mach number. All flow field characteristics are heavily influenced by the presence of a transonic buffet cycle, thus, these cases may, in an instantaneous sense, temporarily go against the general observed trends. Due to the extreme flow conditions observed, these cases will be revisited throughout the chapter.

As shown in Figure 5.4, instantaneous Schlieren snapshots for $\alpha = -10°$ at M = 0.65 reveal how flow field characteristics vary across the transonic buffet cycle. These observations are also similar for the case at $\alpha = -11°$ at M_∞ = 0.65. However, the focus lies on the former, for which PIV data is also available.

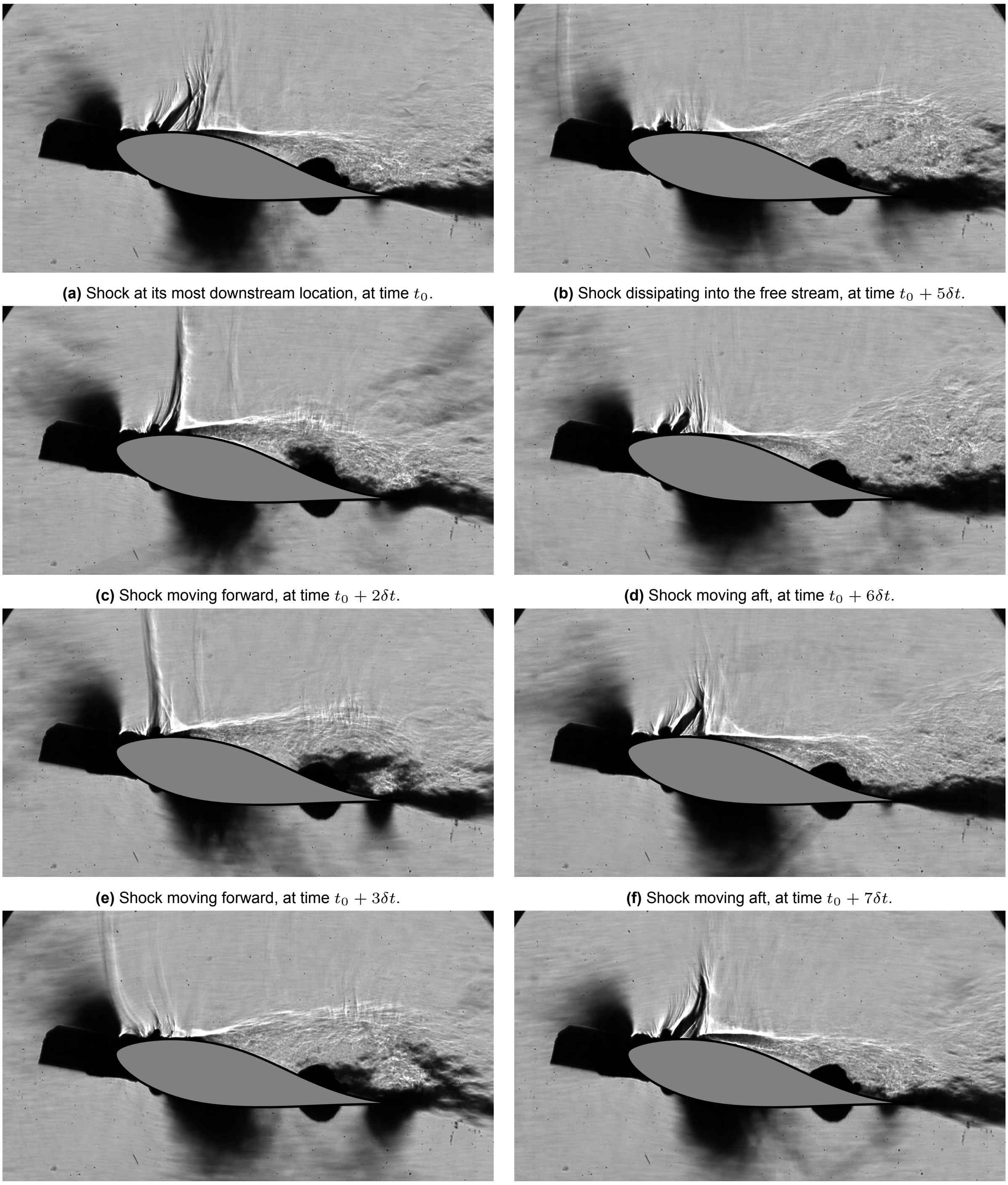

(a) Shock at its most downstream location, at time t_0.

(b) Shock dissipating into the free stream, at time $t_0 + 5\delta t$.

(c) Shock moving forward, at time $t_0 + 2\delta t$.

(d) Shock moving aft, at time $t_0 + 6\delta t$.

(e) Shock moving forward, at time $t_0 + 3\delta t$.

(f) Shock moving aft, at time $t_0 + 7\delta t$.

(g) Shock dissipating into the free stream, at time $t_0 + 4\delta t$.

(h) Shock at its downstream location, at time $t_0 + 8\delta t$.

Figure 5.4: Instantaneous Schlieren visualizations of the transonic buffet cycle, illustrating the periodic variation in shock strength as it oscillates, along with the cyclic expansion and contraction of the wake.

Given the non-zero incidence, this may be most comparatively classified as a type II transonic buffet on the suction side of the airfoil. As shown by the consecutive snapshots, the shock wave dynamics are near sinusoidal, initially strengthening and then weakening during its upstream movement, later propagating into the oncoming flow as a free shock wave. Qualitatively, this may be described as a combination of Type A and Type C buffet, supporting the observations on the development of this phenomena at high angles of attack made by Giannelis et al., 2018. Following the discussion, it is expected that the onset of transonic buffet characteristics at lower absolute AoAs with Mach numbers

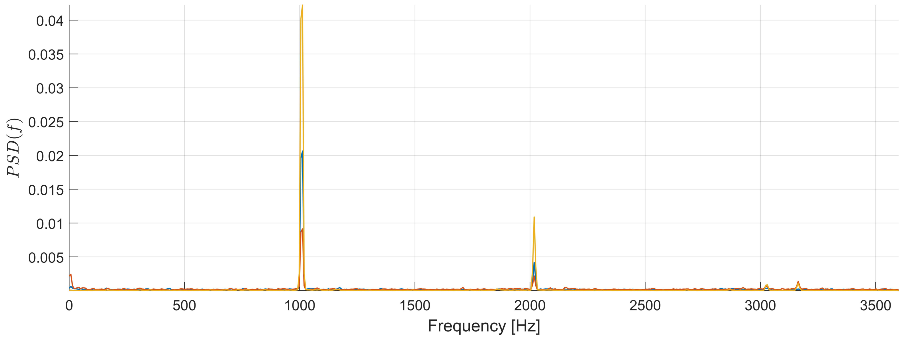

Figure 5.5: Power Spectral Density at the different windows considered, for the case at $\alpha = -10°$ at M = 0.65.

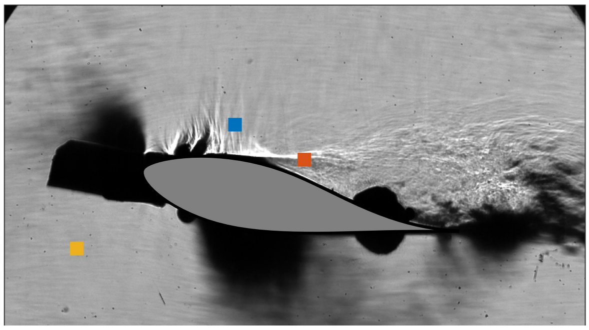

Figure 5.6: Windows considered for the spectral analysis.

greater than 0.65 may display behaviour more in line with a type A description.

Evidently, from Figure 5.4, an oscillating shock wave with varying strength has a significant influence on separation. Here, the fluctuating shear layer is an indication of a highly unsteady expansion and contraction of the wake and separation area. During an upstream movement of the shock, with flow separating at the shock foot, the wake region and separated area are greatest. With a weakened shock wave dissipating into the free stream as a free wave, the flow separation stabilises at a more downstream location. During its downstream movement, the shock wave strength increases, ultimately causing the point of separation to move upstream and eventually originate at the shock foot. Thus, the wake region and separation are greatest during the shock wave's upstream movement closer to the LE. These are the least during the shock's downstream movement close to its most aft location.

These observations warrant a quantitative analysis through phase-averaged flow field characteristics, as these may greatly differ from a mean flow analysis.

The spectral contents of the transonic buffet cycle were obtained from an analysis of the instantaneous Schlieren visualisations. The Power Spectral Density (PSD) is presented in Figure 5.5, with Figure 5.6 visualising the location of windows considered for this calculation.

It is immediately clear that the transonic buffet cycle has narrow-band frequency spectra centred around a frequency of 1010Hz. The non-dimensional frequency can then be calculated through the definition of the Strouhal number, shown earlier in Equation 2.28. For a frequency of 1010Hz, a freestream velocity of 212.37ms^{-1} (M_∞ = 0.65), and a chord length of 67mm, the Strouhal number is St = 0.324. This finding is significantly higher than the values observed in the literature for supercritical airfoils, which was in the order of 0.05-0.08.

Instantaneous PIV frames also confirm the presence of shock waves, and the significant variation in wake characteristics at its minimum and maximum position along the chord, as shown in Figure 5.7.

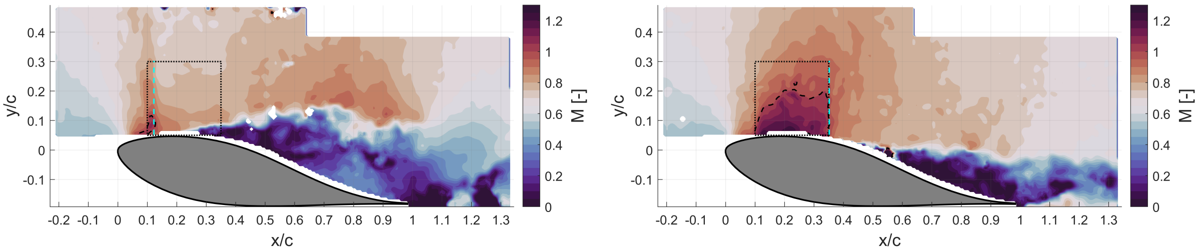

(a) Shock wave at its most upstream position $x/c \approx 11\%$

(b) Shock wave at its most upstream position $x/c \approx 35\%$

Figure 5.7: Detected shock waves during the transonic buffet cycle. The dotted box represents the shock detection window, and the dashed cyan line represents the x/c location.

Unfortunately, sensor cropping limits did not allow the PIV experiments to resolve this cycle. Nevertheless, the definition of phases for the transonic buffet cycle and instantaneous analysis of PIV frames will provide valuable insights into the phase-averaged mean flow developments for this case.

5.2.3. Compressibility in tripped vs. free-transition conditions

Despite not being able to quantify the effects of compressibility under free vs. fixed transition due to collecting quantitative data for experiments with fixed transition only, a brief qualitative comparison may provide insights into flow field developments. To this end, a qualitative comparison is made between the Schlieren results with free transition and with fixed transition at $x/c = 5\%$ on the suction side. It was first hypothesized that the addition of the strip would delay separation and shift the shock wave location aft, resulting in a weaker shock wave.

Oil flow visualizations

First, the efficacy of the transition strip and the development of the boundary layer are visualized in Figure 5.8.

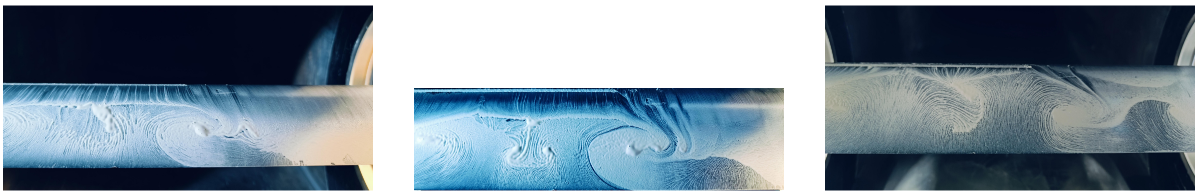

(a) α=-6°, M_∞ = 0.5 **(b)** α=-6°, M_∞ = 0.6 **(c)** α=-10°, M_∞ = 0.6

Figure 5.8: Oil flow visualization results for the development along the airfoil's suction side between a fixed transition at $x/c = 5\%$ (left span) and free-transition (right span) along the airfoil's suction side

The turbulent boundary layer after the transition strip induces a greater friction force near the leading edge region, for which more oil is displaced compared to the laminar one. This is an indication that the transition strip is successful. In the case of free transition, the flow seems to transition naturally at a significantly more downstream location. Although hard to visualize in the free transition case, both conditions develop flow separation. Given the Schlieren analysis in the previous section, this supports the suggestion that the visible shear layer corresponds to the point of separation along the suction side of the airfoil.

These observations are consistent with those drawn from instantaneous Schlieren snapshots for free-transition experiments, shown in Figure 5.9.

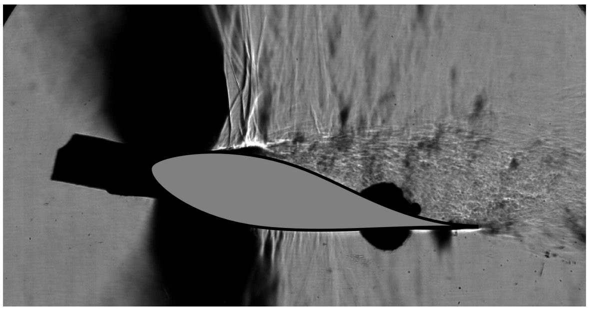

(a) M_∞ = 0.65

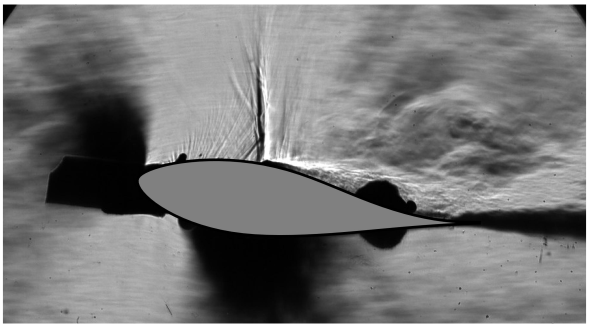

(b) M_∞ = 0.65

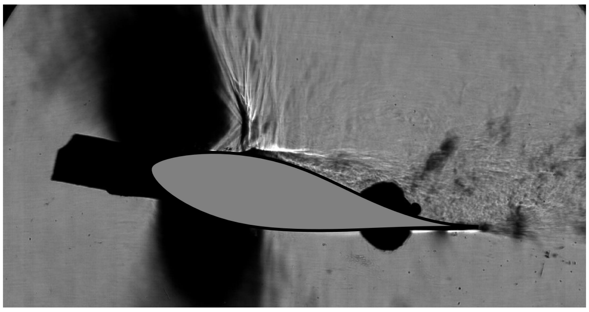

(c) M_∞ = 0.6

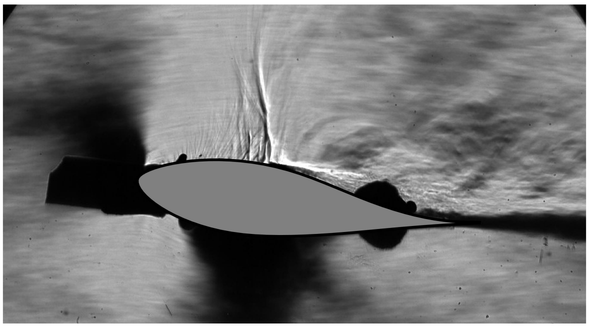

(d) M_∞ = 0.6

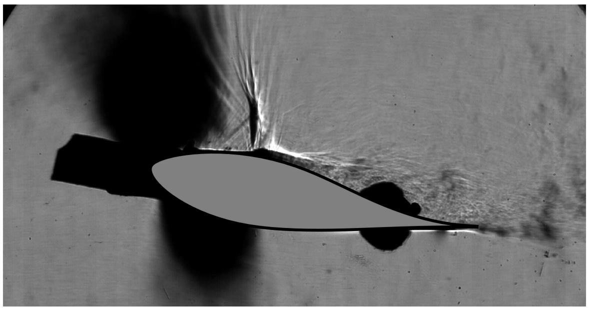

(e) M_∞ = 0.55

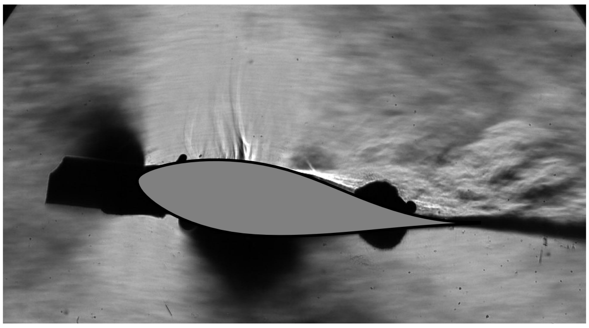

(f) M_∞ = 0.55

Figure 5.9: Schlieren images for cases at $\alpha = -10°$ (left) and $\alpha = -6°$ (right) with free-transition. Mach number increases from 0.55 (bottom row) to 0.65 (top row).

The trends with increasing Mach number and AoA steepness were also consistent with those described for fixed transition. Namely, greater Mach numbers and steepness of AoA result in the emergence of stronger and more oscillatory shock waves. Shock location and separation were, on average, also seen to move upstream with increased AoA steepness. All cases also developed trailing edge separation, even in the absence of shocks. How, then, do the flow field features compare for different boundary layer conditions?

Difference in shock wave characteristics

The most noticeable difference in flow features is the increased emergence and strength of shock waves for free transition. This observation is illustrated across the entire test domain by Figure 5.10, with cases like $\alpha = -4°$ at Mach 0.6.

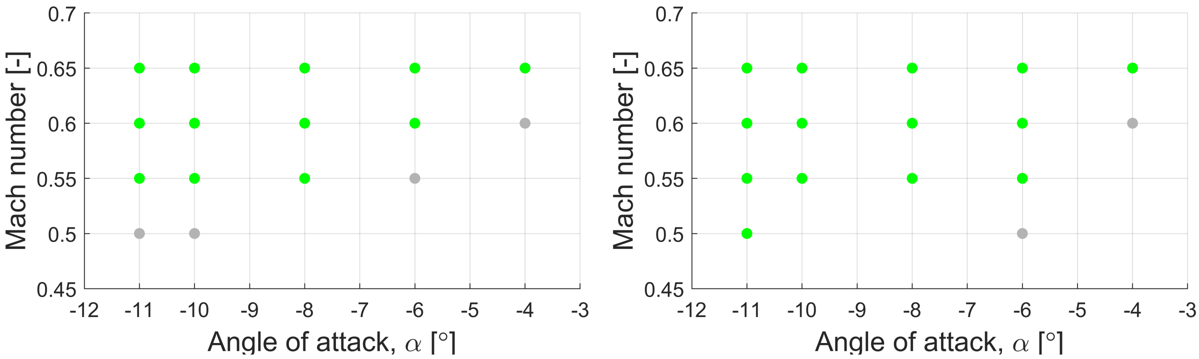

Figure 5.10: Identification of shock waves from Schlieren visualization in the (α, M) domain. Green markers indicate shock waves, while grey markers represent cases with no observed shock. Results are shown for fixed transition (left) and free transition (right).

It is important to emphasize that, under the same test conditions, detected shock waves in both fixed and free transition Schlieren images show significant differences in strength, average location, intermittency, dynamics, and boundary-layer interaction. On average, shock waves are further downstream in the case of free-transition and show more unstable oscillations characterized by a wider frequency spectrum. Given the strong density gradients at the transition strip, its impact on the flow field may have been greater than expected and, perhaps, wanted. Nevertheless, the results still allow for a meaningful discussion.

Comparing both free and fixed transition Schlieren snapshots, one can notice a clear λ structure indicative of a strong laminar SWBLI, extending far away from the airfoil surface. This structure is not so prominent for fixed transition, for which a strong interaction may occur, but with a much lesser-degree of shock smearing, as discussed in section 2.2.

Transonic buffet was also identified in free transition conditions at $\alpha = -10°$ and $-11°$ at M_∞ = 0.65. A strong three-dimensional development across the wind span is observed in free transition, characterized by the overlap of various shock waves as shown in Figure 5.9a, in contrast to the more two-dimensional buffet in fixed transition. The transition strip tends to stabilize the flow downstream, resulting in a more pronounced buffet cycle with a narrower frequency spectra. As transition takes places at the shock foot in the case of a laminar boundary layer, it is likely that this experiences high levels of unsteadiness, amplified by the already unsteady shock oscillations.

Difference in separation characteristics

The large differences in shock wave developments across free and fixed transition experiments make it difficult to draw general comparisons across all test conditions. Given the scope of this thesis, the observed effects of compressibility on separation in tripped and free-transition experiments are only described qualitatively through a case-by-case analysis of observable phenomena in Schlieren images. This approach highlights the need for a further dedicated investigation.

As observed in Figure 5.9, a strong laminar SWBLI with separation at the shock foot is present in the cases at $\alpha = -10°$. Compared with the fixed-transition experiments shown in Figure 5.2, the greater strength and more downstream location of the shock in free-transition induces an earlier separation of the boundary layer. At Mach 0.65, where the shock strength is comparable in strength, both feature separation at the foot.

A similarly strong laminar SWBLI structure is identified in the cases at $\alpha = -6°$. Again, it is observed that the more downstream location and greater strength of shocks induce separation at an earlier location compared to fixed-transition experiments. In contrast, the experiment at Mach 0.55 displays conditions in which the turbulent boundary layer detaches first.

Motivated by the previous observation, it can be shown that separation manifests in a significantly different manner at lower angles of attack. Figure 5.11 presents instantaneous Schlieren images at $\alpha = -4°$ at Mach 0.6 for tripped and free transition experiments. This test condition was chosen for its steady shear layer development, as then the observations hold in the mean sense.

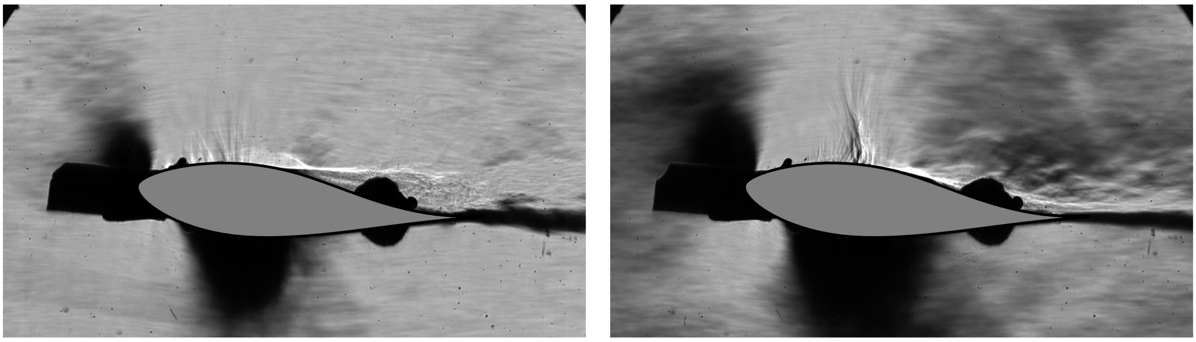

(a) Fixed transition at $x/c = 5\%$ **(b)** Free transition

Figure 5.11: Schlieren images for cases at $\alpha = -4°$ at Mach 0.6 for tripped and free transition experiments

Interestingly, the boundary layer detaches further downstream at these conditions in the case of free transition, even in the presence of a shock wave. Recalling the strong effect of the transition strip observed in Figure 5.2, the increased boundary layer thickness alone, without the presence of normal shock waves, may contribute to the reason why the turbulent boundary layer is highly susceptible to the adverse pressure gradients encountered due to the airfoil curvature. As discussed in literature, it is also plausible for the laminar boundary layer not to separate even in the presence of the shock wave, as the laminar SWBLI exhibit the largest degree of shock-smearing and thus reduced adverse pressure gradients. A combination of these effects may likely explain the non-intuitive earlier detachment of the turbulent boundary layer. A similar situation was observed at $\alpha = -11°$ at Mach 0.5. Unfortunately, the lack of Schlieren data for shallower angles of attack at low Mach numbers limits further observations that could support these claims.

5.3. Mean Flow field analysis

5.3.1. Velocity field and separation characteristics

The velocity fields u and v are the first flow field variables derived from the PIV data. These are visualised for the selected test conditions in Figure 5.12 and Figure 5.13, respectively.

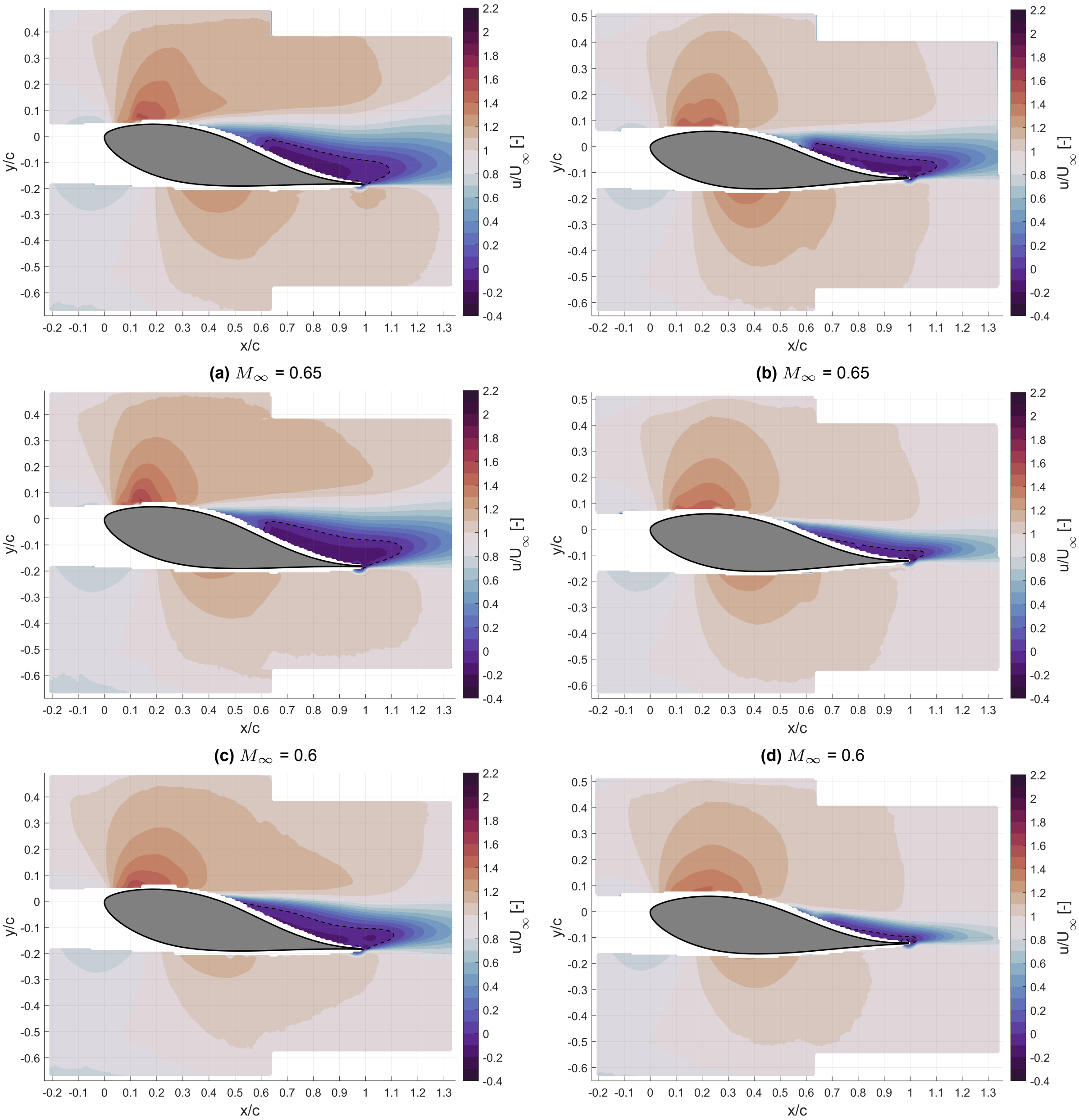

(a) M_∞ = 0.65 **(b)** M_∞ = 0.65

(c) M_∞ = 0.6 **(d)** M_∞ = 0.6

(e) M_∞ = 0.5 **(f)** M_∞ = 0.5

Figure 5.12: Mean non-dimensional freestream-aligned velocity field, u/U_∞, for cases at $\alpha = -10°$ (left) and $\alpha = -6°$ (right). Mach number increases from 0.5 (bottom row) to 0.65 (top row). The dashed line encloses the region where $u \leq 0$, indicating flow reversal.

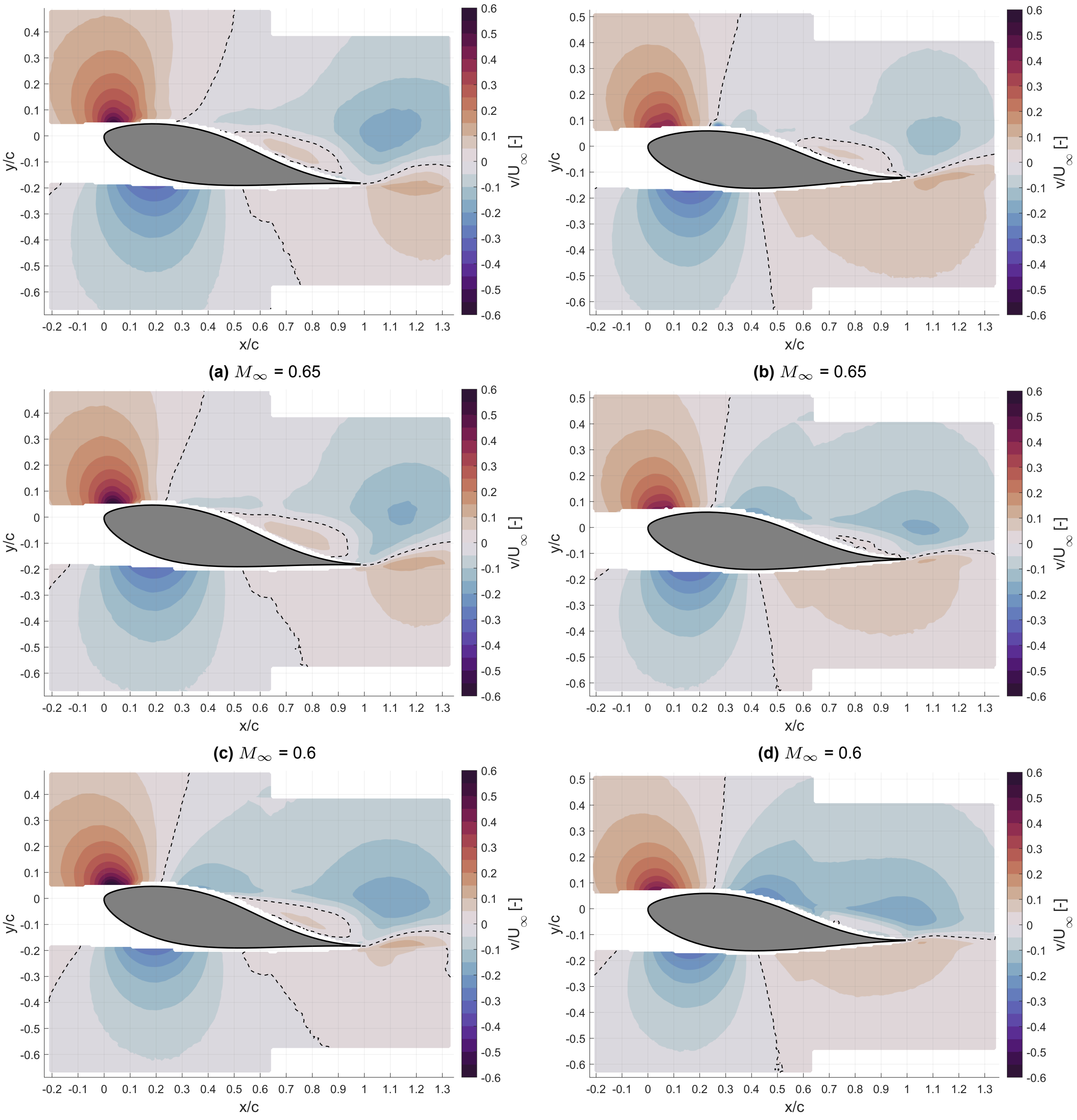

(a) M_∞ = 0.65 (b) M_∞ = 0.65 (c) M_∞ = 0.6 (d) M_∞ = 0.6 (e) M_∞ = 0.5 (f) M_∞ = 0.5

Figure 5.13: Mean non-dimensional vertical velocity field, v/U_∞, for cases at $\alpha = -10°$ (left) and $\alpha = -6°$ (right). Mach number increases from 0.5 (bottom row) to 0.65 (top row). The dashed contour corresponds to $v = 0$.

The mean flow over the suction side experiences rapid acceleration near the leading edge, reaching a maximum u velocity between $x/c \approx$10-15% for $\alpha = -10°$, and at a more downstream location $x/c \approx$ 20% for $\alpha = -6°$. Here, the flow experiences large deflections and accelerations due to the highly curved airfoil surface. Despite having a much lesser magnitude over the flow field, the mean vertical velocity component is highly localized close to the leading edge, reaching up to v/U_∞ = 60%. More importantly, this component is non-negligible in what would be considered the free stream at $x/c \approx$-10-20% for this FOV, easily reaching values up to v/U_∞=20%.

A significant u velocity deficit in the mean field initiating near the mid-chord section of the airfoil is observed. Unfortunately, the wide region with no velocity data around the airfoil surface limits an accurate identification of the velocity deficit's origin along the chord. Nevertheless, the velocity deficit in the mean field seems to move upstream with greater absolute AoAs and Mach numbers. An analysis of both mean velocity fields near the trailing edge confirms the presence of a separated boundary layer on the suction side of the airfoil, as suggested by the recirculation region ($u \leq 0$) in Figure 5.12, but also by the positive v velocity component.

For $-4° \leq \alpha \leq -8°$, raising the Mach number results in a broader and larger u velocity deficit. This growth is most prominent at $-6°$, where separation characteristics rapidly change with varying Mach numbers. At $\alpha = -11°$ and $-10°$, however, the mean flow field displays more irregular velocity deficit qualitative trends. To this end, a more quantitative analysis on the separation of the mean flow is performed. The extent to which the non-dimensional separated area of the mean flow, $A_{sep,mf}$, varies across all test conditions is documented in Table 5.5. The selected metric $u < 0$ provides an adequate measure of the actual recirculation area, however, this still serves as an indication rather than an exact measure. Furthermore, the white-space region imposes additional limitations on the calculated area. The case at $\alpha = -4°$ is highly sensitive to this, as separation is confined close to the surface.

Table 5.5: Non-dimensional separated area of the mean flow, $A_{sep,mf}$, mean non-dimensional separated area, $\bar{A}_{sep}$, and corresponding standard deviation, $\sigma_{\bar{A}_{sep}}$, for all test conditions. Areas non-dimensionalized by c^2.

AoA [°]	M_∞ [-]	$A_{sep,mf}[-]$	$\bar{A}_{sep}$ [-]	$\sigma_{\bar{A}_{sep}}$ [-]
-4	0.5	0.0016	0.0038	0.0023
-4	0.55	0.0017	0.0044	0.0023
-4	0.6	0.0008	0.0037	0.0026
-6	0.5	0.0049	0.0077	0.0044
-6	0.55	0.0061	0.0090	0.0046
-6	0.6	0.0101	0.0141	0.0078
-6	0.65	0.0279	0.0354	0.0171
-8	0.5	0.0165	0.0213	0.0100
-8	0.55	0.0176	0.0241	0.0109
-8	0.6	0.0156	0.0223	0.0114
-10	0.5	0.0311	0.0348	0.0145
-10	0.55	0.0291	0.0360	0.0197
-10	0.6	0.0425	0.0557	0.0342
-10	0.65	0.0355	0.0520	0.0228
-11	0.5	0.0376	0.0486	0.0242
-11	0.55	0.0135	0.0278	0.0142
-11	0.6	0.0220	0.0382	0.0177

Based on the measured non-dimensional separated area of the mean flow, $A_{sep,mf}$, it is clear that increases in absolute AoAs lead to greater separation of the mean flow. However, for most cases, there is an irregular relationship between the Mach number and the extent of the separated area, with $\alpha = -10°$ and $-11°$ displaying both a substantial decrease and increase in area with increasing Mach number. This is not too surprising, as recalling the Schlieren results, in conditions with supersonic flow, more pronounced shock waves, and highly unsteady flow fields, the mean flow field may provide only a limited representation of the highly unsteady nature of the flow. This is also observed for $\alpha = -4°$, although here separation of the mean flow is confined close to a region where no velocity data is available, hence, the calculated area for $\alpha = -4°$ may not be greatly representative. Only for $\alpha = -6°$ did the separated area of the mean flow increase consistently with increased Mach number, becoming five times as large from 0.0049 at M_∞ = 0.5 to 0.0279 at M_∞ = 0.65.

A more comprehensive understanding of separation characteristics is achieved by also analyzing the mean non-dimensional instantaneous separated area, $\bar{A}_{sep}$, and the corresponding standard deviation $\sigma_{\bar{A}_{sep}}$, also documented in Table 5.5. The measure $\bar{A}_{sep}$ provides a time-averaged measure of the separation region.

Based on the mean non-dimensional separation area, $\bar{A}_{sep}$, there is a more consistent trend towards increasing separation with increasing Mach number. For $\alpha = -6°$, this becomes ~360% larger from 0.0077 at M_∞ = 0.5 to 0.0354 at M_∞ = 0.65, with significant variations emerging for $M_\infty > 0.6$. For $\alpha = -10°$, separation is already prominent at low Mach numbers, yet grows by ~50% from 0.0348 at M_∞ = 0.5 to 0.0520 at M_∞ = 0.65, with significant variations emerging again for $M_\infty > 0.6$. Larger absolute AoA and Mach numbers result in a larger standard deviation, $\sigma_{\bar{A}_{sep}}$, suggesting higher flow unsteadiness. This is consistent with the unsteady shear layer development observed from Schlieren images. This analysis shows that increasing the Mach number has the most significant effect on separation at $\alpha = -6°$, while the greatest degrees of separation unsteadiness is achieved for $\alpha \geq -10$.

It is emphasized that the measure $\bar{A}_{sep}$ is greatly indicative, and its true value lies in the identification of significant variations of this measure across Mach number increases. That being said, the irregular variation of $A_{sep,mf}$ and $\bar{A}_{sep}$ coupled with high unsteadiness at $\alpha = -11°$ may suggest non-linear flow field developments at these conditions, but more importantly also question the robustness of the metric employed to measure separation. It is then useful to analyze the spatial probability distribution of the separated flow to support the discussion of the observed trends in a time-averaged sense. The spatial probability fields for separation are presented in Figure 5.14.

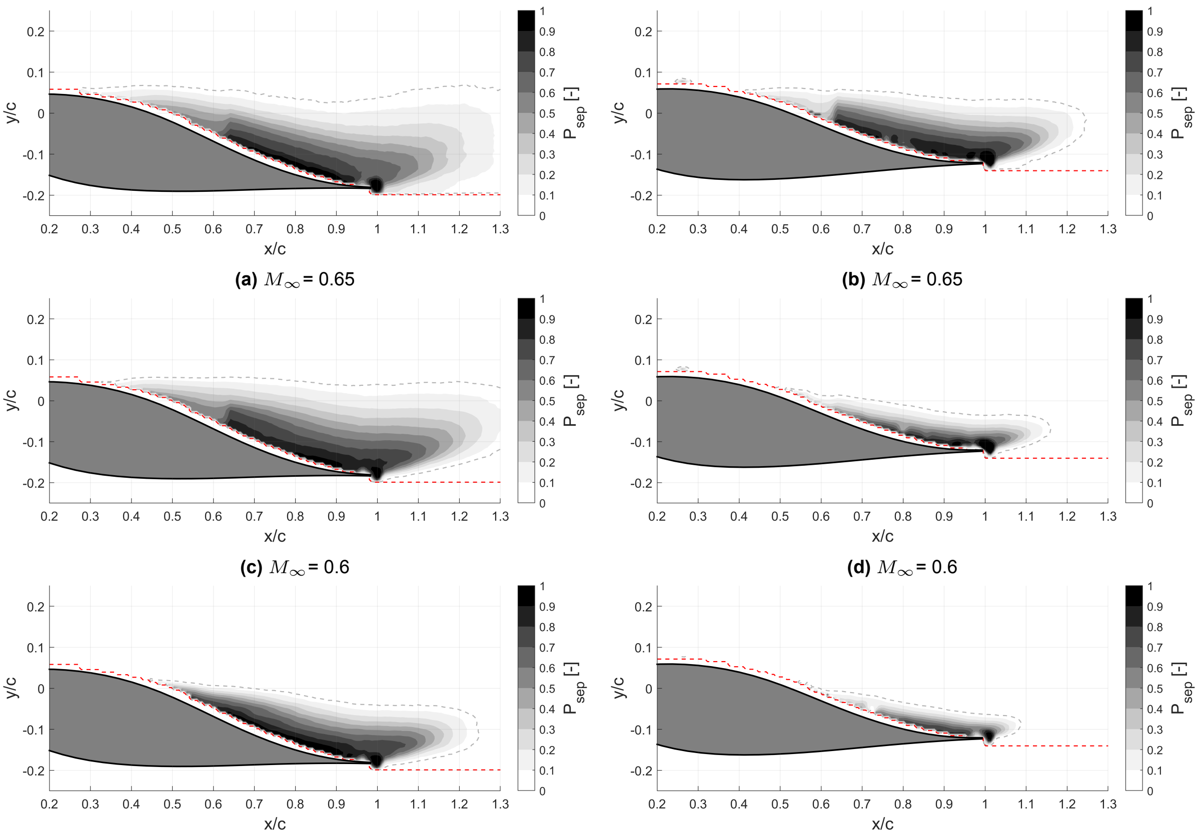

(a) M_∞ = 0.65 **(b)** M_∞ = 0.65

(c) M_∞ = 0.6 **(d)** M_∞ = 0.6

(e) M_∞ = 0.5 **(f)** M_∞ = 0.5

Figure 5.14: Spatial probability distribution of separated flow for cases at $\alpha = -10°$ (left) and $\alpha = -6°$ (right). Mach number increases from 0.5 (bottom row) to 0.65 (top row). The dashed contour represents a 5% probability. The unmasked region lies above the red line.

The spatial probability distribution of the separated area aligns well with the trend of increasing separation as the Mach number increases. This result highlights how separation characteristics vary drastically with increased Mach number for $\alpha = -6°$, while these are already prominent at $\alpha = -10°$ even at the lower Mach number. Once more, increased Mach numbers suggest an upstream movement of the separated region along the chord, consistent with what is observed from Schlieren images. In addition, the extent of the spatial separation probability downstream into the wake increases. Analyzing the region $P_{sep} \geq$ 50%, its extent downstream varies from $x/c \approx 1.03\%$ at M_∞ = 0.5 to $x/c \approx 1.12\%$ at M_∞ = 0.65 for $\alpha = -6°$. For $\alpha = -10°$, this extends to $x/c \approx 1.12\%$ for both M_∞ = 0.5 and M_∞ =

0.65, however, the case at M = 0.65 displays an overall greater region affected by separation. More interestingly, relative to $\alpha = -6°$, there is not a significant difference in the spatial probability of separation between the cases at M_∞ = 0.6 and M_∞ 0.65 for $\alpha = -10°$. It is believed that once a certain threshold defined by the AoA and Mach number is reached, separation grows and then becomes less sensitive to further variations in Mach number. As a result, these test conditions may capture the onset of the drag divergence phenomenon described previously in section 2.2. This will be assessed through a quantitative drag analysis.

5.3.2. Mach number field and supersonic region characteristics

Given the shock waves identified through Schlieren results, it is instructive to analyze the mean Mach number field to generate insights into the location, extent and intensity of compressibility and transonic flow features in the mean flow. The mean Mach number fields for the selected test conditions are shown in Figure 5.15.

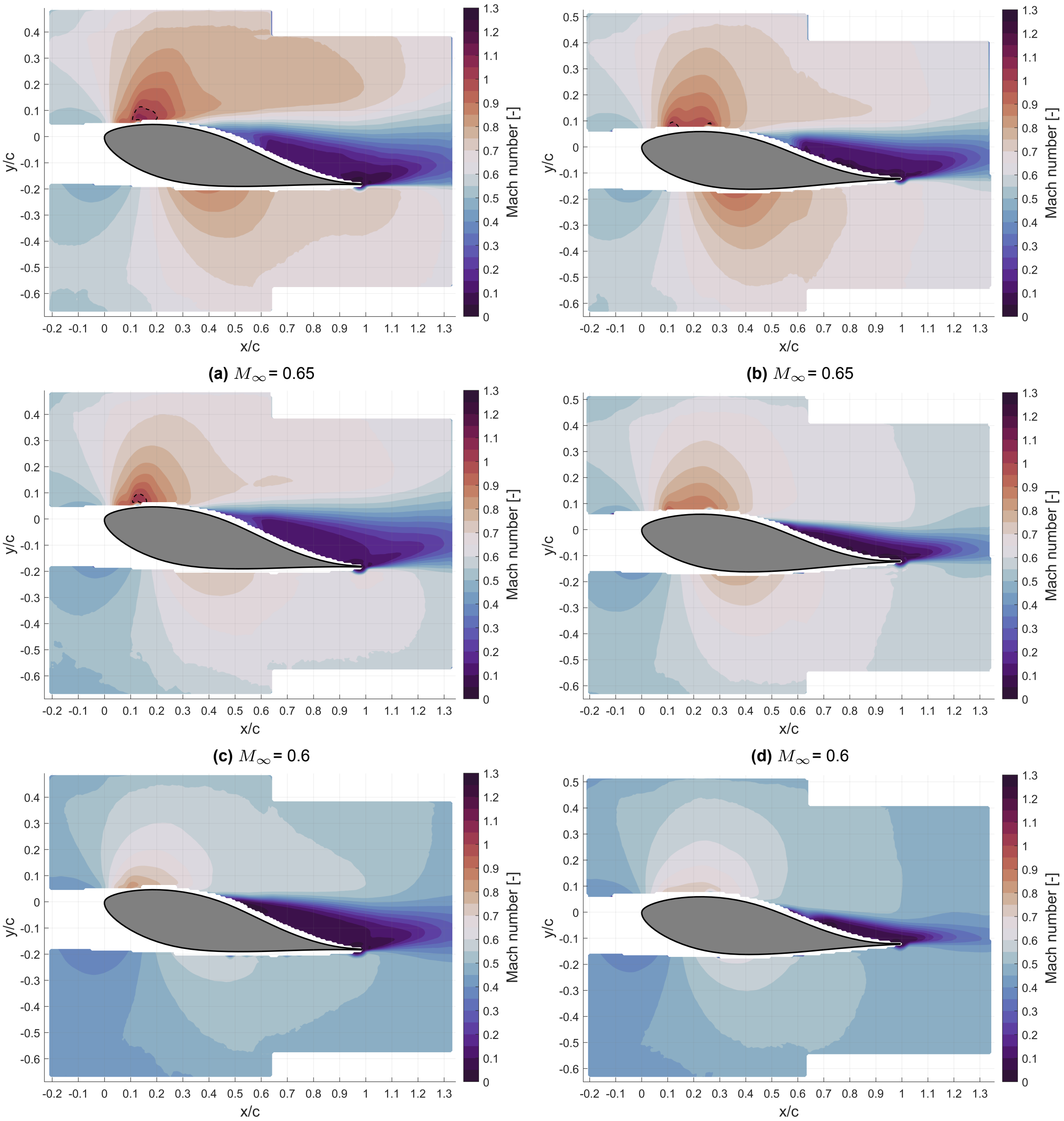

(a) M_∞ = 0.65 **(b)** M_∞ = 0.65

(c) M_∞ = 0.6 **(d)** M_∞ = 0.6

(e) M_∞ = 0.5 **(f)** M_∞ = 0.5

Figure 5.15: Mean Mach number field for cases at $\alpha = -10°$ (left) and $\alpha = -6°$ (right). Mach number increases from 0.5 (bottom row) to 0.65 (top row). The sonic line (M = 1) is indicated by the dashed contour.

As anticipated, the Mach number field achieves its highest values in the suction surface region near the leading edge of the airfoil at $x/c \approx$ 10-15%. The lowest Mach numbers are found in the wake region, where flow separation and reversal have been observed. A supersonic region in the mean flow develops at the highest free stream Mach numbers.

Growth of the supersonic region of the mean flow growth is observed with increased free stream Mach numbers. This is most prominent at higher absolute AoAs, evident from a comparison between $\alpha = -10°$ and $\alpha = -6°$. This behaviour is expected, as higher freestream Mach numbers lead to greater accelerations across the airfoil surface, encouraging its development into sonic conditions. In addition, greater angles of attack also result in greater accelerations near the leading edge due to the sharp flow deflections. Based on the available velocity data, the mean flow for $\alpha = -6°$ experiences a maximum local Mach number of $M \approx$ 0.7-0.75 at M_∞ = 0.5, reaching sonic conditions of $M \approx$ 1-1.05 at M_∞

= 0.65 over a small region spanning $\sim$ 5%c. For $\alpha = -10°$ a maximum local Mach number of $M \approx$ 0.8-0.85 was measured for M_∞ = 0.5, reaching sonic conditions $M \approx$ 1.05-1.1 over a region spanning $\sim$ 10%c. A more quantitative analysis is possible by examining the trends in instantaneous probability of developing supersonic flow P_{sup} and the size of the non-dimensional supersonic area of the mean flow, $A_{sup,mf}$, as presented in Table 5.6. Once again, it is emphasized that these results are indicative.

Table 5.6: Probability of supersonic flow, P_{sup}, non-dimensional supersonic area of the mean flow, $A_{sup,mf}$, mean non-dimensional supersonic area, $\bar{A}_{sup}$, and corresponding standard deviation, $\sigma_{\bar{A}_{sup}}$, for all test conditions. All areas are non-dimensional by c^2.

AoA [°]	M_∞ [-]	P_{sup} [%]	$A_{sup,mf}$ [-]	$\bar{A}_{sup}$ [-]	$\sigma_{\bar{A}_{sup}}$ [-]
-4	0.5	26.4	0.0000	0.0001	0.0001
-4	0.55	43.5	0.0000	0.0001	0.0002
-4	0.6	74.7	0.0000	0.0002	0.0004
-6	0.5	1.1	0.0000	0.0000	0.0000
-6	0.55	5.2	0.0000	0.0000	0.0000
-6	0.6	43	0.0000	0.0002	0.0003
-6	0.65	98.7	0.0007	0.0027	0.0020
-8	0.5	33.3	0.0000	0.0000	0.0001
-8	0.55	63.9	0.0000	0.0001	0.0002
-8	0.6	97.4	0.0009	0.0019	0.0018
-10	0.5	2.3	0.0000	0.0000	0.0000
-10	0.55	54	0.0000	0.0004	0.0006
-10	0.6	93.2	0.0014	0.0029	0.0026
-10	0.65	97.1	0.0037	0.0103	0.0092
-11	0.5	95.8	0.0005	0.0005	0.0003
-11	0.55	91.8	0.0003	0.0006	0.0005
-11	0.6	98.9	0.0022	0.0025	0.0012

The results and consistent trends across all angles of attack indicate that increasing the freestream Mach number raises the probability of supersonic flow development across the suction side of the airfoil. For $\alpha = -6°$, this probability grows from $\sim$ 1.05% to 98.73% from M_∞ = 0.5 to 0.65. For $\alpha = -10°$ this probability grows from $\sim$ 2.33% to 97.08% from M_∞ = 0.5 to 0.65.

For most cases with $M_\infty \leq 0.6$, despite the increasing probability of instantaneous supersonic flow, it remains insufficient to be reflected in the mean flow. For example, at $\alpha = -4°$, supersonic flow is detected in ~74.68% of frames at $M_\infty \leq 0.6$, yet an analysis of the supersonic area of the mean flow, $A_{sup,mf}$, indicates no presence. While P_{sup} might be a good preliminary measure of the supersonic characteristics of the flow field, a more complete picture is obtained by taking into account $A_{sup,mf}$, which suggest that these become significant only at larger absolute AoAs for the largest freestream Mach numbers. At M_∞ = 0.6, $A_{sup,mf}$ increases from 0 to 0.0009 to 0.0014 for $\alpha = -6°$, $-8°$ and $-10°$. At M_∞ = 0.65, $A_{sup,mf}$ increases to 0.007 and 0.0014 for $\alpha = -6°$, $-10°$. In addition to the increased emergence of supersonic flow with an increased freestream Mach number, the results also indicate an increased prominence of the supersonic region with increased absolute AoAs.

The analysis is complemented with an investigation on the mean non-dimensional supersonic area, $\bar{A}_{sup}$, and its corresponding standard deviation, $\sigma_{\bar{A}_{sup}}$, tabulated in Table 5.6. For $\alpha = -6°$, $\bar{A}_{sup}$ increases from 0 at M_∞ = 0.5, to 0.0027 at M_∞ = 0.65, becoming significant only at M_∞ = 0.65. For the same freestream Mach number range, $\alpha = -10°$ displays the highest measures observed, increasing from 0 to 0.0103, yet becoming already significant at M_∞ = 0.6. A consistent trend is once again observed, supporting the observations of the increased prominence of a supersonic area with increased absolute AoAs and Mach numbers. The relatively high standard deviation, $\sigma_{\bar{A}_{sup}}$, displayed at higher Mach numbers for $\alpha = -6°$ and $-10°$, and prior insights on highly unsteady instantaneous flow field features, motivate an analysis on the spatial probability distribution of supersonic flow. This is visualized in Figure 5.16.

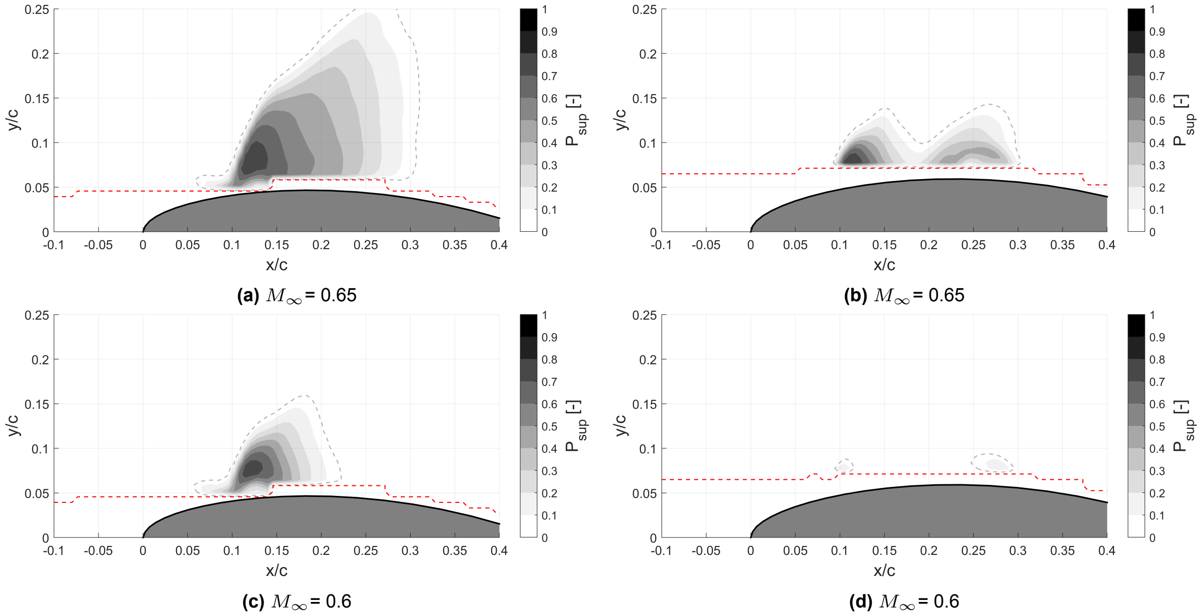

Figure 5.16: Spatial probability distribution of supersonic flow for cases at $\alpha = -10°$ (left) and $\alpha = -6°$ (right). The dashed contour represents a 5% probability. The unmasked region lies above the red line.

The results highlight a clear increase in the extent of the spatial probability distribution, with increasing freestream Mach number and absolute AoAs. Analyzing the region where $P_{sup} \geq 50\%$ for $\alpha = -10°$, the region extends between $x/c \approx$ 10-15% at M_∞ = 0.6, spanning 10-19% at M_∞ = 0.65. Furthermore, the shape of the region varies between the considered cases. At the highest Mach number, the supersonic flow distribution is relatively smooth for $\alpha = -6°$. In contrast, at $\alpha = -10°$, the contour lines become more vertically aligned. This suggests the presence of stronger normal shock waves, as the contours resemble the averaged shape of multiple instantaneous near-vertical discontinuities in the flow field. In addition to analysing the distribution's extent and shape, the distribution itself appears to be highly smeared across the supersonic region, supporting the observations of an unsteady supersonic region development that is driven by the oscillatory movement of shock waves across the chord.

So far, a combination of qualitative and quantitative analysis of Schlieren images, mean velocity fields and Mach number fields provide strong evidence that separation and supersonic flow features become increasingly unsteady with higher freestream Mach numbers. An analysis on the standard deviation of the mean Mach number field, presented in Figure 5.17, provides further evidence.

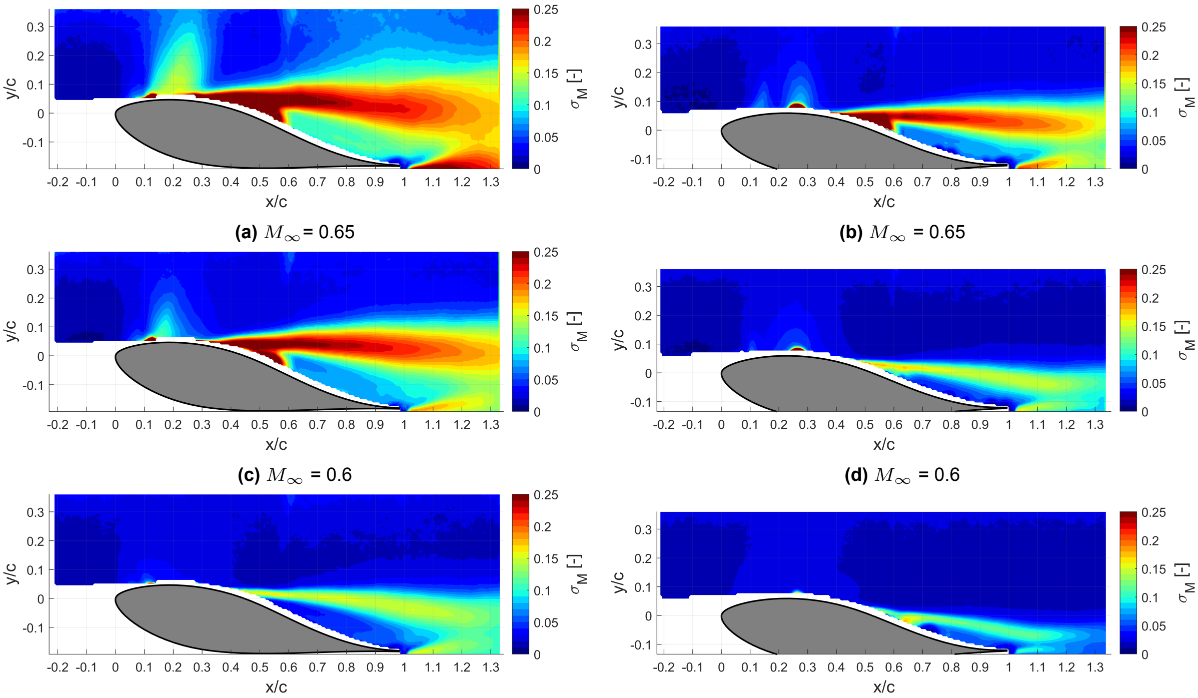

(a) M_∞ = 0.65 **(b)** M_∞ = 0.65

(c) M_∞ = 0.6 **(d)** M_∞ = 0.6

(e) M_∞ = 0.5 **(f)** M_∞ = 0.5

Figure 5.17: Standard deviation of the mean Mach number field for cases at $\alpha = -10°$ (left) and $\alpha = -6°$ (right). Mach number increases from 0.5 (bottom row) to 0.65 (top row).

For all conditions tested, a shear layer can be identified originating along the mid-chord region, corresponding to the horizontal zone with a relatively high standard deviation. This starts as a relatively thin zone which expands and diffuses towards the wake. Increasing the freestream Mach number or AoA thickens the zone affected by the shear layer and displays more pronounced unsteadiness, increasing its upstream extent. Relative to the standard deviation in the free stream, $\sigma_M \approx 0.015$, the shear layer at $\alpha = -6°$ is approximately 12 times greater at M_∞ = 0.5, easily raising over 17 times as large at M_∞ = 0.65. Furthermore, its origin along the chord is increasingly unsteady. At $\alpha = -10°$, for example, its origin is confined to a region spanning $\lesssim$ 10%c at M_∞ = 0.5, spanning larger distances $\approx$ 30%c at M_∞ = 0.65. Just below the shear layer, it is possible to observe a relatively low standard deviation corresponding to the recirculation region, which is again observed to grow and display greater unsteadiness with increased Mach numbers.

Of equal interest is the region where supersonic flow has been identified. Observations based on $\alpha = -10°$, where significant supersonic flow has been identified, support the findings of an increasingly unsteady shock wave development. Conditions at M_∞ = 0.5 display no unsteady developments, becoming noticeable at M_∞ = 0.55, but significant for M_∞ = 0.65, introducing a degree of unsteadiness 10 times larger than in the freestream within a region that is consistent with the descriptions based on Figure 5.16.

The previous sections have identified the growth and development of supersonic flow and separation characteristics with increased freestream Mach numbers and angles of attack. Separation is present in all tested conditions and has been observed to be most sensitive to an increase in the Mach number at $\alpha = -6°$. At higher absolute AoAs, separation is already prominent, adhering to the general Mach number trends observed and achieving significant growth already at lower freestream Mach numbers, after which a lesser degree of sensitivity and greater degrees of unsteadiness are observed. Supersonic flow becomes significant at high freestream Mach numbers and AoAs, with strong evidence of unsteady shock wave development. A later analysis of shock waves, focused on the transonic buffet cycle identified at $\alpha = -10°$, will provide valuable insights into their effect on the flow field and aerodynamic loading.

Now, the focus is shifted to subsection 5.3.3, which analyses the mean reconstructed pressure field.

Determining this field is an intermediate step essential for determining aerodynamic loads and crucial for connecting the observable mean flow field developments and their effects on mean aerodynamic loads.

5.3.3. Reconstructed mean pressure field

Defined as the force exerted per unit area by the random motion of the molecules in a fluid, the static pressure is a thermodynamic variable with a direct influence on the loading of an airfoil. The mean non-dimensional static pressure fields, as inferred from the velocity data and referred to as the pressure coefficient, c_p, are presented in Figure 5.18 for the selected cases.

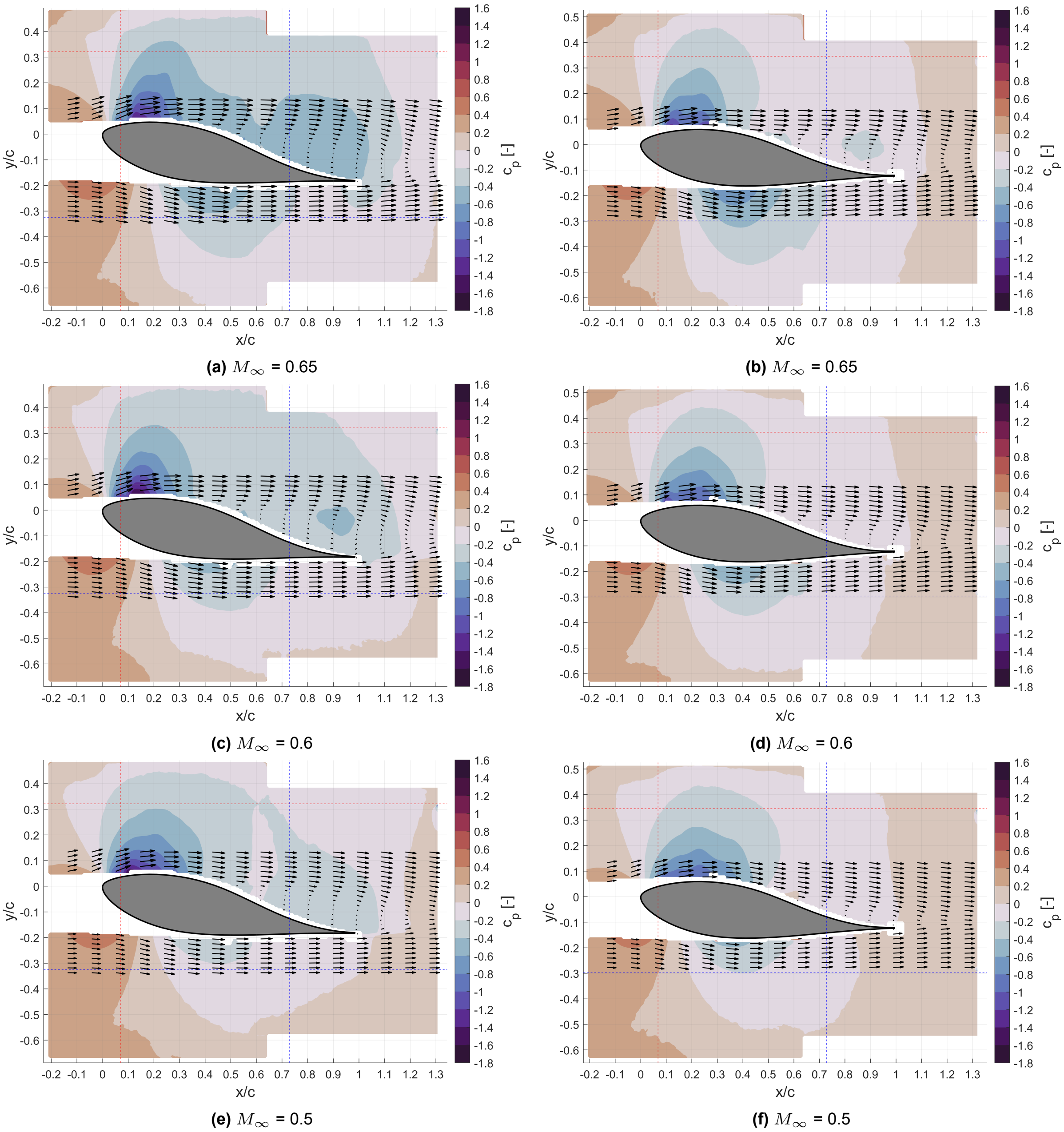

Figure 5.18: Mean pressure coefficient field for cases at $\alpha = -10°$ (left) and $\alpha = -6°$ (right). Mach number increases from 0.5 (bottom row) to 0.65 (top row). The arrows represent local velocity magnitude and flow direction.

Given the presence of separated flow and a growing recirculation region near the trailing edge of the airfoil, an attempt is made to visualize this region in Figure 5.18 by overlaying velocity vectors to indicate both direction and magnitude over a selected area. The recirculation region is clear from the significantly lower velocity magnitudes and flow reversal occurring near the airfoil surface, also extending into the wake.

For all cases, the mean c_p field contours near the recirculation region indicate a relatively constant pressure field development downstream of the suction peak. Recalling, the theoretical model used to reconstruct the mean pressure field gradient, this expresses a dependency on the mean velocity and velocity gradient field. Therefore, the nearly uniform pressure is consistent with what is expected from a mean flow region with low velocities and velocity gradients. From the observations of a growing separated region with increased Mach numbers and absolute AoAs, the pressure coefficient at the airfoil surface is expected to remain flatter over a larger extent with increased Mach numbers. A more quantitative analysis of the pressure coefficient along the surface of the airfoil may confirm this, but for now, a more qualitative discussion of the field is presented.

As anticipated from the mean velocity and Mach number fields, a suction peak is prominent near the leading edge of the airfoil where flow velocities are greatest. This is reflected in the lowest pressure coefficient values within the field. Due to the airfoil curvature and negative angle of attack, the pressure side also experiences considerable flow accelerations near the mid-chord- section, and the c_p is also reaches negative values. This reduces mean lift generation, as this is determined by the pressure difference between the suction and pressure surfaces, for which performance requires a larger pressure difference.

Having qualitatively analyzed the mean pressure field in the context of mean flow field developments, the next step is to examine the mean pressure coefficient distribution along the airfoil chord, as this directly determines the aerodynamic loads acting on the airfoil. This provides the foundation for a comprehensive analysis of aerodynamic load developments.

As described in chapter 4, the mean pressure coefficient field is linearly extrapolated by using data along the wall-normal direction at each point defining the airfoil surface within $10\% \leq x/c \leq 95\%$. Furthermore, the extrapolation on the pressure surface will only be considered beyond $x/c \geq 20\%$ due to the crude extrapolation over the shadow region for lower x/c. The result is an estimate of the pressure distribution at the airfoil surface. As this is once again largely indicative, the analysis aims to identify trends across the selected cases. The extrapolated pressure coefficient distribution along the airfoil surface for the selected cases is shown in Figure 5.19.

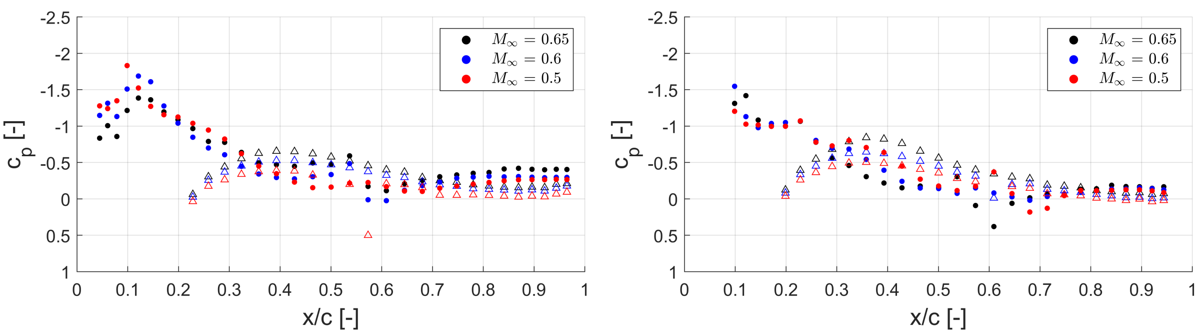

(a) α = $-10°$ **(b)** α = $-6°$

Figure 5.19: Mean pressure coefficient distribution for cases at $\alpha = -10°$ (left) and $\alpha = -6°$ (right). Marker colour differentiates freestream Mach numbers: 0.5 (red), 0.6 (blue), 0.65 (black). Filled circles represent the suction surface, while unfilled triangles denote the pressure surface.

First, an analysis of the development of the pressure coefficient field and its distribution along the airfoil for $\alpha = -6°$. Despite the lack of extrapolated data near the leading edge, a suction peak occurs around $x/c \approx 10 - 15\%$. There is no significant variation in the strength of the suction peak observed with increasing freestream Mach number, remaining within the range $-c_p = 1.5 - 2$. However, it is believed that higher freestream Mach numbers results in a stronger suction force at this AoA. An adverse pressure gradient is observed shortly after the suction peak, extending towards $x/c \approx 45\%$, and becoming stronger at increased freestream Mach numbers. All distributions, although at a different rate, gradually flatten to a nearly uniform pressure toward the trailing edge due to flow separation. Due to stronger adverse pressure gradients at higher Mach numbers, the distribution achieves uniform conditions further upstream. Beyond $x/c \geq 75\%$, no significant developments can be observed in each distribution, with slightly more negative c_p achieved at higher Mach numbers. However, the difference in the uniform c_p between distributions is small. Analysing the distribution along the pressure surface, a significant portion extending from $30\% \lesssim x/c \lesssim 60\%$ experiences a negative c_p lower than in the suction surface. The pressure distribution on the pressure side is strongly affected by the freestream Mach number in this region, with higher Mach numbers leading to more negative values. The combination of stronger adverse pressure gradients on the suction surface and increased suction forces along the pressure side with an increase in freestream Mach number leads to the expansion of a region that negatively impacts lift generation. The mid-chord section effectively experiences a reduction in lift-generating efficiency as the Mach number increases. In contrast, the leading edge and trailing edge efficiency remain largely unchanged.

Following the discussion on $\alpha = -10°$, A more prominent suction peak is observed within $x/c = 10 - 20\%$. Here, a reduction in the suction strength is observed with increased angles of attack. The difference between distributions is significant, on the order of $\delta c_p \gtrsim$ 0.5 between M_∞ = 0.5 and 0.65. A stronger adverse pressure gradient relative to the one at $\alpha = -6°$ is observed, with a subtle indication in the extrapolated data that the pressure gradient becomes more favourable at higher Mach numbers. However, the limited resolution, the accuracy of pressure determination and extrapolation, and the short region before flattening and separation make any conclusions uncertain. Once again, the distribution on the suction surface gradually flattens to a uniform pressure towards the trailing edge but remains significantly higher than for $\alpha = -6°$, especially at the highest Mach number. The effect of the Mach number is now more significant towards the trailing edge, remaining at a more negative c_p. Looking at the pressure surface, reliable extrapolation data within $x/c \leq 20\%$ is unavailable due to the large shadow region, therefore, no definitive conclusions can be drawn regarding lift-generation capabilities. However, it is believed that increasing the Mach number leads to higher c_p values on the pressure surface, which, to an extent, may offset the effects due to a reduction in suction strength. Along the pressure surface within $30\% \lesssim x/c \lesssim 60\%$, the distribution is still largely influenced by the freestream Mach number, once again reaching negative values. The difference between the suction and pressure distribution is now significantly lower for $\alpha = -10°$ due to the increase in suction force over the suction surface. While this region still contributes negatively towards lift, its effect is lesser and is less sensitive to Mach number variations within the tested range. Similarly, the trailing edge is observed to be more efficient at producing lift due to the increase in suction force at $\alpha = -10°$ relative to $-6°$, as both angles feature near-identical pressure-side distributions in the region $x/c \geq 75\%$.

The previous sections have provided evidence of how the mean flow field characteristics and developments with increased Mach number manifest significantly differently at $\alpha = -10°$ and $-6°$. This has been achieved through an analysis of the separation region, supersonic region and mean pressure distribution along the airfoil. It is worth emphasizing that the discussed trends can be extended and applied to the other angles of attack tested, for which the selected cases have provided sufficiently contrasting conditions. The differences in how compressibility effects are manifested across the test conditions are expected to be reflected in the determination of mean aerodynamic loads, as will be discussed further in section 5.5.

Before discussing the mean aerodynamic loads, the prominence of shock waves, the distinct transonic buffet cycle, and the significant uncertainties in the supersonic and separation characteristics observed for $\alpha = -10°$ at $M_\infty = 0.65$ suggest the need for further flow field analysis. It is perhaps obvious, yet important, to investigate the extent to which the instantaneous flow field deviates from its time-averaged representation. Such an analysis could provide insights into the robustness and significance of the observed trends in the mean flow, particularly in the presence of highly unsteady flow conditions. section 5.4 aims to present a phase-averaged analysis focused on the flow field developments at $\alpha = -10°$ at $M_\infty = 0.65$, thus taking into account its temporal evolution throughout the transonic buffet cycle.

5.4. Phase-averaged analysis

Through an analysis of instantaneous Schlieren images, section 5.2 documented significant shock wave oscillations and the varying extent of separation throughout the transonic buffet cycle at $\alpha = -10°$ at $M_\infty = 0.65$. The approach outlined in chapter 4 was used to associate instantaneous PIV data with a specific phase of the buffet cycle, based on the instantaneous separation area and shock wave location. This section aims to describe the flow field development across the transonic buffet cycle phases, thus supporting an interpretation of the phase-averaged aerodynamic loading.

5.4.1. Phase distinction

The phases defined are repeated for convenience: (1) Shock at its most upstream position. (2) Shock during its downstream movement. (3) Shock at its most downstream position. (4) Shock during its upstream movement. (No shock) No shockwave detected. Through Schlieren images, the last phase is observed to most likely occur near the shockwave's most upstream position and the beginning of its downstream movement.

To distinguish between phases 2 and 4, the approach assumes that the shock wave location is correlated with the separation area, a concern validated by analyzing the joint Probability Density Function (PDF) between the shock wave location and the separated area, presented in Figure 5.20.

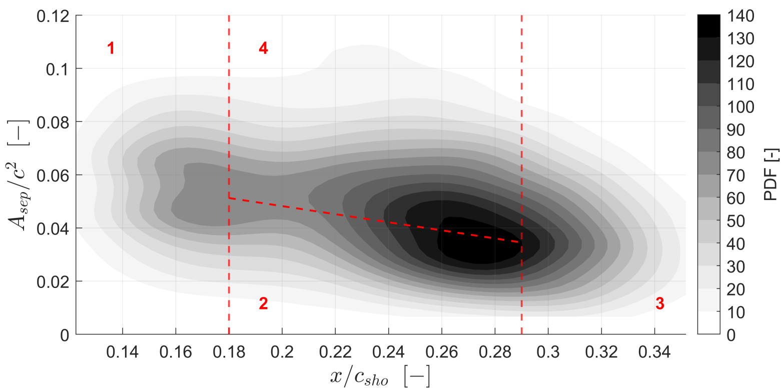

Figure 5.20: Joint Probability Density Function between shock wave location and separated area. for $\alpha = -10°$ at $M_\infty = 0.65$. Red dashed lines represent the distinction between the four different shock phases, identified through the red numering.

The joint PDF is characterized by a negative slope, confirming a negative, moderate correlation between the shock wave location and the extent of the separated area as observed through the Schlieren images. After careful consideration, this analysis resulted in the formal definition of the different phases of the transonic buffet cycle, shown in Table 5.7. In addition, the total frames attributed to each phase, n_{phase}, is included.

Table 5.7: Definition for the different phases of the transonic buffet cycle at $\alpha = -10°$, $M_\infty = 0.65$.

Phase	Shock Threshold	Separation Threshold	n_{phase}
No Shock	-	-	1533
1	$(x/c)_{sho} \leq 0.18$	-	441
2	$0.18 < (x/c)_{sho} \leq 0.29$	$A_{sep}/c^2 < f(x/c_{sho})$	619
3	$(x/c)_{sho} > 0.29$	-	501
4	$0.18 < (x/c)_{sho} \leq 0.29$	$A_{sep}/c^2 \geq f(x/c_{sho})$	906

To more accurately capture the correlation observed, the separation threshold was defined as

$$f((x/c)_{sho}) = -0.1520(x/c)_{sho} + 0.0786 \tag{5.1}$$

5.4.2. Supersonic and separation characteristics

Having accounted for the temporal development of the flow field through phase definitions, a quantitative analysis is carried out on the phase-averaged flow field features. The focus is now on a comparison between the supersonic and separation characteristics across the different phases. A summary of the supersonic and separated area characteristics is presented in Table 5.8. Measures are provided for the respective area of the phase-averaged flow,$A_{\ldots,ph}$, the mean area of the phase-averaged flow, $\overline{A}_{..,ph}$, and corresponding standard deviation, $\sigma_{\overline{A}_{..,ph}}$. The data for the time-averaged characteristics is also tabulated for comparison, under the label 'Mean flow'

The analysis is supplemented by the results for the phase-averaged Mach number field, shown in Figure 5.21, and by a study on the phase-averaged spatial probability distribution for the separated area and supersonic area, illustrated by Figure 5.22.

The following discussion may serve as confirmation that the phases were well-defined, as these demonstrate to be a good averaged representation of the instantaneous characteristics across the different stages of the transonic buffet cycle observed previously through the Schlieren images in Figure 5.4.

Table 5.8: Measures for separation and supersonic area across the different phases of the transonic buffet cycle at $\alpha = -6°$, $M_\infty = 0.65$.

Phase	$A_{sep,ph}$ [-]	$\overline{A}_{sep,ph}$ [-]	$\sigma_{\overline{A}_{sep,ph}}$	$A_{sup,ph}$ [-]	$\overline{A}_{sup,ph}$ [-]	$\sigma_{\overline{A}_{sup,ph}}$
Mean Flow	0.0355	0.0520	0.0228	0.0037	0.0103	0.0092
No Shock	0.0454	0.0616	0.0224	0.0000	0.0026	0.0032
1	0.0420	0.0550	0.0193	0.0026	0.0046	0.0023
2	0.0184	0.0289	0.0090	0.0122	0.0150	0.0057
3	0.0241	0.0358	0.0166	0.0235	0.0253	0.0068
4	0.0455	0.0613	0.0171	0.0118	0.0144	0.0058

For now, the following preliminary claims are made based solely on an interpretation of the Schlieren images inFigure 5.4. The supersonic area trends measured through $A_{sup,ph}$ and $\overline{A}_{sup,ph}$ consistently characterise phases 1 and 3 with the lowest and highest area, respectively. This is expected, as a downstream located shock features the longest extent of supersonic flow, and the contrary for phase 1. Phases 2 and 4 are characterized by a similar level, while the phase-average for PIV frames with no shocks display the lowest supersonic activity.

As expected, and partly by definition, the separation trends measured through $A_{sep,ph}$ and $\overline{A}_{sep,ph}$ both consistently characterize phases with an upstream shock position (1 and 4) with the highest separation area. separation is greatest during the shock waves' upstream movement, phase 4. Here, the shock wave is strong, with the point of separation being attached to the shock foot. Compared to phase 4, the slight reduction in the separated area at the shock wave's most upstream position, phase 1, may be a result of the downstream shift in the point of separation due to the loss in shock strength, weaker SWBLI, and lower adverse gradients. These, along with more claims, will be verified in a coming analysis. The summarised trends consistently characterise phases with a downstream shock position (2 and 3) with the lowest separated area. Compared to phase 2, the increased separated area at the shock waves' most downstream position, phase 3, is a result of the maximum shock strength and stronger SWBLI, which brings the point of separation upstream towards the shock foot.

Despite the fact that separation is likely to occur at the shock foot for both phase 3 & 4, the latter displays a greater separation area due to the more upstream point of separation. The separation at phase 2 is the lowest of all. Here, the shock wave regains strength, but the point of separation is most aft.

The measures for the separated area for PIV frames with no detected shock waves indicate a level in the order of phase 1 and 4. The measures for the supersonic area indicate a level similar to that of phase 1. These observations support the previous claims that this condition occurs near the shock's most upstream position, where the shock is weakest, yet previous phase developments have a significant influence on the wake.

With the definition of phases from the joint PDF in Figure 5.20, and the transonic buffet analysis through Schlieren images, it is already possible to anticipate the supersonic and separation characteristics for each phase. The next step is to present quantitative data to support the preliminary interpretations and claims. The discussion is complemented with the analysis of the PIV phase-averaged Mach number field, Figure 5.21, and the spatial distribution for separated and supersonic flow Figure 5.22. The phase-averaged Mach number fields provide a measure for shock wave strength, and intensity of the wake region, while the spatial distributions provide a measure for the extent of these characteristics. The trends for $A_{sep,ph}$ and $A_{sup,ph}$ can be readily visualized in Figure 5.21 by the areas enclosed by the cyan and black dashed lines, while Figure 5.22 provides representation for $\overline{A}_{sep,ph}$ and $\overline{A}_{sup,ph}$..

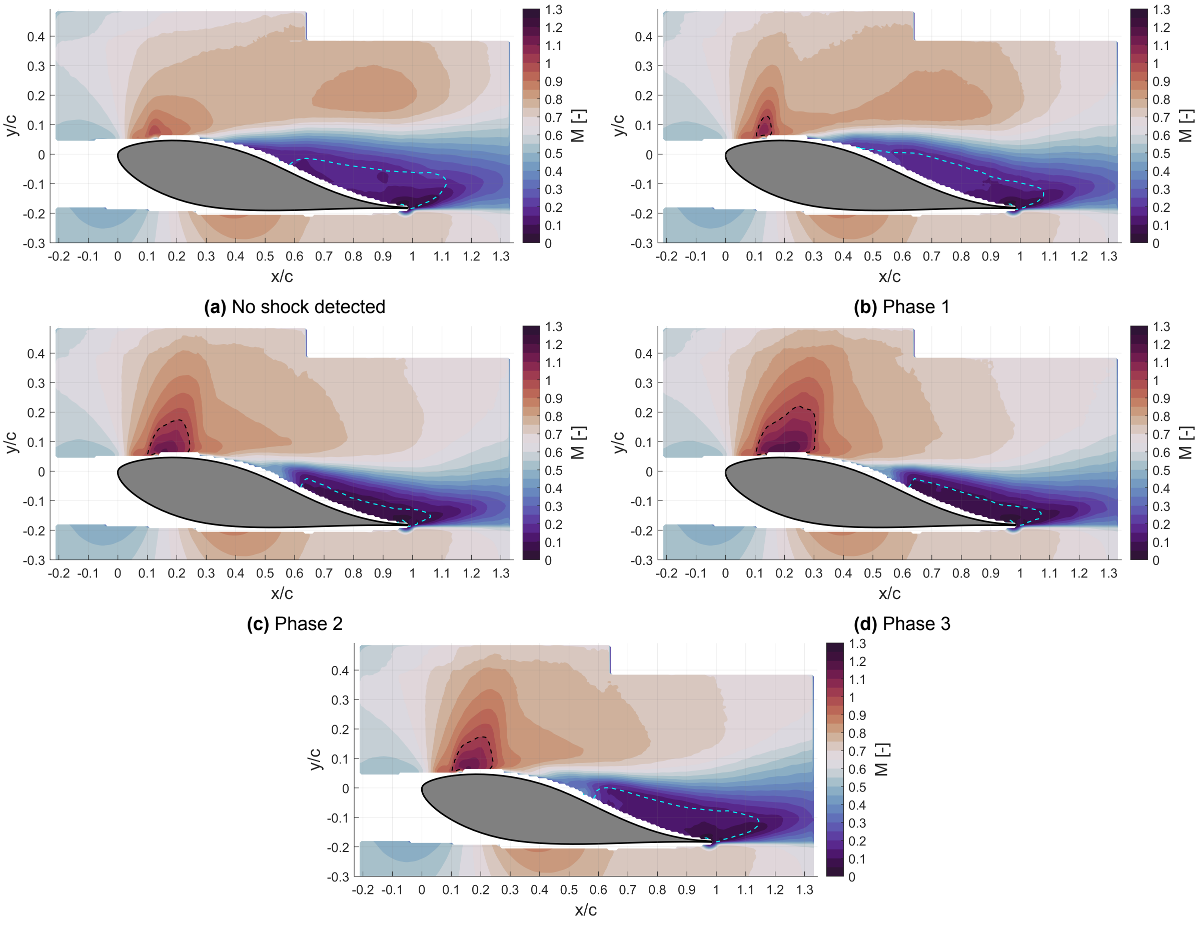

(a) No shock detected

(b) Phase 1

(c) Phase 2

(d) Phase 3

(e) Phase 4

Figure 5.21: Phase-averaged Mach number field for the transonic buffet cycle at $\alpha = -10°$, M_∞ = 0.65. The sonic line (M = 1) is indicated by the black dashed contour. The cyan dashed line encloses the region where $\bar{u} \leq 0$, indicating flow reversal.

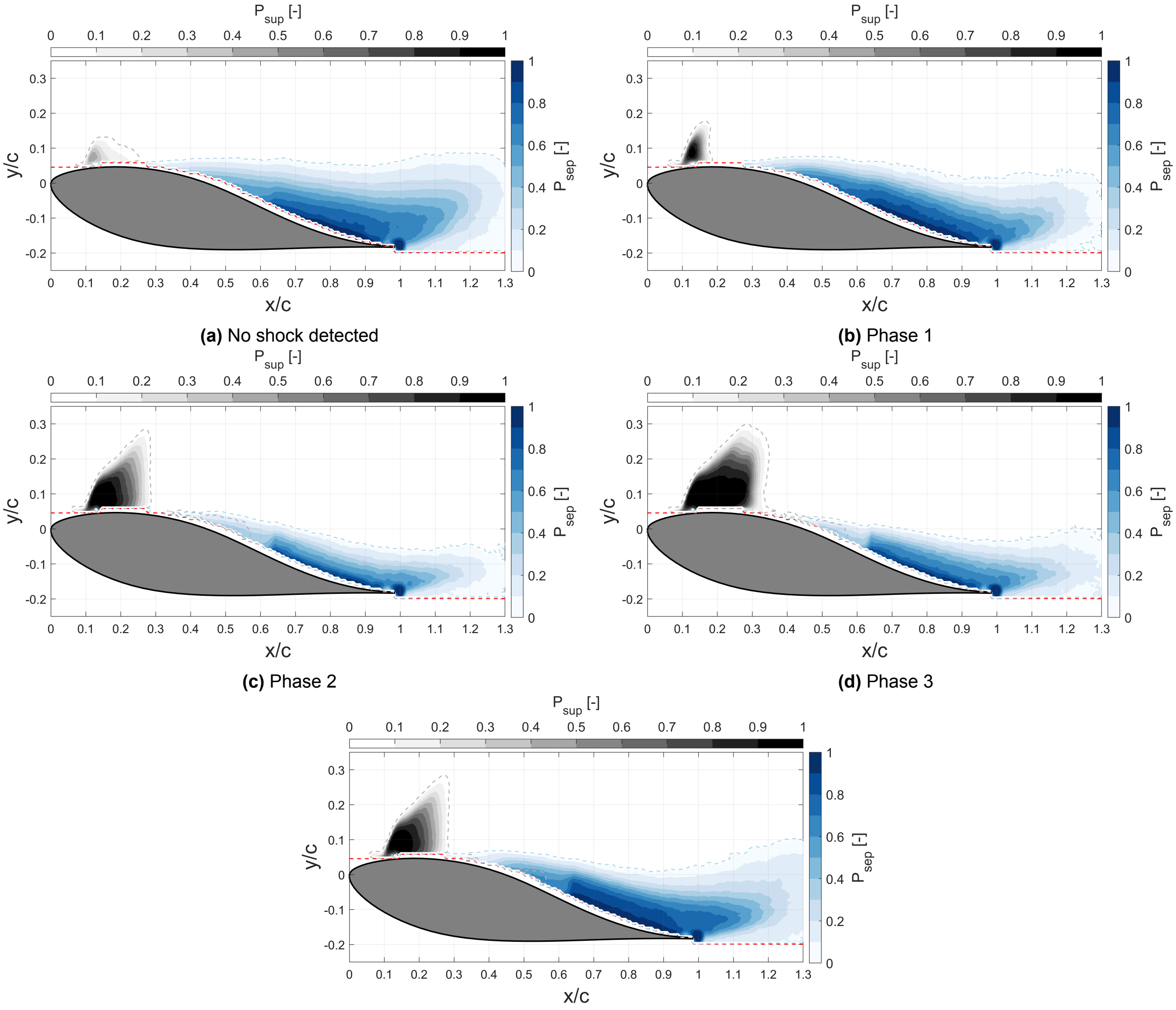

(a) No shock detected
(b) Phase 1
(c) Phase 2
(d) Phase 3
(e) Phase 4

Figure 5.22: Phase-averaged supersonic and separation spatial distribution field for the transonic buffet cycle at $\alpha = -10°$, M_∞ = 0.65. The respective dashed contours represent a 5% probability. The unmasked region lies above the red dashed line.

From these results it is possible to support some of the previous claims made based on the shock wave strength and location. Upon inspection, phases 'No shock' and 1 exhibit a maximum average local Mach number $M \approx 0.9 - 1$ and $M \approx 1.05 - 1.1$. Only for phase 1 is there a significant probability for supersonic flow confined to $x/c \approx 10 - 15\%$. For phase 2 and 4, the supersonic characteristics are similar, with a maximum local Mach number $M \approx 1.15 - 1.2$ achieved within a small region close to the airfoil, and the supersonic area extending well within $x/c \approx 10 - 25\%$. Phase 3, by far, represent the strongest shocks, with a significant region experiencing a local Mach number $M \approx 1.15 - 1.2$ and the supersonic area extending well within $x/c \approx 10 - 32\%$.

The separated region for phases with an upstream shock position, 'No shock', 1 and 4, cover a significantly larger vertical and horizontal extent compared to phases 2 and 3 with a more downstream position, consistent with Schlieren observations. Evidently, phase 2 displays the smallest separated area and aft origin, as the shock waves here are regaining their strength. Despite the limited resolution near the airfoil surface, and the indicative nature of the separation metric used, the separation probability distribution suggests that separation is indeed more likely to originate at the shock foot for phases 3 and 4, where the shock wave is strongest and most downstream located, whereas a larger gap between the spatial distributions exist for phases 'No shock, '1 and 2, where the shock wave is weaker and more upstream located. With these observations, the previous claims to interpret the phase-averaged trends in Table 5.8, relying on Schlieren-based interpretations on shock wave strength, location and separation characteristics, are now confirmed. A coming section is able to provide a fuller picture by supporting claims made on the intensity of the adverse pressure gradient.

Other observations are now discussed for a more comprehensive understanding of the flow field. Outside of the wake, the flow is accelerated to satisfy the conservation of mass across the test section. This is most noticeable for phases ’No shock’ and 1, where the wake has its most upstream influence on the outer flow. In these phases, the outer flow past the suction peak remains accelerated over a larger extent, in the order $M \approx 0.7$. Being limited to represent ’bounded flow’ conditions due to the tunnel walls, it is anticipated that the wake blockage effects may become significant across the transonic buffet cycle due to the large wake. Furthermore, a difference in wake deflection angle is observed across the cycle, with phases ’No shock’ 1 and 4 deflecting more towards the suction side, suggesting an existing region of low pressure consistent with the more accelerated flow over the suction side experienced in these conditions.

The following section aims to connect the phase-averaged flow field characteristics discussed in this section to the phase-averaged aerodynamic loads via the pressure field, its distribution along the airfoil and the total pressure field.

5.4.3. Reconstructed pressure and total pressure

The contribution of Reynolds stresses has been neglected in the reconstruction of the phase-averaged pressure fields. The contribution is non-negligible, as it will be later discussed. The motivation for this lies in a later analysis of the phase-averaged loads, were unphysical trends were observed with their inclusion. Nevertheless, the phase-averaged loads when accounting, and neglecting the Reynolds stress contributions will still be presented in section 5.5.

The pressure field, its distribution along the airfoil surface and the total pressure deficit will be analysed to support a discussion on the aerodynamic loads, beginning with the pressure field in Figure 5.23. As the lower airfoil surface has been assumed to experience mean flow conditions, the focus lies on analysing the developments on the suction side of the airfoil.

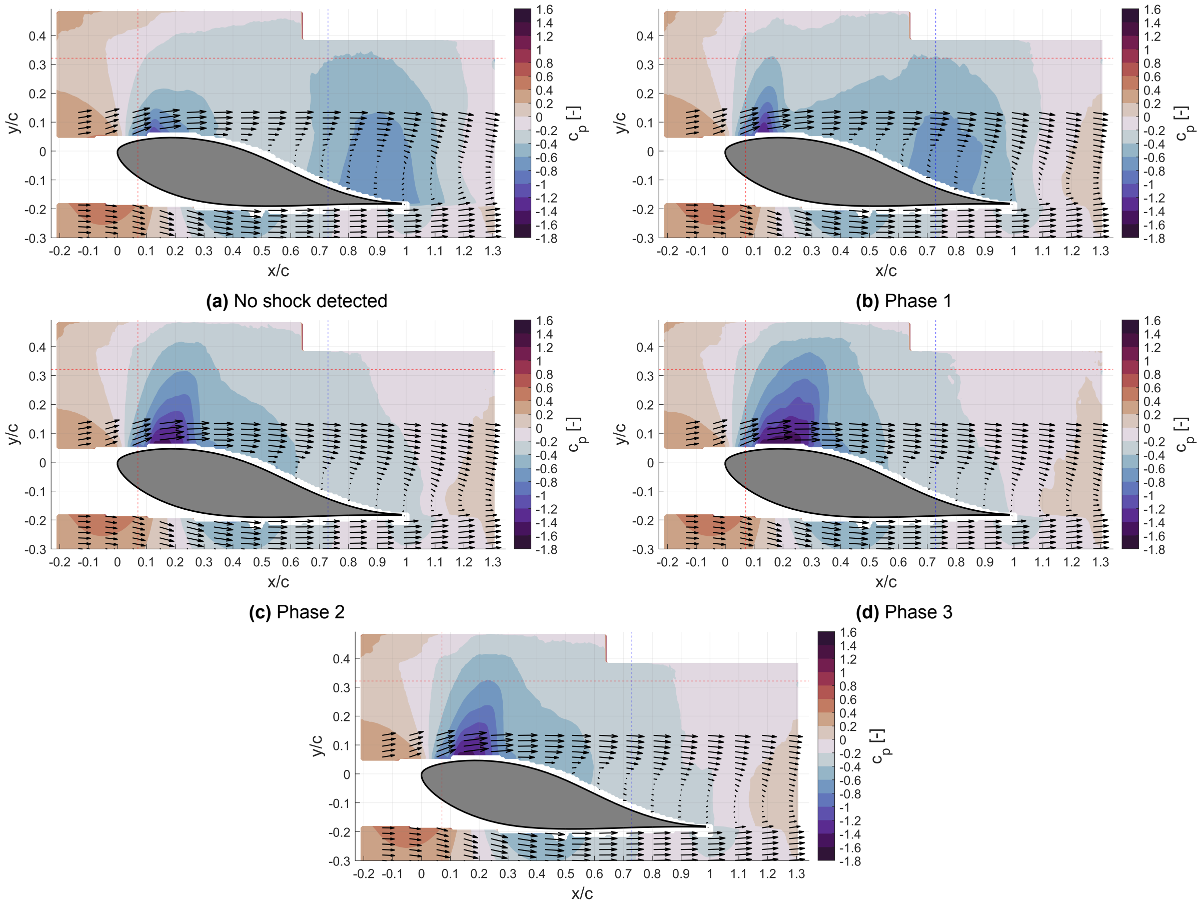

(a) No shock detected

(b) Phase 1

(c) Phase 2

(d) Phase 3

(e) Phase 4

Figure 5.23: Phase-averaged pressure coefficient field for the transonic buffet cycle at $\alpha = -10°$, M_∞ = 0.65. The arrows represent local velocity magnitude and flow direction.

A noticeably strong suction force is observed, coinciding with the location and extent of the supersonic region. Above the TE region, phases 2, 3 and 4 display a more efficient pressure recovery to freestream values. The phases 'No shock' and 1 display more significantly negative c_p values above the TE region. With separation already present in all phases, it seems that, under these specific circumstances, the shock waves in phases 2, 3 and 4 contribute to a more efficient pressure recovery towards freestream conditions.

Above the wake region, $y/c > 0.2$, the results for phase 'No shock' and 1 indicate a large downstream extent for which c_p remains considerably negative, compared to the other phases. This is likely attributed to the effects of both a high-speed outer flow, as observed through the Mach number field, and the weak shock-induced pressure rise.

The pressure is once again extrapolated to the surface of the airfoil for all considered phases. The results are indicative, shown in Figure 5.24. The mean flow pressure coefficient field is plotted. All phase-averaged pressure-side results assume the same mean-flow conditions; thus, a comparison is made only on the suction-side distribution.

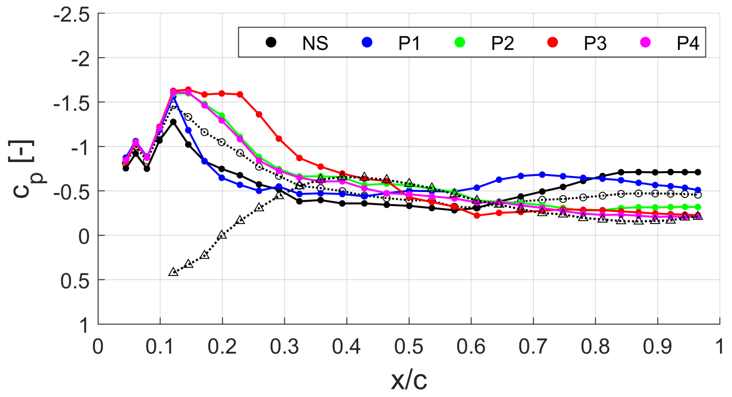

Figure 5.24: Phase-averaged pressure coefficient distribution for the transonic buffet phses at $\alpha = -10°$, M_∞ = 0.65. Marker colour differentiates all phases. Filled circles represent the suction surface, while unfilled triangles denote the pressure surface. The unfilled circles represent the mean flow distribution over the suction surface.

A comparable suction peak is present for all phases near the LE region. The suction peak is narrowest for phases 'No shock' and 1, and the flow experiences a severe adverse pressure gradient past $x/c \gtrsim 11\%$. This adverse pressure gradient at a relatively upstream location, in the absence of a strong shock, helps to explain why the flow is still greatly separated over a large extent. In contrast, the remaining phases show an extension of the suction peak. Phases 2 and 4 display a similar distribution, with the shock-induced pressure rise smeared across $15\% \lesssim x/c \lesssim 25\%$ due to the phase-averaging procedures. The suction peak for phase 3 displays the largest extent as, only after $x/c \approx 25\%$, is a sharp pressure rise observed. The behaviour of all distributions in within $30\% \lesssim x/c \lesssim 65\%$ is similar, slowly reaching a uniform pressure value due to the presence of separated flow ahead. Interestingly, the phase 'No shock' displays consistently higher c_p values. Phases 1,2,4 display similar levels, while phase 3 begins with a more negative c_p than the rest and ends with a higher one. For phases with well-developed shock waves, 2,3 and 4, there is a considerable pressure rise at $x/c \approx 61$, consistent with the location with a sharp increase in likelihood for separated flow, as detected in the previous phase-averaged flow analysis. This is not so noticeable for phases 'no shock' and 1, as separation occurs more chaotically at a more upstream location. Past $x/c \geq 70\%$, a relatively inefficient pressure recovery is again observed for phases 'no shock' and 1, while phases 3 and 4 tend well towards the suction-side pressure value. Phase 2 displays behaviors in between the described. Based solely on the phase-averaged suction-surface distributions, it is evident that the extension of the supersonic region benefits the suction force near the LE region for phases 2,3,4, while also improving the efficiency of the mid-chord section in the production of lift. Conversely, the TE region suction force is greatest in the absence of strong shocks, but this also results in large negative c_p values, which contributes to pressure drag.

The primary means to determine the phase-averaged aerodynamic drag relies on the pressure information along the wake of the airfoil, motivating a study of the total pressure deficit in the wake. This provides a measure of the momentum deficit and energy losses due to viscous phenomena. Thus, the total phase-averaged pressure deficit is proportional to the phase-averaged drag. The total pressure deficit of the mean flow is included for comparison.

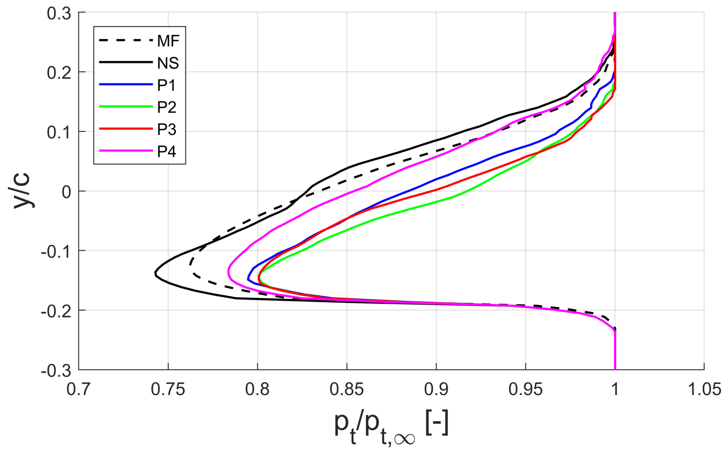

Figure 5.25: Phase-averaged total pressure deficit in the wake at a distance $x/c = 1.2$ for the transonic buffet cycle at $\alpha = -10°$, M_∞ = 0.65. The line colour differentiates all phases. The dashed line, 'MF', represents the time-averaged flow.

Phase 'No shock' displays the largest deficit in total pressure, reaching values around $\sim 75\%$ of the freestream total pressure, over a vertical extent spanning $\sim 55\%c$. This is followed by phase 4, reaching $\sim 78\%$ of the freestream total pressure. The remaining phases reach a similar total pressure ratio of $\sim 79\%$, however, the differences in the deficit along $y/c > 0$ are consistent with the effects related to the size of the wake, with phases 2 and 3 displaying the narrowest deficits due to the narrowest wakes. Based on the flow field analysis, the phase-averaged drag can be expected to be highest during phase 'No shock', followed by phase 4, and reaching its lowest in phases 2 & 3.

Until now, a detailed analysis has been presented in section 5.3 and section 5.2 of instantaneous and mean flow field characteristics and trends with increasing Mach number and, thus, compressibility effects. This was synthesised through the results at $\alpha = -6°$ and $-10°$. Furthermore, the analysis of the data at $\alpha = -10°$ at $M_\infty = 0.65$ revealed significant deviations between the phase-averaged flow fields and the mean flow representation, highlighting the extreme effects of compressibility. Now, section 5.5 presents the mean aerodynamic loads derived for all test conditions, connecting the previous discussions on the observed flow field developments to provide a comprehensive understanding of their evolution. Additionally, the phase-averaged aerodynamic loads during transonic buffet are analysed to emphasise their significant deviations from the mean flow under extreme compressibility effects.

5.4.4. Reynolds stresses contribution

Results are now presented for the Turbulent Kinetic Energy (TKE) field in Figure 5.26 to aid in a more comprehensive understanding of the phase-averaged aerodynamic loads. This provides a measure for the turbulence intensity, and, thus, momentum mixing.

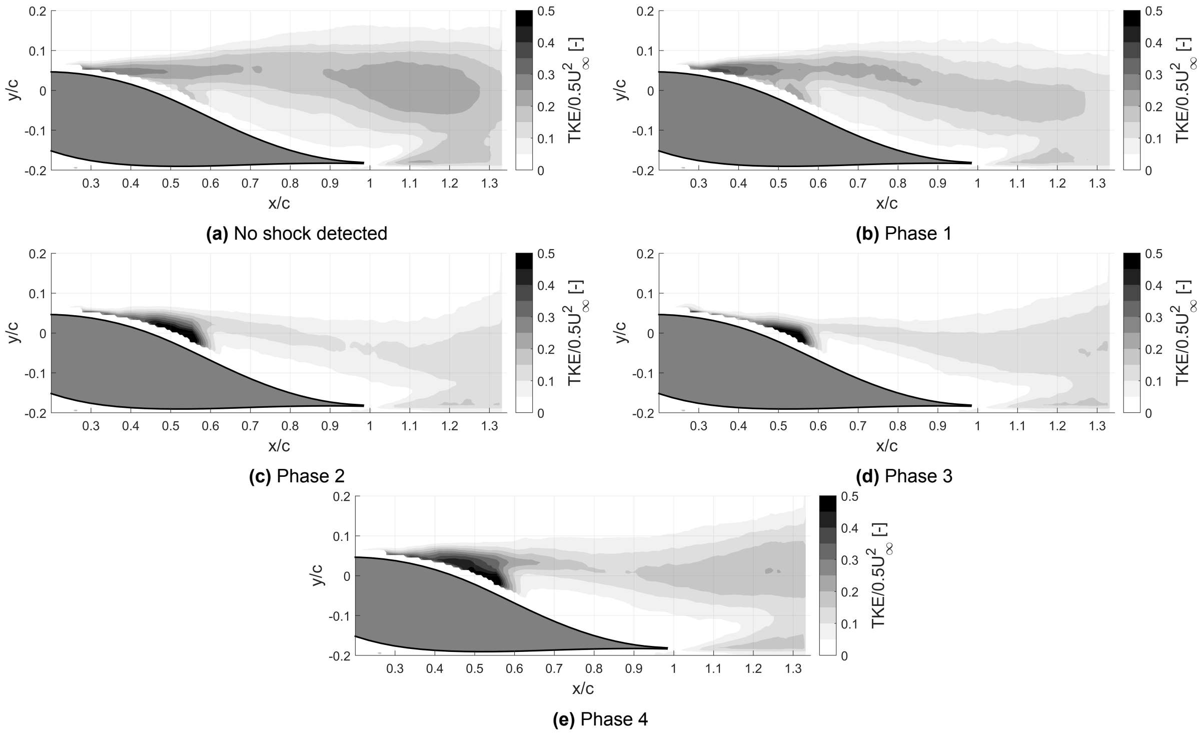

Figure 5.26: Phase-averaged Turbulent Kinetic Energy field for the transonic buffet cycle at $\alpha = -10°$, M_∞ = 0.65. The unmasked region lies above the dashed red line.

As expected, the greatest values for the TKE are achieved close to the airfoil surface at the shear layer. This is most prominent for phases 2, 3 and 4, reaching values of up to 50% of the freestream and featuring stronger SWBLI than in phases 1 and 'No shock'. What is interesting to observe is the increase and relatively high values for TKE in the wake region for phases 'No shock', 1 and 4. This could be a result of the highly unsteady shear layer and its interaction with the recirculating region.

Despite the lower shock wave strength in phases 'No shock' and 1, these phases feature the broadest areas with relatively high levels of turbulence. For phase 1, a wide region featuring a turbulence level of 20-25% of the freestream energy is present, almost twice as in phases 2 and 3. Phases 2 and 3 feature a narrower and less turbulent wake, with phase 4 featuring conditions at levels in between all phases.

While the TKE values near the airfoil and in the wake have an apparent significant level of energy, section 5.5 will show unphysical results and trends observed in the phase-averaged loads when accounting for the Reynolds stresses in the reconstruction of the pressure field raise questions about how well these Reynolds stresses can be resolved with the limited number of frames per phase. For this reason, these are not included in the phase-averaged analysis. Therefore, a potential improvement to the theoretical approach to the phase-averaged analysis lies in the proper inclusion of these stresses.

5.5. Aerodynamic loading

5.5.1. Mean flow results

After an extrapolation of the velocity data in the shadow region of the freestream, deriving the corresponding Mach number and pressure, and defining a contour integral according to the description provided in chapter 4, the mean integral aerodynamic coefficients $c_{l,ct}$ and $c_{d,ct}$ are determined. In addition, the drag estimated from the wake integral quantities, $c_{d,wd}$, is calculated. These results are summarised in Table 5.9. The results for using `XFOIL` are also included to be taken as indicative and to highlight the discrepancy in the estimated coefficients between the methods.

Table 5.9: Mean lift and drag coefficients obtained using the contour-based method, represented by the subscript 'ct'. Drag based on the wake deficit method is represented by the subscript 'wd'. Simulation values from XFOIL are included for comparison.

α [°]	M_∞ [-]	$c_{l,ct}$	XFOIL c_l	$c_{d,ct}$	$c_{d,wd}$	XFOIL c_d
-4	0.5	-0.263	-0.248	0.0507	0.0229	0.0169
-4	0.55	-0.261	-0.263	0.0619	0.0228	0.0192
-4	0.6	-0.174	-0.261	0.0731	0.0214	0.0224
-6	0.5	-0.425	-0.514	0.0675	0.0260	0.0239
-6	0.55	-0.407	-0.495	0.0762	0.0281	0.0271
-6	0.6	-0.360	-0.462	0.0869	0.0412	0.0307
-6	0.65	-0.311	-0.420	0.1162	0.0750	0.0354
-8	0.5	-0.547	-0.679	0.0690	0.0632	0.0335
-8	0.55	-0.547	-0.656	0.0946	0.0720	0.0377
-8	0.6	-0.531	-0.624	0.1319	0.0788	0.0427
-10	0.5	-0.659	-0.742	0.1002	0.0853	0.0518
-10	0.55	-0.654	-0.712	0.1291	0.0949	0.0575
-10	0.6	-0.674	-0.678	0.1683	0.1577	0.0638
-10	0.65	-0.678	-0.636	0.2088	0.1740	0.0711
-11	0.5	-0.693	-0.771	0.1409	0.1323	0.0618
-11	0.55	-0.724	-0.741	0.2041	0.1248	0.0681
-11	0.6	-0.742	-0.705	0.2640	0.1677	0.0753

In the following illustrations and discussions, the lift coefficient based on the contour integral, $c_{l,ct}$ is referred to as c_l, and the drag coefficient based on the wake deficit integral, $c_{d,wd}$ is referred to as c_d. All error bars are derived from the variability of the coefficients due to changes in the contour and x-location for the wake integral according to Table 4.1 and Table 4.2, with the results made available in Appendix A. The aerodynamic coefficient trends across the (α,M_∞) domain are visualized in Figure 5.27.

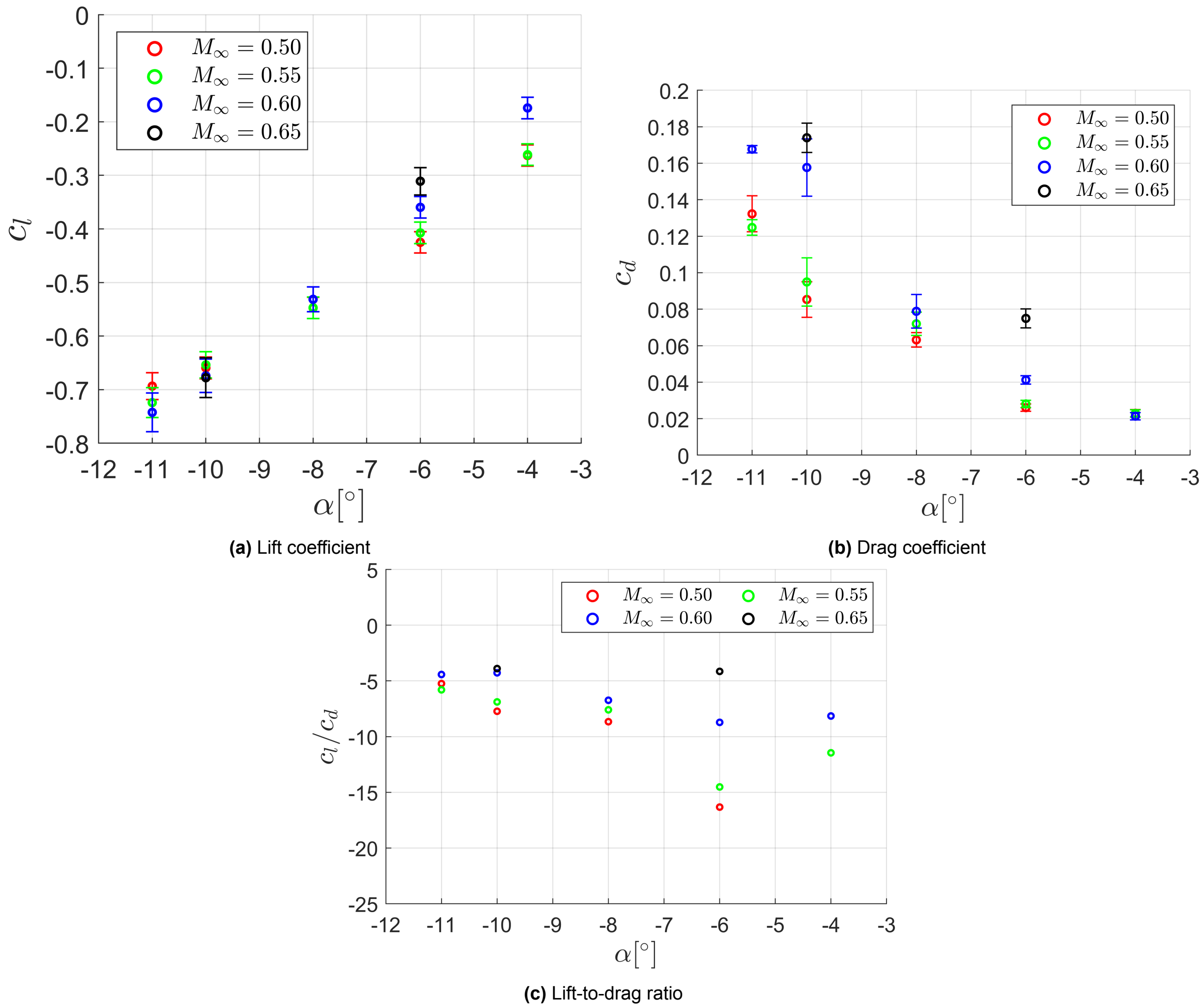

Figure 5.27: Contour-based lift and wake deficit drag coefficient data for all cases. Error bars correspond to 1σ due to variations in the contour definition.

The analysis begins with a general discussion of the results. As expected, a clear trend towards more negative mean lift coefficients with decreasing angles of attack is observed. The drag coefficient shows an increase with more negative angles of attack. The aerodynamic coefficients show a minimal difference between M_∞ = 0.5 and 0.55 within $\alpha \leq -10°$, consistent with the minimal differences observed in the mean flow fields. For $M_\infty \geq 0.6$, however, significant differences were observed in the mean flow field with increasing compressibility effects, reflected in the aerodynamic coefficients, especially in the drag which displays a significant increase for $M_\infty \geq 0.6$. At $\alpha = -6°$, the results indicate c_d = 0.026, 0.412, 0.075 for $M_\infty = 0.5, 0.6, 0.65$, an overall increase of ~175% between the M_∞ 0.5 and 0.65. At $\alpha = -10°$, the results indicate c_d = 0.0853, 0.1577, 0.1740 for $M_\infty = 0.5, 0.6, 0.65$, with a significant increase of ~80% already present between M_∞ 0.5 and 0.6, followed by a relatively short difference between M_∞ 0.6 and 0.65. The mean lift trends are more complex, with increasing Mach numbers resulting in a clear reduction in the mean lift for $\alpha \leq -6°$. At $\alpha = -8°$, the reduction is minimal, insignificant at $\alpha = -10°$ and even slightly reversed at $\alpha = -11°$. These results suggest a clear effect of compressibility on the mean aerodynamic coefficients, but also a difference in how these manifest across the (α,M_∞). Fortunately, the mean flow analysis presented in section 5.3 for two distinct AoAs, $\alpha = -10°$ and $-6°$, provides a foundation for understanding the manifestation of compressible phenomena and their effects across the (α,M_∞) domain.

Recalling the analysis at $\alpha = -6°$, the results showed significant growth and upstream movement of the separation region and small accelerations over the LE suction side of the airfoil, with increased M_∞. In addition, a significant acceleration is present in response to the relatively low incidence and highly curved pressure-side surface, comparable to the suction-surface accelerations. These observations are reflected in the pressure distributions, with a consistently weak suction peak, and an inefficient mid-chord section with detrimental performance as M_∞ increases. The TE section showed a flat pressure distribution as a result of separation, with minor contributions to the lift, and revealed negligible variations with different Mach numbers. These observations remain consistent with the detrimental lift and drag performance observed at $\alpha = -6°$ with increased M_∞, with similar developments observed for $\alpha = -4°$.

In comparison, the suction side at $\alpha = -10°$ shows a more accelerated mean flow due to the increased incidence, much more than on the pressure surface, and resulting in the emergence of supersonic flow. The prominence of the supersonic region is greatly amplified with increased M_∞. The results also show significantly higher levels of separation at a more upstream location at the lowest Mach numbers. Separation becomes significant past $M_\infty > 0.6$, more abruptly than for $\alpha = -6°$. These observations are reflected in the pressure distribution. Despite the increased accelerations on the suction side, it is believed that the emergence of prominent shock waves and separation beyond $M_\infty > 0.6$ has an upstream influence on the LE region flow, leading to weaker suction peaks. Due to the intensity of the separated area, the mid-chord and TE region remain inefficient in producing lift. Increasing M_∞ results in lower pressures over the separated region, which benefits the lift-production capability. However, this flat and increasingly low pressure distribution experienced along the aft portion of the airfoil when increasing M_∞ contributes massively to the pressure drag. These observations remain consistent with the lift and drag performance determined for $\alpha = -10°$ with increased M_∞.

5.5.2. Phase-averaged results

The phase-averaged aerodynamic loads have also been determined for the different phases of the transonic buffet cycle. Table 5.10 tabulates the phase-averaged aerodynamic loads obtained with, and without the inclusion of Reynolds stresses. The mean aerodynamic loads are also presented under the label 'Mean flow', and the results without the inclusion of Reynolds stresses are also included.

Table 5.10: Mean flow and phase-averaged aerodynamic loads determined with the inclusion of Reynolds stresses (subscript RS), and otherwise without the contribution of Reynolds stresses.

Phase	$c_{l,RS}$	$c_{d,RS}$	c_l	c_d
Mean flow	-0.68	0.174	-0.65	0.139
0	-0.63	0.165	-0.72	0.202
1	-0.59	0.099	-0.65	0.115
2	-0.56	0.086	-0.59	0.093
3	-0.57	0.086	-0.60	0.094
4	-0.53	0.107	-0.58	0.118

As observed, the inclusion of Reynolds stresses results in phase-averaged loads that are not centred around the mean flow loads. In fact, the lift values are all significantly below the mean lift. On the other hand, the results derived without the inclusion of Reynolds stresses display a more physical behaviour, where the mean flow loads are a weighted average of the loads over different phases. Moving forward with the aerodynamic loads derived without the contribution of Reynolds stresses, these are illustrated in Figure 5.28, with visible error bars.

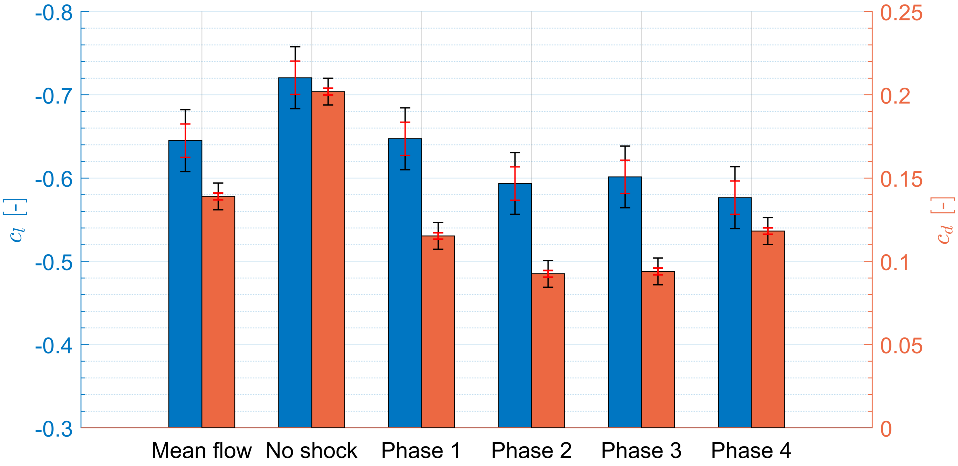

Figure 5.28: Phase-averaged aerodynamic loads across the different stages of the transonic buffet cycle at $\alpha = -10°$, $M_\infty = 0.65$. The mean aerodynamic loads are shown for comparison, under the label 'Mean flow'.

The phase-averaged results indicate an oscillatory loading centered around the mean flow values. The highest lift values are associated with phases 'no shock' and 1. In contrast, the lowest values are associated with phases 2, 3 and 4. For these phases, and the uncertainty level determined for this test condition (Black error bars), the difference between the lift coefficients is not significant. If one were to assume a maximum uncertainty level equal to the results from Ragni et al., 2009 (Red error bars), then phase four is, arguably, the phase with the lowest lift coefficient $c_l =$. Overall, a significant difference in the phase-averaged lift coefficient is appreciated between phase 'No shock' and phase 4, $\Delta c_l = 0.14$, which is ~22% of the mean flow lift coefficient. The highest drag coefficient is also associated with phase 'No shock'. All remaining phases display a lower phase-averaged drag coefficient, with phases 2 and 3 displaying the lowest values. The difference in the phase-averaged drag coefficients are significant, greater than the conservative uncertainty estimate used in this thesis. The difference between phase 'No shock' and phase 2 corresponds to $\Delta c_d = 0.112$, which is ~80% of the mean flow drag coefficient.

The phase-averaged flow field developments reflect clearly the observed trend in the phase-averaged drag coefficient. The highest value for the drag coefficient is attributed to phase one, which coincides with the greatest extent of the separated area and the greatest total pressure deficit. While the shock wave does introduce wave drag due to the loss of total pressure across the shock, it seems that the dominant contribution to the drag coefficient is the extent of the separated area, which results in the phases with the most downstream shock locations displaying the lowest drag values due to their lower extent of separation. The phase-averaged separation characteristics provide a useful estimate for the drag, but the data do not allow for a distinction in why phases 1 and 4 display significant levels of drag despite comparable phase-averaged separation characteristics. On the other hand, an analysis of the total pressure deficit alone is perfectly able to describe the trends in the drag coefficient.

An analysis of the phase-average lift coefficient is, again, more complex. While insightful, an analysis of the complex phase-averaged pressure distribution is limited to resolving the variation in the lift trend. For this, the contributions to the lift across the contour are explicitly analysed. The individual contributions of the pressure term, and the momentum term are illustrated in Appendix B. From these, it is important to know that the pressure term is the dominant contribution over all contour segments. The contribution of the momentum term is almost negligible over the top and bottom contour segments, while this becomes more influential over the right and left contour segments. Across different phases, the left contour segment contributions remain largely unchanged. On the other hand, the right contour segment contributions do differ substantially.

Figure 5.29 presents the following: The contributions for the top and bottom contour segments are added to arrive at the total contribution to the lift due to the top and bottom segments. Likewise, the contributions for the left and right contour segments are added to arrive at the total contribution to the lift due to the left and right segments. For example, the total contribution to the lift due to the top and bottom surfaces is $\partial l_{top,bot}/\partial x = f(x) = p_{bot} + (\rho vv)_{bot} - p_{top} - (\rho vv)_{top}$. The mathematical signs are consistent with the integral orientation, yielding a negative lift force. The phase-averaged aerodynamic lift is the result of directly integrating $\partial l_{top,bot}/\partial x$ and $\partial l_{rig,lef}/\partial y$ along the corresponding contour segment lengths. By integrating the contributions and applying non-dimensionalisation with the freestream dynamic pressure, the explicit contributions to the lift coefficient are tabulated in Table 5.11

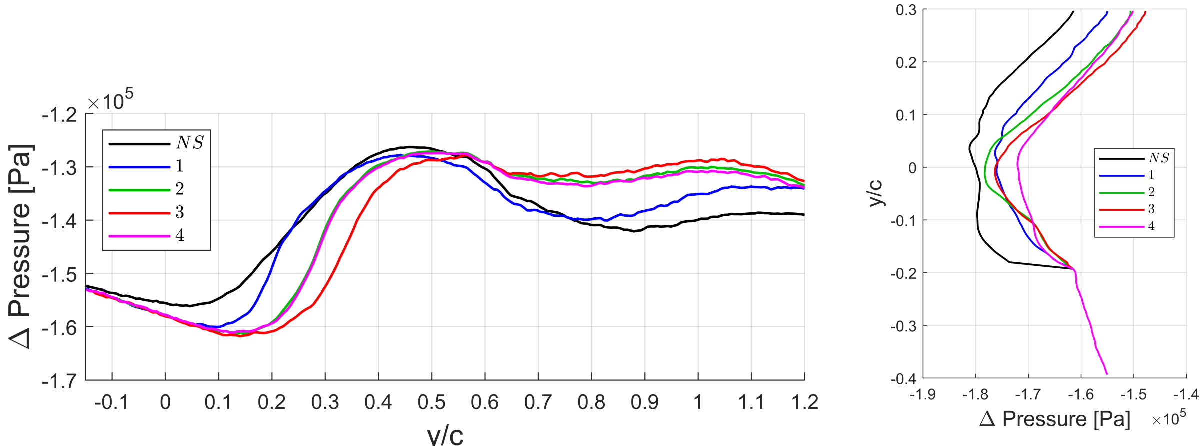

(a) Total contribution to the lift due to the top and bottom contour segments

(b) Total contribution to the lift due to the left and right contour segments

Figure 5.29: Contribution of the various segments to the phase-averaged lift coefficient

Table 5.11: Contribution to the lift coefficient from the (1) top and bottom contour segments, (2) left and right contour segments.

Phase	$\delta c_l^{(1)}$	$\delta c_l^{(2)}$	Total c_l
Mean flow	-0.2571 (40%)	-0.3916 (60%)	-0.65
No Shock	-0.2821 (39%)	-0.4384 (61%)	-0.72
1	-0.2832 (44%)	-0.3640 (56%)	-0.647
2	-0.2504 (42%)	-0.3431 (58%)	-0.594
3	-0.2792 (46%)	-0.3223 (54%)	-0.601
4	-0.2608 (45%)	-0.3157 (55%)	-0.577

It is noted that the contribution of the left and right contour segments to the lift is consistently greater than the contribution of the top and bottom contour segments. This is likely a result of the distance between the contour segments to the airfoil, as the left and right boundaries are significantly closer to the airfoil compared to the top and bottom boundaries.

An analysis of Figure 5.29a yields similar conclusions to the analysis of the phase-averaged pressure distribution along the surface. When integrating the differential contributions across top and bottom contour segments, the resultant contribution to the lift coefficient $\delta c_l^{(1)}$ is observed to be greatest for phase 'No shock', and lowest for phase 2. Based on the contribution $\delta c_l^{(1)}$, it is not able to reflect the total phase-averaged lift trends, and an analysis of $\delta c_l^{(2)}$ must be made.

From analysis of Figure 5.29b and explicit load contributions, the integrated contribution due to the left and right contour segments, $\delta c_l^{(2)}$, identifies phase 'No shock' with the greatest contribution across all phases, while phase 2 has, one again, the lowest. Results show that the low-pressure region present in the wake of the airfoil in phase 'no shock', relative to the other phases, is greatly responsible for its highest lift value.

A reason for this significant region of low pressure to exist only in phase 'No shock' lies in the absence of a shock wave. There is no abrupt increase in pressure, allowing it to maintain relatively low levels. In addition, the strong region of recirculation observed through Schlieren and PIV data displays high energy levels and mixing with the outer flow, which helps maintain high flow accelerations and low pressures. As a result of lacking a mechanism to initiate recovery into freestream conditions, phase 'No shock' also displays the highest of pressure-induced drag. On the contrary, the presence of shock waves does result in an abrupt increase in static pressure and more efficient recovery to freestream conditions. This, coupled with the smaller separated region to maintain the pressure level, results in lower drag. These observations are similar to those derived for the time-averaged cases, where a shift in aerodynamic loads from the leading edge to the trailing edge is observed.

While phases 2,3,4, with the greatest extension of the supersonic area, boast the greatest contributions to the aerodynamic forces near the LE, these are phases in which the TE has a lesser contribution. The opposite is true for phases 'No Shock' and 1. The results indicate that the transonic buffet cycle periodically shifts the aerodynamic load contribution between the LE and TE, and that these variations significantly affect the flow field and aerodynamic forces across the cycle.

5.6. Compressibility and its implication for wind turbines

Extensive work has been devoted to the analysis of time-averaged flow fields and mean aerodynamic loads for all the test conditions of the FFA-W3-W11 airfoil. Furthermore, the extensive work is presented for the phase-averaged flow field and aerodynamic load for the transonic buffet cycle at $\alpha = -10°$, M_∞. While these analyses were primarily focused on the flow field and aerodynamic performance, it is also important to take a step back and consider these results and their implications in the bigger context of wind turbines.

Recalling the results of the previous sections, the analysis of time-averaged flows indicated a significant effect of compressibility in the flow field, reflected in the large variation in aerodynamic loads. The lift characteristics were most affected at $\alpha = -6°$, dominated by significant separation levels and low accelerations over the suction side. The drag, however, displayed consistently significant variations due to separation and wake losses for test cases satisfying $\alpha \leq -6°$ and $M_\infty \geq 0.6$, for which the development of shock waves was observed to be highly detrimental. During the transonic buffet cycle, a significant periodic variation of aerodynamic coefficients is observed. The phase-averaged separation and shock wave characteristics vary substantially across phases. Across all phases, the phase-averaged lift coefficient varied by approximately 22% of the time-averaged lift coefficient, while phase-averaged drag coefficient variations reached a significant 80% of the time-averaged drag coefficient.

Several aspects of the present work, and the implications of its limitations, must be taken into account when discussing any findings in the context of wind turbines.

- The present work focuses solely on the FFA-W3-211 airfoil, used in the blade tip region of some wind turbine designs.
- The present work focuses on two-dimensional, wind turbine airfoil-level flow fields and aerodynamic loads. In practice, wind turbine blades are three-dimensional and operate in three-dimensional unsteady flows with added complexities of aeroelasticity, harsh environmental conditions, floating motion (For offshore wind turbines), and wind gusts.
- Experimental test conditions and setup are limited in their ability to capture the expected conditions at the wind turbine level. To mention a few, the freestream Mach number range tested is arguably too high for the current expected values around the blade tip. The Reynolds number of the present work is a factor of 10 lower than the Reynolds number experienced at the blade tip. A fixed-transition by using a strip is not guaranteed to emulate real flow conditions, which likely have different transition behaviours.
- The use of a non-intrusive means to assess aerodynamic loading by inferring flow field data, and the inherent uncertainty of such a method.

At present, compressibility is understood to be a potential concern near the blade tip region. While the study focuses solely on the FFA-W3-211 airfoil used at the blade tip of several modern turbines designs, other blade tip airfoils have similar geometries and are unique in their high relative thickness compared to conventional aviation airfoils. Therefore, these may display similar behaviours in a time-averaged sense. The relatively high Mach numbers, relatively low Reynolds numbers, simplified two-dimensional steady freestream, fixed-transition, and other experimental setup considerations do limit an accurate representation of the actual three-dimensional flow over the three-dimensional blade tip. This is especially true when analysing transonic buffet, as there is a substantial difference in how it manifests over two-dimensional and three-dimensional flows. Furthermore, this work explores extreme Mach number conditions in the context of wind turbines, yet offers a Reynolds number scaling that falls significantly short of real conditions. Recalling the results from M. C. Vitulano et al., 2024, the emergence of supersonic flow and shock waves is significantly greater at higher Reynolds numbers of the order 9 million. Thus, an experimental campaign at more comparable Reynolds numbers might observe the effects of compressibility playing a significant role already at lower Mach numbers, which may potentially come closer to the expected operational Mach numbers at the tip. For this, further investigation is necessary, and should also consider that wind turbines also operate in off-design conditions.

Given all limitations and their implications, what is the value of the current work and its findings? First, it is important to acknowledge that compressibility had a significant effect on the flow field and aerodynamic performance of the FFA-W3-211 airfoil at the tested conditions. Second, it is important to recall why compressibility is a source of concern in the first place. In general, wind turbine design and operation still rely on the assumption of incompressible flow through models such as BEM (Sørensen et al., 2018). What this means is that new wind turbine designs, including the IEA 15MW and IEA 22MW offshore wind turbines, rely on static lift and drag polars to model aerodynamic loads (Jonkman et al., 2009; Zahle et al., 2024), with a simple correction due to the effect of compressibility, at best. Wind turbine control systems used in operation also rely on aerodynamic polars that may be limited in their ability to capture compressibility effects. Assuming compressibility does affect the blade tip region, the limited knowledge, treatment and modelling of its effects could mean the control strategy chosen is not optimal for the turbine's performance and/or structural integrity. As a result, compressibility becomes a source of concern when it significantly changes the aerodynamic time-averaged lift and drag polars beyond their incompressible counterpart.

How this fundamental study at an airfoil-level can be used to foreshadow any variation in performance or concerns about structural integrity at a wind-turbine level is limited. What holds true, is that any changes in the aerodynamic performance across blade sections, including the tip, has an effect in wind turbine performance and loading as highlighted by chapter 2, but also on the control strategy for operation. The significant variations in time-averaged lift and drag coefficients due to the effects of compressibility observed in this thesis may serve as motivation for continued experimentation on its effects. While the phase-averaged analysis of the identified transonic buffet is presented for extreme compressibility conditions beyond what is expected of current large-scale wind turbines ($M_\infty = 0.65$), it does offer insight into the severity of transonic buffet for aerodynamic loading and the flow field. In addition to variations in the aerodynamic loads themselves, the mean-flow and phase-averaged analysis show a shift in the loading along the airfoil surface, hinting towards variations in the aerodynamic moment with increasing Mach numbers, but also across phases of the transonic buffet cycle. What also holds true, is that continued investigation at higher Reynolds numbers may find compressibility effects already significant at conditions closer to operational tip Mach numbers. Even if future results at higher Reynolds numbers observe very rare, intermittent emergence of supersonic flow and shock waves, these can pose a severe risk for structural integrity through fatigue over its lifetime.

In the context of wind turbines, and as a result of the aforementioned limitations, the present work may be regarded as an early contribution to the foundation and motivation for continued experimental investigations in assessing the effect of compressibility on the aerodynamic performance at wing turbine airfoil and full-scale level.

6 Conclusion

The accelerated demand and rapid advancements for wind energy power generation capabilities has driven the trend towards increased rotor sizes. This growth introduces new aerodynamic challenges, raising concerns of compressibility effects in modern, large-scale wind turbines, particularly near the blade tip region where local Mach numbers are the greatest. Despite recent studies, the understanding of compressibility and its aerodynamic implications at the wind turbine and airfoil level remain limited, particularly from an experimental perspective.

This thesis aimed to experimentally investigate the effects of compressibility on the time-averaged aerodynamic loading and flow field features of the FFA-W3-211 wind turbine airfoil at Mach numbers within 0.5-0.65 and angles of attack from $-4°$ to $-11°$. Experimental campaigns were conducted in the TST-27 wind tunnel at TU Delft using Schlieren and PIV techniques, and a non-intrusive load determination method relying on the pressure field reconstruction via PIV velocity data. The momentum contour integral method was adopted to determine the aerodynamic lift, while a wake deficit method was used to determine the aerodynamic drag.

The schlieren and PIV data highlight the main flow features across the test space. The emergence of supersonic flow and shock waves has been confirmed through instantaneous data. Shock waves emerge at lower freestream Mach numbers as the magnitude of the AoA increases, and a fully developed transonic buffet cycle was identified at $\alpha = -10°$ with $M_\infty = 0.65$. For $\alpha = -6°$, supersonic flow is only significant at $M_\infty = 0.65$, with intermittent shock waves developing within a relatively small extent. In contrast, for $\alpha = -10°$, supersonic flow is already significant at $M_\infty = 0.60$, with unsteady shock waves developing within a relatively larger extent. A noticeable amount of flow separation is found to be already present at the lowest magnitudes of Mach number and AoA, with significant growth observed when increasing Mach and AoA magnitudes for moderate angles of attack $\alpha \leq -6°$. At $\alpha = -6°$, the mean separated area increases dramatically by a factor of ~360% from $M_\infty = 0.5$ to 0.65. Although separation is already prominent at $\alpha = -10°$, this still grows significantly by a factor of ~50%.

The analysis of time-averaged aerodynamic loads confirms that compressibility has a measurable and non-negligible influence on the aerodynamic performance of the FFA-W3-211 airfoil. The observed trends across different Mach numbers and AoAs could are reflected in the complex interplay between flow separation, shock waves, SWBLI and their dynamics. The results at $\alpha = -6°$ display a 30% reduction in lift coefficient with increasing Mach number from $M_\infty = 0.5$ to 0.65, from $c_l = -0.43$ to -0.31, and a 190% increase in drag coefficient from $c_d = 0.026$ to 0.075. The results at $\alpha = -10°$ display an interesting behaviour for the lift coefficient with increasing Mach number from $M_\infty = 0.5$ to 0.65, displaying a plateau with values close to $c_l = -0.65$ to -0.67, and an significant 100% increase in drag coefficient from $c_d = 0.085$ to 0.174.

To quantify the effects of transonic buffet on the flow field and aerodynamic loads across different phases of the buffet cycle, phase-averaging was used. The results show that the transonic buffet cycle periodically shifts the aerodynamic load contribution between the LE and TE, and that these variations significantly affect the flow field and aerodynamic forces across the cycle. The phase-averaged lift coefficient varies periodically across all phases in a range of approximately ∼22% of the time-averaged lift coefficient. The period variation in phase-averaged drag coefficient reaches up to ∼80% of the time-averaged drag coefficient. These were observed to be a result complex interplay of shock waves, separation and their interaction.

Through an analysis of Schlieren and PIV data, this thesis demonstrates that compressibility has a significant influence on the flow field and aerodynamic performance of the FFA-W3-211 wind turbine airfoil. While the limitations of a two-dimensional, airfoil-level experimental campaign are not necessarily representative of full-scale wind turbine conditions, the observed variations in time-averaged aerodynamic loads call for a need of continued investigation. In particular, these results challenge the incompressible flow assumptions made in wind turbine design and operation, which rely on static airfoil polars that do not necessarily capture the full effects of compressibility. Furthermore, extreme shock-wave related phenomena like transonic buffet can significantly alter the flow field and aerodynamic loads compared to the incompressible case. These may pose new challenges to structural integrity and turbine performance, even if such events occur for brief periods or intermittently.

6.1. Recommendations for the present study

6.1.1. Experimental setup

- The use of a calibration object is recommended, as it can be used to consistently scale various experiments. When using multiple FOVs, calibration objects can be used to align the data to the same grid.
- One of the greatest improvements to the present study would be a consistent means to set the angle of attack of the airfoil model. This thesis employed the use of a digital angle meter to set the angle of attack. In conditions were the tunnel is completely shut off, the use of this meter is viable, and only requires careful calibration. When the tunnel is in stand-by mode, small vibrations in the wind tunnel and the high sensitivity of the meter make it hard to pinpoint the exact angle setting. This is a big concern, as the unified velocity field is the result of merging the data for two separate runs, with a potential mismatch in the model incidence. In the present study, it is estimated that the maximum mismatch in incidence between a nominal and inverted configuration is around half a degree, which can result in a significant difference in the flow fields. If possible, one would rather set the angle of attack through a mechanical system.
- This thesis has assumed that the camera is aligned with the wind tunnel, such that the nominal and inverted configuration data can be merged based only on a spatial translation of the data collected. In practise, likely, the camera is not aligned with the wind tunnel, and a rotational translation must also be applied to the data.
- The present study has attempted to analyse a transonic buffet cycle by means of phase-averaging. Under the conditions tested, the PIV measurements taken at 2500Hz were not entirely able to resolve the 1000Hz buffet cycle. A future study interested in analysing the transonic buffet cycle could potentially use a camera with greater temporal resolution, paying attention to keep an adequate spatial resolution. In theory, it would also be possible to further crop the sensor to obtain a higher temporal resolution, but this must be high enough to capture enough of the flow field, especially when also deriving aerodynamic loads with the momentum contour-based approach. If only interested in time-averaged analysis, then it is best to opt for further spatial resolution, rather than temporal resolution.
- The present study lacks additional experimental data at the tested conditions that could serve as a verification of the aerodynamic loads derived. As a recommendation, it is possible to employ the wake rake technique to verify the aerodynamic loads.

6.1.2. Theoretical approach

- In the thesis, an external, and rather limited, approach to estimating the uncertainty of the aerodynamic coefficients has been employed. A more accurate estimate can be made by successfully applying the uncertainty propagation analysis on the intermediate variables required to determine the aerodynamic loads.
- This is a combination of theoretical and experimental recommendations. In the present study,

the limited nominal FOV did not allow a classification of PIV frames along the pressure side of the airfoil into a phase of the transonic buffet cycle. As a result, the phase-averaged flow fields assume that the flow over the can be represented by the mean flow. All phases use the same mean velocity field over the pressure-side of the airfoil, and its analysis becomes redundant. While no shock waves were observed to develop in the pressure-side, this assumption is yet to be verified. For a transonic buffet cycle with global influence, it can be plausible that the pressure side of the airfoil is also affected across the buffet cycle.

6.1.3. Data processing approach

- Corrections to the PIV data, for factors such as particle slip, are not performed in this thesis. This correction is likely to have effects on the pressure field near the shock region, and may potentially translate to a better estimate of the aerodynamic coefficients.
- At present, the PIV data is linearly interpolated to a global, uniform grid to allow for straightforward data handling in reconstructing the pressure field. This introduces an uncertainty in the velocity field, which has not been quantified, and which propagates into the aerodynamic loads. A more accurate approach would involve an alternative method that uses all FOV data in their original grid (Given the data is properly defined in the same coordinate system). This will, however, make the reconstruction of the pressure field more complex.
- Due to a lack of time, the PIV data for the scaled-down model of the FFA-W3 airfoil is not analysed. This data is available for a limited number of test conditions and may provide insights into the effect of blockage on the results.

References

Aditya, A., De Tavernier, D., Schrijer, F., Van Oudheusden, B., & Von Terzi, D. (2024). Experimental investigation of the occurrence of transonic flow effects on the ffa-w3-211 airfoil. *Journal of Physics: Conference Series*, *2767*(2), 022031.

Anderson, J. (2011). *Ebook: Fundamentals of aerodynamics (si units)*. McGraw hill.

Babinsky, H., & Harvey, J. K. (2011). *Shock wave-boundary-layer interactions* (Vol. 32). Cambridge University Press.

Balat, M. (2009). A review of modern wind turbine technology. *Energy Sources, Part A*, *31*(17), 1561–1572.

Bannink, W. J. (1987). *Derde jaars praktikum compressible aerodynamics hsl2* [Unpublished manuscript, Delft University of Technology], Delft University of Technology.

Barbir, F., Veziro□lu, T., & Plass Jr, H. (1990). Environmental damage due to fossil fuels use. *International journal of hydrogen energy*, *15*(10), 739–749.

Baur, T. (1999). Piv with high temporal resolution for the determination of local pressure reductions from coherent turbulence phenomena. *Proc. 3rd Int. Workshop on PIV-Santa Barbara*, 101–106.

Bertagnolio, F., Sørensen, N. N., Johansen, J., & Fuglsang, P. (2001). Wind turbine airfoil catalogue. *[No journal title]*.

Blume, P. A. (2007). *The labview style book*. Pearson Education.

Campobasso, M. S., Sanvito, A. G., Drofelnik, J., Jackson, A., Zhou, Y., Xiao, Q., & Croce, A. (2018). Compressible navier-stokes analysis of floating wind turbine rotor aerodynamics. *International Conference on Offshore Mechanics and Arctic Engineering*, *51975*, V001T01A031.

Cao, J., Qin, Z., Ju, Y., Chen, Y., Shen, W. Z., Shen, X., & Ke, S. (2023). Study of air compressibility effects on the aerodynamic performance of the iea-15 mw offshore wind turbine. *Energy Conversion and Management*, *282*, 116883.

Chen, T., & Liou, L. (2011). Blockage corrections in wind tunnel tests of small horizontal-axis wind turbines. *Experimental Thermal and Fluid Science*, *35*(3), 565–569.

Council, G. W. E. (2024). Gwec global wind report 2024. *GWEC: Brussels, Belgium*.

Crouch, J. D., Garbaruk, A., Magidov, D., & Travin, A. (2009). Origin of transonic buffet on aerofoils. *Journal of fluid mechanics*, *628*, 357–369.

D'Aguanno, A. (2023). Physics and control of transonic buffet.

D'Aguanno, A., Corduas, A., Schrijer, F., & van Oudheusden, B. (2025). Non-intrusive estimation of the buffet loads on a supercritical airfoil with scbs. *Experiments in Fluids*, *66*(4), 80.

De Tavernier, D., & Von Terzi, D. (2022). The emergence of supersonic flow on wind turbines. *Journal of Physics: Conference Series*, *2265*(4), 042068.

Deck, S. (2005). Numerical simulation of transonic buffet over a supercritical airfoil. *AIAA journal*, *43*(7), 1556–1566.

Donker Duyvis, F. (2005). Laser sheet probe design for piv in high speed wind tunnels. *Proc. PIVNET II International Workshop on the Application of PIV in Compressible Flows, Delft, the Netherlands*.

Elsenaar, A. (1997). Separation in transonic flow: A shocking experience.

Enevoldsen, P., & Xydis, G. (2019). Examining the trends of 35 years growth of key wind turbine components. *Energy for sustainable development*, *50*, 18–26.

Gaertner, E., Rinker, J., Sethuraman, L., Zahle, F., Anderson, B., Barter, G. E., Abbas, N. J., Meng, F., Bortolotti, P., Skrzypinski, W., et al. (2020). *Iea wind tcp task 37: Definition of the iea 15-megawatt offshore reference wind turbine* (tech. rep.). National Renewable Energy Lab.(NREL), Golden, CO (United States).

Gamble, H. (1951). Some effects of reynolds number on a cambered wing at high subsonic mach numbers.

Giannelis, N. F., Levinski, O., & Vio, G. A. (2018). Influence of mach number and angle of attack on the two-dimensional transonic buffet phenomenon. *Aerospace Science and Technology*, *78*, 89–101.

Giannelis, N. F., Vio, G. A., & Levinski, O. (2017). A review of recent developments in the understanding of transonic shock buffet. *Progress in Aerospace Sciences*, *92*, 39–84.

Gibb, J. (1990). The cause and cure of periodic flows at transonic speeds.

Gielen, D., Boshell, F., Saygin, D., Bazilian, M. D., Wagner, N., & Gorini, R. (2019). The role of renewable energy in the global energy transformation. *Energy strategy reviews*, *24*, 38–50.

Haines, A., Holder, D., & Pearcey, H. (1957). *Scale effects at high subsonic and transonic speeds, and methods for fixing boundary-layer transition in model experiments*. HM Stationery Office.

Hand, M., Simms, D., Fingersh, L., Schreck, S., & Larwood, S. (2001). *Nrel unsteady aerodynamics experiment in the nasa-ames wind tunnel: A comparison of predictions to measurements* (tech. rep.). NREL TP-500-29494, Jun.

Hartmann, A., Feldhusen, A., & Schröder, W. (2013). On the interaction of shock waves and sound waves in transonic buffet flow. *Physics of Fluids*, *25*(2).

Herriot, J. G. (1947). *Blockage corrections for three-dimensional-flow closed-throat wind tunnels, with consideration of the effect of compressibility* (tech. rep.).

Hilton, W. F., & Fowler, R. (1947). Photographs of shock wave movement.

Hossain, M. A., Huque, Z., & Kammalapati, R. R. (2013). Propagation of shock on nrel phase vi wind turbine airfoil under compressible flow. *Journal of Renewable Energy*, *2013*(1), 653103.

Hubbert, M. K. (1949). Energy from fossil fuels. *Science*, *109*(2823), 103–109.

Iovnovich, M., & Raveh, D. E. (2012). Reynolds-averaged navier-stokes study of the shock-buffet instability mechanism. *AIAA journal*, *50*(4), 880–890.

Jacquin, L., Molton, P., Deck, S., Maury, B., & Soulevant, D. (2009). Experimental study of shock oscillation over a transonic supercritical profile. *AIAA journal*, *47*(9), 1985–1994.

Jones, B. (1936). *The measurement of profile drag by the pitot-traverse method*. H.M. Stationery Office.

Jonkman, J., Butterfield, S., Musial, W., & Scott, G. (2009). *Definition of a 5-mw reference wind turbine for offshore system development. national renewable energy laboratory, golden* (tech. rep.). CO, Technical Report No. NREL/TP-500-38060.

Krogstad, P.-Å., & Eriksen, P. E. (2013). “blind test” calculations of the performance and wake development for a model wind turbine. *Renewable energy*, *50*, 325–333.

Lee, B. (1990). Oscillatory shock motion caused by transonic shock boundary-layer interaction. *AIAA journal*, *28*(5), 942–944.

Lee, B. (2001). Self-sustained shock oscillations on airfoils at transonic speeds. *Progress in Aerospace Sciences*, *37*(2), 147–196.

Liang, Y. B., Zhang, L. X., Li, E. X., Liu, X. H., & Yang, Y. (2014). Design considerations of rotor configuration for straight-bladed vertical axis wind turbines. *Advances in Mechanical Engineering*, *2014*, 1–15.

Mabey, D. (1981). Oscillatory flows from shock induced separations on biconvex aerofoils of varying thickness in ventilated wind tunnels. *1981. 14*.

McDevitt, J. B., & Okuno, A. F. (1985). *Static and dynamic pressure measurements on a naca 0012 airfoil in the ames high reynolds number facility* (tech. rep.).

Mezzacapo, A., Vitulano, M. C., Tomasso, A., & De Stefano, G. (2023). Cfd prediction of wind turbine blade compressible aerodynamics. *International Conference on Computational Science and Its Applications*, 113–125.

Moise, P., Zauner, M., Sandham, N. D., Timme, S., & He, W. (2023). Transonic buffet characteristics under conditions of free and forced transition. *AIAA Journal*, *61*(3), 1061–1076.

Moulden, T. H. (1984). Fundamentals of transonic flow. *(No Title)*.

Nations, U. (n.d.-a). The 17 goals. https://sdgs.un.org/goals

Nations, U. (n.d.-b). What is climate change? https://www.un.org/en/climatechange/what-is-climate-change#:~:text=But%20since%20the%201800s%2C%20human,sun's%20heat%20and%20raising%20temperatures.

of Energy, U. D. (2023). Airfoils, where the turbine meets the wind. https://www.energy.gov/eere/wind/articles/airfoils-where-turbine-meets-wind

Pearcey, H. (1955). Some effects of shock-induced separation of turbulent boundary layers in transonic flow past aerofoils.

Pearcey, H. (1958). *A method for the prediction of the onset of buffeting and other separation effects from wind tunnel tests on rigid models: This report was presented at the fourteenth meeting of the wind tunnel and model testing panel, held from 20th to 21st october, 1958, in copenhagen, denmark*. North Atlantic Treaty Organization, Advisory Group for Aeronautical Research …

Pearcey, H., & Holder, D. (1962). *Simple methods for the prediction of wing buffeting resulting from bubble type separation*. NPL.

Pirani, S. (2018). *Burning up: A global history of fossil fuel consumption*. Pluto Press.

Raffel, M., Willert, C. E., Scarano, F., Kähler, C. J., Wereley, S. T., & Kompenhans, J. (2018). *Particle image velocimetry: A practical guide*. springer.

Raghunathan, S., Mitchell, R., & Gillan, M. (1998). Transonic shock oscillations on naca0012 aerofoil. *Shock Waves*, *8*, 191–202.

Ragni, D., Ashok, A., Van Oudheusden, B., & Scarano, F. (2009). Surface pressure and aerodynamic loads determination of a transonic airfoil based on particle image velocimetry. *Measurement Science and technology*, *20*(7), 074005.

Ragni, D., Schrijer, F., Van Oudheusden, B., & Scarano, F. (2011). Particle tracer response across shocks measured by piv. *Experiments in fluids*, *50*, 53–64.

Ristić, S., Isaković, J., Ilić, B., & Ocokoljić, G. (2004). Review of methods for flow velocity measurement in wind tunnels. *Scientific Technical Review*, *44*, 60–71.

Samimy, M., & Lele, S. (1991). Motion of particles with inertia in a compressible free shear layer. *Physics of Fluids A: Fluid Dynamics*, *3*(8), 1915–1923.

Schepers, J. G., Boorsma, K., Sørensen, N., Sieros, G., Rahimi, H., Heisselmann, H., Jost, E., Lutz, T., Maeder, T., Gonzalez, A., et al. (2018). Final results from the eu project avatar: Aerodynamic modelling of 10 mw wind turbines. *Journal of Physics: Conference Series*, *1037*(2), 022013.

Settles, G. S. (2001). *Schlieren and shadowgraph techniques: Visualizing phenomena in transparent media*. Springer Science & Business Media.

Shourangiz-Haghighi, A., Haghnegahdar, M. A., Wang, L., Mussetta, M., Kolios, A., & Lander, M. (2020). State of the art in the optimisation of wind turbine performance using cfd. *Archives of Computational Methods in Engineering*, *27*, 413–431.

Sørensen, N. N., Bertagnolio, F., Jost, E., & Lutz, T. (2018). Aerodynamic effects of compressibility for wind turbines at high tip speeds. *Journal of Physics: Conference Series*, *1037*(2), 022003.

Thiery, M., & Coustols, E. (2006). Numerical prediction of shock induced oscillations over a 2d airfoil: Influence of turbulence modelling and test section walls. *International journal of heat and fluid flow*, *27*(4), 661–670.

Tijdeman, H. (1977). Investigations of the transonic flow around oscillating airfoils. *NLR-TR 77090 U*.

Timmer, W., & Bak, C. (2023). Aerodynamic characteristics of wind turbine blade airfoils. In *Advances in wind turbine blade design and materials* (pp. 129–167). Elsevier.

Tropea, C., Yarin, A. L., Foss, J. F., et al. (2007). *Springer handbook of experimental fluid mechanics* (Vol. 1). Springer.

UNFCCC. The paris agreement. In: In *Proceedings of the paris climate change conference*. Climate Change Association. 2015.

Van Oudheusden, B. W., Scarano, F., Roosenboom, E. W., Casimiri, E. W., & Souverein, L. J. (2007). Evaluation of integral forces and pressure fields from planar velocimetry data for incompressible and compressible flows. *Experiments in fluids*, *43*, 153–162.

Van Oudheusden, B. (2008). Principles and application of velocimetry-based planar pressure imaging in compressible flows with shocks. *Experiments in fluids*, *45*(4), 657–674.

Van Oudheusden, B., Scarano, F., & Casimiri, E. (2006). Non-intrusive load characterization of an airfoil using piv. *Experiments in Fluids*, *40*, 988–992.

van Rijswijk. (2012). Tst-27 transonic control.

Vitulano, M. C., De Tavernier, D. A. M., De Stefano, G., & von Terzi, D. A. (2024). Numerical analysis of transonic flow over the ffa-w3-211 wind turbine tip airfoil. *Wind Energy Science Discussions*, *2024*, 1–19.

Vitulano, M., De Tavernier, D., De Stefano, G., & Von Terzi, D. (2024). Numerical analysis of static and dynamic wind turbine airfoil characteristics in transonic flow. *Journal of Physics: Conference Series*, *2767*(2), 022013.

Vos, R., & Farokhi, S. (2015). *Introduction to transonic aerodynamics* (Vol. 110). Springer.

White, F. M. (1991). Viscous fluid flow 2nd ed. *New York*.

Wood, D. (1997). Some effects of compressibility on small horizontal-axis wind turbines. *Renewable energy*, *10*(1), 11–17.

Yan, C., & Archer, C. L. (2018). Assessing compressibility effects on the performance of large horizontal-axis wind turbines. *Applied Energy*, *212*, 33–45.

Zahle, F., Barlas, T., Lonbaek, K., Bortolotti, P., Zalkind, D., Wang, L., Labuschagne, C., Sethuraman, L., & Barter, G. (2024). *Definition of the iea wind 22-megawatt offshore reference wind turbine* (tech. rep.). National Renewable Energy Laboratory (NREL), Golden, CO (United States).

A
Aerodynamic load sensitivity to contour definition

The sensitivity of the time-averaged lift and drag coefficient for all FFA-W3-211 airfoil experiments is illustrated in Figure A.1 and Figure A.2.

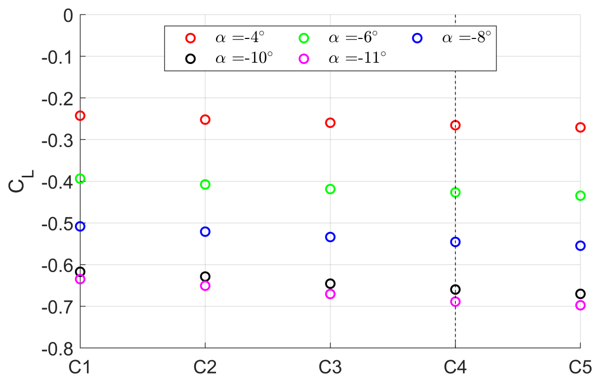

(a) M_∞ = 0.5

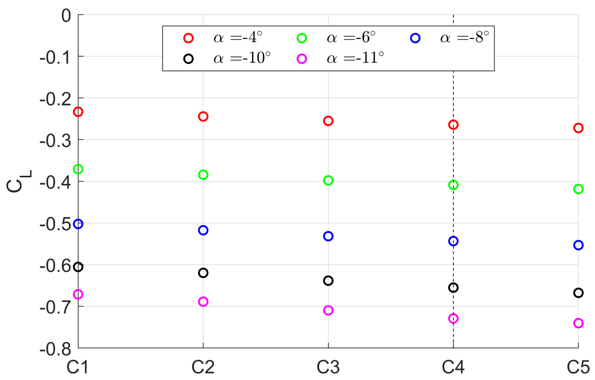

(b) M_∞ = 0.55

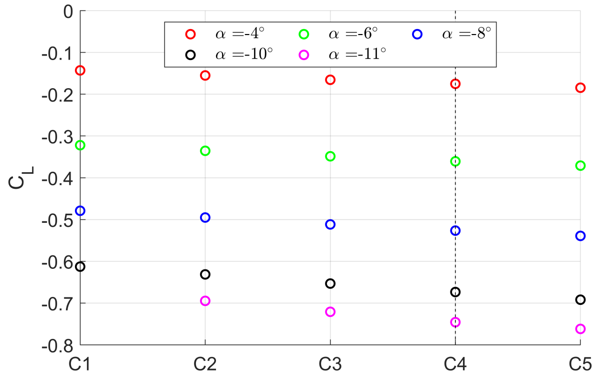

(c) M_∞ = 0.6

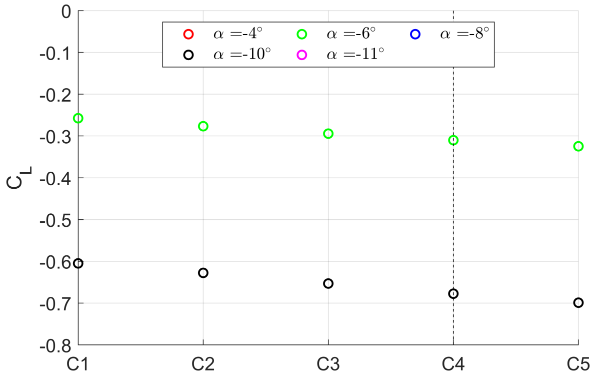

(d) M_∞ = 0.65

Figure A.1: Sensitivity of the lift coefficient for different contour variations, for all AoAs and freestream Mach numbers. The dashed line coincides with Contour 4, from which all results have been derived and from which the sensitivity was performed.

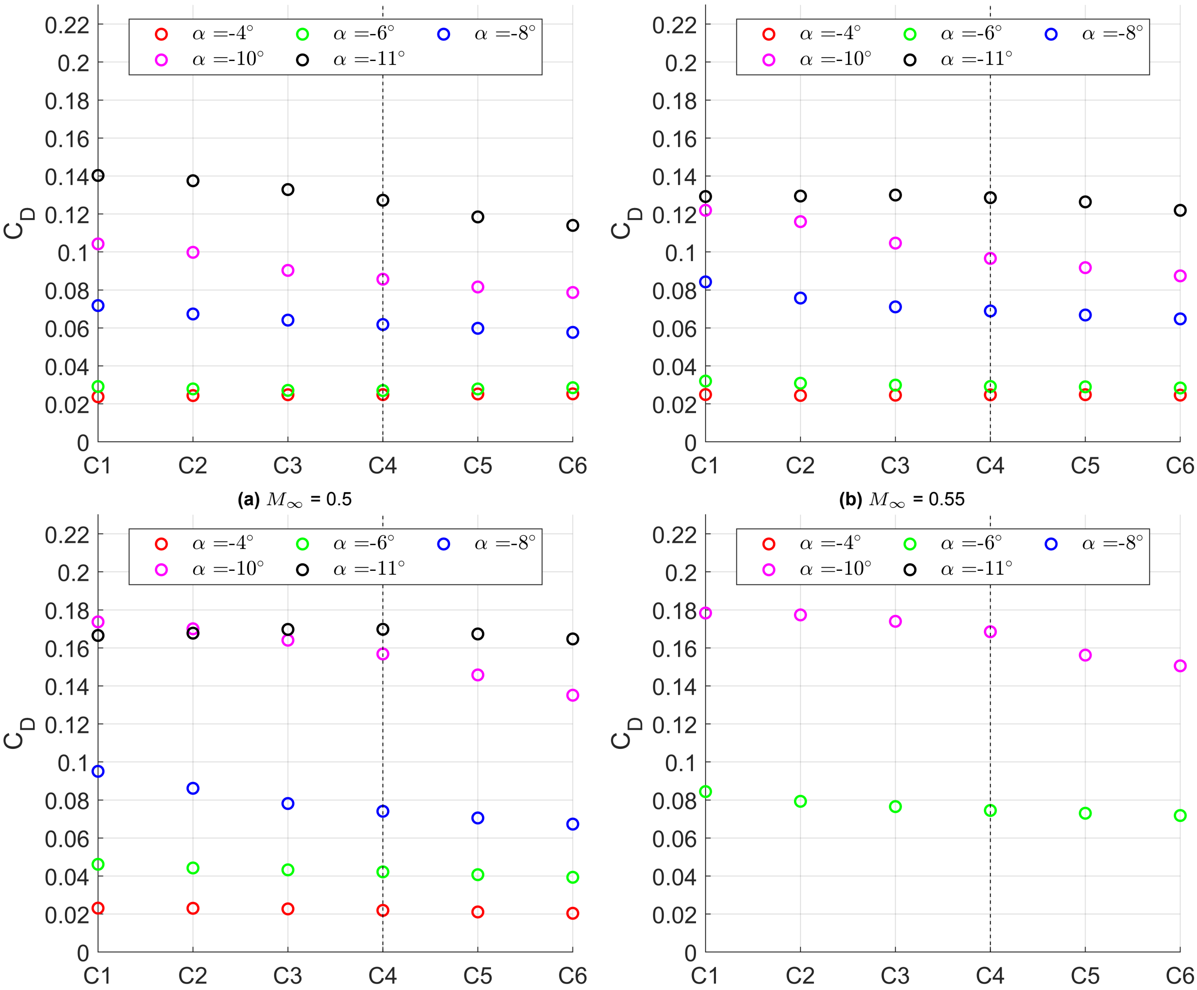

(a) M_∞ = 0.5

(b) M_∞ = 0.55

(c) M_∞ = 0.6

(d) M_∞ = 0.65

Figure A.2: Sensitivity of the lift coefficient for different contour variations, for all AoAs and freestream Mach numbers. The dashed line coincides with Contour 4, from which all results have been derived and from which the sensitivity was performed.

B

Phase-averaged lift contributions across the contour segments

The individual contributions to the phase-averaged, in terms of the pressure and momentum terms, for all of the four segments defining the contour are illustrated in Figure B.1. The pressure term is the dominant contribution over the top and bottom contour segments. Both the pressure and momentum terms have a comparable contribution along the left and right contour segments.

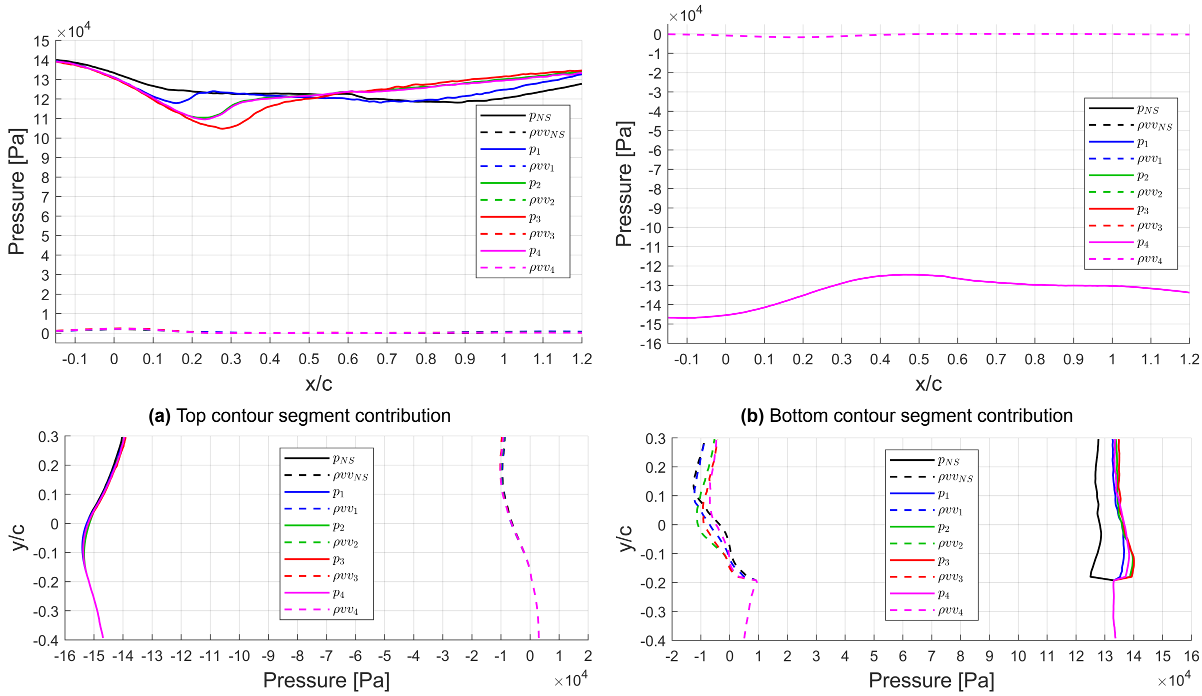

(a) Top contour segment contribution

(b) Bottom contour segment contribution

(c) Left contour segment contribution

(d) Right contour segment contribution

Figure B.1: Contribution to the lift across the four contour segments. Line colour distinguishes phase. The

C

Mean flow field for the NACA 0012 experiments

The mean non-dimensionalized u and v velocity fields for the NACA 0012 experiments are shown in Figure C.1.

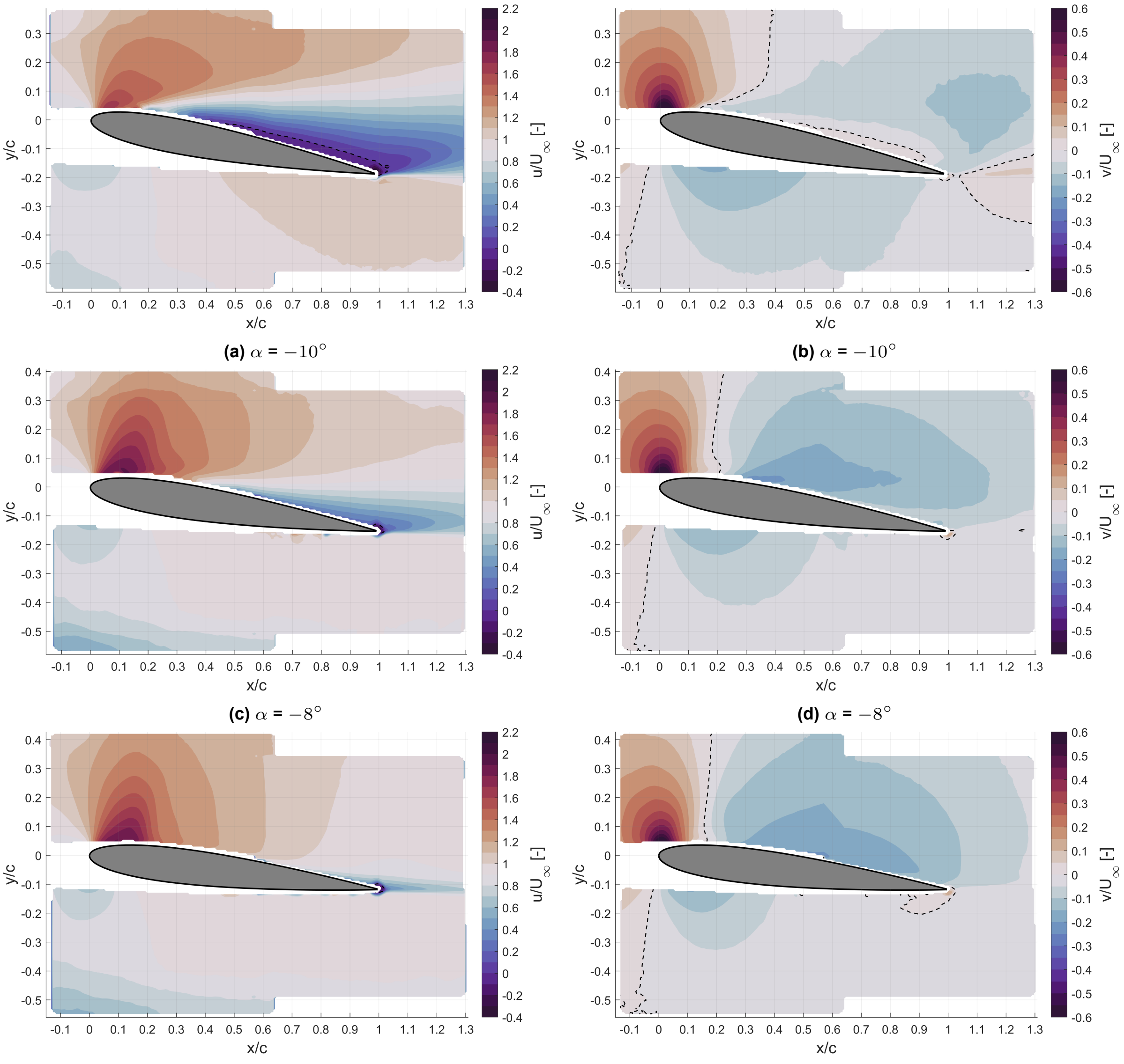

(a) $\alpha = -10^\circ$ (b) $\alpha = -10^\circ$
(c) $\alpha = -8^\circ$ (d) $\alpha = -8^\circ$
(e) $\alpha = -6^\circ$ (f) $\alpha = -6^\circ$

Figure C.1: Mean non-dimensional freestream-aligned velocity field, u/U_∞ (left), and vertical velocity field, v/U_∞ (right), for the NACA 0012 experiments at $\alpha = -6^\circ, -8^\circ$ and -10° at $M_\infty = 0.6$. The dashed line encloses the region where $u \leq 0$ or $v \leq 0$.

The mean Mach number field and the mean pressure coefficient field for the NACA 0012 experiments are shown in Figure C.2.

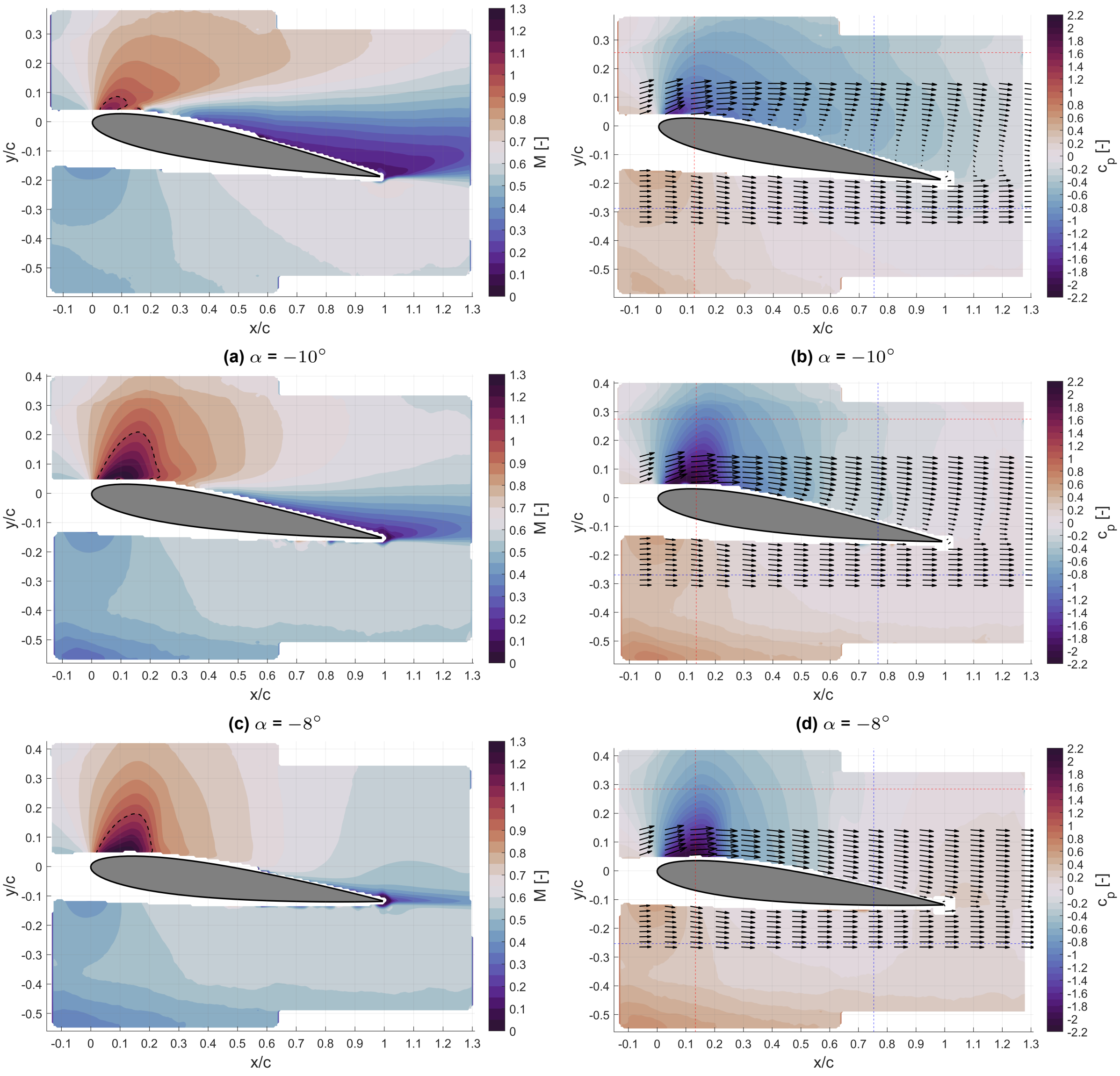

(a) α = $-10°$ (b) α = $-10°$

(c) α = $-8°$ (d) α = $-8°$

(e) α = $-6°$ (f) α = $-6°$

Figure C.2: Mean Mach number field, M (left), and mean pressure coefficient field, c_p (right), for the NACA 0012 experiments at $\alpha = -6°, -8°$ and $-10°$ at $M_\infty = 0.6$.

In Figure C.3, an estimate of the wake thickness is visualised through the total pressure deficit in the wake. As observed, $\alpha = -6°$ shows the narrowest wake.

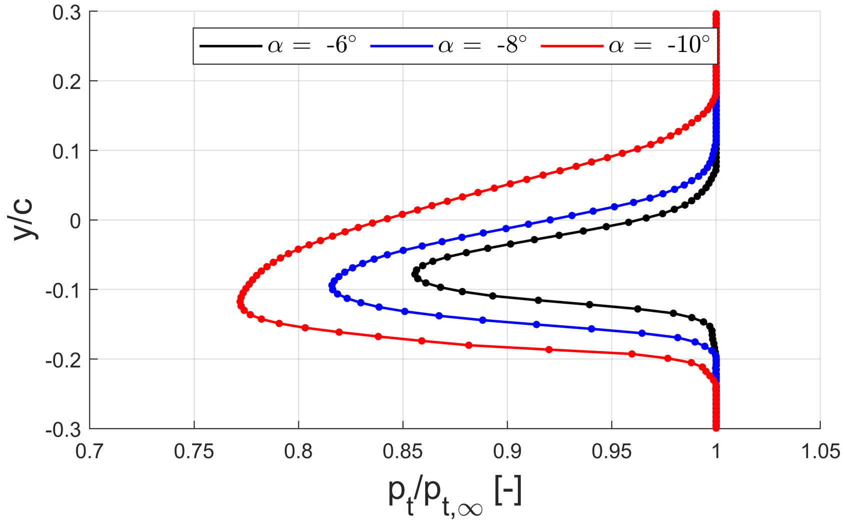

Figure C.3: Total pressure wake deficit for the NACA 0012 experiments at a distance $x/c = 1.2$, for $M_\infty = 0.6$